

Finite Element Simulation of Water Cooling Process  
of Steel Strips on Runout Table

By

Fuchang Xu

B.Sc., University of Science and Technology Beijing, China, 1984

M.Sc., University of Science and Technology Beijing, China, 1987

A THESIS IN PARTIAL FULFILLMENT OF  
THE REQUIREMENT FOR THE DEGREE OF

DOCTOR OF PHILOSOPHY

in

THE FACULTY OF GRADUATE STUDIES  
(Mechanical Engineering)

THE UNIVERSITY OF BRITISH COLUMBIA

March 2006

© Fuchang Xu, 2006

## Abstract

This study engages in acquiring reliable heat transfer data from experimental tests using a test facility of industrial scale for an effective FE simulation of the water cooling processes of steel strips on run-out table (ROT).

General 2D FE programs are developed for the direct and inverse heat transfer analyses. Both the Flux Zoning Method (FZM) and Flux Marching Method (FMM) are proposed to specify the heat fluxes in the inverse analysis. Parametric studies have been conducted and show that the direct analysis program may produce results with a higher accuracy, and that the FZM and FZM are suitable for obtaining an accurate relationship between the heat flux and the surface temperature in the impingement zone and in the parallel zone, respectively.

The direct numerical investigations show that the isothermal condition does not exist for thermocouples (TC) with separate measuring junction in the water cooling process, and that the temperature difference between the two separate TC wires is affected strongly by the conduction of the surface TC wires in the impingement zone and by the progressing speed of black zone front in the parallel zone, respectively. The numerical analyses also show that the horizontal distance between TCs should be less than 8–10 mm to warrant a real 2D inverse calculation, and that there is a minimum depth for the embedded TCs for an undisturbed surface temperature field.

The inverse analysis results of experimental tests show that the heat transfer behaviour at the stagnation for stationary plates is mainly and greatly affected by the water temperature, slightly by the steel grade and hardly by water flow rate. By contrast, the cooling behaviour in the parallel zone is obviously affected by the flow rate and hardly by the water temperature. It is also found that the plate's motion evidently reduces the heat flux magnitude.

Extensive 1D simulations to the cooling processes of the steel strips on an industry ROT show that the final coiling temperatures of steel strips may be predicted with a reasonable accuracy. Also, initial studies show that 2D modellings may have modest impact on the accuracy of the coiling temperature prediction.

## Table of Contents

<b>Abstract</b> .....	ii
<b>Table of Contents</b> .....	iii
<b>List of Tables</b> .....	viii
<b>List of Figures</b> .....	ix
<b>List of Symbols and Abbreviations</b> .....	xv
<b>Acknowledgements</b> .....	xvii
<b>Chapter 1 Introduction</b> .....	1
1.1 Controlled Cooling and Its Benefits.....	1
1.2 Controlled Cooling Systems.....	2
1.3 Heat Transfer during Water Cooling Process on Runout Table (ROT).....	3
1.4 Experimental and Numerical Investigations.....	5
1.5 Objectives of This Study.....	6
<b>Chapter 2 Backgrounds and Literature Review</b> .....	8
2.1 Water Jet Impingement Cooling.....	8
2.1.1 Hydrodynamics of water jet impingement.....	8
2.1.2 Representative investigations.....	12
2.1.3 Research work at UBC:.....	17
2.2 Temperature Measurement Errors.....	20
2.2.1 Thermocouple (TC) thermometry.....	20
2.2.2 Measurement errors using TC .....	22
2.2.3 Section summary and discussion.....	25
2.3 Numerical Methods for Inverse Heat Conduction Problem (IHCP) .....	27
2.3.1 Common techniques.....	28
2.3.2 Typical previous studies.....	30
2.3.3 Specification of heat flux.....	32

2.4 TC Installation.....	33
2.4.1 Horizontal distance.....	34
2.4.2 Vertical depth.....	34
2.4.3 Effective TC depth.....	35
<b>Chapter 3 Program for Direct and Inverse Heat Conduction Analyses.....</b>	<b>37</b>
3.1 Program for Direct Analysis.....	37
3.1.1 Formulation.....	37
3.1.2 Implementation and validation.....	40
3.2 Formulation for Inverse Analysis.....	40
3.2.1 Objective function.....	40
3.2.2 General calculation form of heat flux.....	42
3.2.3 Iterative and sequential algorithms.....	44
3.2.4 Convergence norm.....	47
3.2.5 Flux zoning method (FZM) .....	48
3.2.6 Flowchart.....	49
3.3 Parametric Study to FZM.....	49
3.3.1 Test procedure and data.....	51
3.3.2 Triangular heat flux inputs.....	52
3.3.3 Impulse-like heat flux inputs.....	56
3.4 Summary.....	61
<b>Chapter 4 Flux Marching Method (FMM) for IHCP in Water Jet Cooling.....</b>	<b>62</b>
4.1 Progression of Water Jet Cooling Zones.....	62
4.1.1 Stationary plate case.....	62
4.1.2 Moving plate case.....	64
4.1.3 Moving speed of waterfront in stationary cases.....	64
4.2 Drawback of FZM.....	66
4.3 Main Features of FMM.....	69
4.4 Numerical Tests.....	73
4.4.1 Test procedure and setup.....	73
4.4.2 FE model.....	75

4.4.3 Realization of waterfront movement.....	76
4.5 Results and Discussion.....	77
4.5.1 Reduction of peak value using FZM.....	78
4.5.2 Shape change of heat flux using FZM.....	79
4.5.3 Mis-prediction of surface temperature using FZM.....	81
4.5.4 Effect of speed mismatch using FMM.....	81
4.5.5 Effect of flux jump using FMM.....	87
4.6 Summary and Prospects.....	89
4.7 Flowchart for the IHCP Solution Procedure.....	90
<b>Chapter 5 Appropriate Installations of Thermocouples in Water Jet Cooling.....</b>	<b>93</b>
5.1 Error in the Measured Temperatures.....	93
5.2 Stationary Case.....	96
5.2.1 Effect of TC wire conduction.....	96
5.2.2 Effect of drilling a hole.....	100
5.2.3 Effect of plate material.....	104
5.2.4 Effect of contact with water.....	105
5.2.5 Section summary.....	106
5.3 Moving Case.....	107
5.3.1 Motivation of study.....	107
5.3.2 FE Model.....	107
5.3.3 Results and discussion.....	111
5.3.4 Section summary.....	121
5.4 Appropriate TC Position.....	122
5.4.1 General modelling aspects.....	122
5.4.2 Appropriate horizontal distance.....	123
5.4.3 Appropriate vertical depth.....	125
5.4.4 Effective TC depth.....	127
5.4.5 Section summary.....	129
5.5 Summary.....	130

<b>Chapter 6 Heat Transfer Behavior under a Circular Water Jet</b> .....	131
6.1 Experimental Tests.....	131
6.1.1 Tests using stationary plates.....	131
6.1.2 Tests using moving plates.....	134
6.2 Validation and Application of the Effective Depth Approach (EDA).....	137
6.3 Heat Transfer in the impingement Zone of Stationary Plates.....	143
6.3.1 Initial investigations.....	143
6.3.2 Heat transfer behaviour.....	145
6.3.3 Section summary.....	155
6.4 Heat Transfer in the Parallel Zone of Stationary Plates.....	156
6.4.1 Case study.....	157
6.4.2 Parameter effects.....	159
6.5 Heat Transfer for the Moving Plates.....	162
6.6 Summary.....	164
<b>Chapter 7 Simulation of Run-out Table Cooling Process</b> .....	165
7.1 Simplification of Governing Equation.....	165
7.2 Modeling and Implementation.....	169
7.2.1 Numerical method.....	169
7.2.2 Initial condition.....	169
7.2.3 Boundary condition.....	170
7.2.4 Temperature dependences of thermophysical properties.....	174
7.2.4 Latent heat.....	175
7.2.6 Microstructure evolution and property predication.....	175
7.2.7 Program structure.....	176
7.3 Studies on ROT Cooling.....	179
7.3.1 Case study.....	179
7.3.2 Parametric study.....	184
7.4 Investigation of Necessarity of 2D Simulation of ROT Cooling.....	191
7.4.1 2D transverse modelling.....	191
7.4.2 2D longitudinal modelling.....	195

7.5 Summary.....	201
<b>Chapter 8 Conclusions and Future Work.....</b>	<b>202</b>
8.1 Conclusions.....	202
8.2 Suggestions and Future Work.....	208
<b>Bibliography .....</b>	<b>212</b>
<b>Appendix A Finite Element Matrix Equations for Conduction Heat Transfer.....</b>	<b>220</b>

## List of Tables

Table 4.1	Test scheme and result using FZM.....	74
Table 4.2	Node in calculation zone.....	76
Table 4.3	Calculated heat flux accuracy at TC3 with speed mismatch in FMM....	85
Table 5.1	Data for FEM model.....	97
Table 5.2	Heat flux type notation.....	110
Table 5.3	Minimum depth for practical water cooling.....	126
Table 6.1	Experimental tests using stationary plates.....	132
Table 6.2	Hydrodynamic parameters at the stagnation point.....	132
Table 6.3	Comparison of results using different approaches.....	137
Table 7.1	Bank state code.....	180
Table 7.2	Examples of cooling parameters.....	180
Table 7.3	Examples of calculation results.....	181
Table 7.4	Effect of time step on the coiling temperature for Case 192.....	185
Table 7.5	Longitudinal modelling parameters and results.....	196

## List of Figures

Figure 1.1	A typical hot rolling strip mill.....	1
Figure 1.2	Controlled cooling systems.....	2
Figure 1.3	Schematic of jet configurations.....	4
Figure 2.1	Schematic of the boiling curve.....	9
Figure 2.2	Variation of HTC with temperature for saturated water.....	9
Figure 2.3	Velocity and pressure distribution.....	10
Figure 2.4	Heat transfer regions for steady state water jet.....	11
Figure 2.5	ROT test facility at UBC.....	17
Figure 2.6	Schematic arrangements of TCs.....	19
Figure 2.7	Seebeck voltage.....	21
Figure 2.8	Measuring junctions.....	21
Figure 2.9	Parameters for TC installation.....	33
Figure 3.1	Boundary conditions for a general heat conduction problem.....	38
Figure 3.2	FZM FE Model for inverse calculation.....	48
Figure 3.3	Flowchart for FZM IHCP solution procedure.....	50
Figure 3.4	Triangular heat flux inputs.....	52
Figure 3.5	Effect of measurement error level.....	53
Figure 3.6	Effect of number of future steps.....	54
Figure 3.7	Effect of regularization parameter.....	55
Figure 3.8	Impulse-like heat flux inputs.....	56
Figure 3.9	Effect of regularization parameter.....	57
Figure 3.10	Effect of future step number.....	58
Figure 3.11	Calculated heat flux.....	60
Figure 4.1	Progression of cooling zones.....	63
Figure 4.2	Example of measured temperatures.....	65

Figure 4.3	FZM FE model for verifications.....	67
Figure 4.4	Heat flux required for a same cooling curve.....	68
Figure 4.5	Effect of distribution of heat flux components on the required heat flux.....	69
Figure 4.6	FMM FE Model for inverse calculation.....	70
Figure 4.7	Overstepping of heat flux.....	73
Figure 4.8	Crucial part of typical heat fluxes.....	74
Figure 4.9	FE-model for numerical test.....	75
Figure 4.10	Comparison of heat fluxes.....	77
Figure 4.11	Internal temperature directly calculated in case 2.....	78
Figure 4.12	Input $q_p$ vs. ratio.....	79
Figure 4.13	$V_w$ vs. ratio.....	79
Figure 4.14	Shape change of heat flux using FZM.....	80
Figure 4.15	Heat flux space distribution at time 12 s.....	80
Figure 4.16	Surface temperature differences using FZM.....	82
Figure 4.17	Comparison of $T_s$ Vs. heat flux.....	82
Figure 4.18	Effect of higher speed mismatch using FMM.....	83
Figure 4.19	Intensification of higher speed mismatch.....	84
Figure 4.20	Calculated heat fluxes with higher speed mismatch.....	85
Figure 4.21	Calculated heat fluxes with lower speed mismatch.....	86
Figure 4.22	Calculated heat flux accuracy with speed mismatch.....	87
Figure 4.23	Assigned heat fluxes along the second zone.....	88
Figure 4.24	Effect of heat flux jump.....	88
Figure 4.25	Flowchart for IHCP solution procedure.....	92
Figure 5.1	Typical temperature profiles during water cooling.....	94
Figure 5.2	Inversely calculated heat flux.....	95
Figure 5.3	FEM model for analysis of effect of wire.....	96
Figure 5.4	Disturbed field of surface temperature around the wires.....	98
Figure 5.5	Effects of wire conduction on surface temperatures.....	98
Figure 5.6	Calculated temperature gradient along the wires.....	99

Figure 5.7	Example of FEM model for the effect of hole or cave.....	100
Figure 5.8-a	Effect of 6 mm hole on temperature filed.....	101
Figure 5.8-b	Effect of cave at 6 mm on temperature field.....	101
Figure 5.9	Disturbed temperature fields at 6 mm.....	102
Figure 5.10	Effect of 4 mm hole on temperature filed.....	102
Figure 5.11	Effect of 6 mm hole and K-plus wire.....	103
Figure 5.12	The effect of the inserted third metal.....	104
Figure 5.13	Cooling waterfront and TCs.....	108
Figure 5.14	Typical mesh and sampling points.....	109
Figure 5.15	Types of heat flux profiles.....	109
Figure 5.16	Space distribution of heat flux.....	111
Figure 5.17	Temperature profile results of 3D and 2D analyses.....	112
Figure 5.18	Comparison of temperature difference in 2D and 3D.....	113
Figure 5.19	Effect of the progressing speed of water cooling zones .....	114
Figure 5.20	Effect of stopping distance.....	116
Figure 5.21	Effect of heat flux magnitude.....	117
Figure 5.22	Effect of heat flux magnitude and progressing speed.....	117
Figure 5.23	Effect of the depth of hole and heat flux type.....	118
Figure 5.24	Time instant vs. the depth of hole and heat flux type.....	119
Figure 5.25	Effect of initial temperature.....	120
Figure 5.26	Effect of specific heat.....	121
Figure 5.27	Input of practical heat flux.....	123
Figure 5.28	Temperature vs. TC distance.....	124
Figure 5.29	Minimum depth of TC for ideal cooling.....	125
Figure 5.30	Minimum depth of TC for practical water cooling.....	126
Figure 5.31	Null-calorimeter techniques for carbon steel.....	127
Figure 5.32	Coincidence of temperature for practical cooling.....	128
Figure 5.33	Effective and actual depth of TC.....	129
Figure 6.1	Example A of measured temperatures.....	133
Figure 6.2	Example B of measured temperatures.....	133

Figure 6.3	Example of TC arrangements for moving plates.....	135
Figure 6.4	Example of measured temperatures in moving plate tests.....	136
Figure 6.5	An enlarged portion of Figure 6.4.....	136
Figure 6.6	Boiling curves using different modellings for test #6.....	138
Figure 6.7	Boiling curves using different modellings for test #9.....	138
Figure 6.8	Sensitivity of results to the effective depth for #24.....	139
Figure 6.9	Relationship between the actual depth and effective depth.....	140
Figure 6.10	Overall view of heat flux on the top surface for Test #25.....	142
Figure 6.11	Comparison of results with and without EDA for Test #25.....	142
Figure 6.12	Heat flux in the impingement zone – Two components of heat flux assumed.....	144
Figure 6.13	Heat flux in the impingement zone - One heat flux assumed.....	145
Figure 6.14	Water temperature vs. surface temperature at $Q_w = 15$ l/min.....	146
Figure 6.15	Water temperature vs. surface temperature at $Q_w = 30$ l/min.....	147
Figure 6.16	Effect of water temperature at $Q_w = 15$ l/min.....	147
Figure 6.17	Effect of water temperature at $Q_w = 30$ l/min.....	149
Figure 6.18	Effect of water temperature at $Q_w = 45$ l/min.....	149
Figure 6.19	Effect of water flow rate at $T_w = 30$ °C.....	150
Figure 6.20	Effect of water flow rate at $T_w = 40$ °C.....	151
Figure 6.21	Effect of water flow rate at $T_w = 70$ °C.....	151
Figure 6.22	Effect of water flow rate at $T_w = 80$ °C.....	152
Figure 6.23	Effect of water flow rate at $T_w = 50$ °C.....	152
Figure 6.24	Effect of water flow rate at $T_w = 50$ °C for SS316.....	153
Figure 6.25	Effect of steel grade at $T_w = 30$ °C.....	154
Figure 6.26	Temperature-dependent conductivity.....	155
Figure 6.27	Effect of steel grade at $T_w = 50$ °C.....	156
Figure 6.28	Comparison of cooling curves at TC3 using different approaches for #25.....	157
Figure 6.29	Comparison of peak heat fluxes at the first four locations for #25.....	158
Figure 6.30	Comparison of cooling curves by FMM and EDA for #25.....	158
Figure 6.31	Comparison of cooling curves for #3.....	159

Figure 6.32	Boiling curves at TC3 by FMM for #24 ( $T_w = 30^\circ\text{C}$ ) and #27 ( $T_w = 50^\circ\text{C}$ ).....	160
Figure 6.33	Boiling curves at TC3 by FMM for #22 ( $Q_w = 30$ ) and #24 ( $Q_w = 45$ ).....	161
Figure 6.34	Boiling curves at TC3 by FMM for #3 (DQSK) and #22 (SS316).....	162
Figure 6.35	Effects of the plate's speed and initial temperature on the peak heat flux.....	163
Figure 7.1	Coordinate system used for modeling.....	165
Figure 7.2	Cooling zones under one active jetline.....	171
Figure 7.3	Design of the cooling zone lengths.....	172
Figure 7.4	HTC in air cooling zone.....	173
Figure 7.5	HTC in impingement cooling zone.....	174
Figure 7.6	Schematic illustration of a typical ROT.....	179
Figure 7.7	Prediction accuracy.....	182
Figure 7.8	Temperature profiles for Case 192.....	183
Figure 7.9	HTC profiles around the first bank for Case 192.....	183
Figure 7.10	Temperature profiles around the first bank for Case 192.....	184
Figure 7.11	Effect of impingement width on the coiling temperature for Case 192 .....	185
Figure 7.12	Effect of the starting temperature on the coiling temperature for Case 192.....	186
Figure 7.13	Effect of the strip speed on the coiling temperature for Case 192.....	187
Figure 7.14	Effect of the strip thickness on the coiling temperature for Case 192....	187
Figure 7.15	Effect of the strip conductivity on the coiling temperature for Case 192 .....	188
Figure 7.16	Effect of the strip specific heat on the coiling temperature for Case 192 .....	189
Figure 7.17	Effect of the distance $b_1$ on the coiling temperature for Case 192 .....	190
Figure 7.18	Effect of the distance $L_2$ on the coiling temperature for Case 192 .....	191
Figure 7.19	2D transverse modelling .....	192

Figure 7.20	Effect of transverse HTC difference on the coiling temperature for Case 192 .....	193
Figure 7.21	Effect of transverse HTC difference on the coiling temperature for Case 192 .....	194
Figure 7.22	Temperature distributions on cross section .....	195
Figure 7.23	Movement of model piece .....	197
Figure 7.24	HTC values for the two-jetlines cases.....	197
Figure 7.25	2D-temperature and 1D-2D-temperature difference for Case 752-1....	198
Figure 7.26	2D-temperatures and gradient for Case 752-4.....	200
Figure 8.1	Extra TCs and nozzles for future tests.....	209

## List of Symbols and Abbreviations

$c_p$	Specific heat, J /kg·°C
$C_\alpha$	Seebeck coefficient of thermocouple, $\mu\text{V/K}$
$C_{\alpha s}$	Seebeck coefficient of third metal, $\mu\text{V/K}$
<b>C</b>	Heat capacity matrix
$h$	Heat transfer coefficient (HTC), $\text{W/m}^2\cdot^\circ\text{C}$
$i$	$i^{\text{th}}$ time step
<b>J</b>	Number of heat flux components
$k$	Conductivity, $\text{W/m}\cdot^\circ\text{C}$
$k_x, k_y$	Conductivities in the $x$ - and $y$ -directions, $\text{W/m}\cdot^\circ\text{C}$
<b>K</b>	Heat conduction matrix
<b>L</b>	Number of measurement points
<b>N</b>	Number of total time steps
$n$	Iteration step
$n_x, n_y$	Components of outward normal vector
<b>Q</b>	Flux load vector, J
$q^b$	Heat generation per unit volume, $\text{W/kg}$
$q$	Heat flux, $\text{W/m}^2$
$q^i$	Heat flux at the $i^{\text{th}}$ time step, $\text{W/m}^2$
$q_j$	Component of heat flux vector, $\text{W/m}^2$
<b>q</b>	Heat flux vector, $\text{W/m}^2$
$\mathbf{q}^i$	Heat flux vector at the $i^{\text{th}}$ time step, $\text{W/m}^2$
<b>S</b>	Total boundary domain
$S_1$ to $S_5$	Parts of the boundary domain
<b>T</b>	Temperature, °C
$T_s$	Prescribed temperature or surface temperature, °C
$T_f$	Fluid (ambient) temperature, °C
<b>T</b>	Temperature vector, °C
$\dot{\mathbf{T}}$	Vector of temperature derivate to time, °C/s

$\mathbf{T}_m^i$	Measured temperature vector at the $i^{\text{th}}$ time step, °C
$\mathbf{T}_c^i$	Calculated temperature vector at the $i^{\text{th}}$ time step, °C
$t$	Time, s
$x, y$	Lagrangian coordinates, m
$\mathbf{X}$	Total sensitivity matrix for multi-dimensional problem
$\mathbf{X}^i$	Sensitivity matrix at the $i^{\text{th}}$ time step
$\rho$	Density, kg/m <sup>3</sup>
$\Delta t$	Time step, s
$\Delta T$	Temperature difference, °C
$\Delta \mathbf{T}$	Temperature difference vector, °C
$\alpha$	Regularization parameter
$\sigma$	Stefan Boltzmann constant, W/m <sup>2</sup> ·K <sup>4</sup>
$\varepsilon$	Emissivity
FE	Finite element
FTS	Future time step
HTC	Heat transfer coefficient
IHCP	Inverse heat conduction problem
TC	Thermocouple
1D	One dimensional
2D	Two dimensional
3D	Three dimensional

## Acknowledgements

A Ph.D. thesis is never the result of the author but an achievement of many persons.

My sincerest gratitude and deep appreciation go to my supervisor Prof. Dr. Mohamed S. Gadala for his judicious academic advice, for his financial and personal support. His invaluable guidance and encouragement had been the foundation and source for me to effectively proceed and finish this work. His careful revision enormously contributed to the production of this thesis.

Many thanks also go to Prof. Dr. M. Militzer and Dr. V. Prodanovic for their valuable suggestions and insightful discussions at various stages of this work.

Thanks to my colleagues in FE-lab and in the Strategic Group for their help and suggestions. They had also shared their knowledge, experience and culture with me and thus my view had been broadened.

Special thanks to my family and my mother who offered continuous moral support and encouragement. To them and my past-away father, I dedicate this thesis.

Fuchang Xu

## Chapter 1

### INTRODUCTION

#### 1.1 Controlled Cooling and Its Benefits

Steel strip is one of the most versatile hot rolled products with a wide variety of applications ranging from automobile bodies to soft drink cans. For the production line shown in Figure 1.1 [1], steel strips are produced from slabs approximately 250 mm thick. The slabs are reheated in a reheating furnace to hot rolling temperatures close to 1250 °C, rolled sequentially by the roughing and finishing mills, and turned into strips of about 1 mm to 20 mm in thickness. After being rolled, the strips are cooled down to 550–650 °C while they pass through a so-called run-out table (ROT).

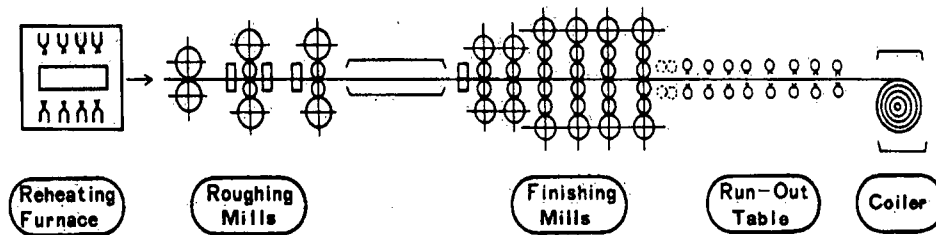


Figure 1.1 A typical hot rolling strip mill [1]

While the geometry and surface quality of steel strips are mainly influenced by the rolling deformation procedures, the microstructure and mechanical properties are highly dependent on the controlled cooling procedure on a ROT. The controlled cooling process of steel refers to the cooling process very specially designed and applied immediately after the finishing stand. In a controlled cooling process, the cooling start and finish temperatures, and the cooling rates are exercised accurately according to the expected properties in terms of phase composition, size, and distribution.

One of the benefits due to this process is grain refinement. A finer grain size leads to an increase in strength, an improved notch toughness and resistance to brittle fracture; and contributes to an appreciable reduction in carbon content, while still maintaining the same strength level. The lower carbon content improves formability and contributes to superior notch toughness and weldability. In short, a controlled cooling process will assure a balanced

combination of mechanical properties, and narrows the gap in the properties between the as-hot rolled high strength, low alloy steels and those requiring a special heat treatment step.

## 1.2 Controlled Cooling Systems

Typically 50–100 m in length, a ROT is made up of a set of cooling banks placed above and under the strips, and an array of motorized rollers. Cooling systems are required to have a large cooling efficiency, and to be capable of producing the desired microstructures and mechanical properties. There are three main types of cooling systems used for the controlled cooling process of steel strips on a ROT: water spray, laminar flow (circular jet) and water curtain, as shown in Figure 1.2 [2].

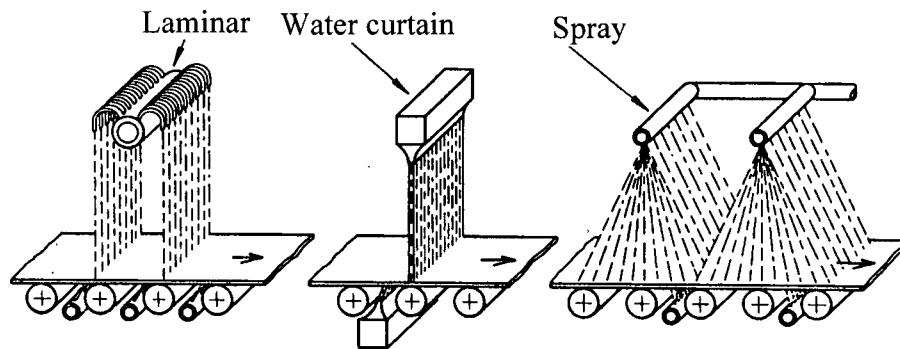


Figure 1.2 Controlled cooling systems [2]

In a water spray system, the water as coolant impinges from a row of specially designed nozzles onto the strip. The water spray is often used to cool the bottom surface and to sweep the top surface to ensure the accuracy of pyrometer measurements. This kind of cooling system is not included in this study and will not be discussed any more.

The laminar flow is preferred because it can penetrate the vapour film on the cooled surface and increase the coolant residence time. While each of the laminar cooling apparatus consists of two or four rows of U-pipes, this system creates low-pressure, laminar flow streams, and therefore has a higher cooling efficiency than the water spray system.

In the water curtain system, the strip is cooled by a planar jet, which spans the entire width of the strip. In addition to the advantages of a laminar jet system, it also improves the uniformity of cooling in the strip's transverse direction.

Typical cooling conditions on a ROT for the strip hot rolling [3] are:

Cooling rate:	5–150 °C/s
Cooling efficiency:	10–400 kJ/kg
Heat flux:	$10^5$ – $10^7$ W/m <sup>2</sup>
Heat transfer coefficient (HTC):	$10^3$ – $10^5$ W/m <sup>2</sup> ·°C

The basic requirements for the cooling system are summarized as follows. First, cooling must be uniform in every location of the top and bottom surfaces, the edge and centre, and the leading and trailing ends. Also, there must be no hard spots at any location. Second, any distortion and residual stress due to water-cooling must be minimized. Third, the cooling rate and the cooling start and finish temperatures must be accurately controlled. These requirements are not simple ones because, for example, there are already temperature variations between the centre and the periphery of a strip, even immediately after the finish rolling.

### **1.3 Heat Transfer during Water Cooling Process on Run-out Table (ROT)**

Although this cooling process has been used in the steel industry for decades, it is still mainly a trial and error procedure when new products are developed. This is because the thermal events during the cooling process are very complex, and a fundamental understanding of this process is not yet complete.

In a typical hot strip rolling mill, for example, a steel strip leaves the last finishing stand at temperatures ranging from 750 to 1000 °C, and is rapidly transported along a ROT; the strip is subsequently or alternatively subjected to air-cooling and water-cooling. Due to the high temperatures of a steel strip during the water-cooling periods, the nucleate boiling is typically confined to a small region beneath the jet, while the film boiling exists over most of the surface at locations upstream and downstream of the stagnation point. It is clear that there are conductive heat transfers in three directions, i.e., width, thickness and length directions within the strip. It is also obvious that there appears heat loss due to the conduction of the strip to the water and the rolls and due to the radiation of the strip to the air.

As for the water-cooling mechanism, both the laminar flow and water curtain systems belong to jet impingement cooling with continuous cross sections. They may be either free-surface

jet or plunging jet, as shown in Figure 1.3 [4]. The free-surface jet is injected into an immiscible atmosphere, and the liquid travels relatively unimpeded to the impingement surface. The bottom surface cooling as well as the top surface cooling (when there is no residual water) can be classified in this category. The plunging jet impinges onto a pool of liquid covering the surface, where the depth of the pool is less than the nozzle-surface spacing. If there is a residual water layer on the top surface from the other jets, this kind of jet appears.

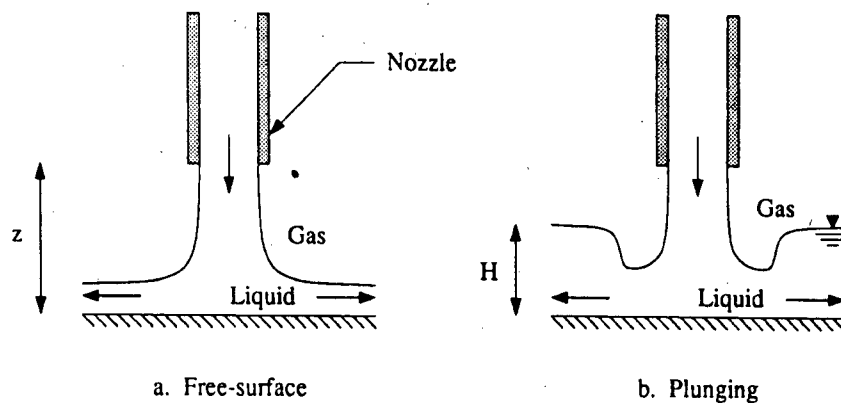


Figure 1.3 Schematic of jet configurations [4]

For stationary cases [5–12], i.e., when the cooled plate does not move, the cooled area on the top surface is symmetrical to the water jetline for the water curtain or a row of circular nozzles, or axisymmetrical to the stagnation point for a single circular jet. When water impinges onto the cooling surface, it first vertically hits the plate and then moves transversely or radially. With the spreading out of the cooling water the plate cools down. This stationary cooling process exists only in laboratory conditions.

For moving cases [13–22], i.e., when the workpiece moves, the heat transfer is no longer symmetrical to the water jetline for the water curtain or a row of circular nozzles; and it is only symmetrical to the moving direction of workpiece for a single circular jet. On the side where the water flow and workpiece move in the same direction, the thickness of the vapour layers beneath the pools and in the film boiling regime decrease because vapour flow may be promoted by the workpiece motion. By contrast, the vapour layer thickness may increase due

to stretching toward the jet by such a motion on the other side where the water flow and workpiece travel in the opposite direction.

Making the cooling process on a ROT even more complicated is the variation of the thermal conductivity and the specific heat of the strip with temperature, and the phase transformation as the strip is cooled typically from about 800–900 °C to 550–650 °C. The latent heat of phase transformation has an effect on the temperature profile and the final temperature. It is worth noting that the latent heat may vary with the cooling rate and the temperature of the strip.

#### **1.4 Experimental and Numerical Investigations**

There is considerable interest in controlling the local temperature of the strip as a function of time to achieve the desired metallurgical and mechanical properties. Thus, it becomes a necessity to understand, predict and simulate successfully the controlled cooling process on a ROT. To realize these objectives, it is essential to obtain the accurate HTC or heat flux value and its distribution along length and width. Therefore, numerous investigations have been done that provide insight into the fundamentals of the complex cooling process.

Extensive work has been done at the University of British Columbia on the novel properties of steel strips using an industry-scale cooling facility [23–27]. They include the following:

- 1) Studying and modelling the evaluation of austenite microstructure and the optimum “conditioning” of austenite before transformation for optimum grain refinement.
- 2) Studying and modelling the thermal behaviour of a stationary or moving steel plate, cooled by the circular jet under complex cooling conditions similar to the industrial ones.
- 3) Studying and modelling the austenite decomposition of steel under complex cooling conditions.
- 4) Setup of the quantitative relations between chemistry, microstructure, and property as a guide for steel grade (alloy) design and steel processing.

## 1.5 Objectives of This Study

The aim of this research is to establish procedures and modelling strategies for an effective and robust finite element simulation of the controlled cooling process of steel strips on a ROT. To successfully realize this objective, several aspects of subtasks ought to be considered as follows:

- 1) Development of a general two-dimensional finite element heat transfer analysis program  
The program should be capable of analyzing both the state-steady and transient heat conduction problems. Different heat transfer boundary conditions should be adopted, including time and temperature dependent convection and radiation boundary conditions. The program should take into account the heat generation option due to phase transformation and the temperature dependence of thermophysical properties. The program should be capable of using a mixture of different types of elements.  
The program can be used either for the transient heat transfer to simulate the cooling process as a function of time or for the steady-state heat transfer to simulate the cooling process as a function of location.
- 2) Development of an algorithm for the inverse heat conduction problem (IHCP)  
Based on the literature review, an iterative and sequential inverse heat transfer analysis procedure will be developed and implemented into the proposed 2D FE program. In this method, the least-squares technique, sequential function specification, and regularization are used; simplifications in the sensitivity matrix calculation and the iterative technique are to be adopted to reduce the CPU time while maintaining accuracy; both absolute and relative norms are used to obtain a reasonable convergent solution.
- 3) Development of new techniques for the IHCP  
A new method will be developed to specify the heat fluxes on the cooled surface in IHCP. This new method should take the effect of water movement into account. The profiles of heat fluxes simulating those that occur in ROT applications will be used to investigate the accuracy and stability of the proposed inverse algorithm with the new technique.  
A method to compensate for the effect of the holes for installing thermocouples (TC) will also be developed and discussed for simplifying the inverse calculation procedure.
- 4) Investigations of TC locations and temperature measurement errors

The developed FE program will be used to investigate the appropriate locations of TCs and the probable temperature measurement errors. In UBC experimental tests, both imbedded and surface TCs with a separation measuring junction are originally used to measure the temperatures at different locations. It is generally known that both the holes for installing the TCs and the attachment of TCs to the surface will disturb the temperature field. The magnitude and pattern of their influence under water jet cooling conditions are not reported. Also a detailed study on the appropriate locations of TCs for inverse calculation problems has not been found, and an initial probe will be presented in this study.

5) Determination of surface heat flux and heat transfer behaviour

The developed inverse analysis program and techniques will be used to determine the heat flux during a water jet cooling process. Special procedures for specifying the heat flux distribution on the target cooling surface will be checked and compared. An analysis of data and comparisons with other resources will be performed.

6) Simulation of ROT cooling process

The final stage of this study includes two tasks:

(i) Development of a special program for ROT simulations

This work focuses on the frame work of the FE program. Models and correlations for boundary conditions, microstructure evolutions and mechanical properties from other researchers can be implemented. The program will be used to predict the final coiling temperature of the steel strip.

(ii) Investigation of 2D modelling for ROT applications

The effect of transverse and longitudinal heat transfer on the accuracy of coiling temperature predictions will be investigated.

## Chapter 2

### BACKGROUND AND LITERATURE REVIEW

This chapter presents various aspects regarding water jet impingement cooling. They include representative research studies, temperature measurement, and IHCP as well as TC installation. The literature review of the simulation of a real ROT cooling process is presented in Chapter 7.

#### 2.1 Water Jet Impingement Cooling

##### 2.1.1 Hydrodynamics of water jet impingement

Before focused on water jet impingement cooling, the heat transfer modes between the water and hot surfaces are first discussed. Figure 2.1 schematically shows the boiling curve for a saturated liquid pool cooling at a steady-state condition [4]. The single-phase forced convection regime represents heat transfer in the absence of boiling, i.e. at a lower surface temperature. When the surface temperature increases and reaches the onset of nucleate boiling, discrete bubbles begin to detach from the surface and the convection coefficient increases. The transition boiling regime refers to the formation of unstable vapour blankets, while the film boiling regime represents heat transfer from the hot surface to water across a vapour film (layer). If the initial surface temperature is high enough, there is consequently convective heat transfer, nucleate boiling, transition boiling, and finally film boiling.

Figure 2.2 depicts HTC variations with the surface temperature for a transient pool cooling process [7]. When a hot surface is cooled down by water, the first cooling stage is the stable film boiling; during this stage there is an uninterrupted film of steam between the hot surface and the impinging water, and HTC is low. Reaching the so-called Leidenfrost temperature, this steam film collapses, causing the transferable heat flow density to increase rapidly and HTC to rise sharply. HTC is continuously increasing, passing through the transition regime and reaching a maximum at the burnout point. After passing the burnout point and entering the nucleate boiling and then the free convection

regime, HTC decreases rapidly. It is clear that surface temperature has a major influence on HTC.

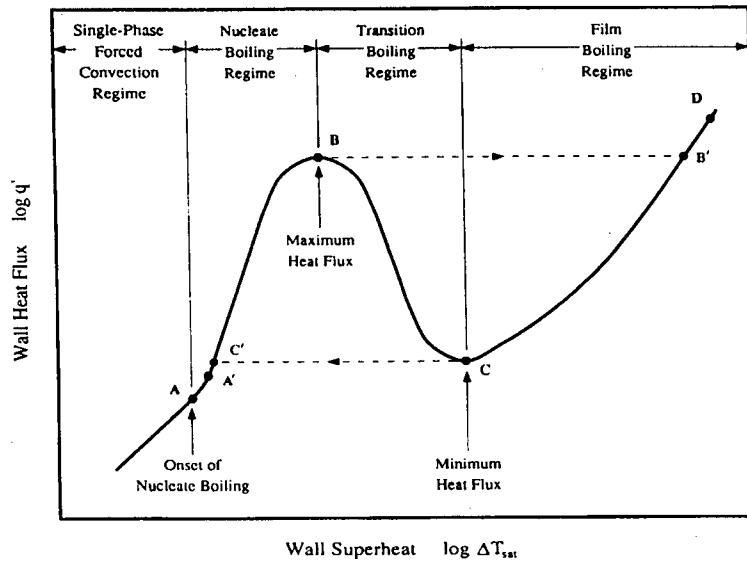


Figure 2.1 Schematic of the boiling curve [4]

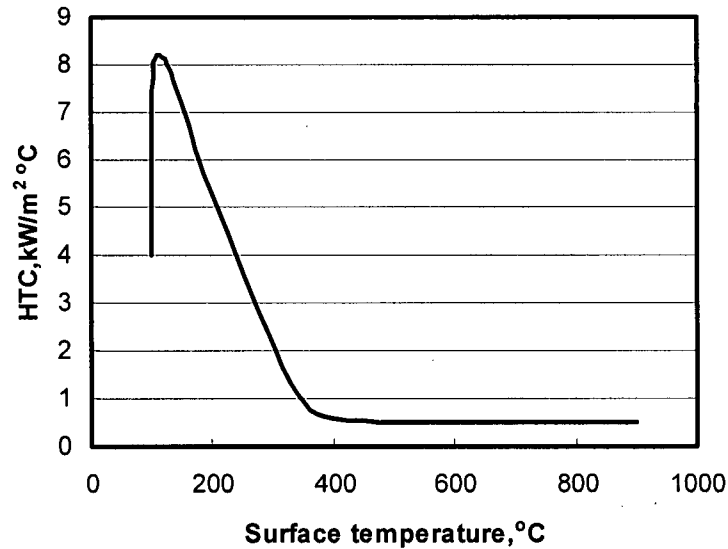


Figure 2.2 Variation of HTC with temperature for saturated water [7]

In addition to the surface temperature, there are a variety of factors affecting water jet impingement cooling. Among them are jet velocity, jet diameter, pressure, and the saturation temperature of water.

The jet velocity (also called impact velocity) with which water vertically hits the plate can be calculated by:

$$V_j = \sqrt{V_n^2 \pm 2gH} \quad (2.1)$$

where  $V_j$  is the jet velocity, m/s;  $V_n$  is the water velocity at nozzle exit, m/s;  $g$  is the gravitational acceleration, m/s<sup>2</sup>;  $H$  is the vertical distance from nozzle exit to plate surface, m. Positive and negative signs refer to the cooling on the top surface and bottom surface, respectively.

The water jet diameter  $D_j$  is the diameter of the area between the plate's surface and water at the instant when water hits the surface. It can be calculated by:

$$D_j = D_n \cdot \sqrt{V_n/V_j} \quad (2.2)$$

where  $D_n$  is the nozzle diameter.

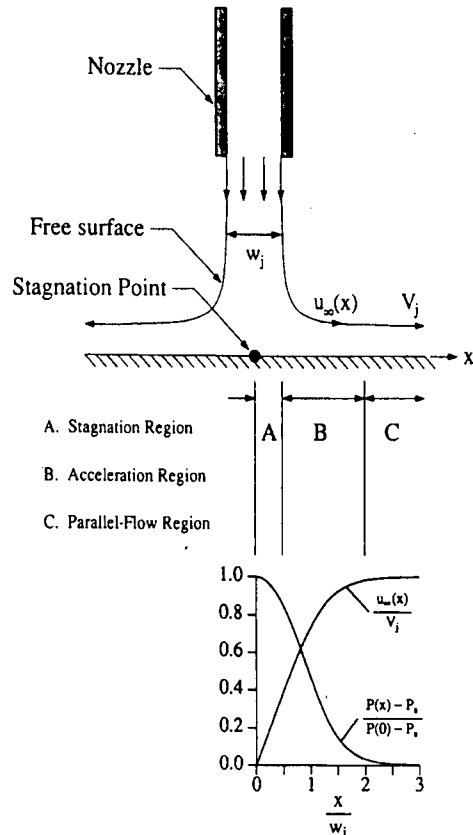


Figure 2.3 Velocity and pressure distribution [4]

The pressure at the stagnation point is given by:

$$P_s = P_a + \frac{1}{2} \rho V_j^2 \quad (2.3)$$

where  $P_a$  is the atmospheric pressure and  $\rho$  is the density of water.

The saturation temperature  $T_{sat}$  can be obtained from the saturation table of water according to the pressure.

Figure 2.3 illustrates the representative distributions of the streamwise velocity and pressure for a planar, free-surface jet (water curtain) [4]. When water vertically impinges with the jet velocity onto the cooling surface, its streamwise velocity accelerates from zero at the stagnation point (directly beneath the jet) to the jet velocity with increasing streamwise distance. It is accompanied by the monotonic decrease of pressure from a maximum at the stagnation point to the ambient value. The stagnation region  $A$  and acceleration region  $B$  roughly form the impingement region. In the parallel flow zone the wall jet flows parallel to the surface; the water velocity is assumed constant and equal to the jet velocity, and the pressure is equal to the ambient pressure.

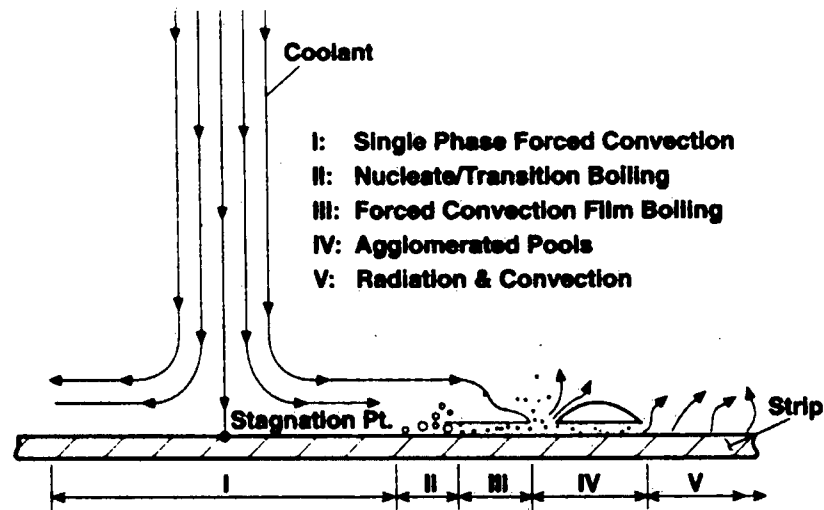


Figure 2.4 Heat transfer regions for steady state water jet [5]

For a single steady state free water jet with a stationary plate (in the following only “plate” is used), the cooled area on the top surface can be divided into five different heat transfer regions, as shown in Figure 2.4 [5]. The first region is called the impingement

zone and is located just beneath the jet. In this region, heat transfer is performed by single-phase forced convection, and the cooling effectiveness is very high; the surface temperature drops sharply to a low temperature such that boiling is not possible. Different research shows that this zone may extend about 2 to 4 times the nozzle diameter or the curtain width [5–9].

The water is heated as water spreads outwardly, the surface temperature is kept at a higher level, and then the onset of the boiling is eventually reached, forming a comparatively narrow nucleate-transition boiling region. In the third region the forced convection film boiling occurs, the cooling water reaches the spherical state, and the heat transfer gradually decreases. Thereafter, due to surface tension effects, the water may agglomerate into pools, overriding the vapour layer. In this region, the water insulates with the plate surface through a vapour film that runs away irregularly from the plate, and the heat loses by convection between the vapor layer and the plate surface, and particularly by radiation from the unwetted surface beneath the pools to the ambient. For the last region, the plate is still dry and not covered by water; heat transfer occurs by the radiation and convection from the dry plate to the surroundings.

For the cooling process on a ROT, the heat transfer may be different since the plate is moving at high speed. This will be discussed in Chapter 4.

### **2.1.2 Representative investigations**

The above example of water jet impingement cooling clearly shows that water jet cooling involves a large number of subprocesses, and each of them is a complicated heat transfer process taking place on stationary or moving surfaces. Much research, both experimental and/or numerical, has been performed for a fundamental understanding of the cooling process of hot strips/plates. The experimental tests should determine the cooling capacity of the used facility by measuring the temperature profiles to provide important information for the process design and development. In addition, the measured temperatures in experiments are usually utilized for estimating the surface heat flux or HTC, which is used for recognizing the heat transfer mode and for further numerical simulations of the cooling process.

Surveys show that most of the experimental investigations have worked on the heat transfer phenomenon with a single jet on stationary plate [5–12] or moving at a speed much lower than the operational speed of a strip on a ROT [13–22].

Ochi et al. [8] experimentally investigated the transient boiling heat transfer to a circular water jet impinging on a hot plate. The test plate was made of stainless steel of 210×50×2 mm in dimension and was heated up to 900–1100 °C. The distance from the nozzle exit to the cooling surface was 25 mm; nozzle diameters were 5, 10, and 20 mm; the water subcooling ranged from 5 to 80 °C and the impinging velocity changed from 2 to 7 m/s. The temperature at the bottom surface was measured, and the temperature and flux at the top cooling surface was inversely calculated using the finite difference method (FDM).

In the experiments, it was observed that a stable film boiling was maintained over the whole cooling surface of the heated plate, and the temperature fell linearly with time. At the end of the film boiling, the water contacted the plate surface on the impingement zone and the heat flux increased. Then the cooling surface of the impingement zone got completely wet and the wet zone advanced outwards. It was found that the heat flux at the stagnation point was higher with a decreasing nozzle diameter. It was also observed that the heat flux was highest at the stagnation point, and that the impingement zone was in the range  $r/D_n \leq 1.28$  for the experimental cases.

The following empirical correlation obtained shows the effect of the water subcooling  $\Delta T_{sub}$ , jet velocity  $V_j$ , and nozzle diameter  $D_n$  on the minimum heat flux  $q_{min}$ :

$$q_{min} = 3.18 \times 10^5 \cdot (1 + 0.383 \Delta T_{sub}) (V_j / D_n)^{0.828} \quad (2.4)$$

It is readily observed that the minimum heat flux is linear with the subcooling. A similar correlation was observed by Ishigai et al. [9] whose experimental tests had a jet velocity and subcooling in the range of 0.65–3.5 m/s and 5–55 °C.

Chen et al. [13–15] studied the heat transfer phenomena of a circular water jet impinging upward onto both a stationary and moving metal plate. In the work, the bottom surface of a low carbon steel plate of 355 mm in width by 254 mm in length by 6.35 mm in thickness was electrically heated slowly and uniformly to a temperature of 240 °C and 88 °C, while other surfaces were thermally insulated to minimize heat loss to the ambient. The plate was cooled by water from a circular nozzle of 4.76 mm in diameter.

The distance from the nozzle exit to the plate surface was 90 mm. The water temperature ranged from 25 to 27 °C. A nozzle exit velocity of 2.66 m/s and a jet velocity of 2.30 m/s were maintained. The plate moving speed was 0.5 m/s.

Results showed that the HTC was larger at the stagnation point than at other locations, and was about 210 kW/m<sup>2</sup>·°C at a plate surface temperature of 240 °C. The HTC values at larger  $r/D_n$  locations were reduced because the temperature gradient decreased as the distance from the stagnation point increased. It was suggested that the transient phenomenon, rather than boiling, dominated the heat transfer mechanism when the plate surface temperature was 88 °C.

Moving plate tests were conducted using a longer plate of 609 mm in length to achieve steady state heat transfer on the moving plate with 0.14–1.44 m/s. The tests revealed that the surface motion had no appreciable effect on local HTC near the stagnation point, while the overall heat transfer rate and cooling effectiveness increased with the increase of the moving speed.

Stevens et al. [16] investigated the effects of the jet Reynolds number, nozzle-plate spacing, and jet diameter on local HTC for round, single-phase free liquid jets impinging onto a flat uniform constant heat flux surface. In the experiment the nozzle diameters were 2.2, 4.1, 5.8, and 8.9 mm with 39 mm in length. Test Reynolds numbers ranged from 4000 to 52000 such that turbulent flow prevailed in all tests. It was found that in the region of  $r/D_j \leq 0.75$  the HTC was nearly constant; beyond that the HTC decreased sharply. It was concluded that the impingement zone was around 1.5 times the nozzle diameter.

Zumbrunnen et al. [17-18] measured the heat transfer distributions on moving and stationary plates cooled by a planar liquid jet. The experiments were transient because of the short length of the plates. In the experiment, the plate surface temperatures were measured and utilized with a numerical solution to the one-dimensional heat transfer energy equation for constant thermophysical properties to determine the local HTC. Two nozzle widths of 10.2 mm and 20.3 mm were used. The plate moved at less than one half of the impingement velocity, with an actual maximum moving speed of 0.8 m/s.

It was found that for  $t \leq 0.6$  s, the local Nusselt numbers were generally larger than those at larger times. For a given time, Nusselt numbers had two local maxima: one beneath the

jet due to the enhanced heat transfer by the high shear flow associated with fluid acceleration away from the stagnation point; the other adjacent to the jet caused by the transition to turbulence and subsequent growth of the turbulent boundary layer.

It was verified that plate motion had different effects on the different cooling regimes. First, the maximum Nusselt number did not shift as a consequence of plate motion and remained fixed at the stagnation points. That is, the HTC in the single-phase forced convection zone were not appreciably influenced by the surface motion.

Second, the critical Reynolds number of the transition of turbulence depended on the relative velocity between the plate and flow, and the pressure gradient in the vicinity of the jet. The data showed that the transition was delayed in the flow direction.

Third, when nucleate boiling occurred over the entire surface of the moving plate (plate surface temperature  $T_s=644$  °C, jet velocity  $V_j=2.60$  m/s, and plate velocity  $V_p=0.6$  m/s), the position of peak heat transfer shifted from the jet centerline in the direction opposite to the plate motion because nucleate boiling was more effective at the higher plate temperatures.

The following local heat flux correlation was obtained by Filipovic [19-20] for the impingement zone on stationary plates:

$$q_{im} = C(\Delta T_{sub})V_j^{0.5}D^{-0.608}\Delta T_{sat}^{0.14} \quad (2.5)$$

where  $q_{im}$  was the heat flux in the impingement zone in  $W/m^2$ ,  $C$  was a constant decreasing with decreasing subcooling, with  $C=1.3 \times 10^7$  at  $\Delta T_{sub}=80$ °C and  $C=0.81 \times 10^7$  at  $\Delta T_{sub}=65$  °C. Because the coefficient  $C$  related to the subcooling, the heat flux was not a linear relationship to the subcooling.

Hatta et al. [21–22] examined the cooling process of both a stationary and moving plate cooled by a water curtain. The plate was made from 18Cr-8Ni stainless steel of 240 mm in length, 100 in width, and 10 mm in thickness. The plate was heated up to 900 °C and then cooled by water with a temperature of 8–18 °C. Three TCs were used and arranged with a space of 60 mm along the centerline in width. The vertical distance of the nozzle exit to the impinging surface was fixed at 100 mm. For moving cases, the travelling velocity of the plate ranged from 0.48 to 2.4 m/min.

It has been observed that the water formed a thin film as soon as it impinged onto the plate surface. The initial red hot plate surface became darkened within a so-called black

zone near the impinging point. The black zone was assumed to correspond to the wetting zone; i.e., the water-cooling distance is equivalent to the distance from the impinging point to the boundary between the wetting zone and the non-wetting zone. In the black zone the water temperature was below the boiling point. They postulated that the plate surface was unwetted if either of the following two conditions was satisfied:

For stationary plates:

$$\begin{aligned} T_s &> 1100 - 8T_w \\ T_s &> 68 \text{ } ^\circ\text{C} \end{aligned} \quad (2.6)$$

For moving plates:

$$\begin{aligned} T_s &> 1100 - 8.5T_w \\ T_s &> 710 \text{ } ^\circ\text{C} \end{aligned} \quad (2.7)$$

where both the plate surface  $T_s$  and water temperatures  $T_w$  have units of  $^\circ\text{C}$ .

Prior research has provided insight into water jet cooling on a ROT. The main findings can be summarized as follows:

1. The heat transfer greatly depends on the subcooling, and is also affected by jet velocity and jet diameter;
2. The heat transfer is much stronger in the impingement zone than in the parallel zone;
3. The effect of plate movement on the heat transfer is to some extent conflicting.

There are still many important points to be examined. Most of research results in the literature address the jet impingement problem under steady-state conditions; i.e., the test specimens are constantly heated while being cooled by the water impinging jet. As for the tests using transient conditions, the dimensions of the nozzles, the distances of the nozzle to the plate are quite small, and the plate temperatures are low; all of these do not reflect the conditions used in practice on a ROT. The results of such research efforts have been important in providing insight into the problem but, generally, are difficult to apply to practical situations on a ROT.

With respect to temperature measurements and analysis methods, one of the most common procedures used in the literature is to use TCs on the opposite side of the plate

or impeded below the top surface, and to obtain the heat flux distribution on the surface through an inverse analysis. More discussions are presented in Sections 2.3 and 2.4.

### 2.1.3 Research work at UBC

By recognizing those defects in the literature, a ROT test facility of industrial scale has been constructed at the University of British Columbia, as schematically shown in Figure 2.5 [23–27]. This facility consists of a top water bank and a bottom water bank, a top header and a bottom header (not shown), a water pump and pipe circuits and flow control valves, a furnace and apparatuses (not shown) for heating water and measuring water temperatures.

Three nozzles can be set up onto the top header and can be easily changed if necessary. Nozzle dimensions are compatible with those used in the steel industry. The distance between the top nozzles is adjustable from 50 to 90 mm. The vertical distance of the top nozzle exit to the test plate can also be adjusted from 0.6 to 2 m. The top nozzles are used for top surface cooling.

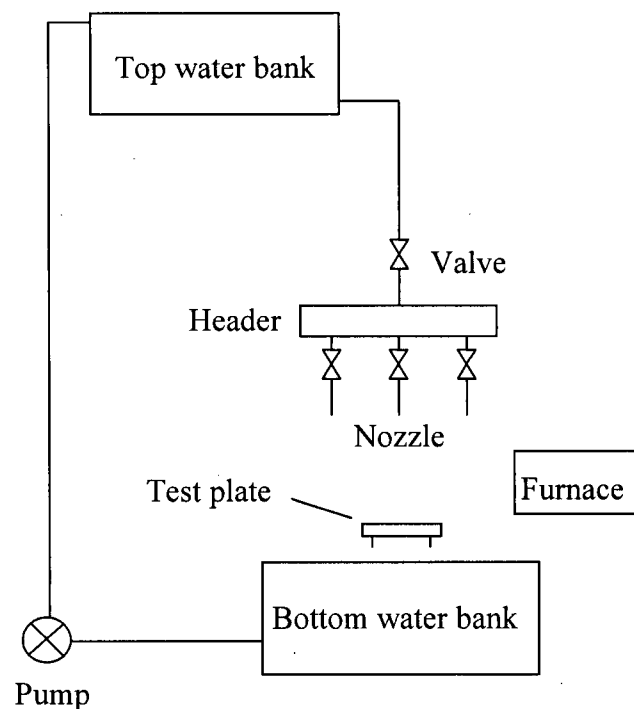


Figure 2.5 ROT test facility at UBC

Only one nozzle is available on the bottom header whose distance to the plate is fixed. The alignment angle of the bottom nozzle to the plate may be changed. This bottom nozzle is used for bottom surface cooling.

Total water flow capacity has a maximum of 138 l/min. The water can be heated to 90 °C. All the abovementioned parameters are very close to those used in the steel industry.

The test plate dimensions are up to 280×280×10 mm for stationary tests. Most of the test plates have a nominal thickness of 7 mm. Although the furnace can heat test plates up to 1200 °C, the initial temperatures of the test plates are roughly 700–900 °C.

The materials of the test plates are carbon steel DQSK (Drawing Quality Special Killed) and stainless steel SS316. The density and specific heat of both steels are assumed to be constant and are 7800 kg/m<sup>3</sup> and 470 J/kg·°C. For the conductivity of DQSK there is the following equation with a correlation coefficient of 0.977 and a standard error of 1.0:

$$k = 60.571 - 0.03849 \times T \text{ (}^\circ\text{C)} \text{ in } W/m \cdot ^\circ\text{C} \quad (2.8)$$

The conductivity of SS316 is also temperature dependent and the following equation is assumed:

$$k = 11.141 + 0.014 \times T \text{ (}^\circ\text{C)} \text{ in } W/m \cdot ^\circ\text{C} \quad (2.9)$$

These equations are valid for temperatures ranging from zero to 1000 °C.

TCs of Type K are used in all experiments for measuring the temperatures. TCs of Type K would normally have an error of approximately 0.75% of the target temperatures when used at a temperature higher than 277 °C. Each of TC wires is around 0.051 mm (0.002") in diameter and is insulated each other and sealed by a metallic protective coat that has an out diameter of about 1.6 mm (1/16").

As shown in Figure 2.6, a total of 16 TCs are used in each test for stationary tests, and are installed at 8 locations in the circumferential direction starting in the center of the plate with an increment of 15.9 mm (5/8") in the radial direction, numbered from 1 at the centre to 8 at the farthest. At each location, an internal TC is installed in a blind hole with a diameter of 1.6 mm (1/16") that is drilled from the plate's bottom surface. The measuring junction is fixed onto the end surface of the hole that is about 1 mm (0.04") below the plate's top surface. A thickness-through hole of the same diameter is drilled

with a centre distance of 3.2 mm (1/8") from the blind hole. The surface TC is inserted in the through-hole and its wires are spot welded on the top surface above the blind hole. It should be noted that the TC wires are welded separately to the designed locations; i.e., the separation junction is adopted (see next section). The distance of wire leads is approximately 1 mm. It should also be noted that an amount of length of wires is bare and is exposed to ambient.

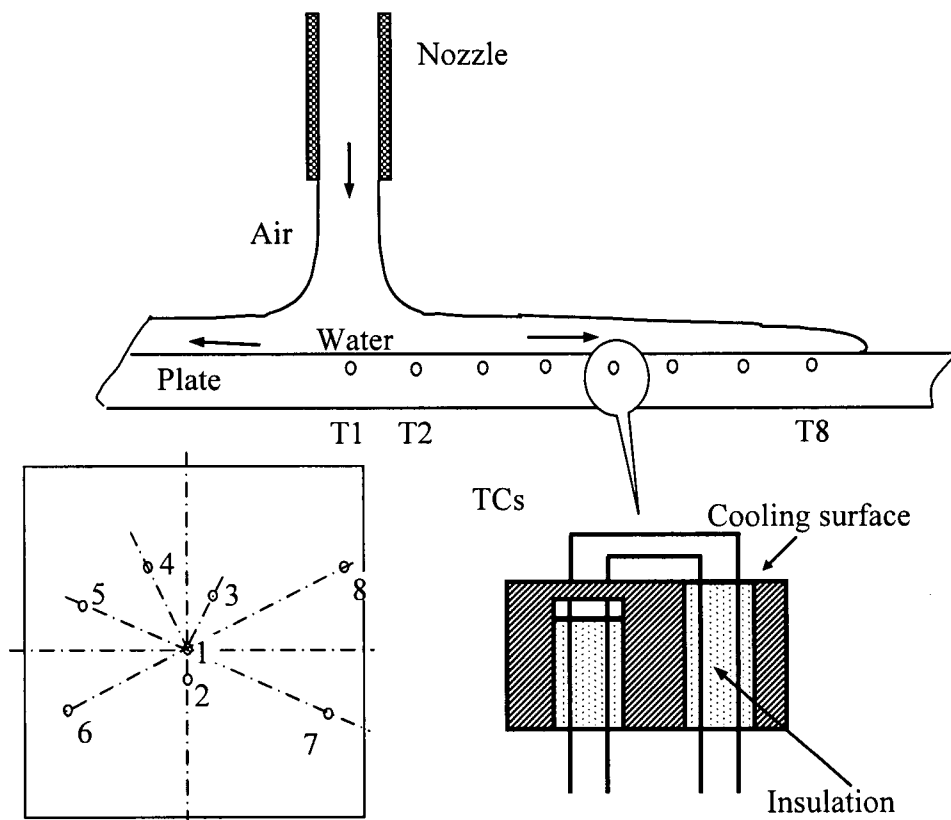


Figure 2.6 Schematic arrangement of TCs

The approach of using a TC on the cooled surface and an imbedded TC to measure the temperatures and then to obtain the heat flux has not been reported in the literature. In the following, this approach will be called "Two-TCs". The rationale behind using this Two-TCs approach is to estimate the temperature gradient directly from the two measured temperatures at that location and then evaluate the surface heat flux from the equation:

$$q = -k \frac{dT}{dy} \quad (2.10)$$

where  $q$  is heat flux in  $\text{W/m}^2$ ,  $k$  is temperature dependent conductivity in  $\text{W/m}\cdot^\circ\text{C}$ , and  $dT/dy$  is the temperature gradient in  $^\circ\text{C/m}$  at the top surface point.

This approach had been used to obtain the heat fluxes and boiling curves [26–27]. It can be seen from those analyses that the heat flux values are generally much higher than those reported in the literature for the same or equivalent cooling conditions. This suggests that this approach may hold its pertinent problems, which is briefly analyzed in Section 2.2.3, after the temperature measurement errors associated with TCs are discussed.

## 2.2 Temperature Measurement Errors

TCs have been used widely in temperature measurement during water-cooling experiments. It is crucial to obtain accurate and reliable temperature measurements in the experiments under the designed cooling conditions. In this section, the measurement error sources associated with TCs are discussed.

### 2.2.1 TC thermometry

A TC consists of two dissimilar metallic wires. The measuring junction is the point where the wires are attached or soldered to the surface of the specimen or the plate. The other ends of the wires are referred to as the reference junction. When the two junctions are at different temperatures, e.g., when the measuring end is heated, an **emf** (electromotive force) is intrinsically developed, and a continuous electric current will be generated and flow in this thermoelectric circuit. This phenomenon is called the Seebeck effect [28-29]. For a given length of homogenous materials, the Seebeck voltage depends on two factors: one being the temperature difference between the two junctions, the other being the Seebeck coefficient. If the circuit is somewhere broken, as shown in Figure 2.7, the net open circuit voltage ( $e_{AB}$ ) can be expressed as

$$e_{AB} = C_\alpha \cdot \Delta T \quad (2.11)$$

where  $C_\alpha$  is the Seebeck coefficient and  $\Delta T$  is the temperature difference between the two junctions. In this study, it is assumed that the Seebeck coefficient  $C_\alpha$  is a material constant and does not change with temperature.

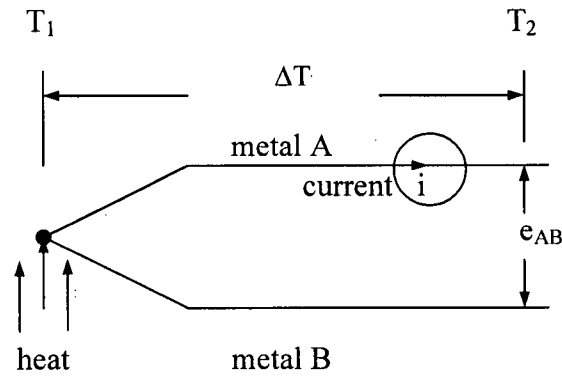


Figure 2.7 Seebeck voltage

There are two common methods to connect the TC wires to the target surface at the measuring junction, as shown in Figure 2.8. The bead-type junction is practically realized by twisting the wires together and then soldering the joint on the specimen, forming a small bead. It is obvious that this kind of junction has a finite volume of bead and hence a large thermal inertia. Therefore, the junction temperature may not be the same as that undisturbed one although the generated **emf** is uniquely related to the temperature at the bead junction.

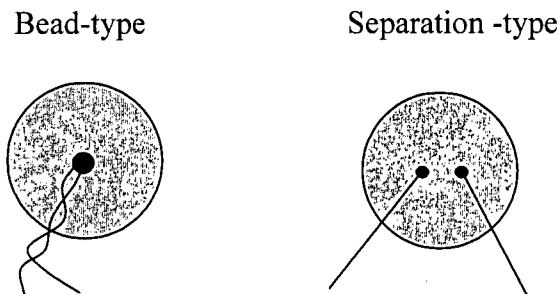


Figure 2.8 Measuring junctions

Another type of TC junction is called separation junction. In this type of junction, the individual wires are separately soldered to the specimen, and the material of the specimen whose temperature is to be measured forms a part of the thermoelectric circuit. The spacing between the two wires ranges from one to two wire diameters. The presence of specimen metal between the two soldered points is assumed not to influence the resulting **emf** as long as the whole measuring junction has a uniform temperature [29]. This kind of measuring junction is also called intrinsic junction because this approach will greatly reduce the thermal inertia of the junction and hence decrease the response time of TC close to zero.

Any other contact between the wires, except the reference junction, and any other contact between the wires and the specimen, except the measuring junction, may result in a premature connection and hence a wrong output of **emf** [29–30]. In addition, the contact resistance of TCs to the parent materials, the change of chemistry compositions of TCs and oxidation of the parent material surface etc may also affect the measurement accuracy. The following discussion is confined to the effects due to the installations of TC to specimen.

### 2.2.2 Measurement errors using TC

The installation of TCs either on the specimen surface or inside will generally deform the original temperature field and will usually cause measurement errors. Most of the following discussions focus on the intrinsic TCs.

Hereby, the concept of “combined wire” should be introduced. The combined wire is a single cylinder of a radius that may be given by

$$r = \sqrt{2}r_w \quad (2.12)$$

and a thermal conductivity

$$k = (k_1 + k_2)/2 \quad (2.13)$$

where  $r_w$  is the radius of a single physical TC wire, and  $k_1$  and  $k_2$  are the individual thermal conductivities of the wires.

Analytical methods are widely used to investigate the errors associated with TCs on the surface or inside [29–31]. In these studies, the dimensions of the parent solid are taken as a semi-infinite body, and generally a steady-state condition is assumed. Also, a single

cylinder to represent the combined wire is used. Analyses show that the wire conduction is the crucial factor among the factors influencing the accuracy of temperature measurement using TCs. Therefore, a reduction of such errors can be obtained by decreasing the heat flux conducted from the measuring point along the wires.

Park et al. numerically examined the error in the measured surface temperature using an intrinsic TC [32]. The simulated process was the quenching of a hot nickel cylinder of 500 °C into cold water of 20 °C. A 2D axisymmetrical FE model with a single combined wire was used first. In this model, the wire of 0.0635 mm in radius was laid along the Y-axis. The surface of the wire and the top surface of the parent plate of 1 mm thick and 4.36 mm wide were specified temperature dependent heat flux as the boundary condition. This analysis indicated an error of about 40 °C that occurred within 0.1 s of immersion and persisted for almost 1.7 s.

A 3D FE model was then developed. In this model, two square columns, each of which had the same cross-area as the wire in the 2D model, were apart of two wire diameters. Different thermal properties were assigned to each of the equivalent wires. The same boundary conditions were specified. This simulation predicted an error of similar magnitude. Unfortunately, the fact that the temperatures at the two wire roots were found being different because of the difference in thermal properties had not been given attention.

The accuracy of intrinsic TCs in the transient radiant heating process was experimentally investigated in [33]. Two intrinsic TCs were installed on each specimen. One was placed on the top surface and the other, directly opposite, on the bottom surface. All TC wires were 0.01" in diameter, with a separation of approximately 0.05" between wires. It was assumed that the heat transfer was one-dimensional and that the TC on the bottom surface was subject to a lower order of errors than that on the top surface exposed to the radiant energy. Consequently, the accuracy of the top surface TC could be determined by comparing the temperature difference between the two measured temperatures with the theoretical one that was obtained from the solution of the heat transfer equation. It was found that all tests produced consistent results, the temperature errors could reach 35 °F, and that the temperature errors increased with increases in heating rates or in specimen thickness. The author attributed the errors to an amount of bare TC wire that lead to more

loss of heat to ambient, and precluded the effect of temperature gradient between the two wires because the included area of the third metal, i.e., the specimen itself, was very small. This postulation may not be justified, since the ratio of separation distance to wire diameter is about 5 and the heating process is highly transient.

Attia et al. studied the distortion in a 2D thermal field around inserted TCs that were presented by combined wires [34–36]. The 2D model was a square with a void or two voids with the  $x$ - $y$  plane perpendicular to the axis of the hole (void). The heat was assumed to flow in one direction from the positive  $y$  side to the negative  $y$  side. It was found that the distortion was symmetrical about both the  $x$ -axis and  $y$ -axis; and that the maximum existed at the top and bottom points of the void when one void was located in the centre of the square; and that the temperature disturbance was inversely proportional to the temperature gradient, the void diameter, and the distance from the boundary.

In reference [37], Attia et al. extended their analyses to the general case of 3D TC installation and focused on the end effect representing the disturbance of temperature field surrounding the bottom of the hole for installing TC. It has been concluded that the eccentric position of TC was the most important factor and caused a significant error, especially when the temperature gradient was large.

The effect of TC wire was also analyzed using a regular 2D FE axisymmetrical model [38]. The TC wire was 0.04 mm in diameter and 10 mm in length that was exposed to the ambient. A constant HTC of  $2 \text{ kW/m}^2 \cdot ^\circ\text{C}$  was applied to the top surface, and the same material properties of  $15 \text{ W/m} \cdot ^\circ\text{C}$  for the conductivity and  $5 \times 10^6 \text{ J/m}^3 \cdot ^\circ\text{C}$  for the specific heat were assumed for the wire and parent object. It was found that an error could be of  $40 \text{ }^\circ\text{C}$  or 4.6% due to wire fin effect.

An approach was then developed to investigate the interaction between the two wires of TC. In this approach, the FE model consisted of two portions: one was a normalized regular 2D FE axisymmetrical submodel representing the TC; the other was the parent object that did not include TC in the FE mesh. The submodel was superimposed at the actual location of the surface TC on the parent material. Its properties were assigned according to its particular location. The top surface of the submodel was exposed to a convective medium, and other surfaces were specified with temperatures as thermal

boundary conditions, also according to its particular location. Unfortunately, no information was given about how to get the specified temperatures. And from the point of view of the author of this thesis, the results shown do not represent the real interactions but only the temperatures at locations with a distance of one or two wire diameters.

The effect of hole for imbedded intrinsic TC was also numerically studied by Li [39]. In this research, the distance of imbedded TC to the surface was fixed at 1.5 mm. It was found that the difference between the temperature at TC tip and the undisturbed one could be up to 100 °C as the cooling time was about 2 s under the conditions that the applied maximum heat flux was 20 MW/m<sup>2</sup> and the plate material was AISI 316. This kind of temperature difference was not significant when the plate material had higher conductivity and the maximum was around 5 MW/m<sup>2</sup>. It was generally concluded that the hole should be included in inverse calculations.

The measurement error due to the installation of surface intrinsic TCs was also investigated by using analytical and numerical methods in Li's work [39]. It was pointed out that the heat flux at the measuring junction was about 10 times as that on the plate surface. The temperature error may reach 300 °C at around 2 s after water cooling.

Li's work did not address the effect of the hole on the surface temperature and did not pay attention to the temperature differences between the two wires for the intrinsic TC.

### **2.2.3 Section summary and discussion**

#### **i) Summary**

The above discussion clearly shows that the fin effect of TC conduction wires may cause significant errors. The indicated temperature would be lower or higher than the undisturbed one for the cooling and heating process, respectively.

The hole for installing TCs will also disturb the temperature field. If there are two adjacent holes a more complicated temperature pattern would occur, and the magnitude of error would be higher.

The isothermal condition for two wires of intrinsic TCs has not been, however, extensively studied and discussed. This is an important for a rapid cooling/heating

process, as in the jet impingement cooling of hot steel plates. It is reasonable to say that these errors may be more significant for a highly transient intensive cooling process.

Moreover, the work in the literature has not addressed the possible effect of water movement on the temperature measurement errors using intrinsic TCs. That would be a critical aspect of intrinsic TC applications.

## ii) Discussion

This discussion is oriented to the appropriateness of the Two-TCs approach. From the point of view of this author, such an approach may not produce credible results. Several reasons support this postulation.

This approach is based on the two measured temperatures, one from the surface TC, noted as  $T_{sm}$ , the other one from the imbedded TC, as  $T_{im}$ . Here, take the notation  $T_{st}$  and  $T_{it}$  for the “true” surface temperature and “true” internal temperature at the corresponding locations. Only when

$$T_{sm} - T_{im} = T_{st} - T_{it} \quad \text{or} \quad T_{sm} - T_{st} = T_{im} - T_{it} \quad (2.14)$$

is valid at any time instant during the cooling process, the true temperature gradient may be estimated correctly. However, this condition is fairly difficult to satisfy. It may be easily concluded that the respective errors in the measured surface temperature and the interior one is different (Chapter 5) because the temperatures are different but have the same nominal error level, even assuming the temperature field has not been disturbed. In fact, the temperature field is greatly affected by both the attachment of TCs and the holes, and the measured temperatures may be far from the true values.

Second, the actual distance between two measurement points is in question because of few reasons. The first one is the methods used to calculate the distance between the two TCs. This is usually obtained by taking the difference between the measured values of the plate thickness and the hole depth. The defect is that the thickness is an average value for the whole plate, and no individual thickness for each location is determined.

The second reason is that the exact locations of the TCs are unknown. It is clear that the two points should be aligned along a vertical line, and the distance should be their vertical space. However, it is very difficult to know the exact location of the interior TC.

Therefore, the top surface point may have a small shift from the interior one. This may lead to a larger error especially when large temperature gradient exists.

Another reason is that the heat transfer is highly transient with large temperature gradient in the transverse direction. It is reasonable to assume that the transverse gradient is not uniform through the thickness. Thus, there will definitely be a temperature difference between the two target points even if the top surface is thermally insulated. The obtained heat flux value from equation (2.10) would be in error because a thermal insulation is already assumed and no vertical heat flux should exist.

Therefore, other options to determine surface boundary condition (heat flux or HTC) are required.

### **2.3 Numerical Methods for IHCP**

The measured temperatures in experiments are usually used to estimate the surface boundary condition, which is used for recognizing the heat transfer mode and for further numerical simulations of the cooling process. Generally, the analysis methods used are associated with temperature measurement approaches.

A variety of numerical methods and computational algorithms have been developed in the literature to obtain the surface boundary condition. By skipping all of the analytical methods and the direct methods, the following discussion focuses on the numerical inverse methods.

An IHCP means that the boundary conditions or the thermophysical properties of material are not fully specified, and they are determined from measured internal temperature profiles. The effects of changes in boundary condition are usually damped and lagged; i.e., the varying magnitude of the interior temperature profile lags behind the changes in boundary conditions and is generally of lesser magnitude. Therefore, an IHCP would be a typically ill-posed problem and would normally be sensitive to the measurement errors. Thus, in general, the uniqueness and stability of an IHCP solution are not guaranteed [40–41].

Among the methods for IHCP are the least-square regularization method [40–41], the sequential function specification method [40], the space marching method [42], the

conjugate gradient method [43], the maximum entropy method [44], and the model reduction method [45]. Important applications of these methods and their numerous modifications have been performed in various branches of thermal engineering [23–25, 39, 46–52]. It is not an appropriate approach to review all of them. Instead, the emphasis in this section is on the computational methods and techniques used in the water jet impingement and similar cooling processes such as quenching.

### 2.3.1 Common techniques

The techniques that stabilize an IHCP solution are highlighted in the following subsections. For simplicity, the following discussion is based on one single heat flux  $q^i$  (for more than one heat flux component, just change the notation to vector form  $\mathbf{q}^i$ ) and multiple measurement points.

#### 1. Least squares

An IHCP may generally be converted into an optimization problem. The sum of squares of the differences between the calculated temperatures and the measured ones are usually targeted as the objective function:

$$S^i = \sum_{j=1}^J (T_{jm}^i - T_{jc}^i)^2 \quad (2.15)$$

This objective function is minimized with respect to the unknown heat flux component  $q^i$  by insuring:

$$\frac{dS^i}{dq^i} = 0 \quad (2.16)$$

The heat flux  $q^i$  can be obtained by solving the above equation.

#### 2. Future time step and function specification

Since IHCP is ill-posed, the inverse solution may not be unique and may be sensitive to measurement random error. To reduce such a sensitivity and to recover the effect of boundary condition changes, in addition to the measured temperatures at the current time step  $\mathbf{T}^i$ , the measured temperatures at future time steps (FTS)  $\mathbf{T}^{i+1}, \mathbf{T}^{i+2}, \dots, \mathbf{T}^N$  (where  $N-1$  is the number of future steps) are also used to estimate the heat flux  $q^i$ . In this case, the objective function becomes:

$$S = \sum_{j=1}^J \sum_{i=1}^N (T_{jm}^i - T_{jc}^i)^2 \quad (2.17)$$

or in vector form

$$S = \sum_{i=1}^N (\mathbf{T}_m^i - \mathbf{T}_c^i)^T (\mathbf{T}_m^i - \mathbf{T}_c^i) \quad (2.18)$$

It is clear that the heat flux  $q^i$  ( $i = 1-N$ ) at different time steps may be different. One way to treat the problem is to make a temporary assumption for the value of  $q^{i+1}, q^{i+2}, \dots, q^N$ . This is called function specification. Thus in this stage, a function specification is always related to the future time step, and is about the function form of the surface heat flux variation with time. The simplest and most widely used assumption is a sequence of constant segments; i.e.,  $q^{i+k} = q^i$  for  $1 \leq k \leq N-1$ . Other assumptions are possible, such as linear function, parabolas, cubics, and exponentials. For the constant and linear assumptions, the objective function has only one variable  $q^i$ . Therefore, the equations and procedure are still valid.

### 3. Regularization

To damp the fluctuation of a solution from the measurement errors, more items may add to the objective function. This procedure modifies the objective function and is called the regularization method. The simplest one is the variable  $\mathbf{q}$  itself.

$$S = \sum_{i=1}^N (\mathbf{T}_m^i - \mathbf{T}_c^i)^T (\mathbf{T}_m^i - \mathbf{T}_c^i) + \alpha \cdot \mathbf{q}^T \cdot \mathbf{q} \quad (2.19)$$

This term  $\alpha \cdot \mathbf{q}^T \cdot \mathbf{q}$  is called the zeroth-order regularization term. The fraction value  $\alpha$  is a weighting factor and is called the regularization parameter.

The higher regularization items such as the difference between the consecutive heat fluxes in time, the difference between the adjacent heat fluxes in space (these two are called the first-order regularization term), the difference between the derivatives of heat fluxes with respect to time or the spatial derivatives of heat fluxes (these two are called the second-order regularization term) are possible to add into the objective function.

It is interesting to note that the first order term is occasionally used and the others infrequently used [39]. It is also important to mention that the zeroth order term reduces

the magnitude of heat flux; the first-order term reduces the magnitude of change in heat flux, and the second-order term decreases the rapid oscillations in heat flux.

It is worth noting that the function specification technique also works as a regularization procedure and stabilizes the solution process. And the function specification and regularization techniques can be used for both a linear and nonlinear IHCP.

#### **4. Whole time domain and sequential approach**

If a method can estimate simultaneously all the parameters for the total time interval, it is called a whole time domain method or simply a whole domain. In this case, all the data from the measurements are input into the objective function, and the function specification is also made for the total number of time steps, if used.

The transient heat conduction is a kind of diffusive process. Therefore, the whole domain method is not an efficient procedure. The most computationally efficient estimation approach is the sequential one. In the sequential procedure, the heat flux  $q^i$  is estimated after  $q^{i-1}$ ; after  $q^i$  is obtained,  $i$  is increased by one and the estimation procedure is repeated.

Improvements to and adaptations of the numerical algorithms to complex applications such as the water-cooling of hot plates by jet impingement on a ROT are still an active area of research for obtaining stable and reliable results. In this study, an FEM-based inverse heat conduction method will be developed and used to determine the surface heat flux and surface temperature from the internal temperature. All the abovementioned techniques will be used in the proposed algorithm in this study (Chapter 3).

#### **2.3.2 Typical previous studies**

Vader et al. [10-11] investigated the convective nucleate boiling on a heated surface cooled by an impinging planar jet of water under a steady-state condition. The temperatures were measured by TCs at the opposite dry face to the cooled top surface. The temperature and heat flux at the cooled surface were found by solving the steady-state equation. In the calculations, the boundary conditions were assigned from the least squares cubic spline fit of the measured temperatures. It was reported that there were uncertainties of  $\pm 10\%$  and  $\pm 12\%$  in the surface temperature and HTC, respectively.

Wolf et al. [12] also studied the local jet impingement boiling heat transfer. A similar procedure as Vader's was used, except that only the top surface temperatures were calculated by solving the heat transfer equation. The heat flux on the top surface was inferred from the measurement of the voltage difference across a definite plate's length. This length was changed to obtain the heat fluxes at different locations from the stagnation line. Overall uncertainties were the surface heat flux,  $\pm 2\%$ , the surface temperature,  $\pm 2^\circ\text{C}$ , and the resulting HTC,  $\pm 7\%$ .

Liu et al. [23–25] investigated the boiling heat transfer on steel plates cooled by a circular jet. In their experimental studies under transient conditions, the temperatures were measured with TCs inserted inside the plates and close to the top surface. The top surface temperatures and heat fluxes were simultaneously calculated out from an FEM-based inverse algorithm based on the zeroth-order regularization. The calculations were only based on current temperatures. The function specification and iteration techniques are not used.

Kumagai et al. [49] studied the transient cooling of a hot plate with an impinging water jet. Temperatures were measured at four points at different depths along the plate thickness ( $Y$  direction) and at nine locations in the width direction ( $X$  direction). An exponential equation with three coefficients was used to describe the temperature profile in the  $Y$  direction, and then the coefficients were determined from the measured temperatures and the least squares method. The approximate temperature curve was extrapolated to the surface to obtain the surface temperature. The gradient at the surface produced the heat flux value.

The error level was also reported by Kumagai et al. [49]. At the stagnation point, this method had an error of 1–3.3 % in the surface temperature estimation and of 10–35 % in the heat flux; at other locations the errors were 1–1.5 % in the surface temperature and 10–15 % in the heat flux after the solid-water contact.

The iterative regularization and the conjugate gradient method were used in the inverse determination of the local HTC for the nucleate boiling on a horizontal pipe cylinder under a steady-state condition [50]. In this work, the Lagrangian functional was defined using the sum of the temperature differences between the measured and calculated ones,

and the governing equation for steady-state heat conduction and all boundary conditions as multiplier terms. The conjugate gradient method was used to find the descent parameter. The iterative technique was adopted to get a more accurate solution of heat flux from the measured temperatures at locations inside the cylinder body. However, the claim of using the regularization technique should be viewed cautiously since no other terms were added into the objective functional.

Kim used an FEM-based inverse model to evaluate HTC during heat transfer of a cylinder cooled by a fan or water [51]. Multiple embedded TCs at the same radius were used to measure the temperatures. In the method, a spatial regularizer composed of the zeroth- and first-order regularization terms was added to the objective function together with the future step technique and the iterative technique. This approach is quite similar to our development.

### **2.3.3 Specification of heat flux**

No matter which theory or principle is used to develop the inverse algorithm, only a limited number of unknown heat fluxes may be obtained mathematically. The number of unknowns may not be greater than the number of temperature measurements for an IHCP. When the geometry of a 2D or 3D heat transfer problem is discretized into the FDM grid or FEM mesh, there are a number of nodes (elements) on the surfaces where the heat flux should be determined. As the algorithm developed is implemented in a numerical program to determine the heat flux during the cooling processes such as water jet cooling, special procedures for specifying the heat flux distribution on the target surface should be set up. This is a challenge for a 2D or 3D IHCP.

No detailed studies have been found in the literature regarding the above point. Most of the published research didn't identify appropriate methods for specifying the heat flux on the cooled surface in a 2D or 3D problem. In [23] the number of heat fluxes is implicitly assumed equal to the temperature measurements, and a local uniform heat flux assumption is used. This will be discussed in detail in Chapter 3 and Chapter 4.

## 2.4 TC Installation

As discussed above, the temperature measurements in water cooling experiments have two purposes. The first one is to determine the cooling capacity of the cooling facility to provide important information for process design and development. The other is to obtain accurate and reliable surface heat fluxes or HTC's under the designed cooling conditions by interpreting the temperature profiles.

Those studies, briefly reviewed in Section 2.2, are important for obtaining a real temperature field but they have put little emphasis on the measurement and application of temperature for an inverse heat conduction analysis. The crucial aspects for an inverse analysis would lie in two categories: to keep the cooling condition undisturbed by TC attachments and to make the temperatures relevant to benefit in reducing the effect of random temperature noise on inverse calculations. Therefore, the installations of TC should be designed accordingly.

Since a surface TC on the cooled surface may change the surface cooling condition as well as cause large errors (Chapter 5), it will not be discussed here and only imbedded TC of the bead type is considered in this discussion.

As shown in Figure 2.9, there are several parameters in installing TCs: the diameter  $D$  or radius  $R$  of a hole for installing TC, the vertical distance  $h$  of TC to the cooled surface, the horizontal distance  $l$  between two adjacent TCs, and the plate's thickness  $H$ .

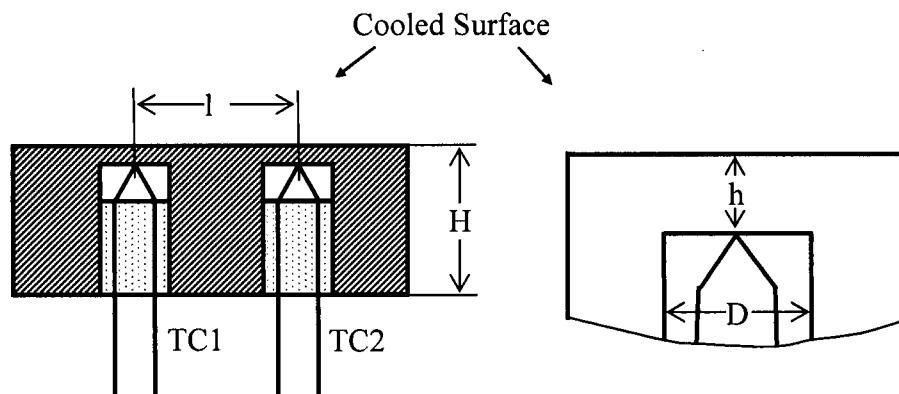


Figure 2.9 Parameters for TC installation

#### 2.4.1 Horizontal distance

Among the measures to reduce sensitivity and to improve the accuracy of inverse calculation results, the correlation of the temperatures at different locations should be considered. As shown in Figure 2.9, if the temperature at location TC2 is strongly affected by the heat source at location TC1 and vice versa, the influence from the errors in temperatures at these two locations may be diminished. Thus, the inverse calculation becomes more stable and reliable. This discussion makes it clear that the distance  $l$  between two TCs should be kept to a reasonable range. Unfortunately, little work has been done on this critical issue.

The importance of determining the critical distance between two TCs becomes more crucial for the water jet impingement cooling process in which the cooling conditions are highly transient and any material point outside of the impingement zone is not cooled simultaneously. Analysis to experimental results shows that the progressing speed of the water cooling zones is fairly slow and is 1 to 6 mm/s (Chapter 4). The temperature at TC2 may hardly relate to the heat flux at location TC1 if the TC distance is around 16 mm, which was used in the literature [23–27].

#### 2.4.2 Vertical depth

As TCs are implanted below the cooled surface through holes drilled from the plate's backside, it is inevitable to have a distance between TCs and the surface. When determining an appropriate vertical depth of TC, two conflicting factors should be discussed.

The first factor is the suppression effect. The higher frequency fluctuations of boundary conditions is increasingly damped and suppressed with the increasing of the depth. From heat transfer conduction theory there is an exponential correlation in the form:

$$\frac{\Delta T}{\Delta T_0} = \exp\left(-\sqrt{\frac{\pi f}{\alpha}}x\right) \quad (2.20)$$

where  $\Delta T_0$  and  $\Delta T$  are the amplitude of the temperature changes at the surface and at depth  $x$ , respectively;  $\alpha$  is the thermal diffusivity of the specimen; and  $f$  is the frequency of fluctuations. If the detection limit is defined at 5% of the surface amplitude and the depth is set at 2 mm, a sensor can capture only a frequency up to 10 Hz for steel plates.

To reduce the lagging effect in inverse calculation, TC should be as close to the cooled surface as possible; i.e., the depth  $h$  in Figure 2.9 should be a small value. In reference [23–27]  $h$  was set up at around 1 mm. For most of steels the thermal diffusivity is about  $9.55 \times 10^{-5} \text{ m}^2/\text{s}$ , so the dimensionless time step can be 1.0 with a time step of 0.01s. This number implies that the inverse calculation may not meet a difficult problem.

On the other side, as the depth is designed at a very small value, the surface temperature above the void would be much lower than the undisturbed one, and a cold spot is formed, which has a major influence on the cooling condition. The inversely obtained heat flux may not reflect the real heat transfer mode even if the measured temperature is without noise, and is interpreted with a higher accuracy. In this respect the distance  $h$  should be a value with which the surface temperature will be very close to the undisturbed, and as a result the real heat transfer may be attained.

Therefore, it is desirable that a TC is implanted at a depth at which the surface temperature is almost not affected, and at the same time the detection of a higher frequency of boundary condition can be realized. Again, little work has been done on this issue.

#### **2.4.3 Effective TC depth**

Although the surface temperature may be kept undisturbed with an appropriate depth, the internal temperature field is still deformed when an imbedded TC is used. The temperature at the internal sampling point is lower than the undisturbed. If the hole effect should be taken into account for a general modelling, the heat transfer analysis becomes three-dimensional. This is a challenge for an inverse calculation. Therefore, this hole effect is neglected in most inverse calculations. This approach definitely causes an even greater deviation of the calculated heat flux from the real one (Chapter 6).

Developed by Beck et al. [53] and frequently used in aerospace research [54], the “null-calorimeter” technique postulates that the measured temperature at the tip of TC, which is installed in a hole, will closely follow the undisturbed surface temperature if the ratio of the hole diameter to the TC depth is kept at 2.2.

Literature survey shows that the “null-calorimeter” concept has not been introduced into the cooling process of steel. So it is of interest to investigate whether this idea is

applicable to steel cooling. Moreover, it would be useful to develop an approach in which the hole may not be included in the geometry and its effect can be compensated by adjusting the TC distance in the modelling of inverse analysis. This approach is called the “effective depth approach (EDA)” in this study (Chapter 5).

## Chapter 3

### PROGRAM FOR DIRECT AND INVERSE HEAT CONDUCTION ANALYSES

To study the water cooling of hot steel plates by jet impingement, a 2D FE heat transfer analysis program is first developed; and then an algorithm for inverse heat transfer analysis is formulated and implemented into the 2D FE heat transfer analysis program. The Flux Zoning Method (FZM) is discussed and used for specifying the heat fluxes on the nodes at the target surface. Parametric studies are performed with abrupt heat flux inputs. Validation results show the proposed method and procedures are robust and reliable and have an acceptable level of accuracy [55–56].

#### 3.1 Program for Direct Analysis

##### 3.1.1 Formulation

The modeling and experimental procedures are based on a 2D planar and axisymmetric assumption. For completeness of the treatment, a brief outline of the equations for a direct FE formulation for 2D planar transient conduction heat transfer problem is given in the following section. A detailed account of this formulation and the formulation for axisymmetric transient heat conduction problem may be found in reference [57–58].

The general governing equation for 2D conduction heat transfer problems, shown in Figure 1, is written in the form:

$$\frac{\partial}{\partial x} \left( k_x \frac{\partial T}{\partial x} \right) + \frac{\partial}{\partial y} \left( k_y \frac{\partial T}{\partial y} \right) + q^b = c_p \rho \frac{\partial T}{\partial t} \quad (3.1)$$

where  $T$  is the temperature, °C;  $q^b$  is the heat generation rate per unit volume, W/m<sup>3</sup>;  $k_x$  and  $k_y$  are the conductivities in the  $x$ - and  $y$ -directions, respectively, W/m·°C;  $\rho$  is the density, kg/m<sup>3</sup>;  $c_p$  is the specific heat, J/kg·°C;  $t$  is the time, s; and  $x, y$  are the Lagrangian coordinates of the point.

The boundary condition (BC) may be one or a combination of the followings cases:

**Prescribed temperature:** This is an example of the *Dirichlet* BC. The prescribed temperature  $T_s$  may be a function of time and boundary coordinate (spatial function):

$$T = T_s(x, y, t) \quad \text{on } S_1 \quad (3.2.a)$$

**Prescribed heat flux:** The specified heat flux ( $q_s$ ) may be a spatial function or a function of time:

$$-k \frac{\partial T}{\partial n} = q_s(x, y, t) \quad \text{on } S_2 \quad (3.2.b)$$

where  $q_s$  is the specified heat flow per unit area,  $\text{W/m}^2$ ,  $n$  is the normal of the point considered. The prescribed heat flux is an example of the Cauchy's or Neumann BC. If  $q_s$  is zero, it will represent a natural BC.

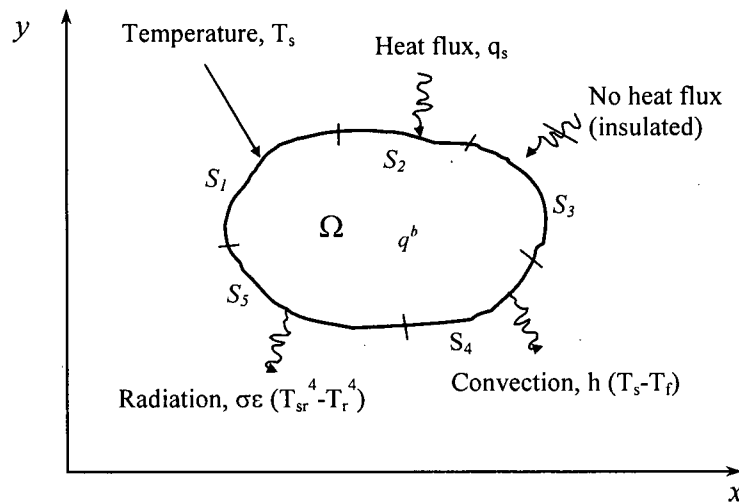


Figure 3.1 Boundary conditions for a general conduction problem

**Convection heat exchange:** When due to contact with a fluid medium, there is a convective heat transfer on part of the body surface,  $S_4$ :

$$-k \frac{\partial T}{\partial n} = h(T_s - T_f) \quad \text{on } S_4 \quad (3.2.c)$$

where  $h$  is the convection heat transfer or film coefficient,  $\text{W/m}^2 \cdot ^\circ\text{C}$ , which may be temperature dependent;  $T_s$  is the surface temperature ( $^\circ\text{C}$ ) on  $S_4$ , and  $T_f$  is the fluid temperature ( $^\circ\text{C}$ ), which may be a spatial or time function.

**Radiation:** Assuming a grey body, the BC is given by:

$$-k \frac{\partial T}{\partial n} = \varepsilon \sigma [T_{sr}^4 - T_{er}^4] \quad \text{on } S_5 \quad (3.2.d)$$

where  $\varepsilon$  is the emissivity of the body's surface,  $\sigma$  is the Stefan-Boltzmann constant ( $\text{W/m}^2 \cdot \text{K}^4$ ),  $T_{sr}$  is the absolute temperature of surface  $S_5$  (K), and  $T_{er}$  is the known absolute temperature of the external radiative source (K). The radiation boundary condition may be dealt with as a nonlinear convective boundary condition with an equivalent temperature dependent film coefficient,  $\kappa$ ; where:

$$\kappa = \varepsilon \sigma (T_{sr}^2 + T_{er}^2) (T_{sr} + T_{er}) \quad (3.2.e)$$

With the use of a weighted residual Galerkin procedure, the final FE equations may be written as:

$$\mathbf{C} \dot{\mathbf{T}} + \mathbf{K} \mathbf{T} = \mathbf{Q} \quad (3.3)$$

where  $\mathbf{C}$  is the equivalent heat capacity matrix;  $\mathbf{K}$  is the equivalent heat conduction matrix;  $\mathbf{T}$  and  $\dot{\mathbf{T}}$  are vectors of the nodal temperature and its derivatives, respectively;  $\mathbf{Q}$  is the equivalent load vector. Detailed expressions of the matrices in equation (3.3) are given in Appendix A.

A general family of solution algorithms for equation (3.3) may be obtained by introducing a parameter  $\alpha$  where ( $0.0 \leq \alpha \leq 1.0$ ) such that

$${}^{t+\alpha\Delta t} \dot{\mathbf{T}} = \frac{1}{\Delta t} ({}^{t+\Delta t} \mathbf{T} - {}^t \mathbf{T}) = \frac{1}{\alpha \Delta t} ({}^{t+\alpha\Delta t} \mathbf{T} - {}^t \mathbf{T}) \quad (3.4a)$$

$${}^{t+\alpha\Delta t} \mathbf{T} = \alpha {}^{t+\Delta t} \mathbf{T} + (1 - \alpha) {}^t \mathbf{T} \quad (3.4b)$$

If  $\alpha = 0$ , an explicit Euler forward method is obtained; if  $\alpha = 1/2$ , an implicit trapezoidal rule is obtained; and if  $\alpha = 1$ , an implicit Euler backward method is obtained.

Substituting equation (3.4) into equation (3.3) yields:

$${}^{t+\alpha\Delta t} \left[ \mathbf{K} + \left( \frac{1}{\alpha \Delta t} \right) \cdot \mathbf{C} \right] \Delta \mathbf{T} = {}^{t+\alpha\Delta t} (\mathbf{Q}^b + \mathbf{Q}^s) + {}^{t+\alpha\Delta t} (\hat{\mathbf{Q}}^h + \hat{\mathbf{Q}}^r) + {}^{t+\alpha\Delta t} (\hat{\mathbf{Q}}^c + \hat{\mathbf{q}}^c) \quad (3.5)$$

where  $\alpha \neq 0$ . The definition of all terms is given in Appendix A.

Depending on the value of  $\alpha$ , the solution procedure may be either conditionally stable ( $\alpha < 0.5$ ) or unconditionally stable  $\alpha \geq 0.5$ .

### **3.1.2 Implementation and validation**

In the developed program, the geometry domain can be discretized into an assembly of triangular and quadrilateral isoparametric 2D finite elements. The triangular elements may have three or six nodes whereas the quadrilateral elements may have four, eight, or nine nodes. The program is capable of dealing with a mixture of element types.

Various types of boundary conditions discussed above are adopted in the program. The values of HTC or heat flux may be a function of both time and space. The heat flux may be specified as surface or nodal input. It is worth noting that numerical experiments showed that using the nodal heat flux is better than using the surface heat flux when an inverse calculation with flux marching method (FMM) (Chapter 4) is involved.

Nonlinearities may arise from the dependence of thermophysical properties on temperature, as in the case of a radiation boundary condition. In the developed program, nonlinearities are handled in a step-wise staggered approach; i.e., the values of the parameters at the current step are calculated based on the temperature at the previous step and are assumed to be constant during the current step. The heat generation due to phase transformation can be treated in a similar way, if considered. In fact, heat generation is, if not specially stated, not considered in all calculations in this study because the austenite is transformed to martensite under the cooling conditions in experiments. The developed program is capable of handling both steady-state and transient heat transfer cases.

Various verification cases have been performed to assess the accuracy, reliability and stability of the 2D FE program for direct heat transfer calculations. Verification cases were solved using both the commercial program ANSYS [59] and the home program developed; the differences between the results from the developed program and ANSYS were shown within less than 0.5% in all cases. Details of these verification cases and results comparisons are omitted for space consideration.

## **3.2 Formulation for Inverse Analysis**

### **3.2.1 Objective function**

The key points discussed in Section 2.3 are summarized in the following for the introduction of the proposed objective function. An IHCP may be generally converted

into an optimization problem. The objective function of the optimization problem may be considered as the sum of the squares of the differences between calculated and measured temperatures. Because inverse problems are generally ill posed, the solution to the IHCP may not be unique and would normally be sensitive to measurement errors. To reduce such sensitivity, information at a number of future time steps is employed to estimate the heat flux  $q^i$  at the current step. And a temporary assumption, normally called a function specification, would be normally considered for the values of heat fluxes at all time steps considered. The function specification technique works as a regularization procedure and stabilizes the solution process. To damp the solution fluctuation due to the measurement errors, the objective function may be made more extensive by including more terms in the expression. A commonly used scalar quantity in this regard is the zeroth-order term based on the heat flux vector  $\mathbf{q}$  with a weighting factor,  $\alpha$ , which is normally called the regularization parameter.

Based on the above discussion, an objective function in the least-squares method, with the future time steps technique and regularization, may be expressed as follows:

$$F(\mathbf{q}) = \sum_{i=1}^N (\mathbf{T}_m^i - \mathbf{T}_c^i)^T (\mathbf{T}_m^i - \mathbf{T}_c^i) + \alpha \sum_{i=1}^N \mathbf{q}^{iT} \mathbf{q}^i \quad (3.6)$$

where  $\mathbf{T}_m^i$ ,  $\mathbf{T}_c^i$  are the experimentally measured and the theoretically calculated temperature vectors at the  $i^{\text{th}}$  time step in a computation window of size  $N$  (Section 3.2.3 B), respectively;  $\mathbf{q}^i$  is the heat flux vector at the  $i^{\text{th}}$  time step,  $\alpha$  is the regularization factor and  $N$  is the number of total steps considered in the computation window.

The heat flux and temperature vectors are

$$\mathbf{q} = [\mathbf{q}^1 \quad \mathbf{q}^2 \quad \dots \quad \mathbf{q}^N]^T \quad (3.7a)$$

$$\mathbf{q}^i = [q_1^i \quad q_2^i \quad \dots \quad q_J^i]^T \quad (3.7b)$$

$$\mathbf{T}_m^i = [T_{1m}^i \quad T_{2m}^i \quad \dots \quad T_{Lm}^i]^T \quad (3.8)$$

$$\mathbf{T}_c^i = [T_{1c}^i \quad T_{2c}^i \quad \dots \quad T_{Lc}^i]^T \quad (3.9)$$

where  $L$  is the number of measurements,  $J$  the number of heat flux components that can be determined for flux space distribution on surface. It is obvious that  $J$  must be less than or equal to  $L$ , the number of measurements.

It should be noted that the dimensions of the heat flux vector  $\mathbf{q}^i$  at each step is  $l \times J$  while the total heat flux vector  $\mathbf{q}$  is  $J \times N$  as it includes the data in  $N$  steps; and the temperature vector  $\mathbf{T}^i$  at each step is  $l \times L$ .

Note that higher order regularization parameters involving the spatial derivatives of  $\mathbf{q}$  are not adopted in this study. The rationale is due to the fact that heat fluxes in the water jet impingement cooling may dramatically change in space, and therefore it is not appropriate to confine the changing rate of the heat flux in space.

By defining  $\Delta \mathbf{T} = (\mathbf{T}_m^1 - \mathbf{T}_c^1 \quad \mathbf{T}_m^2 - \mathbf{T}_c^2 \quad \dots \quad \mathbf{T}_m^N - \mathbf{T}_c^N)^T$  where  $\Delta \mathbf{T}$  has dimensions of  $l \times (L \times N)$ , equation (3.6) may be rewritten as

$$F(\mathbf{q}) = \Delta \mathbf{T}^T \Delta \mathbf{T} + \alpha \mathbf{q}^T \mathbf{q} \quad (3.10)$$

### 3.2.2 General calculation form of heat flux

It should be noted that the temperature  $\mathbf{T}^k$  would be determined or affected only by the heat fluxes  $\mathbf{q}^m$  where  $m \leq k$ . Mathematically,  $\mathbf{T}^k$  may be expressed as an implicit function of the heat flux:

$$\mathbf{T}_c^k = f(\mathbf{q}^1, \mathbf{q}^2, \dots, \mathbf{q}^k) \quad (3.11a)$$

or in a successive form as:

$$\begin{aligned} \mathbf{T}_c^k &= f(\mathbf{T}_c^{k-1}, \mathbf{q}^k) \\ \mathbf{T}_c^{k-1} &= f(\mathbf{T}_c^{k-2}, \mathbf{q}^{k-1}) \\ &\vdots \\ \mathbf{T}_c^2 &= f(\mathbf{T}_c^1, \mathbf{q}^2) \\ \mathbf{T}_c^1 &= f(\mathbf{T}_c^0, \mathbf{q}^1) \end{aligned} \quad (3.11b)$$

The following linear equation is valid by neglecting the terms of higher order:

$$\mathbf{T}_c^k = \mathbf{T}_c^{k*} + \frac{\partial \mathbf{T}_c^1}{\partial \mathbf{q}^1} (\mathbf{q}^1 - \mathbf{q}^{1*}) + \frac{\partial \mathbf{T}_c^2}{\partial \mathbf{q}^2} (\mathbf{q}^2 - \mathbf{q}^{2*}) + \dots + \frac{\partial \mathbf{T}_c^k}{\partial \mathbf{q}^k} (\mathbf{q}^k - \mathbf{q}^{k*}) \quad (3.12)$$

The values with an '\*' superscript in equation (3.12) may be considered as initial guess values that would ultimately lead the temperature  $\mathbf{T}_c^{k*}$ .

Here, the first derivative of temperature  $\mathbf{T}_c^i$  with respect to heat flux  $\mathbf{q}^i$  is defined as the sensitivity matrix:

$$\begin{aligned} \mathbf{X}^i &= \frac{\partial \mathbf{T}_c^i}{\partial \mathbf{q}^i} \\ &= \begin{bmatrix} a_{11}(i) & a_{12}(i) & \dots & a_{1J}(i) \\ a_{21}(i) & a_{22}(i) & \dots & a_{2J}(i) \\ \vdots & \vdots & \ddots & \vdots \\ a_{L1}(i) & a_{L2}(i) & \dots & a_{LJ}(i) \end{bmatrix} \\ a_{rs}(i) &= \frac{\partial T_{cr}^i}{\partial q_s^i} \end{aligned} \quad (3.13)$$

where  $i=1, 2, \dots, N$ ,  $r=1, 2, \dots, L$ , and  $s=1, 2, \dots, J$ . The sensitivity matrix  $\mathbf{X}^i$  is an  $L \times J$  matrix. The optimality of the objective function may be obtained by letting  $\partial F / \partial \mathbf{q} = 0$  (note that  $\partial F / \partial \mathbf{q}$  should be done with respect to each component  $\mathbf{q}^i$ , with  $i=1, 2, \dots, N$ ), and as a result the following set of equations is obtained:

$$\left\{ \sum_{i=1}^N \left( \frac{\partial \mathbf{T}_c^i}{\partial \mathbf{q}^j} \right)_{\mathbf{q}^j = \mathbf{q}^{j*}}^T \left( \frac{\partial \mathbf{T}_c^i}{\partial \mathbf{q}^j} \right)_{\mathbf{q}^j = \mathbf{q}^{j*}} + \alpha \mathbf{I} \right\} (\mathbf{q}^j - \mathbf{q}^{j*}) = \sum_{i=1}^N \left( \frac{\partial T_c^i}{\partial \mathbf{q}^j} \right)_{\mathbf{q}^j = \mathbf{q}^{j*}}^T (\mathbf{T}_m^i - \mathbf{T}_c^{i*}) - \alpha \mathbf{q}^{j*} \quad (3.14)$$

$j = 1, 2, \dots, N$

where  $\mathbf{q}^{j*}$  is the initial guess of heat fluxes, and  $\mathbf{T}_c^{i*}$  is the calculated temperature vector with the initial guess values.

Recalling equations (3.12) and (3.13), equation (3.14) may be rearranged and rewritten in the following form:

$$(\mathbf{X}_{\mathbf{q}=\mathbf{q}^*}^T \cdot \mathbf{X}_{\mathbf{q}=\mathbf{q}^*} + \alpha \mathbf{I})(\mathbf{q} - \mathbf{q}^*) = \mathbf{X}^T \Delta \mathbf{T} - \alpha \mathbf{q}^* \quad (3.15)$$

where  $\mathbf{X}$  is labeled as the total sensitivity matrix for a multi-dimensional problem and has the following form:

$$\mathbf{X} = \begin{bmatrix} \mathbf{X}^1 & 0 & 0 & 0 \\ \mathbf{X}^2 & \mathbf{X}^1 & 0 & 0 \\ \vdots & \vdots & \ddots & 0 \\ \mathbf{X}^N & \dots & \mathbf{X}^2 & \mathbf{X}^1 \end{bmatrix} \quad (3.16)$$

It should be noted that the dimension of matrix  $\mathbf{X}$  is  $(L \times N) \times (J \times N)$ . Also, it is worth noting that performing the calculation in equation (3.15) may be easily done in the entire time domain, and no function specification for  $\mathbf{q}^i$  is needed. If the total sensitivity is known and accurate, iteration may not be required to obtain a final solution.

### 3.2.3 Iterative and sequential algorithms

#### 1. Function specification and iteration technique

The form of the governing differential equation for both the temperature  $\mathbf{T}(\mathbf{x}, t)$  and the sensitivity coefficient  $\mathbf{X}(\mathbf{x}, t)$  is the same [39] and, therefore, the same FE program may be used to calculate them. While this is efficient from the programming point of view, it may not be practical, especially when the temperature time history is somewhat long, the density of mesh is high, and the coefficients at all points are not all needed to get the heat flux  $\mathbf{q}$ .

An alternative way is to calculate the sensitivity matrices at each time step for the target points. Such a procedure would still require an extensive calculation time and a higher cost when the number of time steps considered and/or the number of heat flux components are reasonably large.

A perturbation algorithm [23] was used to obtain the sensitivity matrices  $\mathbf{X}^1$  (only the information at the current step was included in the work presented in [23]). First, a given value  $\mathbf{q}^{1*}$  is assumed for all components of the heat flux vector  $\mathbf{q}^1$ ; the direct heat transfer calculation is conducted to get the temperature distribution, say  $\mathbf{T}_0^1$ , for the given future steps at each TC location. Then, one component of heat flux  $\mathbf{q}^1$ , say the  $J^{th}$  component, is increased a reasonable amount, such as 10%, to obtain new temperatures,  $\mathbf{T}_j^1$ . The ratios of temperature difference at each TC location to the difference of the  $J^{th}$  heat flux component are the sensitivity coefficients. Such a perturbation is repeated for each component of the heat flux  $\mathbf{q}^{1*}$  until all sensitivity matrix components of  $\mathbf{X}^1$  are obtained.

The above method would be adopted in this study. By applying this approach, several issues should be resolved. First, the heat fluxes  $\mathbf{q}^{i*}$  for  $i = 2 \dots N$  in the consecutive steps should be assigned. As mentioned in Section 3.2.1, the function specification would

stabilize the solution process. Moreover, it would simplify the calculation of the total sensitivity matrix  $\mathbf{X}$ . A constant assumption is used in this study, i.e.,  $\mathbf{q}^{1+k^*} = \mathbf{q}^{1^*} = \mathbf{q}^*$  for  $1 \leq k \leq n_{\text{FTS}}$ . Therefore, all sensitivity matrices  $\mathbf{X}^i$  for  $i=1,2,\dots,N$  may be obtained from the above method by one assignment when the direct calculation is performed for  $N$  steps.

The second issue is the nonlinearity. The whole sensitivity matrix  $\mathbf{X}$  is independent of the heat flux  $\mathbf{q}$  only if the conductivity  $k$  and specific heat  $c_p$  are not functions of the temperature or if the average values for these quantities are used when the dependencies on temperature exist. The thermophysical properties of most steels are temperature dependent. If this kind of dependency is considered, all properties should be updated at the beginning of each time step, which is time-consuming, especially for large size models. Moreover, such changes in properties would not be very large and would not significantly change the magnitude of  $\mathbf{X}$ . Also, updating the material properties at the beginning of each time step would be based on the temperatures  $\mathbf{T}^{k^*}$  obtained from the initially given values of heat flux  $\mathbf{q}^*$ , which is essentially an approximation. The assumption of a constant value is, therefore, justified. As a slight modification to the above assumption, another option is to update the sensitivity matrix  $\mathbf{X}$  every  $M$  steps (in our numerical experiments,  $M=10$ ). Both methods led to similar results of inverse calculation, so the use of constant sensitivity matrix is justified.

Other factors affecting the accuracy of the calculated heat fluxes are the future information and the addition of regularization parameters. To improve the accuracy due to these factors, the iterative technique with convergence limits is adopted in this study.

Some modifications to equation (3.15) are to be considered. The term  $\alpha \mathbf{q}^*$  (eventually  $\alpha^n \mathbf{q}$  in the iterative process) would lead to an increment  $\Delta^1 \mathbf{q}$  and a better estimation for the first value of  ${}^1 \mathbf{q}$ . This term makes the calculation more cumbersome with very little benefit in convergence and, therefore, will be neglected, and the equations may be written as:

$$(\mathbf{X}^T \mathbf{X} + \alpha \mathbf{I}) \Delta^1 \mathbf{q} = \mathbf{X}^T \Delta \mathbf{T}^* \quad (3.17a)$$

$${}^1 \mathbf{q} = \mathbf{q}^* + \Delta^1 \mathbf{q} \quad (3.17b)$$

$$(\mathbf{X}^T \mathbf{X} + \alpha \mathbf{I}) \Delta^n \mathbf{q} = \mathbf{X}^T \Delta^{n-1} \mathbf{T} \quad (3.17c)$$

$${}^{n+1}\mathbf{q} = {}^n\mathbf{q} + \Delta^n\mathbf{q} \quad (3.17d)$$

where  $n$  is the number of iterations.

## 2. Sequential technique and function specification

Starting with either equation (3.15) or equation (3.17), a number of  $N$  flux vectors  $\mathbf{q}^i$  for  $i = 1 \dots N$ , corresponding to each time step, can be estimated simultaneously. When  $N$  is equal to the whole time step in the measurement, the developed method may theoretically be used to obtain the entire time history of heat fluxes.

The focus of this study is, however, more on the application of the method than on the method itself. During the water jet cooling process, the temperature at each measurement point will drop sharply within only a few limited time steps. Such a sharp drop means that a large load or heat flux vector would occur during such a small fraction of the time domain. Other measuring points will have the same phenomena but at a different time window. This means that if the whole domain approach is used there will be a large fluctuation in the load vector, and as a result the convergence of the solution may be significantly affected. Therefore, the number of time steps  $N$  is normally less than 10.

A "computation window" of size  $N$  may be used sequentially to determinate the heat fluxes in the span of time considered. To clarify this procedure, an example is illustrated in the following where  $N = 3$  is assumed at the beginning of the analysis (the same if assuming at any time step). In the first sequence, the heat fluxes at the first three steps may be obtained by iteration as:

$$\begin{pmatrix} {}^{n+1}\mathbf{q}^1 \\ \mathbf{q}^2 \\ \mathbf{q}^3 \end{pmatrix} = \begin{pmatrix} {}^n\mathbf{q}^1 \\ \mathbf{q}^2 \\ \mathbf{q}^3 \end{pmatrix} + \begin{pmatrix} \Delta\mathbf{q}^1 \\ \Delta\mathbf{q}^2 \\ \Delta\mathbf{q}^3 \end{pmatrix} \quad (3.18)$$

The subsequent three heat flux vectors  $\mathbf{q}^4$  to  $\mathbf{q}^6$  may be estimated if the temperatures  $\mathbf{T}^3$  are considered as the initial temperature for the next sequence, and the computation window moves 3 steps; and so on for each subsequent sequence.

The above procedure presents a hybrid approach between a whole domain one and a true sequential one that will be addressed later in the following paragraphs. This hybrid method implies that the heat fluxes at the previous iteration at each time step will be used

in the next iteration for the corresponding time step; i.e., at the  $(n+1)^{\text{th}}$  iteration  ${}^n\mathbf{q}^1$  will be used for the first time step,  ${}^n\mathbf{q}^2$  for the second one and  ${}^n\mathbf{q}^3$  for the third one. There will be no need for function specification.

In this thesis, a completely sequential approach with function specification is used. First, the newly calculated  ${}^n\mathbf{q}^1$  is used for all time steps within the computation window after the first iteration; i.e., a constant function specification is used for this computation window. Second, the computation window moves one time step at the next sequence after obtaining a convergent solution in the current sequence. Once again, using the previous example, the first computation window consists of time step 1 to time step 3; and the second one includes time step 2 to time step 4.

### 3.2.4 Convergence norm

In each time step, the iterative procedure is used until the inversely predicted temperature  $\mathbf{T}_c$  converges to the measured temperature  $\mathbf{T}_m$ . The convergence criteria used to define the acceptance of the predicted temperature are based on an error norm for the  $n^{\text{th}}$  iteration defined by:

$$\text{Error-norm}^n = \|\Delta\mathbf{T}^n\| \quad (3.19)$$

Two convergence criteria for ending the iteration process at each time step are used:

$$\text{Error-norm}^n \leq \delta T \quad (3.20a)$$

or

$$\frac{|\text{Error-norm}^{n+1} - \text{Error-norm}^n|}{\text{Error-norm}^n} \leq \varepsilon \quad (3.20b)$$

The values of  $\delta T$  and  $\varepsilon$  depend on the measurement error level. The rationale behind using absolute criteria is that while the norm at a given previous iteration is already very small, the relative norm criterion is still not satisfied at the last iteration, and therefore, a convergent solution can not be obtained. For example, if assume  $\delta T=0.5$ ,  $\varepsilon=0.05$ , Error-norm<sup>n</sup> = 0.49 and Error-norm<sup>n+1</sup> = 0.46 (here  $n+1$  is the last iteration), then there is:

$$\frac{|0.46 - 0.49|}{0.49} = 0.06 > 0.05 \quad (3.21)$$

### 3.2.5 Flux zoning method (FZM)

The developed inverse analysis algorithm is a general approach that was implemented in a FE program to determine the heat flux during the water jet cooling process. Special procedures for specifying the heat flux distribution on target surface are considered and implemented.

A common approach is to divide the target surface into several subregions; each subregion may correspond to one temperature measurement. The same value of heat flux is assumed for all nodes in a given subregion. The heat fluxes for various subregions are generally not equal, i.e.,  $q_i \neq q_{i+1}$ . The heat flux vector composed of all of heat fluxes on each subregion may be determined using the above inverse algorithm. This approach is named Flux Zoning Method (FZM). The model is schematically illustrated in Figure 3.2. In this figure, two adjacent subregions are plotted.

There are eventually many nodes in each subregion, and the sampling (virtual measurement) point should be located in the middle. Therefore, even number of elements should be used. In fact, the number of nodes in each individual subregion may have little effect on both the calculation procedure and accuracy, and may have a limit only from the consideration of the element aspect ratio.

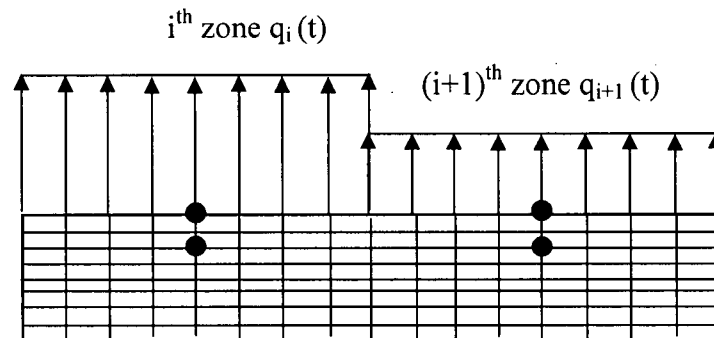


Figure 3.2 FZM FE Model for inverse calculation

This approach is fairly simple and easy to implement. It may also be a good practice for the pool cooling process or cooling surface that is covered simultaneously by water, for example, the impingement zone under the jet water cooling. In fact, the heat flux determined using FZM would be the average one for each subregion, there is

$$q_i(t) = \frac{1}{b-a} \int_a^b q_i(x,t) dx \quad (3.22)$$

where  $a$  and  $b$  are the starting and end points of the subregion.

When the heat flux is nearly constant or does not dramatically change spatially in a given subregion; the obtained heat flux would be a good approximation. However, this approach may not be an appropriate method for the cooled surface outside of impingement because it does not consider the progression of water cooling zones, which will be discussed in detail in Chapter 4.

It is possible that the number of subregions is less than that of the measurements when several TCs line up vertically (in our test configuration).

### 3.2.6 Flowchart

The developed algorithms and the FZM are successfully implemented in the FE program, which is capable of solving both direct and inverse heat transfer problem. Figure 3.3 shows a simplified flowchart for the proposed FZM IHCP solution procedure. In the procedure, the initial guess  $q^*$  of heat flux  $q$  may be taken as zero or any other value. However, the heat flux  $q^2$  obtained at the previous sequence may be used as the initial guess of heat flux at the current step to accelerate and enhance convergence. The numerical results show that such a setup of the initial guess of the heat flux is better than a random guess.

## 3.3 Parametric Study to FZM

The following section provides only highlights of the test cases performed for the inverse analysis using FZM and the results obtained.

### 3.3.1 Test procedure and data

The inverse analysis procedures are tested with verification cases that are designed to simulate the cooling of steel plates on a ROT. Typical values of heat fluxes in these applications are provided as an input for a direct analysis, and the direct calculation data are used to verify the inverse analysis.

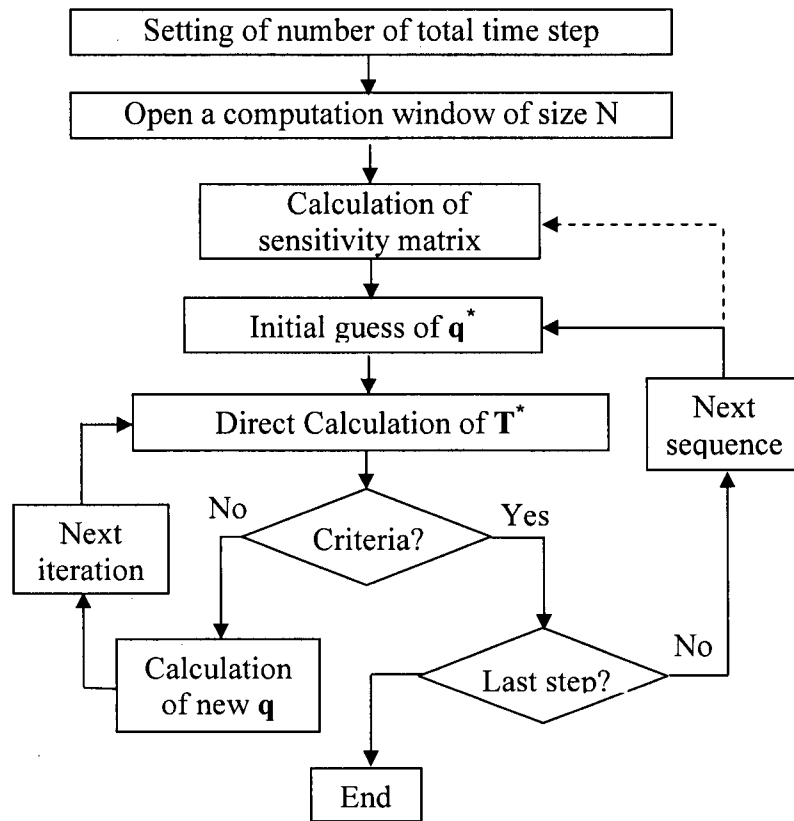


Figure 3.3 Flowchart for FZM IHCP solution procedure

Two cases are tested to investigate the effects of number of total (future) time steps on the elimination of damping and lagging behavior, and to identify the appropriate value of regularization parameters. Triangular and impulse heat flux inputs, with the values that simulate actual conditions in the ROT cooling, are used.

The first stage of the verification involves specifying input heat fluxes and solving a direct heat transfer analysis problem to obtain the corresponding temperature field. The second stage involves an inverse analysis in which the internal temperatures at the target points (here, two locations) calculated from the first stage are used as virtually-measured ones, called as the virtual internal temperature or directly the measured temperature later on. From the virtual internal temperatures the heat fluxes and surface temperatures are inversely calculated. A comparison of the inversely calculated surface temperatures to the directly calculated ones is performed to further verify the accuracy and stability of the inverse analysis algorithm.

To study the effects of measurement errors in internal temperatures on the inversely calculated heat fluxes, random errors are imposed onto the calculated exact internal temperatures with the following equation:

$$T_m = T_{exact} + \sigma \cdot r \quad (3.23)$$

where  $T_m$  is the virtual internal temperature, °C;  $T_{exact}$  is obtained from the direct heat transfer analysis, °C;  $r$  is a normally distributed random variable with zero mean and unit standard deviation; and  $\sigma$  is the standard deviation, °C. In this work, the maximum additive random error  $\sigma$  is  $\pm 3$  °C, making a total difference of up to 6 °C. In the water jet cooling experiment, the plate temperature ranges from about 900 °C to 100 °C. This means that the relative error has a range of about  $\pm 0.33\%$  (at higher plate temperatures) to  $\pm 3\%$  (at lower temperatures). In the following discussion, the error is presented in its absolute value.

The general FE model used for both the direct and inverse analyses is a 2D one with the same mesh, as shown in Figure 3.2. The model is 7 mm high and 20 mm wide. The top surface is evenly divided into two parts, which means that the horizontal distance between sampling points in each subregion is 10 mm. Two components of heat fluxes are applied, and each of them is specified on all nodes in the corresponding subregion. Other surfaces are prescribed as thermally insulated. Four points, two on the surface and two 1 mm beneath the surface points, are selected. The temperatures at the two internal points are used in the inverse analysis to estimate both the heat fluxes and the temperatures of the points on the top surface.

The material is assumed to be carbon steel with a density of 7800 kg/m<sup>3</sup>, a conductivity of 32 W/m·°C, and a specific heat of 470 J/kg·°C for the whole time period. The thermal diffusivity for this steel is about  $9.55 \times 10^{-5}$  m<sup>2</sup>/s.

The time step used for both the both direct and inverse analyses is the same and is equal to 0.01 sec. As mentioned in Section 2.4, the dimensionless time step is 0.955, which maintains stable calculations in the inverse scheme.

In the verification tests, the norms for convergence are assigned to be of the order of magnitude of the imbedded measurement error level. The number of future time steps is determined by successive trials and is kept constant throughout the analysis. More

discussion about the choice of the regularization parameter will be given in following sections.

### 3.3.2 Triangular heat flux inputs

Figure 3.4 shows the two triangular heat flux inputs for the two subregions. They have the same profile and peak value but with a time shift of 0.5 seconds to produce a spatial temperature gradient in the longitudinal direction.

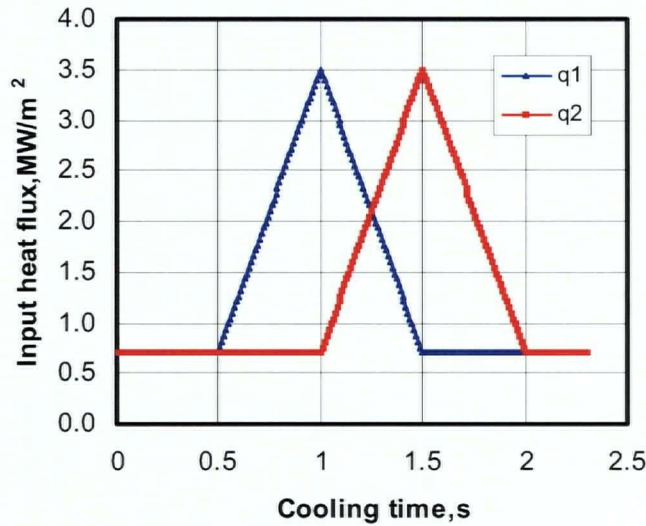


Figure 3.4 Triangular heat flux inputs

Inverse analysis is first performed with the assumption that there is no measurement error in the internal temperatures. For this case, the calculated heat fluxes match exactly with the assumed input values. The regularization parameter has no effect on the results and may be assumed to be zero, and the number of future time steps has little effect on the inversely calculated heat fluxes.

Other cases have been studied with various levels of measurement errors and different regularization parameters and future time steps. Figures 3.5–3.7 show the results of these cases and the corresponding parameters in each case.

Figure 3.5 shows the effect of the measurement error level on the inversely calculated heat flux with a fixed regularization parameter and a fixed number of future steps. As expected, the heat flux fluctuation increases with the increase of error in the virtual internal measured temperature. However, the profile of the calculated heat flux is still in

good agreement with that of the exact input, and the accuracy of the predicted peak flux value is good.

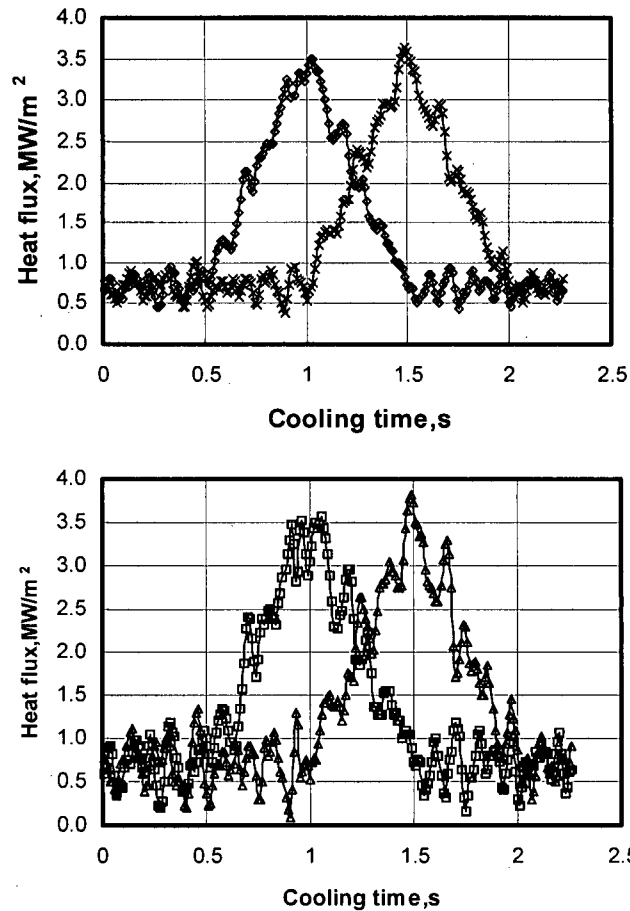


Figure 3.5 Effect of measurement error level  
 $\alpha = 1.0e-11$  3 future steps  
 Error level: upper =  $\pm 0.5$  °C; bottom =  $\pm 1.0$  °C

The effect of the number of future time steps is illustrated in Figure 3.6. In these cases the value of the regularization parameter is kept constant at  $1.0e-11$ , and the error level is fixed at  $\pm 1.0$  °C. Fewer fluctuations of the calculated heat flux are evident with the increase of the number of future steps. An obvious improvement occurs when the number of future steps increases from 3 to 5, whereas there is slightly less impact for increasing the number of future steps to 5 or 7. It may be concluded that using 4–6 future steps is appropriate and reduces fluctuation levels.

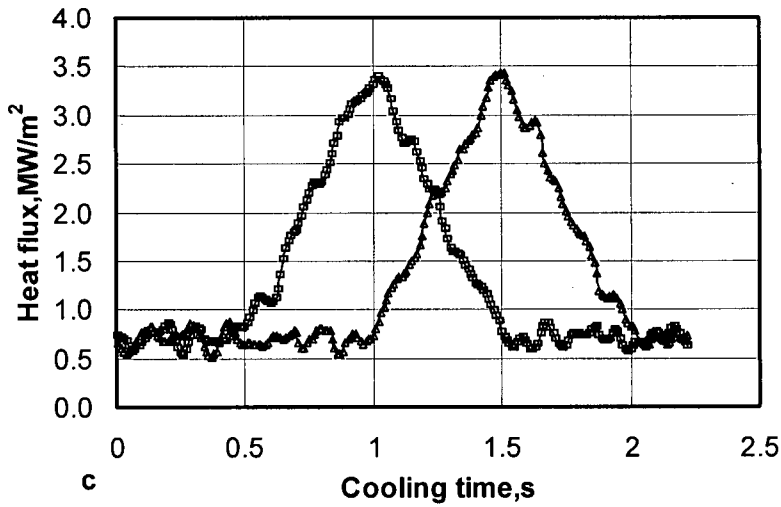
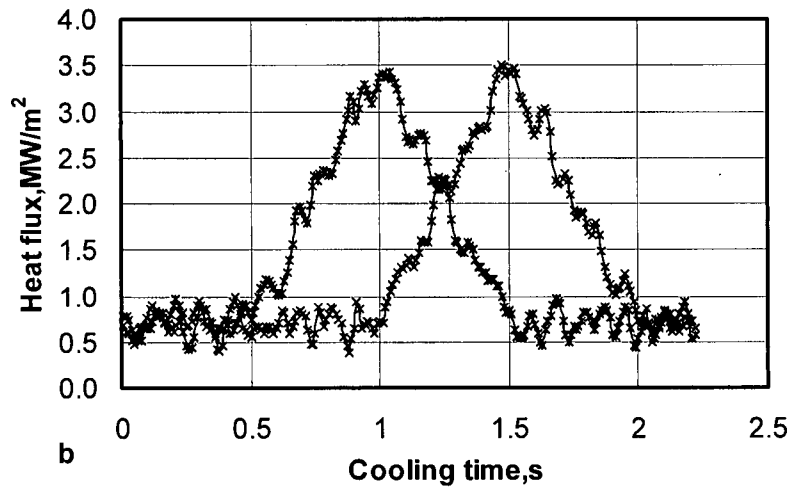
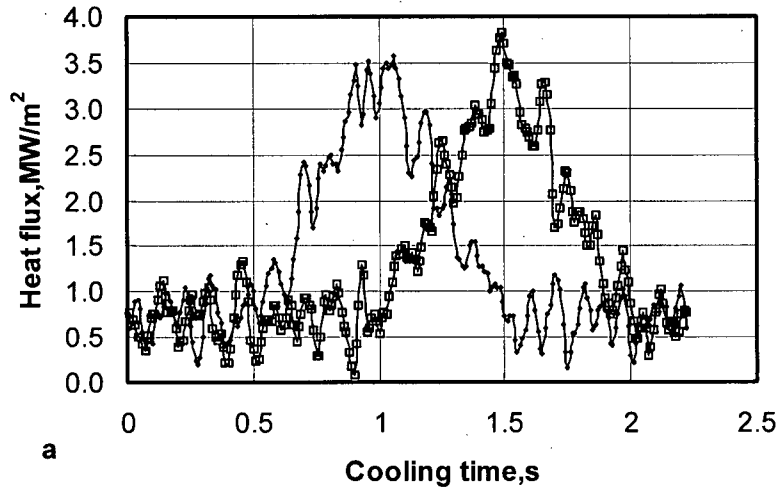


Figure 3.6 Effect of number of future steps

$\alpha = 1.0e-11$  error level =  $\pm 1.0$  °C

a: 4 future steps

b: 6 future steps

c: 8 future steps

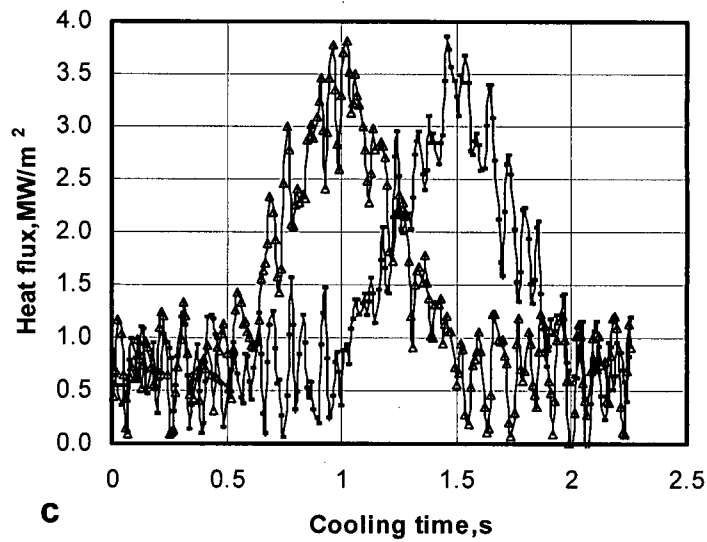
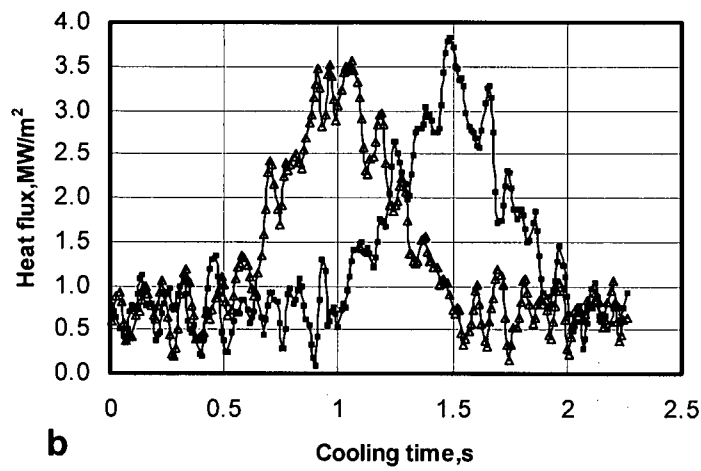
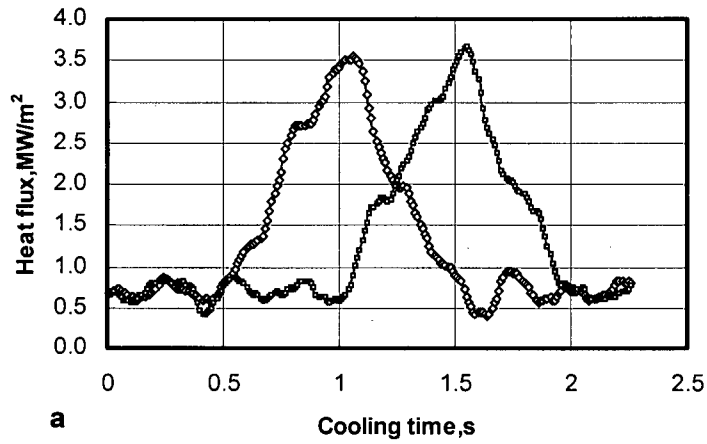


Figure 3.7 Effect of regularization parameter  
 4 future steps error level =  $\pm 1.0$  °C  
 a:  $\alpha=1.0e-10$ ; b:  $\alpha=1.0e-11$ ; c:  $\alpha=1.0e-12$

Figure 3.7 shows the effect of varying the regularization parameter value  $\alpha$  on the calculated heat flux. Numerical experiments showed that this is a much more delicate parameter to control. Stable and accurate results are obtained for a range of values of  $\alpha=1.0e-10$  to  $1.0e-12$ , which is close to the diagonal value of the sensitivity matrix of  $1.0e-10$ . That is quite an interesting discovery.

Lowering the value of  $\alpha$  to less than  $1.0e-14$  will increase fluctuations of the inversely calculated heat fluxes, while increasing the value of  $\alpha$  to greater than  $1.0e-9$  greatly increases the required number of iterations, and in many cases causes divergence. It should be noted that for all the cases considered above, the maximum difference between the exact value of the surface temperature and the inversely calculated one is only around  $5\sim 10$  °C; i.e., the inverse calculation error level is about 10%. This implies that the proposed algorithm might successfully recover both the heat flux and surface temperature.

### 3.3.3 Impulse-like heat flux inputs

To further examine the capacity of the proposed IHCP scheme and its appropriateness to the simulation of impingement cooling, a second test with impulse-like heat fluxes, as shown in Figure 3.8, is performed.

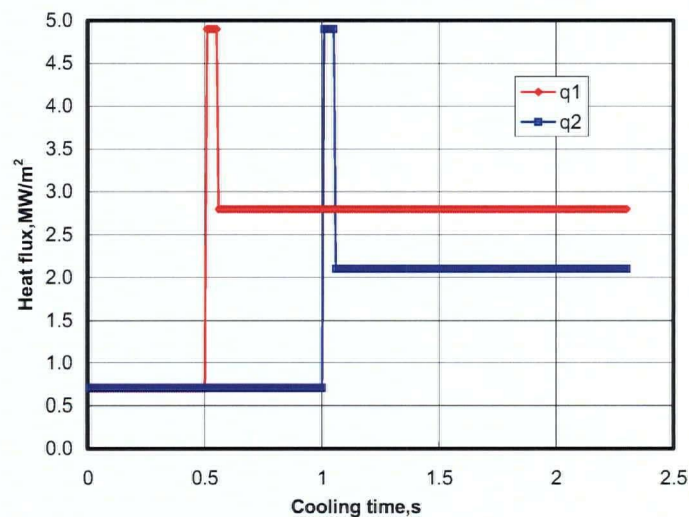


Figure 3.8 Impulse-like heat flux inputs

The impulse test is known to be the most stringent one for the IHCP algorithms. To simulate the real conditions on a ROT, a vary high value of heat flux (in the order of those experienced practically) is applied in a very small time period, equivalent to only five time steps in the solution scheme. The same FE model and procedures discussed in the previous sections are used here.

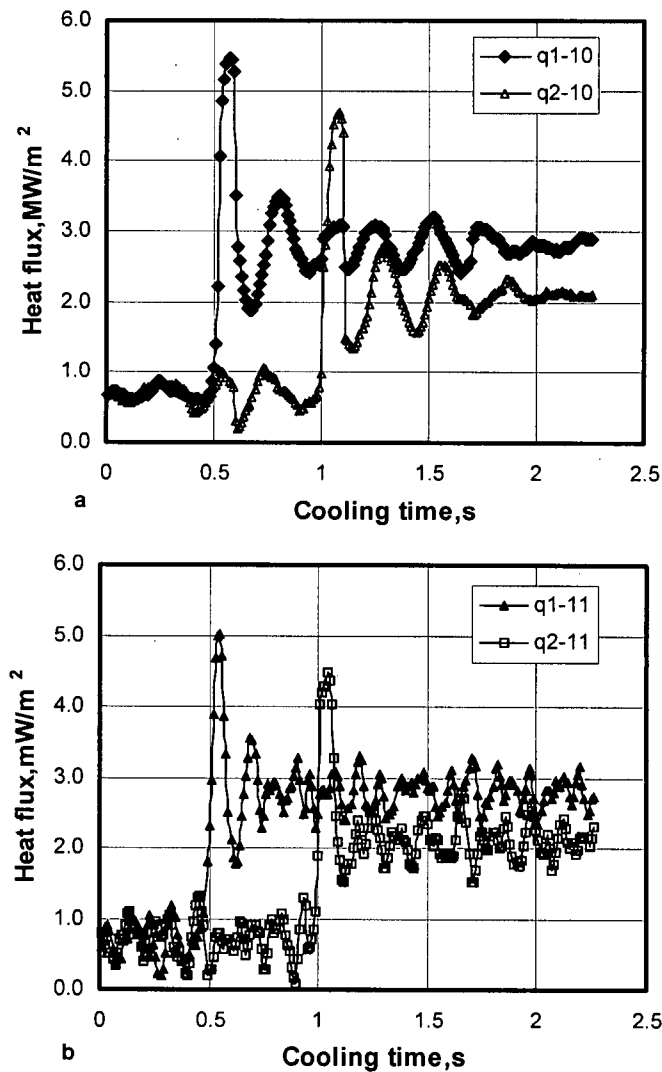


Figure 3.9 Effect of regularization parameter  
 3 future steps, error level =  $\pm 1.0$  °C  
 a:  $\alpha=1.0e-10$  ( $q1-10$ ,  $q2-10$ ) and b:  $1.0e-11$  ( $q1-11$ ,  $q2-11$ )

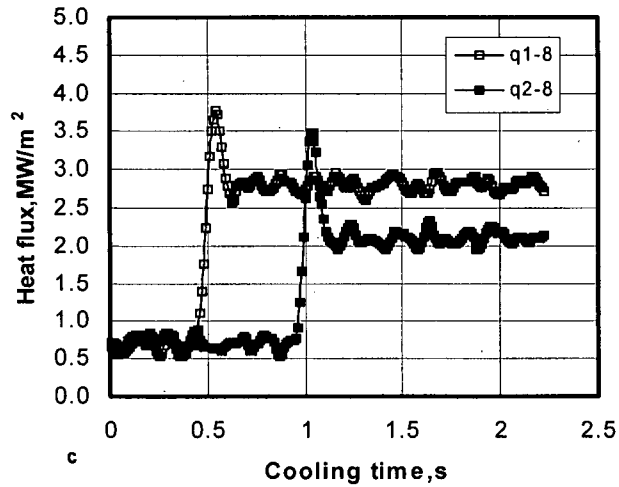
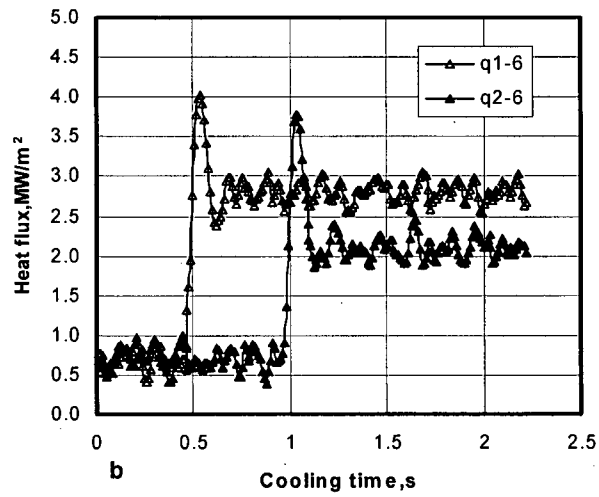
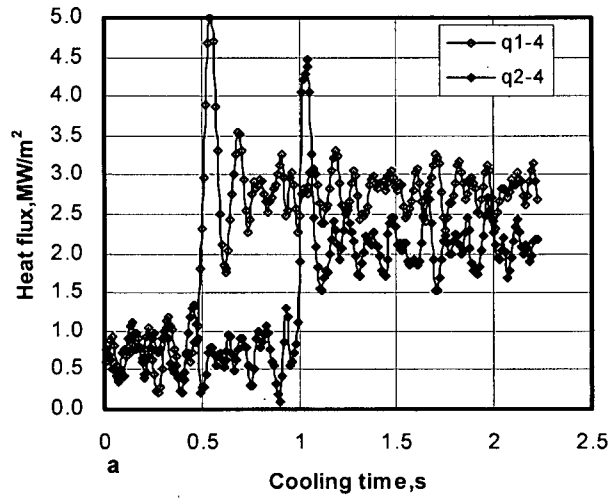


Figure 3.10 Effect of future step number  
 $\alpha=1.0e-11$ , error level =  $\pm 1.0$  °C  
 a: future steps 3 (q1-4, q2-4); b: 5 (q1-6, q2-6); c: 7 (q1-8, q2-8)

The inversely calculated heat fluxes under different conditions are shown in Figure 3.9 to Figure 3.11. As in the previous example, the inversely calculated heat fluxes are almost identical to the input ones when no measurement errors are imposed onto the internal temperatures.

Also in this case, the regularization parameter has no effect on the inverse results and may be assumed to be zero, and the number of future steps has little effect on the inversely calculated heat fluxes.

Similar to the outcome of the previous example, it is found that with the increase of the measurement errors in the input temperatures, the value of both the regularization parameter and the number of future time steps should be increased to obtain acceptable levels of accuracy.

Figure 3.9 shows a comparison between the calculated heat fluxes using different values of the regularization parameter and a level of  $\pm 1$  °C error in the measured temperature. Also, the inverse results show that the peak values of heat fluxes are quite accurate. Even when fluctuations of the calculated values are evident, the average value of the fluctuation represents a good approximation of the exact input. It is also apparent that the regularization parameter has less impact on the fluctuation of the results.

The effect of the number of future steps on the calculated heat flux for the impulse-like heat flux case is shown in Figure 3.10. It may be seen that there is a somewhat large fluctuation when four future steps are used, and that the fluctuation from the measurement errors is damped gradually with the increase the number of future steps. When 7 future steps are used the calculated heat flux value is quite close to the input for the period during which the input heat flux is constant.

However, the peak value is also smeared when the number of future steps increases, although it may still be captured accurately. The damping effect of the future time steps increases significantly when the number of future steps is larger than the number of time steps of the input impulse. This is logical since more weight for the steps with a lower heat flux input is assumed.

With the increase of the measurement error level, both the number of future steps and the value of regularization parameter should be increased to get reasonable results. Figure 3.11 shows the calculated heat flux for error level  $\pm 3.0$  °C. The result is obtained by

using 5 future steps and setting  $\alpha=1.0e-10$ . It is obvious that the fluctuation of the estimated heat flux is quite large. Although the peak value seems to be adequately captured, it is difficult to say that this is a real peak because such a peak may come from a larger measurement error. It should be noted that other choices of future time step numbers and regularization parameter do not produce better results. This indicates that the calculated heat fluxes (if convergence is achieved) would be quite inaccurate if the random error in the actual measured temperature is larger than  $\pm 3.0$  °C.

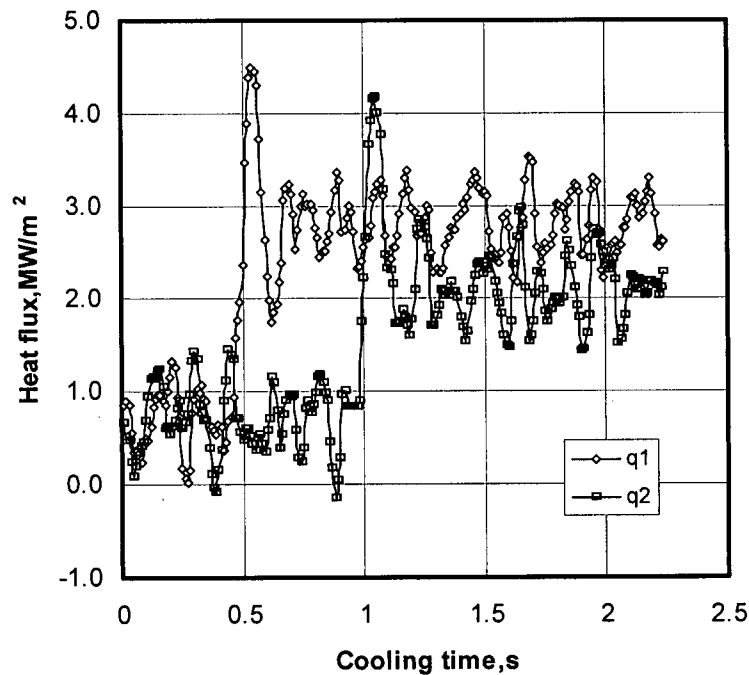


Figure 3.11 Calculated heat flux  
Error level =  $\pm 3.0$  °C, 5 future steps,  $\alpha = 1.0e-10$

From the several examples discussed above, it may be concluded that the proposed inverse calculation is generally stable and accurate but very sensitive to the measurement error. The calculated peak heat fluxes are in reasonable agreements with the inputs only when the error is not larger than  $\pm 3.0$  °C. It is also apparent that the number of future time steps should be around 3, while the regularization parameter value should be equivalent to the diagonal value of the sensitivity matrix. In addition, the inverse calculation error can be controlled within 10% for both heat flux and surface temperature.

### 3.4 Summary

The developed FE program has the following features.

- 1) It can solve steady-state or transient, direct or inverse, plane or axisymmetric heat transfer problems;
- 2) Various types of boundary conditions such as specified surface temperature, surface and nodal flux, convection and radiation as well as heat generation may be considered, all of which may be functions of location and time;
- 3) Temperature dependence of thermal properties may be taken into account;
- 4) Implicit and explicit solution algorithms are available as well as consistent and lumped capacitance matrix;
- 5) Domain discretization with a mixture of different element types is available.

In the proposed algorithm for IHCP, the sensitivity matrix is calculated only once at the beginning of the iterative procedure and used for all steps. The iterative technique is adopted for compensation of the use of regularization parameter and the simplification in the sensitivity matrix calculation. Two criteria are used for convergence. Parametric study results indicate that the use of the least-squares method, the sequential function specification and regularization is appropriate for IHCP in water cooling applications; and that in the inverse calculation the fluctuation of the inversely calculated heat flux due to random errors in the measurement data may be damped by increasing the number of future steps and the value of the regularization parameter.

All calculations show that the proposed algorithm and procedures are very simple, useful and effective, and that they can recover the heat flux and surface temperature histories on the cooling surface with 10% errors when the random error in the internal temperature is within  $\pm 1$  °C.

## Chapter 4

### FLUX MARCHING METHOD FOR IHCP IN WATER JET COOLING

The cooling characteristics of water jet, especially the progression of cooling zones, are first described. A new approach, "Flux Marching Method (FMM)", is then developed to better suit the features of impingement water cooling. Numerical tests have been designed to explore the effectiveness of the FMM and to compare its performance with the more commonly utilized flux zoning method (FZM).

#### 4.1 Progression of Water Jet Cooling Zones

##### 4.1.1 Stationary plate case

The cooling water will spread out radically (circular jet) or longitudinally (planar jet) after it impinges onto the surface of a stationary plate. In the following sections the discussion is confined to a single circular jet, although such a discussion is generally valid for a planar jet; and it is based on experimental results in the literature [4].

For stationary cases, the cooled area on the top surface is axisymmetrical about the stagnation point for a single circular jet. For a steady-state jet cooling process, the cooled area on the top surface can be divided into five different heat transfer regimes: impingement zone with the single-phase forced convection, nucleate-transition boiling regime, forced convection film boiling regime, agglomerated pool cooling regime and dry zone with radiation and convection, as shown in Figure 2.4.

For a transient process using a single stationary jet, the latter four cooling zones should progress outwardly until the full plate is cooled down to the ambient temperature or water temperature.

According to the visual records [25], the cooled area on the top surface can be divided into three zones, as schematically shown in Figure 4.1a. The plate immediately turns grey around the impingement zone as the water impinges onto the plate surface. Outside the darkened zone the plate is still red hot. Shortly after the start of cooling, the grey area around the impingement zone begins to turn black and the cooling water progresses outwards. In this black zone, the cooling effectiveness is very high, and the surface

temperature drops sharply to a low temperature such that the boiling may not be possible. The radiation and air convection cooling are dominant in the red zone. The progression to the black colour is very rapid. As the black zone grows within the grey zone, the grey zone itself also grows outwards but at a considerably lower rate. When the size of the black zone gets close to that of the grey zone, the two zones grow approximately at the same speed. Hence, while the plate is being cooled by a circular jet there is a black zone centered at stagnation point, followed by a relatively small grey circular ring around the black zone, and finally by a bright red zone. It is clear that the black zone grows until it finally covers the entire cooled surface. Such a progression of cooling zones implies that: 1) only the material points in the impingement zone are cooled simultaneously at the same rate; 2) any material point outside of the impingement zone is cooled sequentially at different rates, and the further the point from the stagnation point, the later it is cooled; 3) any material point outside of the impingement zone is first cooled in the grey zone with a low cooling capacity, and its temperature should decrease at a slower rate, and a sharp temperature drop should take place as the front of the black zone approaches. Although the above observations seem obvious; they have not been fully considered in an inverse heat transfer analysis.

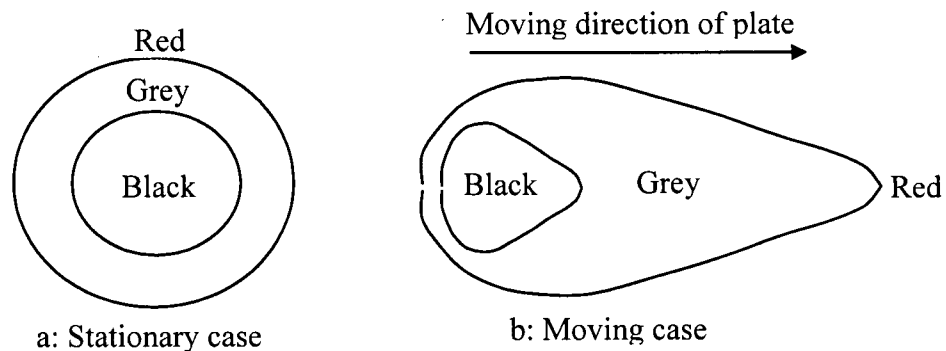


Figure 4.1 Progression of cooling zones

It can be assumed that the initial black zone is equivalent to the impingement zone while in the red zone radiation is dominant.

The progressing speed of the black zone front for stationary cases will be discussed in Section 4.1.3.

#### **4.1.2 Moving plate case**

The abovementioned three cooling zones: black zone, grey zone and red zone still exist for a moving plate; with some important differences that will be discussed below. First, the cooling zones are symmetric only about the moving direction of the plate, and take a pearl shape or a comet shape whose long axis is along the moving direction, as shown in Figure 4.1b. On the side where the water flow and the plate move in the same direction, the water layer thickness may decrease because the flow may be promoted by the plate motion, while the water layer thickness may increase due to stretching toward the jet by such a motion on the other side where the water flow and plate travel in the opposite direction.

Second, it can be assumed that all of the three zones simultaneously move with the same speed, and that the pattern and size of the cooling zones do not change. This means that any of the material points will pass sequentially through the red zone, the grey zone, the black zone, the grey zone and finally back to the red zone. This final return to the red zone occurs because the cooling time is very short and the material somewhat distant from the black and the grey zones does not have enough time to cool down and transfers its heat to the cooled part. The temperature recovery can be verified by simple inspection of the cooling curves, one example of which is shown in Figure 6.5.

Third, the relative moving speed of the water to the plate may be much smaller, even in the moving direction, whereas the water speed definitely decreases in the transverse direction due to the decrease of water flow in this direction. This leads to the assumption that the actual velocity of the water may be neglected, and the plate is cooled by a moving pattern (here a pearl shape) of cooling water, and that the moving speed of the cooling pattern is fairly close to the plate's moving speed.

#### **4.1.3 Progressing speed of black zone front in stationary cases**

It is of interest to investigate the progressing speed of black zone in stationary cases. As discussed in Section 2.1.1, it is suggested that the cooling area outside the impingement zone is classified as a parallel flow zone, and in the parallel zone the wall jet flows parallel to the surface. The water horizontal velocity is also assumed to be constant and equal to the jet velocity, and the pressure is equal to the ambient pressure. This claim

seems problematical. Assuming that the distance of the nozzle exit to the plate is 1.0 m and the water exit velocity is zero, the jet velocity will be around 4.4 m/s. If the water velocity is actually equal to the jet velocity the material points that are outside of the impingement zone and 0.440 m away from the stagnation point will be covered by water in less than 0.1 second; and the temperatures at those points should drop fast to lower values. The experimental data, however, reveals another trend.

Figure 4.2 [27] clarifies this issue. This figure shows 8 temperatures numbered T1 to T8 measured using the configuration shown in Figure 2.6. In the test, TC1 is located at the stagnation point, and TC1 and TC2 are roughly inside of the impingement zone whereas the others are outside of the stagnation zone. Because the distance between TCs is fixed at 15.9 mm, the progressing speed of black zone front can be calculated by estimating the time intervals taken by this front to travel from locations TC2 through TC8 from the measured temperature-time profiles.

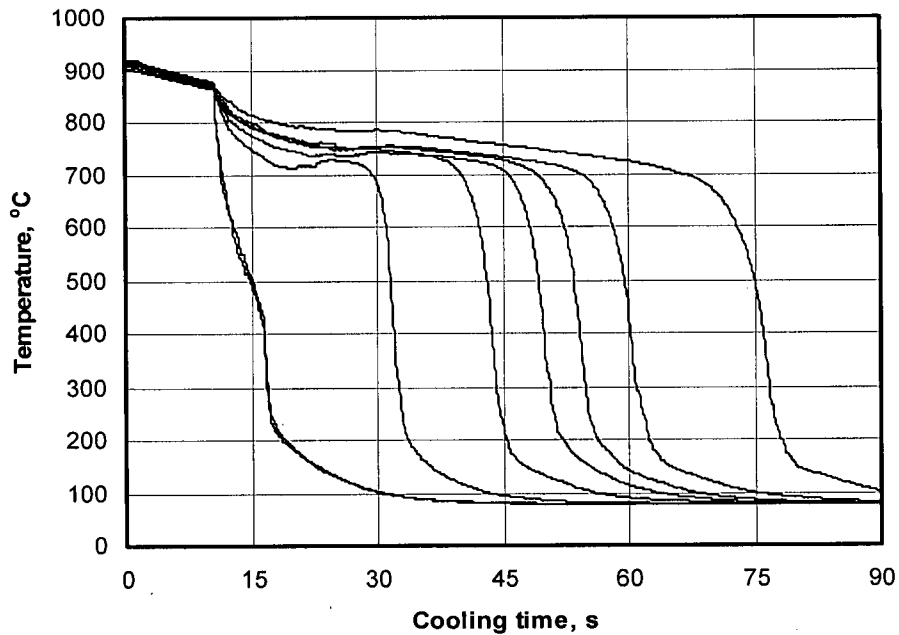


Figure 4.2 Example of measured temperatures  
 From left to right: T<sub>1</sub> to T<sub>8</sub>  
 DQSK; Q<sub>w</sub> = 30 l/min; T<sub>w</sub> = 70 °C; D<sub>n</sub> = 19 mm

If the color of the steel is black, its temperature should be lower than 500 °C. As discussed in Section 4.1.1, the temperature at one point drops dramatically as the black zone front reaches the point and the plate portion turns black. The temperature profiles at locations TC3–TC8 have nearly the same trend: a sharp drop from 700 °C to 200 °C. Therefore, it may be assumed that the time interval between two adjacent temperature curves at 500 °C is the same as that for the cooling water to move across 15.9 mm. Figure 4.2 shows that the time intervals are approximately 17, 12, 6, 4, 5 and 15 seconds for locations TC3 through TC8, respectively. This indicates that the black zone front movement is not uniform, and the average speed is changing from 1 mm/s to 6 mm/s. All of the experimental data show the same range for the progressing speed of the black zone front. In other words, the progressing speed of the black zone front is of 10 mm/s and is much less than the jet velocity.

#### **4.2 Drawback of FZM**

Besides its simplicity and easy implementation, the FZM is proven in Section 3.3 to be reliable and capable of recovering the applied heat flux with a higher accuracy. Because of its averaging feature this approach may also represent a good practice, and the obtained heat flux would be a good approximation wherever the heat flux is nearly constant or does not change dramatically in each subregion, such as the case in pool cooling process or where the cooling surface is covered simultaneously by the water, for example, the impingement zone under the jet water cooling. However, this approach may not be an appropriate one for the cooled surface outside of the impingement zone because it does not consider the water movement.

The following verification analyses clearly depict this drawback of FZM. The procedure described in Section 3.3.1 is also used here. The model is schematically illustrated in Figure 4.3.

The FE model is set for a 16 mm (width) × 7 mm (height) workpiece with 20 elements in both the width and height directions. The sampling point is in the middle of the plate width-wise and 1.05 mm beneath the surface. So, there are 10 elements on each side of

the sampling point. The material has a density of  $7800 \text{ kg/m}^3$ , a conductivity of  $32 \text{ W/m}\cdot\text{C}$  and a specific heat of  $470 \text{ J/kg}\cdot\text{C}$  for the whole time period.

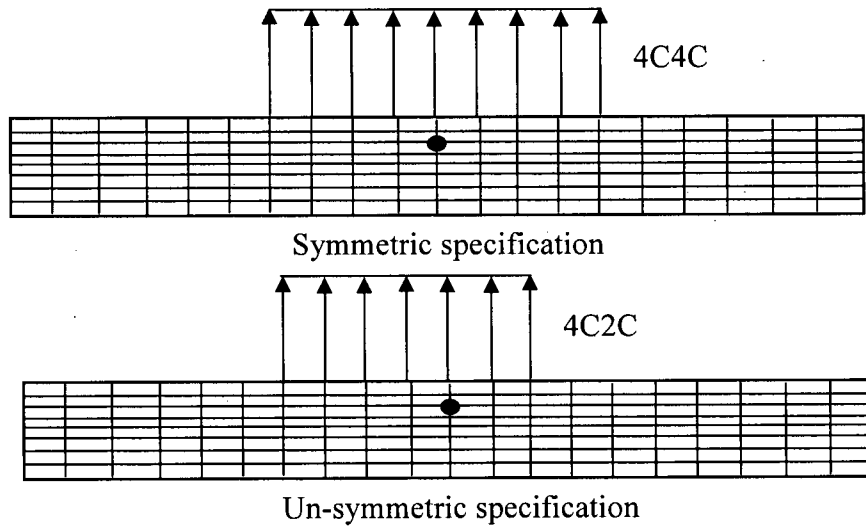


Figure 4.3 FZM FE model for verifications

In the direct analysis heat transfer calculation, the full width of the top surface is assigned a uniform heat flux of  $2.5 \text{ MW/m}^2$ . The calculation time period is 2 seconds. These conditions create a thermal history of the cooling temperature with a starting temperature of  $900 \text{ }^\circ\text{C}$  and an ending temperature of  $733.6 \text{ }^\circ\text{C}$ . The temperature history, without the imposing of random errors, is used as the virtual measured internal temperature for the inverse analysis.

In the first round of inverse calculations, the heat flux is always assigned symmetrically with the sampling point, and the element number on each side changes from 1 to 10.

For the identical input, the required heat fluxes in the inverse calculations are different for the different heat flux assignments, as shown in Figure 4.4. In this graph, the x-axis indicates the number of elements on each side, while the y-axis indicates the required heat flux. It is clear that the heat flux is as high as  $9.8 \text{ MW/m}^2$  as the heat transfer is localized within one element size at each side (totally  $1.6 \text{ mm}$ ). When the cooling surface is doubled the required heat flux dramatically decreases to  $5.3 \text{ MW/m}^2$ . This declining trend becomes mild when continuing to increase the cooling surface from 2 elements at each side. As 5 elements on each side are specified with the heat flux, the required heat

flux is  $3.1 \text{ MW/m}^2$ . The required heat flux decreases slightly from  $3.1$  to  $2.5 \text{ MW/m}^2$  as the cooling area is doubled from 5 elements to 10 elements on each side.

The actual cooling process may be quite a local behaviour. However, the natural choice is to apply the heat flux on the whole subregion if the FZM is used. Thus, quite a large error may exist.

The above results also imply that the cooling capacity 8 mm away from the target location has less effect on the temperature at the target location. It may be inferred that the actual 2D problem may be incorrectly handled by the FZM as several individual 1D problems when the distance between two TCs is larger than 8 mm. In other words, the distance between two TCs should be less than 8 mm if FZM is to be used correctly.

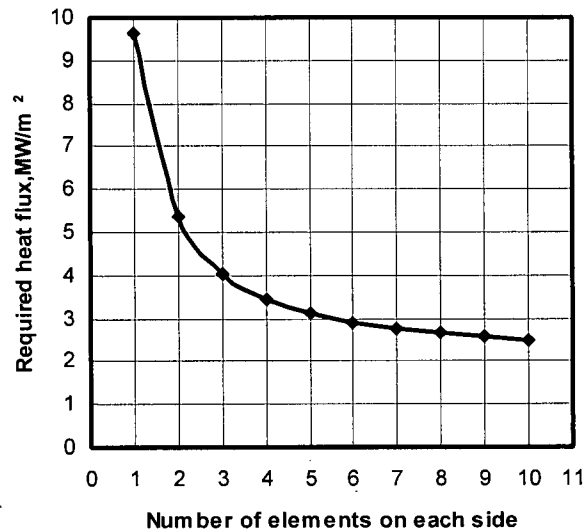


Figure 4.4 Heat flux required for the same cooling curve

Another round of analyses has been performed. In these analyses the total number of elements is fixed at 6 on which the heat flux is specified. However, the heat flux distribution is unsymmetric with respect to the sampling point. The scheme and the results are shown in Figure 4.5. It can be seen that the symmetrically cooling case has the highest cooling capacity, and that the more the cooling area is eccentric from the target location, the more the heat flux is needed. The value of heat flux in the 1C5C case is  $4.7 \text{ MW/m}^2$  and is 16% higher than that in the 3C3C case ( $4.05 \text{ MW/m}^2$ ) and is 88% higher than that in the 5C5C case ( $2.5 \text{ MW/m}^2$ , Figure 4.4).

It should be noted that the cooling pattern in the water jet cooling is fairly close to the 1C5C or the 2C5C during the period of sharp temperature drop. Assuming the progressing speed of black zone front is 3.2 mm/s and 10 elements are used to discretize the 16 mm length, only two-element lengths beyond the target location are covered by water within 1 s that is needed for water to cover the two-element lengths. During this time of 1 s the temperature at the target location would see a sharp drop. This cooling situation may be very close to the 5C2C. When the FZM is used, i.e., the 5C5C scheme, there may be a large error in the estimation of heat flux from the same profile of measured temperature.

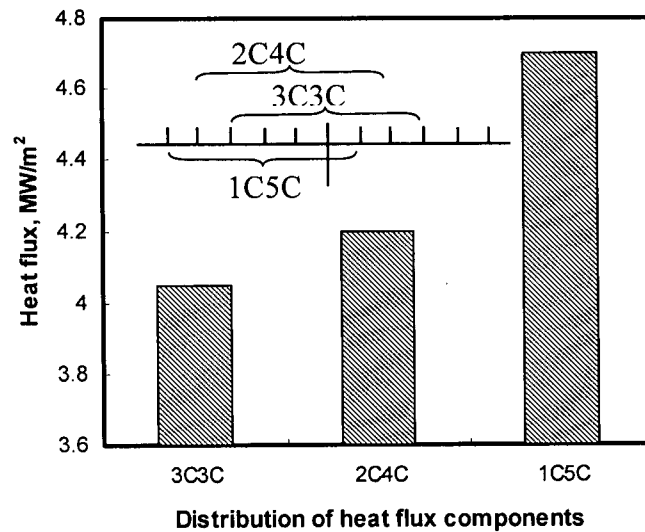


Figure 4.5 Effect of distribution of heat flux components on the required heat flux

As discussed above, the FZM does not correctly consider the cooling stage when the cooling water is progressively covering the surface and a sharp temperature drop takes place at short time interval.

### 4.3 FMM and Its Features

The above discussion suggests that it is crucial to find an appropriate approach that accounts for the water movement. The flux marching method (FMM) is developed based on this requirement. The key points of FMM are highlighted as follows:

1. As in the FZM approach, the target surface is divided into several subregions and each subregion corresponds to one temperature measurement, as schematically shown in Figure 4.6.

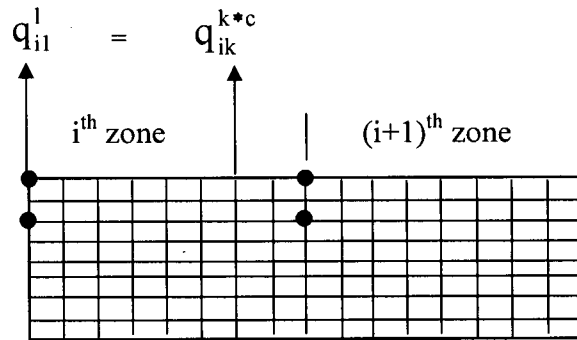


Figure 4.6 FMM FE Model for inverse calculation

2. There would generally be many nodes in each subregion, and the measurement point corresponds to the first node in each subregion. The number of nodes in each individual subregion generally may not be equal and may not relate to the progressing speed of black zone front.
3. The heat flux at the first node is inversely calculated from the internal measured temperature. Because the number of subregions is equal to the number of measurements and only one heat flux in each subregion is considered as unknown, the number of unknowns is equal to the number of measurements and the inverse problem is solvable.
4. For each subregion, the following schemes may be applied:

- a) The heat flux on a given node at the current time step is generally assumed to be equal to the heat flux value on the neighbouring upstream node at the previous time step. This is why the approach is named as flux marching method.

The essence of FMM is like the wave propagation. The procedure is based on the fact that the surface temperature in each subregion does not change much before the instant at which water covers the surface; and on the assumption that the small change of temperature field in each subregion would not affect the

heat transfer along the subregion surface; i.e., the heat transfer at the downstream point that would be cooled at a subsequent time step would be the same as that of an upstream neighbouring point at a prior time step. The heat flux at the first node may be looked at as the impetus of a wave, and the flood of heat flux would sweep the points in each individual subregion.

The progressing speed of black zone front may be different for each subregion, as is the case shown in Figure 4.2. Therefore, to apply the approach discussed above there should be different node numbers for each subregion because the time step is fixed for the whole time domain.

- b) The heat flux on the other nodes at the current time step may be generally assumed to be the value on the prior node at the several previous time steps.

It is convenient and time saving to use the same mesh for different cases. And from a practical point of view, it is sometimes necessary to solve the same problem by using different time steps. These arguments postulate the necessity to modify the approach stated in point 4-a to point 4-b as:

$$q_{ik}^{k*c} = q_{i1}^1 \quad (4.1)$$

where the first subscript  $i$  means  $i^{\text{th}}$  subregion and the second subscript refers to the node sequence number in the subregion. For example,  $q_{ik}$  is the heat flux on the  $k^{\text{th}}$  node in the  $i^{\text{th}}$  subregion; the superscript means the time step. In this equation,  $c$  is an integer.

- c) The heat fluxes on a group of nodes at the current time step is equal to those at the prior group at several time steps.

This situation is needed when a subregion must be discretized with a number of elements that is larger than the number of time steps with which the water moves from the first node to the last node in this subregion. Equation (4.1) can be applied with  $c$  as a fraction.

- d) General interpolation of heat flux

The procedures stated in points 4.a to 4.c require that the discretization of the subregions be uniform along the water moving direction. Although the uniform discretization is not difficult to realize, it may be necessary to consider a

condition with a general mesh. Thus, a linear interpolation procedure merits attention and is discussed in the following:

- i) Use the following equation to determine the time  $ts_{ij}$  that is needed for water to move from the first node to the  $j^{\text{th}}$  node in the  $i^{\text{th}}$  subregion

$$ts_{ij} = \frac{d_{ij}}{v_i} \quad (4.2)$$

where  $d_{ij}$  is the distance between the first node and the  $j^{\text{th}}$  node in the  $i^{\text{th}}$  subregion and  $v_i$  is the progressing speed of black zone front in the  $i^{\text{th}}$  subregion.

- ii) To find the time difference use

$$t_{ij} = t^k - ts_{ij} \quad (4.3)$$

where  $t^k$  is the total calculation time to the current  $k^{\text{th}}$  time step and  $t_{ij}$  is the time difference to be used for interpolation.

- iii) Use the following equations to find the heat flux at the  $j^{\text{th}}$  node in the  $i^{\text{th}}$  subregion at the current  $k^{\text{th}}$  time step:

$$\begin{aligned} q_j^k &= q_1^l \quad \text{when } t_{ij} \leq 0 \\ q_j^k &= q_1^m + \frac{t_{ij} - t^m}{\Delta t^m} * q^{m+1} \quad \text{when } t^m \leq t_{ij} \leq t^{m+1} \end{aligned} \quad (4.4)$$

where  $m < k$

This interpolation approach embodies the previous approaches and may be used for all cases.

Two problems may appear when applying the FMM to the experimental cases: the step-mismatch (overstepping or under-stepping) of heat flux and the jump of heat flux (discussed in Section 4.4).

The overstepping of heat flux is illustrated in Figure 4.7. In the figure,  $q_{iL}$  is the heat flux on the last node of the  $i^{\text{th}}$  subregion and  $q_{i+1F}$  is the heat flux on the first node of the  $(i+1)^{\text{th}}$  subregion. This figure shows that the heat flux on the last node of the  $i^{\text{th}}$  subregion changes later than that on the first node of the  $(i+1)^{\text{th}}$  subregion. This implies that the last

node of the  $i^{\text{th}}$  subregion is cooled down by water later than the first node of the  $(i+1)^{\text{th}}$  subregion. This situation should not happen in practice if the water jumping is not considered. In fact, this situation is due to the inaccurate underestimation of the progressing speed of black zone front at the  $i^{\text{th}}$  subregion. A slight increase of the  $i^{\text{th}}$  the flux marching speed should correct this disoperation. Similarly, the under-stepping means that the heat flux on the first node of the  $(i+1)^{\text{th}}$  subregion may greatly lag behind that on the last node of the  $i^{\text{th}}$  subregion, and a small reduction of the  $i^{\text{th}}$  flux marching speed should be performed.

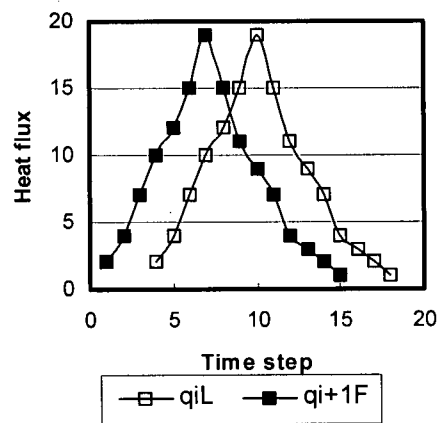


Figure 4.7 Overstepping of heat flux

#### 4.4 Numerical Tests

In the following sections, the study focus is put on the relative effectiveness and capacity of the FZM and FMM in recovering input of heat fluxes that are designed to simulate real-life situations of the water jet cooling process, from the input of virtual temperature measurements for the zones outside of the impingement zone.

##### 4.4.1 Test procedure and setup

The test procedure is the same as that described in Section 3.3.1. In the inverse estimation stage, however, only the data at the current time step is used and no future time steps are assigned; the regularization parameter and the convergence criteria are also fixed at the same value for all cases; except for a special specification, no random error is imposed on

to the calculated temperature, and therefore the virtual measured temperature is without measurement error.

Figure 4.8 shows the crucial part of typical heat fluxes in water impingement cooling that is used as input for the direct heat transfer analyses. The nodes in the impingement zone experiences the given heat flux change simultaneously, while the nodes outside the impingement zone will experience this setup of heat fluxes with a time shift, which simulates the water movement.

Ten cases are studied. The FZM results of the first 7 cases are shown in Table 4.1. In these cases, 4 peak values  $q_p$  and 4 moving speeds  $v$  are adopted. Case 2 will be discussed in detail and the other three cases are presented in Section 4.4.

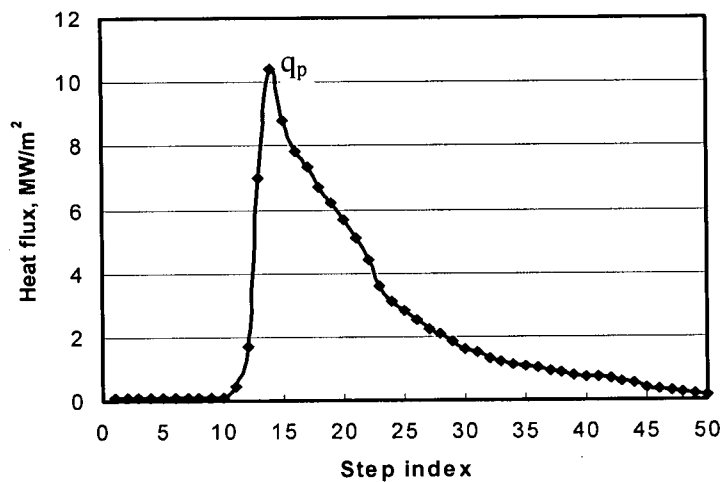


Figure 4.8 Crucial part of typical heat fluxes

Table 4.1 Test scheme and results using the FZM

	$q_p$ , MW/m <sup>2</sup>	Step shift	V, mm/s	Inversely calculated $q_p$ , MW/m <sup>2</sup>					
				TC1		TC2		TC3	
				Value	Ratio	Value	Ratio	Value	Ratio
Case 1	10.4	8	1.25	10.4	1	6.86	0.660	4.68	0.450
Case 2	10.4	5	2	10.4	1	6.88	0.662	5.58	0.537
Case 3	10.4	2	5	10.4	1	7.24	0.696	7.28	0.700
Case 4	10.4	1	10	10.4	1	8.55	0.822	8.82	0.848
Case 5	7.8	5	2	7.8	1	5.16	0.662	4.25	0.545
Case 6	5.2	5	2	5.2	1	3.44	0.662	2.78	0.535
Case 7	2.6	5	2	2.6	1	1.72	0.662	1.38	0.531

#### 4.4.2 FE model

The FE model used for both direct and inverse analyses in these numerical tests is a 2D axisymmetrical one. The domain size is 7 mm in thickness and 80 mm in radial direction. There are 80 elements in the radial direction and 9 elements in the thickness direction. The elements are uniform in the radial direction to ensure an unbiased simulation of the progressing black zone front, while they are variable in the thickness direction with a relatively denser mesh close to the top surface. The 2D mesh is shown in Figure 4.9, noting that the scale is not the same in the  $x$ - and  $y$ -directions.

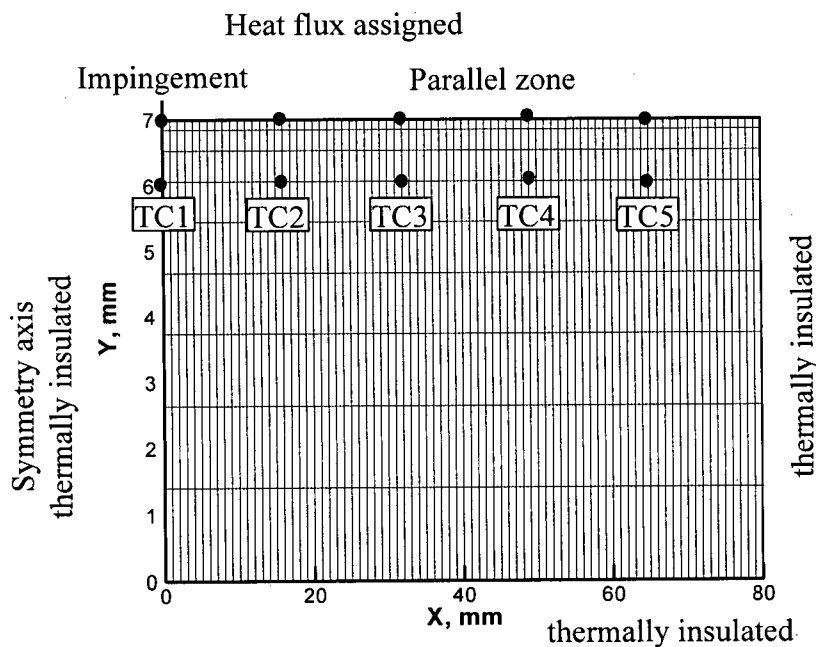


Figure 4.9 FE-model for numerical test

As illustrated in Figure 4.9, the domain is evenly divided into 5 subregions, and each subregion has 16 elements. The first subregion is assumed to be the impingement zone and the others are the parallel zone. Five sampling locations are set up, and the first one is at the stagnation point and the other four sampling locations lie at the intersection between the subregions. At each location, the temperatures at the two points, one on the top surface and one 1 mm beneath the surface point, are sampled in the direct calculation. The temperatures at the internal points are used in the inverse analysis to inversely estimate the heat flux and the temperature of the points on the top surface.

There are 81 nodes in total on the top surface, and they are listed here as 1 to 81 and may be in different calculation zones as stated in Table 4.2.

The sampling nodes are in the middle of each subregion for the FZM (this is an axisymmetrical problem, and node 1 is naturally the middle of the first zone) while they are the first node for the FMM.

The material is assumed to have a density of  $7800 \text{ kg/m}^3$ , a specific heat of  $480 \text{ J/kg}^\circ\text{C}$  and a thermal conductivity of  $20 \text{ W/m}^\circ\text{C}$ .

Table 4.2 Node in calculation zone

	Zone 1	Zone 2	Zone 3	Zone 4	Zone 5
Sampling	Node 1	Node 17	Node 33	Node 49	Node 65
Direct	Node 1 ~16	Node 17 ~32	Node 33~48	Node 49 ~64	Node 65 ~81
FZM	Node 1 ~8	Node 9 ~24	Node 25~40	Node 41 ~56	Node 57 ~81
FMM	Node 1 ~16	Node 17 ~32	Node 33~48	Node 49 ~64	Node 65 ~81

#### 4.4.3 Realization of water movement

The main objective of the current work is to investigate the capacity and accuracy of both FZM and FMM and their suitability for the water movement. The assumed boundary conditions as shown in Figure 4.9 are such that all the sides except the top surface are thermally insulated. This may not be practically accurate, but it should not influence the coming conclusions.

The applied heat flux boundary conditions are calculated and applied on the nodes on the plate's top surface basing on a time-space shift scheme. The scheme insures a space-time marching approach that simulates actual cooling conditions and is briefly explained in the following.

At the first stage (here 30 steps, 3s), the air-cooling is assumed for the top surface, and a uniform heat flux ( $q_1$ ) is applied. At the second stage the water cooling starts and a heat flux value ( $q_2$ ) is read in according to the curve input (see Figure 4.8) and is applied to all the nodes in the impingement zone as well as the first node at the second subregion (later these nodes are called impingement nodes). All other nodes would still be subjected to air-cooling, i.e., the heat flux value of ( $q_1$ ). At the next time step, another heat flux value ( $q_3$ ) is read in and is applied to the impingement nodes. The heat flux history on the

impingement nodes is shifted to the other nodes in the parallel zone according to the assigned speed and element length. This space-time marching approach implies that the cooling condition for all points is almost identical except for a time shift and a small temperature drop due to the longer air-cooling period. At any time instant, there is a space distribution of heat fluxes, and one example will be shown in Figure 4.15.

#### 4.5 Results and Discussion

For the condition stated in case 2, the time history profiles of input heat fluxes at the locations TC2 (TC1 is the same as TC2) through TC5 are presented by the dotted lines in Figure 4.10. For simplicity, the same setting of heat flux is applied to all nodes with a time shift.

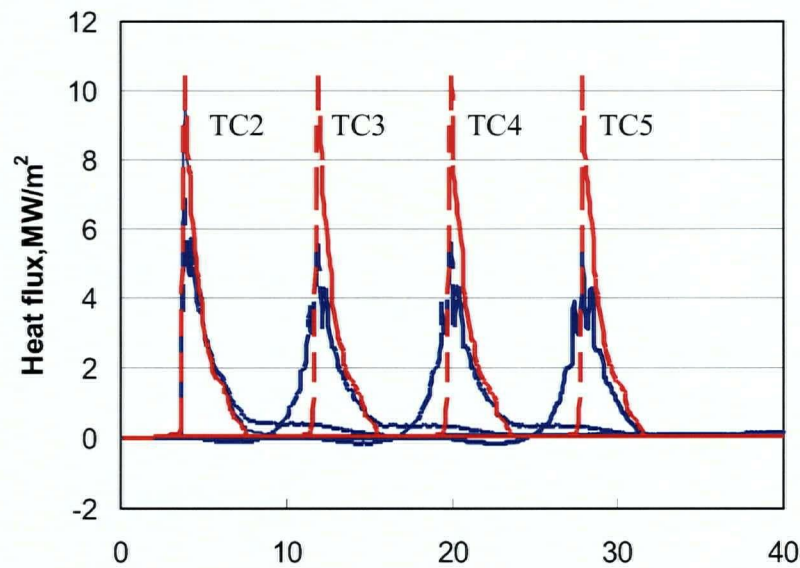


Figure 4.10 Comparison of heat fluxes

Red lines: input; blue lines: calculated using FZM

The calculated internal temperatures from the direct simulation are shown in Figure 4.11. The changes of the internal temperatures are fairly similar to those from the experimental measurements in the stationary plates (see Figure 4.2) except for the large temperature recovery, which happened in moving plate cases (see Figure 6.5). It may be stated that the temperature profiles assemble the features for both stationary and moving plates.

The surface temperature profiles are almost identical to the internal ones except the difference in values, and are not presented here.

The inversely calculated heat fluxes using the FZM are also shown in Figure 4.10 with the solid lines. It is clear that the calculated ones at locations TC3 through TC5 are nearly identical, reflecting the fact that the input ones at these locations are the same. Therefore, the following discussion is limited to locations TC1 to TC3.

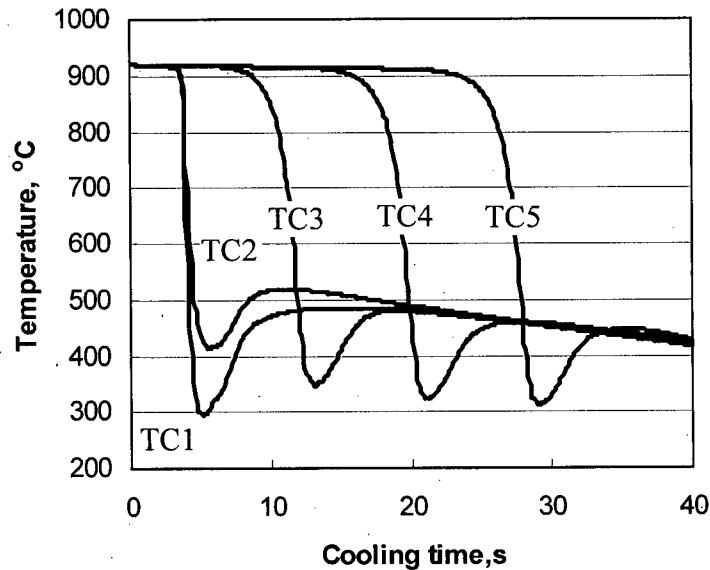


Figure 4.11 Internal temperature directly calculated in case 2

#### 4.5.1 Reduction of peak value using FZM

There are two kinds of discrepancies between the input and the inversely calculated values of heat flux profiles using the FZM. First, the peak values may be underestimated. For example, at location TC1, the calculated one is recovered exactly to the input because the assigned heat fluxes on the nodes in this subregion are the same, and the average value is equal to the value on each node. However, at locations TC2 and TC3, the peak value decreases depending on the location and the progressing speed of black zone front. As shown in Table 4.1 and Figure 4.12, the ratio of the calculated value to the input one is around 0.78 and 0.48 at locations TC2 and TC3, respectively.

This ratio is not affected by the magnitude of input values and is fixed at 0.662 for location TC2 and 0.53 for TC3 when the peak value decreases from  $10.4 \text{ MW/m}^2$  to  $2.6 \text{ MW/m}^2$ . This result shows that the FZM has a limited capacity to capture the peak value.

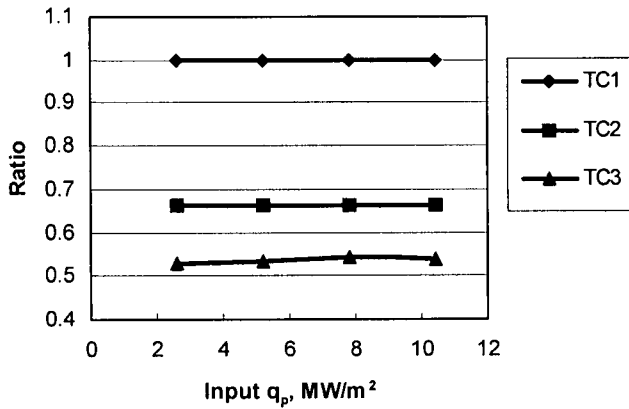


Figure 4.12 Input  $q_p$  vs. ratio

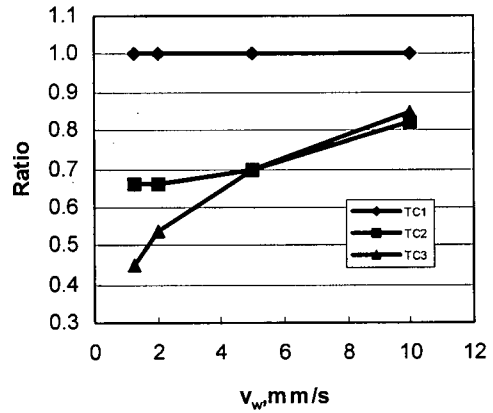


Figure 4.13  $V_w$  vs. ratio

However, as shown in Figure 4.13, the accuracy of the prediction greatly increases when the progressing speed of black zone front  $V_w$  increases. For location TC2, the ratio slightly increases from 0.662 to 0.696 when the speed increases from 2 mm/s to 5 mm/s while the ratio is 0.822 as the speed is 10 mm/s. The increasing intensity is around 24.5%. For location TC3, this ratio increases from 0.45 with a speed of 1.25 mm/s to 0.68 with a speed of 5 mm/s and then to 0.83 with a speed of 10 mm/s, and the increasing intensity is as high as 88.4%.

It can be concluded that the accuracy of peak heat flux predictions using the FZM increases with the increase in the progressing speed of black zone front  $V_w$ . The rationale behind this observation may be attributed to the evidence that a higher portion of the area in each subregion is covered by water when the front moves faster, and that the cooling condition would be similar between such areas. The reason why the increasing intensity at location TC3 is higher than that at location TC2 may be because of the cooling condition at the two sides of TC3 that would be affected by the water speed while only one side of TC2 possesses a similar condition.

#### 4.5.2 Shape change of heat flux using FZM

The second kind of discrepancy between the input and inversely calculated values of heat flux profiles using the FZM is the change in shape of the heat flux profile and is illustrated in Figure 4.14. The figure shows that the heat flux at location TC3 starts to increase at time 9 s while the actual input increases at 12 s. This means that the calculated heat flux increases much earlier than the input one.

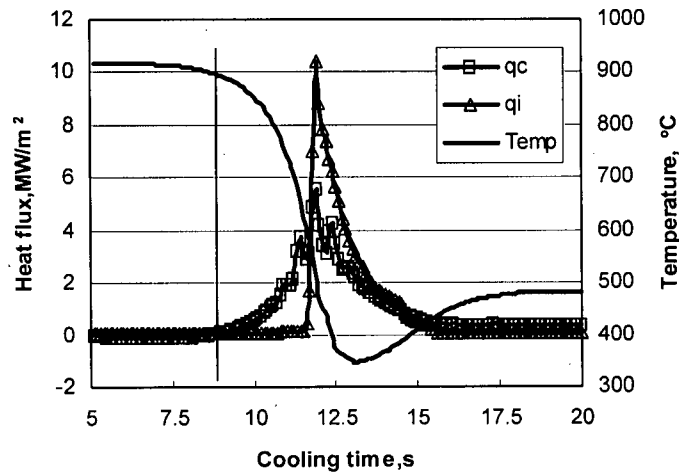


Figure 4.14 Shape change of heat flux using FZM

Despite the inaccuracy of this prediction, it may be considered reasonable if compared to the internal temperature profile and the averaging character of the FZM. At time 9 s the black zone front is 6 mm away from TC3 and will also affect the temperature at TC3, and the internal temperature at TC3 starts a fast and sharp drop, as shown in Figure 4.13. The temperature decrease at TC3 before time 12 s is due to the radial temperature gradient and heat flow in the radial direction. This radial heat transfer is greatly underestimated and is shifted to the effect of vertical cooling when using the FZM. This may be one of the reasons why the estimated heat flux using the FZM increases at an earlier stage. On the other side, there are two elements (2 mm long) in this region being cooled down at time 9 s, so that the FZM should capture this response.

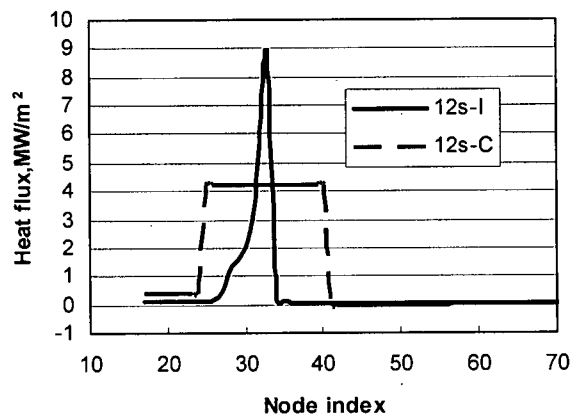


Figure 4.15 Heat flux space distribution at time 12s

The averaging feature of FZM may be further verified by the space distribution of the heat flux, as shown in Figure 4.15, which shows the expected values (in solid line) and the FZM calculated ones (in dashed line). When the input heat flux changes from node to node at each time instant, the calculated heat flux values using the FZM for these nodes are constant and do not reflect the actual conditions.

#### 4.5.3 Mis-prediction of surface temperature using FZM

Because the FZM has an averaging character and may not be able to capture the actual heat flux, the surface temperature predictions will also be inaccurate. Figure 4.16 shows the surface temperature differences when the calculated internal temperatures are considered to be the virtual measured ones with an accuracy of  $\pm 1$  °C. It can be seen that the surface temperature difference may reach 150 °C. Therefore, the FZM may produce an unrealistic relationship between surface temperature and heat flux, as shown in Figure 4.17.

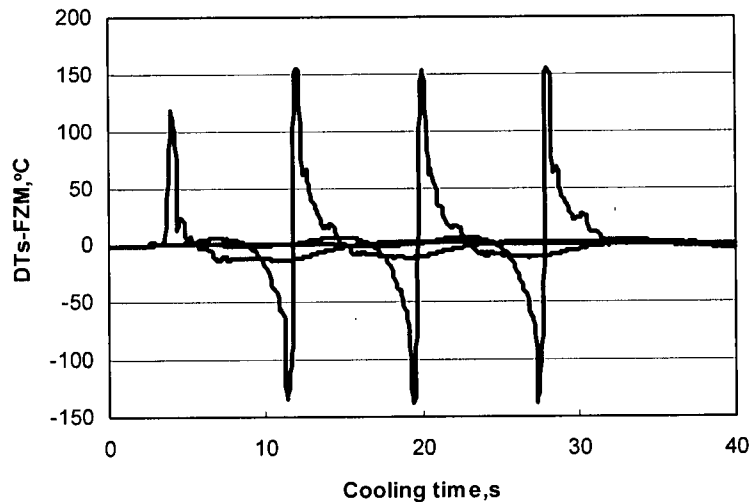


Figure 4.16 Surface temperature differences using FZM

#### 4.5.4 Effect of speed mismatch using FMM

It is to be first noted that if the flux marching speed matches the progressing speed of black zone front, the input heat flux may be exactly recovered for both the peak value and the shape. All calculations relating to the input flux, including the surface temperature

predictions, would be produced with very good accuracy using the FMM. For the cases considered, the FMM surface temperatures only differ by about 10 °C with the same convergent criterion of  $\pm 1$  °C. This prediction accuracy is quite acceptable and will not affect the relationship between the surface temperature and heat flux.

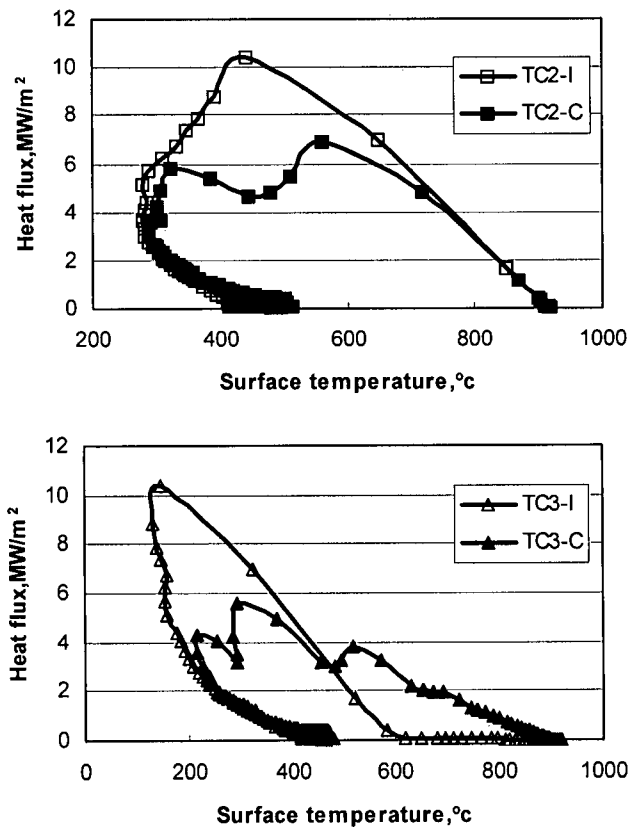


Figure 4.17 Comparison of Ts vs. heat flux

A crucial point in using the FMM is to determine and to closely match the progressing speed of black zone front. A mismatch may cause problems in recovering the required heat fluxes. The influences of speed mismatch are numerically investigated.

Figure 4.18 shows the calculated heat fluxes at TC2 through TC5 with an increase of 5% of the flux marching speed for the second zone only. This figure indicates that the heat flux at TC2 has little change, while all the heat fluxes at TC3 through TC5 are severely affected. At TC3, the heat flux first takes a negative value, indicating a heating process before it starts to increase. Because the temperature at TC3 is reduced by water earlier

than it should be, an amount of heat should be input to maintain the temperature, and therefore a negative heat flux occurs. This heating process would create the wrong temperature field around the sampling point, and the peak value of the heat flux would be mis-predicted.

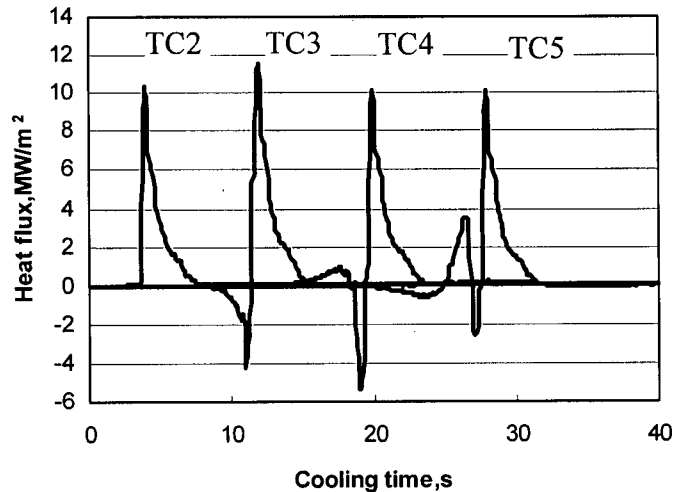


Figure 4.18 Effect of higher speed mismatch using FMM

It is expected that the temperature would be affected by the precedent heat fluxes. When the inaccurate value of the predicted heat flux at TC3 marches to TC4 it will deform the temperature field around TC4. Thus the heat flux at TC4 will be different from the input. In this location the heat flux shows a small positive increase to balance the effect from the negative one due to the marching scheme of the heat flux. The same phenomenon repeats to some extent at locations TC4 and TC5.

If a mismatch of 5% is applied to all locations TC3 to TC5, the distortions of the predicted heat fluxes would be intensified. Figure 4.19 shows one example of the impact of this artificial mismatch on the calculated heat fluxes.

The influencing intensities of the mismatch level on the calculated heat flux accuracy are depicted in Figure 4.20 to Figure 4.21 and Table 4.3. For all cases the peak value of input heat flux is  $10.4 \text{ MW/m}^2$  in the direct calculation, and the flux marching speed at the second subregion is artificially shifted with a deviation. The results at location TC3 are presented.

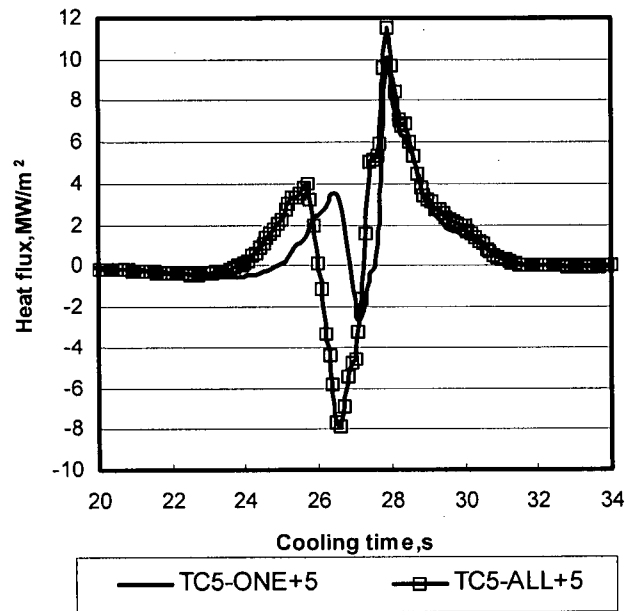


Figure 4.19 Intensification of higher speed mismatch

Figure 4.20 shows the results with a higher speed mismatch. With the increasing of speed mismatch from +5% to +20% the unreal negative heat flux increases from  $-4.2 \text{ MW/m}^2$  to  $-8.6 \text{ MW/m}^2$ , the absolute value of the latter being close to the input peak value. Because of the negative portion the positive heat flux becomes 23% higher than the input value. It is important to note that the positive portions of the heat fluxes are quite close to the input heat flux if the negative portions are neglected.

The deformations of heat flux at TC3 are obtained if the flux marching speed is less than the progressing speed of black zone front. Figure 4.21 shows the deformations of heat flux at TC3 with various values of imposed mismatches at the second subregion. When the speed at the second subregion is slightly smaller than the input value, the marching heat flux from TC2 increases at a later time than the setting and benefits the cooling down of temperature at TC3. Thus less heat should be extracted away by the heat flux at TC3 itself. Therefore, the heat flux at TC3 deviates widely from the input one. As the slower speed mismatch increases, however, the deviation of the calculated heat flux to the input one decreases, and the negative heat flux appears after the positive one. When the progressing speed of black zone front is 20% less mismatched, the positive portion of the heat flux turns closer to the input one.

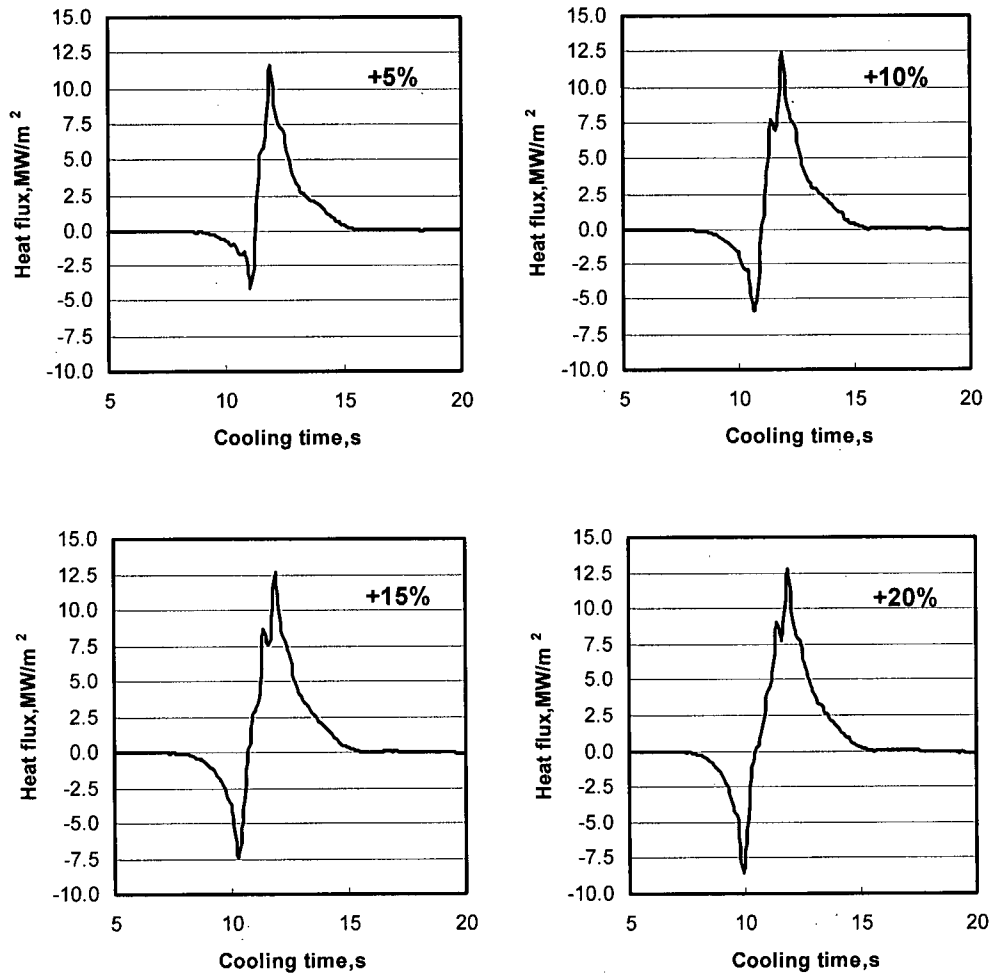


Figure 4.20 Calculated heat fluxes with higher speed mismatch

Table 4.3 Calculated heat flux accuracy at TC3 with speed mismatch in FMM

Speed	5%		10%		15%		20%	
Faster	11.6	111.5%	12.4	119.2%	12.7	122.1%	12.8	123.1%
Slower	5.59	53.8%	7.75	74.5%	8.69	83.6%	10.0	96.2%

The accuracy of the calculated heat flux for the above cases is presented in Table 4.3 and Figure 4.22. Data shows that the calculated heat flux peak value at TC3 is about 11% to 23% higher than the input one with a higher speed mismatch. Compared to a 46.3% deviation with the FZM (Table 4.1 and Figure 4.12), this accuracy is acceptable. Note

that the heat flux at TC2 with the FMM is only slightly affected by the speed mismatch while that with FZM is also greatly influenced.

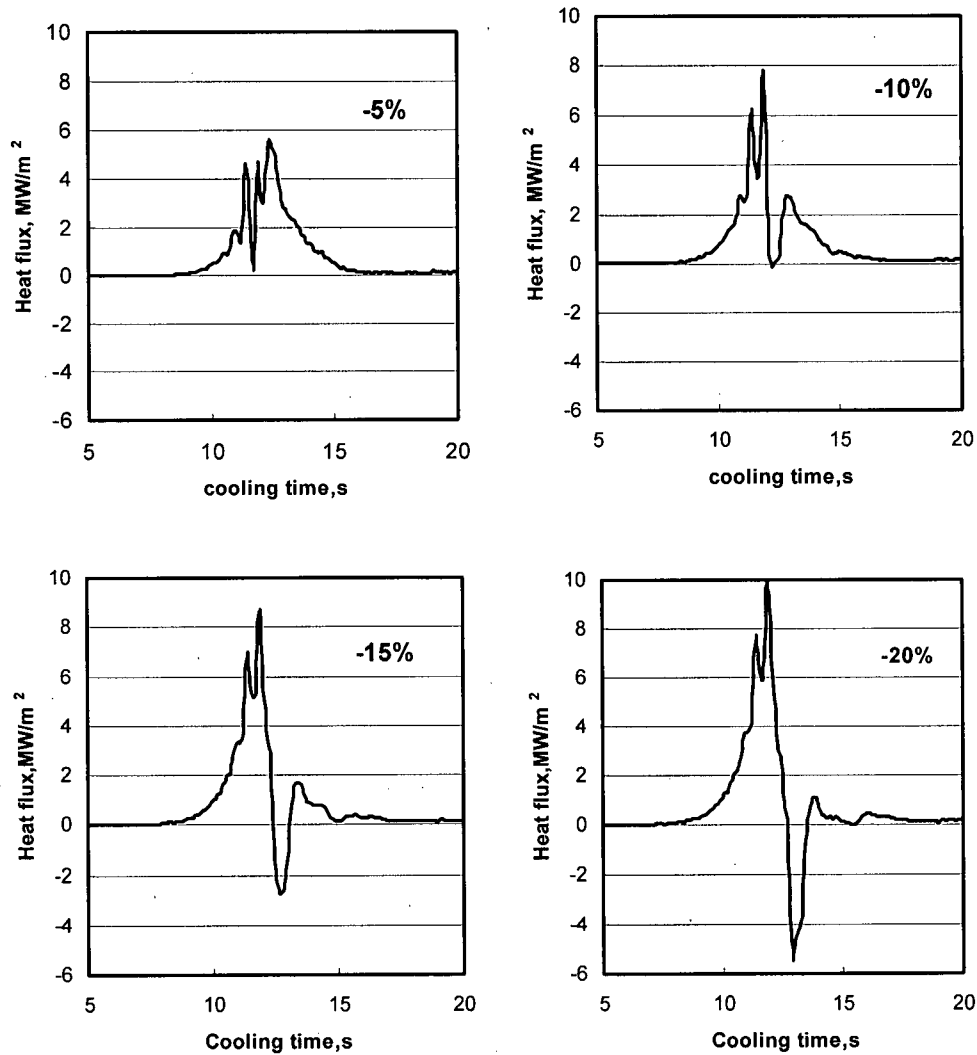


Figure 4.21 Calculated heat fluxes with lower speed mismatch

It is clear from these calculations and analyses that the deformed profiles of the heat flux at TC3 are different for an overestimation or an underestimation of speed. This result is extremely informative and is useful for figuring out whether the speed is overestimated or underestimated. The guideline for setting up the flux marching speed may be that the flux marching speed should be slightly higher rather than lower than the progressing speed of black zone front.

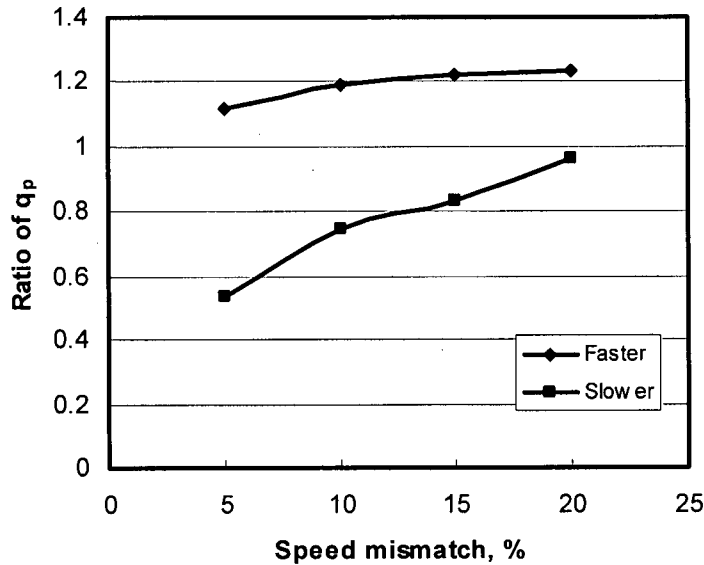


Figure 4.22 Calculated heat flux accuracy with speed mismatch

#### 4.5.5 Effect of flux jump using FMM

For this case, a new specification of heat flux on the top surface is performed in the direct simulation. The heat flux profile shown in Figure 4.8, called here HP1, is simultaneously assigned to all nodes in the impingement zone bound by the TC2, while a profile HP2, which is half of HP1, is assigned to the nodes from the third subregion with a time shift. While the time shift schedule is retained for the nodes in the second zone, the magnitude of heat flux  $q$  is

$$q = \frac{N_2 + 1 - i}{N_2} \text{HP1} + \frac{i - 1}{N_2} \text{HP2} \quad (4.5)$$

$$i = 1, 2, \dots, N_2$$

where  $N_2$  is the number of nodes in the second zone (here  $N_2=16$ ).

This approach will make a smooth transition from a higher value of heat flux at TC2 to a lower one at TC3. The resulting heat fluxes along the second zone are shown in Figure 4.23. In the inverse calculation, two methods are used to specify the heat flux on the nodes in the second zone. One is just to assign the inversely obtained heat flux at TC2 to all nodes, and the results are shown in Figure 4.24.

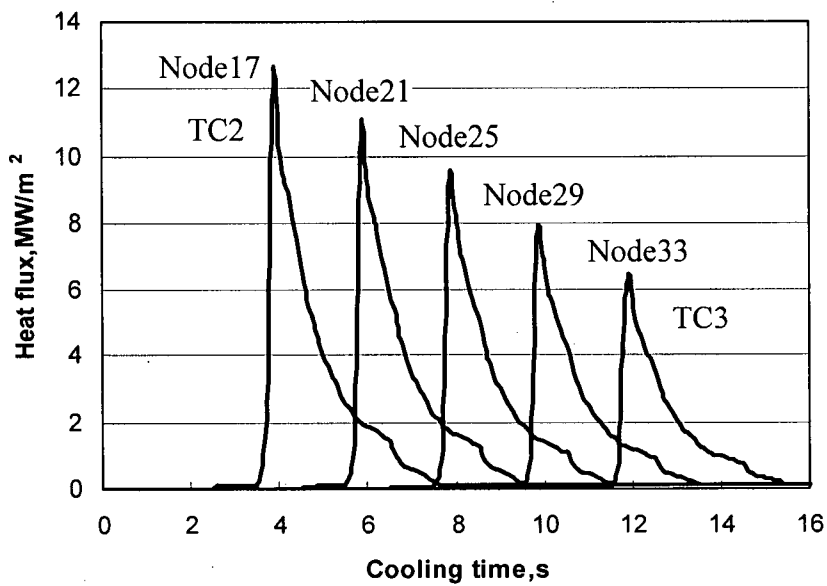


Figure 4.23 Assigned heat fluxes along the second zone

As expected, the heat flux at TC2 is exactly recovered to the input. Note that this value is also assigned to the node 32 in the inverse calculation, the left node to the node 33 where TC3 is located. In the inverse calculation the temperature at TC3 will be lower than it should be because the heat flux at node 32 almost doubles the one assigned in the direct calculation. Thus, a heating flow is required to maintain the input temperature at TC3 and then the negative flux appears. As discussed in the previous section, the wrong heat flux at TC3 disturbs the temperature fields at the downstream nodes, so the heat fluxes must be affected and then deviate from the input.

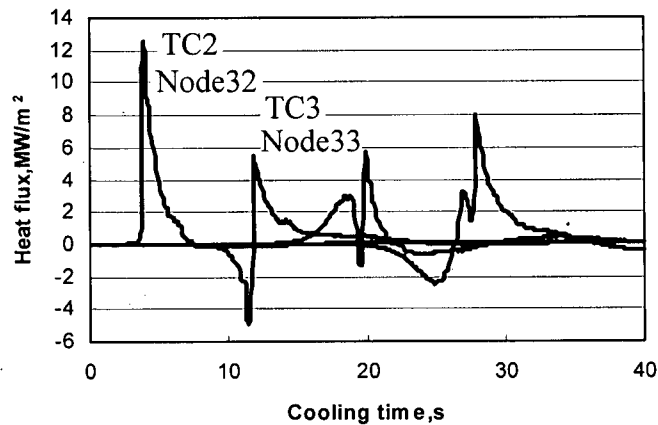


Figure 4.24 Effect of heat flux jump

The solution to this problem is the second method. This method needs some iterations and will be based on the results from the first method or from the FZM. The inversely calculated heat fluxes at TC2 and TC3 from the FZM are also called as HP1 and HP2, respectively. Then the heat fluxes along the second zone are determined according to equation (4.5). If the heat flux at TC3 changes in the second iteration, a third iteration is needed and so on. For this example, three iterations are needed to recover the distribution of heat flux along the second zone and other values at TC4 and TC5.

#### **4.6 Summary and Prospects**

For a stationary water jet the cooled area on the top surface is axisymmetrical about the stagnation point for a single circular jet. Only the material points in the impingement zone are simultaneously cooled; any material points outside of the impingement zone are sequentially cooled, and the further the point from the stagnation point, the later it is cooled. The progressing speed of black zone front is much lower than the jet velocity.

For moving plate cases, the cooling zones are only symmetric about the moving direction of the plate, and become a pearl or comet shape with long axis along the moving direction. The velocity of water can be neglected compared to the plate velocity. The moving speed of the cooling pattern is fairly close to the moving speed of the plate.

The FZM is simple and easy to use and can be used in cases where the target surface is simultaneously cooled by the same medium, such as the cooling in the impingement zone or pool cooling, and in the air cooling stage.

A main feature of the FMM in comparison to the FZM is the capture of the moving effect as propagating wave. In this method, the cooling surface is still divided into several subregions, and each subregion corresponds to one temperature measurement. The heat flux at the first node in each subregion is inversely calculated from the internal measured temperatures, and functions as the impetus of the wave; and the flood of the heat flux would sweep the points in each individual subregion. Thus, the FMM takes the water movement into account and may be more accurate in reflecting the actual cooling process

in jet cooling, and therefore may obtain a more accurate heat flux inversely calculated from the measured temperature.

Using the FMM needs more attention when assigning the flux marching speed and smoothing the jumping of the heat flux. Both overstepping and jumping of the heat flux may cause disturbance in the heat flux profile with a virtual negative heat flux before the real sharp increase of heat flux. Under -stepping (lower mismatch) may damp the real sharp increase of heat flux, and casue a virtual negative heat flux after the real sharp increase of the heat flux. A slight adjustment of flux marching speed may eliminate or greatly reduce the effect from the speed mismatch. A factor should be used when assigning the heat fluxes between two locations where the two inversely calculated heat fluxes are jumping. It is to note that smoothing the distribution, rather than the speed adjustment, should be performed first.

The results from the FZM may benefit the smoothing operation when applying the FMM. The FZM and FMM may be adopted in one calculation such that the FZM is used for the air-cooling stage and the FMM for the water-cooling period.

In this study, although it is implemented in an FE program the FMM is a general approach for assigning the heat fluxes along the cooling surfaces or subregions from the design variables, and can be used in other computational methods. Moreover, it may be possible to assume a heat flux profile with constants and to assign the heat fluxes from the FMM, and then to determine these constants by an inverse method.

#### **4.7 Flowchart for the IHCP Solution Procedure**

Figure 4.25 shows the flowchart for the IHCP solution procedure combining the developed FZM and FMM into one inverse calculation program. The computation window is composed of  $N$  time steps including the current time step and all future steps; and the computation window is shift only one time step after a convergent solution is obtained. The parameter NSTEP is the total time step, and NFLOW is used to guide the calculation method. The FZM is always used first, and the calculation switches to the FMM after the computation step reaches NFLOW. The FZM is adopted through the entire calculation as NFLOW is equal to NSTEP.

In this work, the sensitivity matrix is calculated only once at the beginning of the entire inverse calculation, as the solid line after the operation “next sequence” expresses. However, as the dotted line indicates, it can be newly obtained for each new step or every  $M$  step to take into account the temperature dependence of thermophysical properties. In this study, the latter approach is proved not to be necessary when an iterative technique is adopted in this study. A constant function specification is used when calculating the sensitivity matrix.

The initial guess  $\mathbf{q}^*$  of heat flux  $\mathbf{q}$  may be taken as zero or any other value. However, the heat flux  $\mathbf{q}^2$  obtained at the previous sequence may be used as the initial guess of the heat flux at the current sequence. Numerical results show that the choice of the initial guess of heat flux has little effect on the iteration number. Either the initial heat fluxes or the newly calculated ones should be assigned to the corresponding nodes according to the adopted method, FZM or FMM.

The iteration technique is used to get a more accurate solution. The first heat flux vector at the previous iteration is used for all steps within the computation window; i.e., a constant function specification is performed.

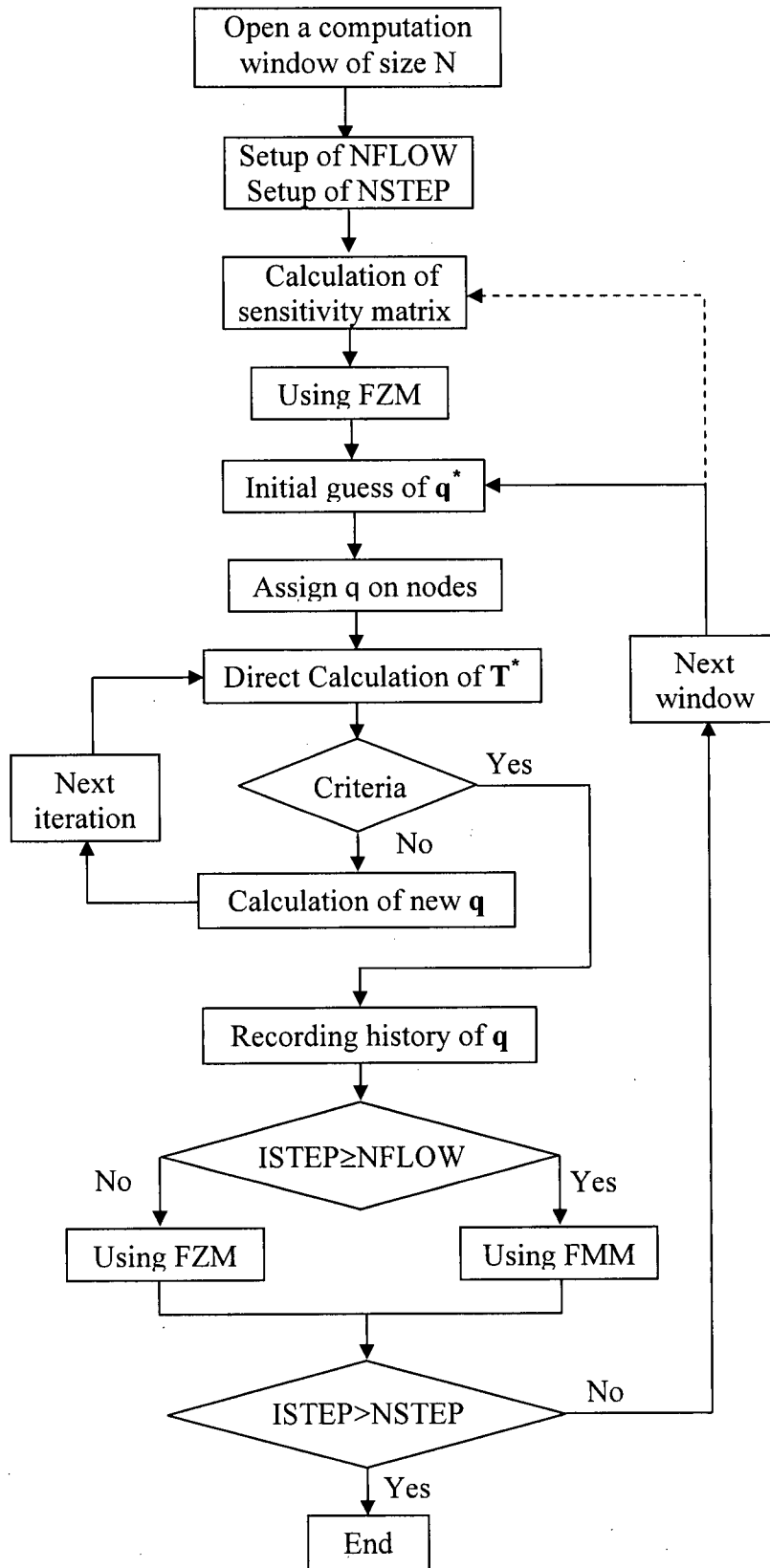


Figure 4.25 Flowchart for IHCP solution procedure

## Chapter 5

### APPROPRIATE INSTALLATIONS OF THERMOCOUPLES IN WATER JET COOLING

The reliability of TCs with a separation measuring junction in the temperature measurement of water jet cooling, and the appropriate TC installations for inverse calculation application cases have been extensively investigated using FE analyses [60–61].

#### 5.1 Error in the Measured Temperatures

While analyzing the experimental data of measured temperatures, significant discrepancies are evident in rapidly decreasing temperature profiles and in the correlation between the inversely calculated surface temperatures and the measured ones. One example is discussed, which gives details of such discrepancies.

Experimental data [27] reveals that the heat transfer behaviour at points on the plate within a  $1.2\text{--}1.7D_n$  around the stagnation point is identical, and may be considered as one dimensional, where  $D_n$  is the nozzle diameter. Therefore, a small cylinder centered at the stagnation point with the hole for TC is modelled for the inverse heat transfer calculation (see Section 6.1 for the detailed geometry model). The temperature dependence of thermophysical properties is considered.

A portion of typical temperature histories at the stagnation point is shown in Figure 5.1. This figure shows the measured internal temperature, the measured surface temperature, the inversely calculated surface temperature based on the internal temperature, and the temperature difference between the measured surface temperature and the calculated one. Both the measured surface temperatures and the internal ones have been filtered by a simple but effective running filtration approach to reduce the noise level. In this technique, the temperatures at a current time step plus 5 prior values and 5 subsequent values are added together, and the average value is taken as the temperature at the current time step. It should be noted that that the difference between the measured internal temperatures and the calculated ones is less than  $0.5\text{ }^\circ\text{C}$ .

It is apparent in Figure 5.1 that during air-cooling ( $t \leq 11$  sec) the measured surface temperature and the internal temperature decrease simultaneously, and their difference is negligible. This is acceptable since the two junctions are separated only by 1 mm, and the plate has a uniform initial temperature. After cooling water impinges onto the plate surface, the measured surface temperature drops very rapidly whereas the measured internal temperature decreases at a much slower rate. The difference between these two temperatures at this time point ( $t \cong 11$  sec) is up to 400 °C, which means that the average spatial temperature gradient is about  $4E5$  °C/m. This sharp drop in surface temperature is expected because of the high transient cooling condition.

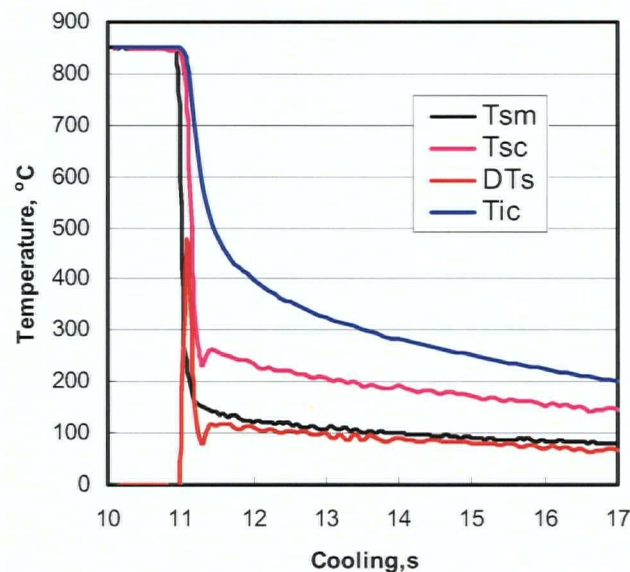


Figure 5.1 Typical temperature profiles during water-cooling  
 $D_n=19$  mm,  $Q_w=45$  l/min,  $T_w=50$  °C, SS316

Ideally, the inversely calculated surface temperatures and the measured ones should be approximately matched, even if the internal temperature is lagged and damped, as proved by the numerical tests in Section 3.4. This is not the case, however, as shown in the figure; and there is a significant discrepancy in the magnitude and somewhat in the decreasing profile of the surface temperature. The calculated surface temperature drops at a much slower rate than the measured one. The difference is as high as 465 °C at the sharp dropping period of temperature, and it decreases slowly thereafter with the decrease of absolute temperature. Even if this large temperature difference can be partially

attributed to the lagging due to the highly transient condition, the nearly constant surface temperature difference of around 100 °C still suggests that there may be a significant error in the measured surface temperature or internal one or both.

A direct heat transfer calculation using the same model has been performed in which the measured surface temperature has been used as the boundary condition. In this case, the calculated internal temperature is in good agreement with the measured one at the air-cooling stage, while the difference between them jumps to about 250 °C as soon as the water hits the plate; the calculated temperature becomes lower than the measured one. This significant difference is nearly kept unchanged during most of the water-cooling period. This trend is slightly different from the trend obtained in the inverse analysis.

From the above data, both the direct and inverse calculations reveal that there is a significant error either in surface temperature measurement (negative drift) or internal one (positive drift) or in both cases.

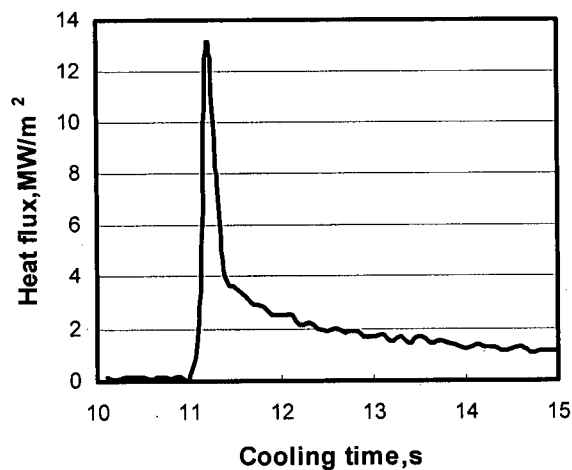


Figure 5.2 Inversely calculated heat flux

Figure 5.2 shows the changing mode of the inversely calculated heat flux with time. Corresponding to the temperature change, the heat flux increases sharply to about 13.1 MW/m<sup>2</sup> as soon as water impinges onto the surface, and then decreases to an average value of around 2.1 MW/m<sup>2</sup> that stays sort of constant during the time period of water-cooling. Compared to the calculated surface temperature, the heat flux fluctuates more widely because the latter is very sensitive to the errors in the measured temperatures. The heat flux value of 2.1 MW/m<sup>2</sup> is consistent with those reported in references [48, 63].

It may be concluded from the above discussion that the results obtained from inverse calculations are reliable, and that most probably the surface temperature measurement is not accurate.

## 5.2 Stationary Case [60]

### 5.2.1 Effect of TC wire conduction

Numerous numerical tests have been conducted where the length of wires and the value of HTC or heat flux have been changed. For space consideration, only the typical case is presented in the following sections. In fact, changing the length of wires and the value of HTC or heat flux does hardly change the results presented.

The example of FE models used for the investigation of the effect of wire conduction is shown in Figure 5.3. Axisymmetric conditions are assumed. A cylinder of 7 mm in height and 7mm in radius is meshed. The choice of the model size is based on the value of the plate thickness (7 mm) and on the fact that the thermal insulation condition may be used on the cylindrical outside surface, as mentioned above. The length of bare portion of TC wire is assumed to be 4 mm based on the installation configuration (Figure 2.6). In the model, the wire is vertical to the plate although it is inclined in the installation. Such a change will not affect the simulation results. The material properties of the TC are taken from reference [29]. Note that only one TC wire is included in one FE model; and two separate models are used for two wires.

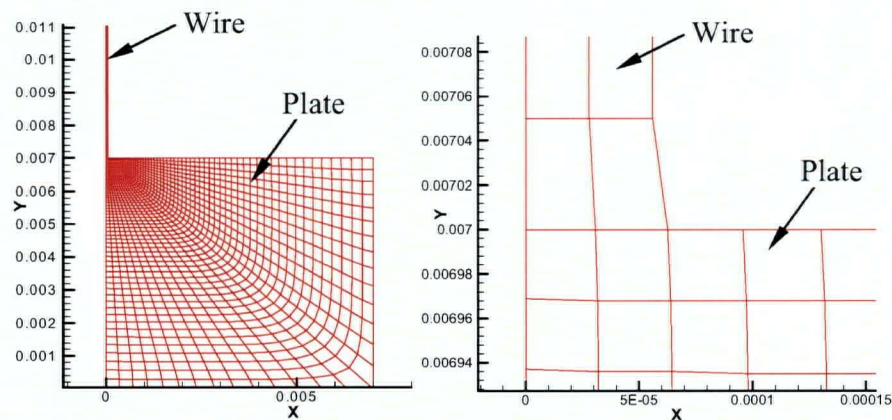


Figure 5.3 FEM model for analysis of effect of wire

The cooling process is divided into two stages: air-cooling and water-cooling. The heat transfer coefficients for the TC wire are chosen to account for the convection and radiation during air-cooling, and the convection during the water-cooling. The full length of the TC wire is assumed immersed in water during the water-cooling stage. It should be noted that a heat convection boundary condition, i.e., a specified HTC, is applied on the outside surface of the TC wire rather than to specify a given heat flux. The rationale behind this choice is to avoid having the TC wire temperature lower than the water temperature. And the wire top is also assumed thermally insulated. The values of the parameters are given in Table 5.1. All these values are typical for air-cooling and water impingement cooling.

Table 5.1 Data for FEM model

	Size (mm)	$\rho$ , kg/m <sup>3</sup>	c, W/kg°C	k, W/m°C	Element	B.C.	
						Top	Bottom & Right side
<b>Plate</b>	b=7 h=7	7800	470	31.5	1484	q=7.0e4 for air cooling q=2.4e6 for water cooling	Thermally insulated
<b>Wire 1 (K-Plus)</b>	d=0.1 h=4.05	8550	419	12.5	162	h=90 for air cooling h=4000 for water cooling	
<b>Wire 2 (K-Minus)</b>	d=0.1 h=4.05	8700	544	58.6	162	h=90 for air cooling h=4000 for water cooling	

Figure 5.4 shows the disturbed field of the surface temperature due to the attachment of TC wires to the surface. At the air-cooling stage, the surface temperature is essentially uniform. As soon as cooling water hits the plate surface and the wires, the temperature field is considerably distorted for both K-plus and K-minus wires. Comparing the curves in Figures 5.4a and 5.4b may conclude that the K-minus wire disturbs the temperature field more than the K-plus wire.

Note that there is a thermal conduction along the wire, and the heat flux at the root point of the wire will be larger than that on the plate surface. More heat is extracted from the plate surface around the wires than other parts. This effect increases as the conductivities of the wires increase and as the heat flux on the plate surface rises.

It is worth noting that the deformation of temperature field due to the attachment of the wire is confined within 0.3 mm for both wires, which implies that the effect of wire attachment on the temperature field may not be coupled if the wires are 1 mm or more

apart from each other. Therefore, the separate simulations by attaching K-plus and K-minus wires, respectively, are an appropriate procedure for modelling this effect.

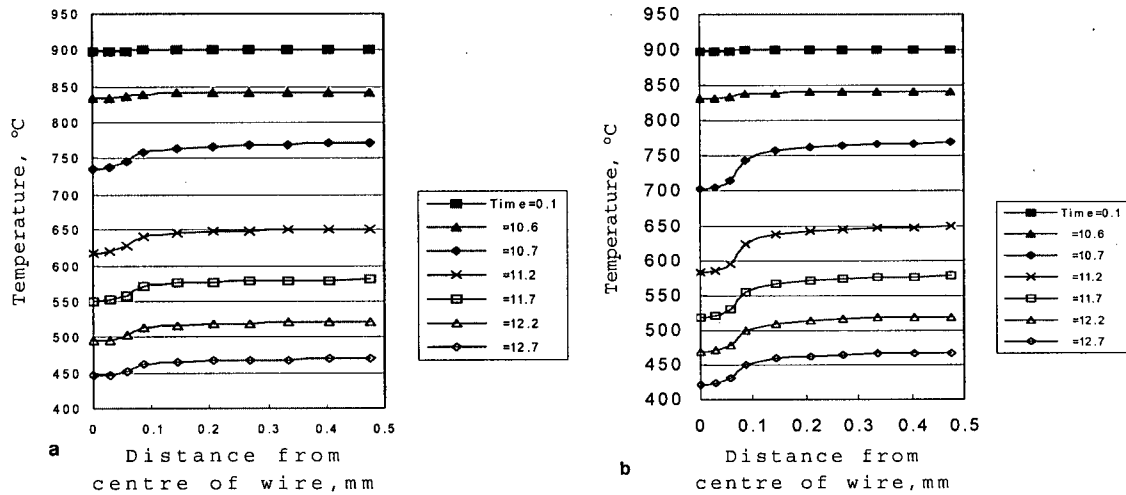


Figure 5.4 Disturbed field of surface temperature around the wires  
a- K-plus wire; b- K-minus wire

Figure 5.5 clearly depicts the effect of TC conduction on the surface temperature history. In the figure, the reference temperature refers to the one without the attachment of wires. The disturbance of the surface temperature is picked up in the first few milliseconds after water impingement, and continues to the rest of the cooling period. Because of the radial disturbance of the temperature field when the TC wire is attached, the reported K-minus and K-plus surface temperature in the figure are those for the wire center at the junction.

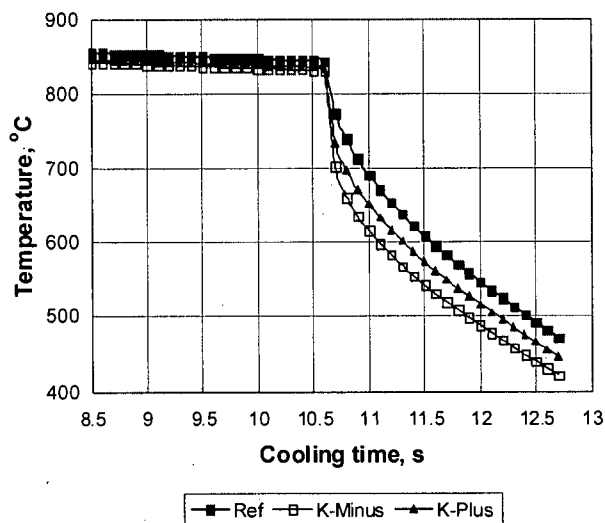


Figure 5.5 Effects of wire conduction on surface temperatures

It is apparent in Figure 5.5 that during the air-cooling, the temperature difference between the two wire roots is negligible, which means that the measuring junction is in an isothermal condition. The temperature at the wire roots is slightly less than the reference temperature. The output of the Seebeck voltage will present the true temperature. However, such a situation is not the case after water impinges on the surface. During the water-cooling stage, the temperature difference between the two wire roots is up to about 30 °C; this occurs just after water impingement and holds approximately constant thereafter. This indicates that the isothermal state for the measuring junction is not a valid assumption. A detailed analysis of this point is presented in Section 5.2.3.

Another issue to be pointed out is that the average value of temperature at the wire root is always less than that at a point 1 mm or more away from the root. The difference is about 45 °C. This means that the measured output is less than the true temperature even if the isothermal condition is assumed for the measuring junction.

The temperature gradients along the wires are shown in Figure 5.6. A larger temperature gradient is evident for the K-plus wire. It is also observed that the temperature along the wire quickly reduces to a very low level because of the very small size and volume.

It is worth mentioning here that the internal temperature is hardly affected by the attachment of TC on the surface.

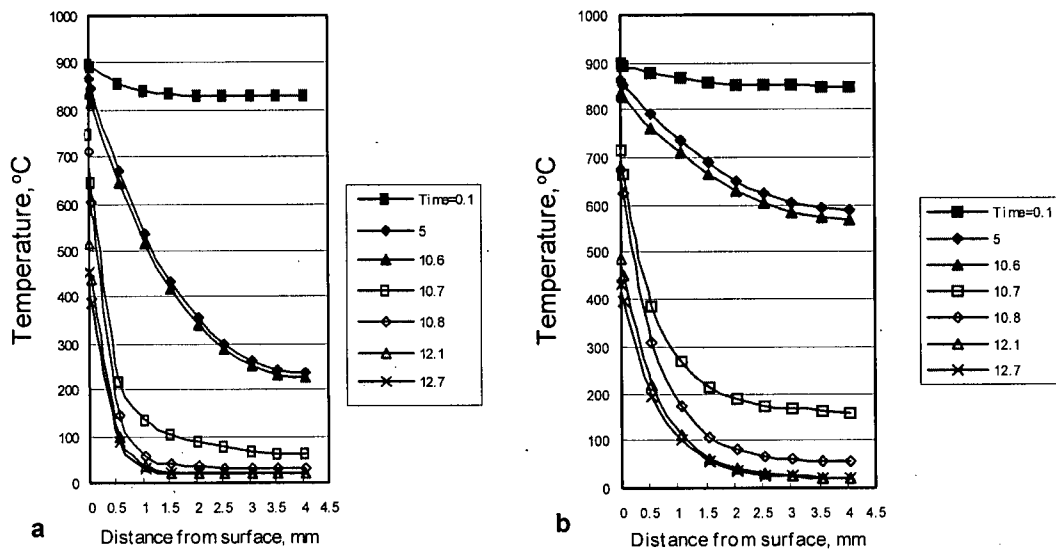


Figure 5.6 Calculated temperature gradient along the wires  
a- K-plus wire; b- K-minus wire

### 5.2.2 Effect of drilling a hole

In the previous sections, all calculations are carried out using a full-solid model. However, in practice internal temperature measurements require small holes for the TC installations. The existence of such a geometric discontinuity will generally disturb the internal temperature field as well as the surface temperature distribution.

In this section, such an effect is investigated using a hole-model and a cave-model. For the two models, hollow cylinders of 7 mm in height and 7 mm in radius are meshed. The FE models for these two cases are shown in Figure 5.7. The hole-model has the same radius as the actual hole dimension in the experiment; that is, 0.8 mm in radius while the depth is 4, 5 and 6 mm to study the disturbance intensity with different depths. The cave is 0.8 mm in radius and 0.8 mm in height at a distance of 6 mm from the bottom of the cylinder. A finer mesh has been assigned around the hole and the cave to capture the thermal gradient and disturbance of the temperature field. The material properties and boundary conditions for the two models are the same as those specified in Table 5.1. All surfaces due to the inclusion of the hole or the cave are prescribed as thermally insulated because excellent insulation measures were taken in the test.

The results from the two models are shown in Figure 5.8 to Figure 5.10. In these figures, *H* stands for the hole model, *C* stands for the cave model and *B* stands for the full-solid model; index-0 is used for the surface temperature and index-1 (or 3) are used for the temperature at 1 mm (or 3 mm) distance beneath the surface corresponding to the hole depth.

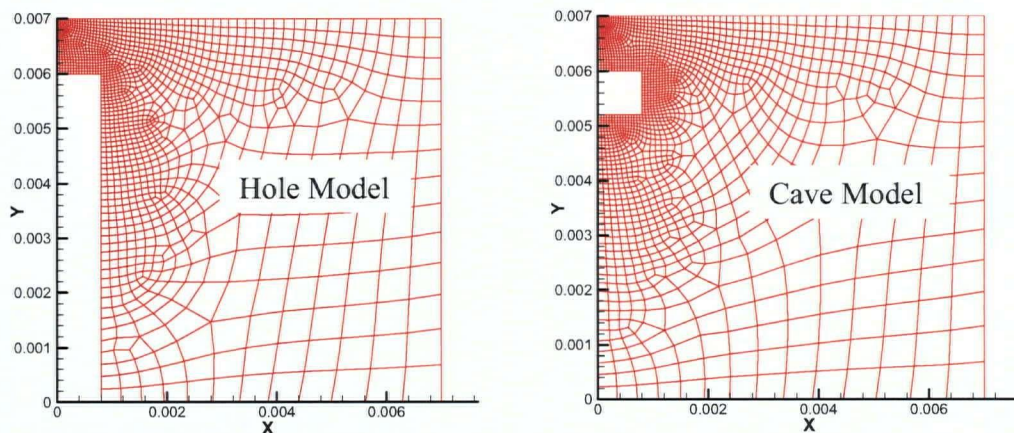


Figure 5.7 Example of FEM model for the effect of hole or cave

Figure 5.8 compares the temperature histories of a model with a 6 mm hole and a cave at 6 mm height with those of a full-solid model. It may be seen that the temperature fields are almost identical for both the hole and the cave cases during the air-cooling or water-cooling. This implies that the thermal insulation condition for the hole model is appropriate, and therefore the hole model will be used for our assessments of other factors.

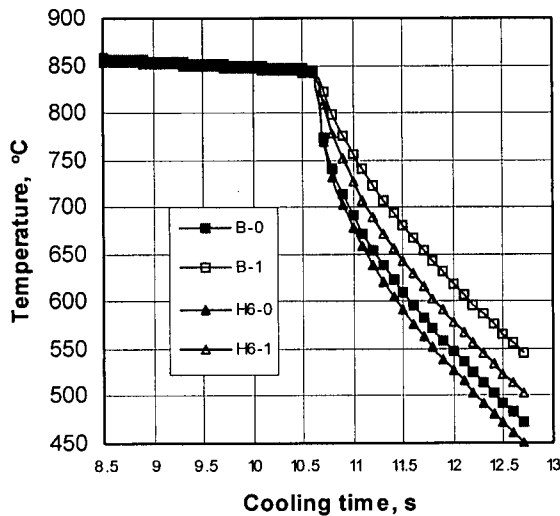


Figure 5.8-a Effect of 6 mm hole on temperature field

B-0: surface temperature without hole  
 B-1: temperature at 1mm depth without hole  
 H6-0: surface temperature with 6 mm hole  
 H6-1: temp. at 1mm depth with 6 mm hole

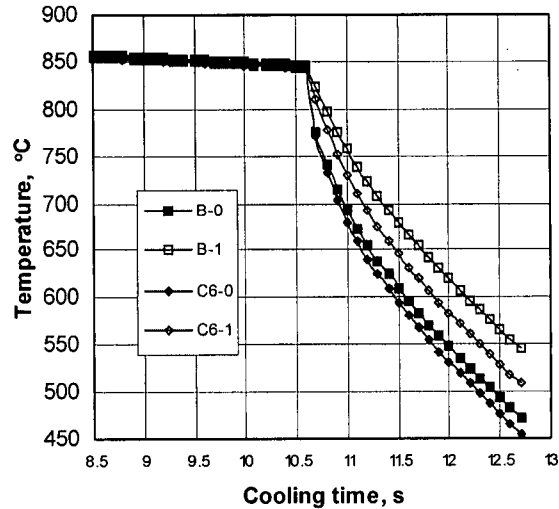


Figure 5.8-b Effect of cave at 6 mm on temperature field

B-0: surface temperature without cave at 6 mm  
 B-1: temp. at 1mm depth without cave at 6 mm  
 C6-0: surface temperature with cave at 6 mm  
 C6-1: temp. at 1mm depth with cave at 6 mm

Comparing the temperature history in the full model with the corresponding one of the model with a hole reveals that there is no difference during the air-cooling period. However, after water impinges on the surface, the difference between the two models appears and starts to increase with the cooling time (Figure 5.9). The temperatures at the hole bottom, where an internal TC will be attached, are lower than those at other points that are at the same height but a few millimeters away. The figure shows a difference of approximately 40°C after 2 seconds from the water impingement. This indicates that the TC reading will not be accurate.

It is important to note that the surface temperature distribution is also affected and that the surface temperature in the hole case is lower than that without the inclusion of a hole. The difference is about 25 °C after 2 seconds from the water impingement.

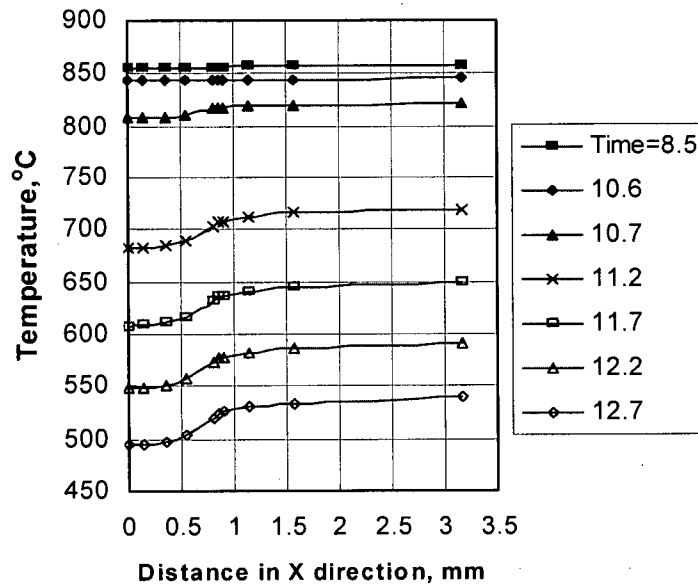


Figure 5.9 Disturbed temperature fields at 6 mm

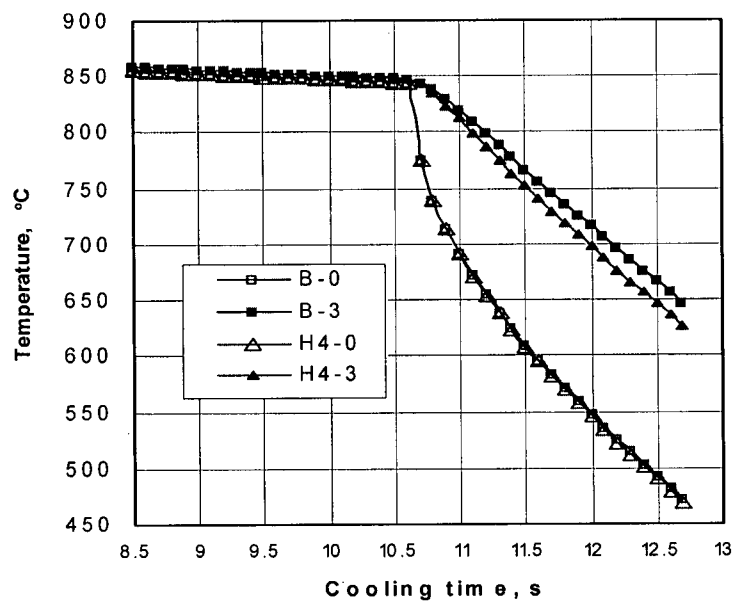


Figure 5.10 Effect of 4 mm hole on temperature field

- B-0: surface temperature without hole
- B-1: temperature at 1mm without hole
- H4-0: surface temperature with 4 mm hole
- H4-1: temp. at 1mm with 4 mm hole

The appropriate depth of the hole is explored here with extensive analyses. One example is shown in Figure 5.10, and detailed discussions are presented in Section 5.4. It is found that the surface temperature difference between the full solid model and the hole model reduces with decreasing hole depth. When the depth is 4 mm for the hole of 0.8 mm in radius, i.e., with 3 mm thick metal material between the top surface and the bottom surface of the hole, the effect of the hole on the surface temperature is negligible. Also, the cooling condition on the top surface is not altered, and the true surface temperature may be obtained if an appropriate measurement is adopted.

Although the internal temperature field is still disturbed when the depth is 4 mm, the magnitude decreases to about 15 °C after 2 seconds from the water impingement.

A combined model where the surface TC wire is attached (as shown in Figure 5.3) and a hole is set up (as shown in Figure 5.7a) is used to investigate the comprehensive effects from both the wire attachment and the existence of a hole. The results are shown in Figure 5.11. These results verify the expectation that the temperature field measurements will be quite inaccurate when the TC is attached to the top surface just 1 mm above the bottom surface of a hole. For example, the surface temperature difference increases to 50 °C after 2 seconds from the water impingement, about 10 °C higher than that with the attachment of TC wires.

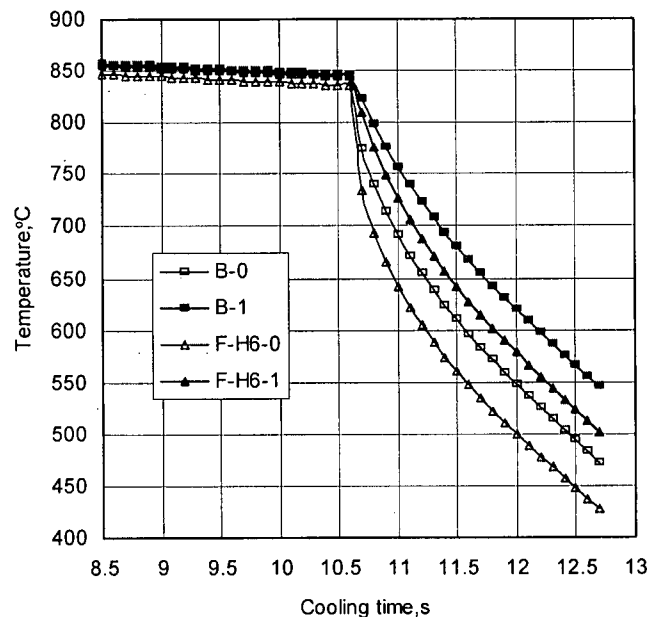


Figure 5.11 Effect of 6 mm hole and K-plus wire

### 5.2.3 Effect of plate material

For an intrinsic TC, the two wires at a separation junction are not directly bonded together, and they are soldered separately to the cooling surface. Therefore, the steel plate between these two wires plays the role of a third metal. According to the law of inserted metals [28], the Seebeck voltage will not change, provided that both wire ends of the measured junction are at the same temperature. As calculated in Section 5.2.1, the temperature difference between the two ends ( $\Delta T_1$ ) is about 30–40°C.

The output of the TCs with a separation junction is the weighted mean of the two individual temperatures with the following correlation (see Figure 5.12):

$$e_{AB1} = e_{AB} - V_1 \quad (5.1)$$

where  $e_{AB1}$  is the measured output voltage;  $e_{AB}$  is the would-be measured output voltage if both wires have the same temperature which may be taken as the average temperature of the two wires;  $V_1$  is the additional voltage due to a third metal whose ends have different temperatures.

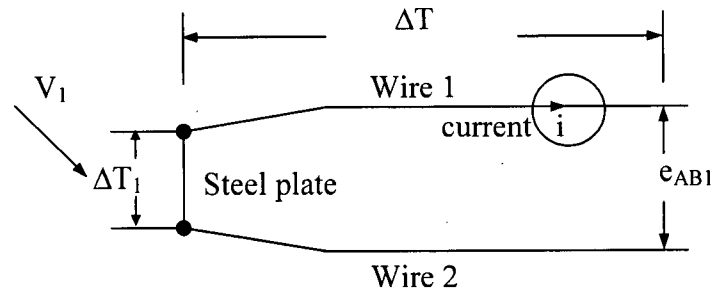


Figure 5.12 The effect of the inserted third metal

Assuming that the reference temperature is zero, there are:

$$e_{AB} = C_{\alpha} \cdot \Delta T = C_{\alpha} \cdot (T_1 + T_2) / 2 \quad (5.2)$$

$$V_1 = C_{\alpha s} \cdot \Delta T_1 = C_{\alpha s} \cdot (T_1 - T_2) \quad (5.3)$$

where  $T_1$  and  $T_2$  is the temperatures at the roots of wires 1 and 2, respectively;  $C_{\alpha}$  is the Seebeck coefficient of the TC;  $C_{\alpha s}$  is the Seebeck coefficient of the third metal, here, the steel plate.

The absolute error of the measured temperature due to the third metal may be calculated by the following equation:

$$error = \frac{C_{\alpha s} \Delta T_1}{C_{\alpha} \Delta T} \Delta T = \frac{C_{\alpha s}}{C_{\alpha}} \Delta T_1 \quad (5.4)$$

From equation (5.4), it is evident that the measured temperature error will become zero when  $\Delta T_1$  is zero, that is, when there is no temperature difference between the two wires. In our experiments, Type-K TC is used and the Seebeck coefficient of the two metal wires is 30.8  $\mu\text{V/K}$  for K-plus and -8.2  $\mu\text{V/K}$  for K-minus [29] respectively. Therefore,  $C_{\alpha}$ , the Seebeck coefficient of type-K TC is 30.8-(-8.2) = 39  $\mu\text{V/K}$ . The Seebeck coefficient of Fe ( $C_{\alpha s}$ ) is 14.4  $\mu\text{V/K}$ . Substituting into equation (5.4) with  $\Delta T_1=30\text{--}40^{\circ}\text{C}$ , the error of the measured temperature would be about 11–15  $^{\circ}\text{C}$ . This implies that the error due to third metal may not be critical.

By adding the errors calculated above, it can be seen that the total error in the surface temperature is around 60  $^{\circ}\text{C}$  due to the attachment of the surface TC on the surface 1 mm above a hole for the imbedded TC. The error value is close to that for the lower surface temperature but is quite different for the high transient period, as shown in Figure 5.1. This suggests that there may be other factors causing the errors.

#### 5.2.4 Effect of contact with water

Water is a kind of electrical or electrochemical conductor. During the water-cooling, the plate surface is covered by a layer of cooling water, and the bare TC wire will work as an electrode, which forms a short circuit between the two TC wires and possibly between the wires and the plate. "Contact" is, therefore, set up between the bare wires, the individual wires and the metal surface. This implies that there are other "equivalent-measuring junctions" other than the one on the metal surface. Therefore, the output of surface TC may not be the true value even if the effect of wire conduction and the existence of a hole are excluded. It can be inferred that the output will be lower than the true one because the "equivalent measuring junctions" are at temperatures ranging between 20 $^{\circ}\text{C}$  (the assumed water temperature and ambient one) and the surface temperature of the plate. A detailed calculation is beyond the scope of this study.

### 5.2.5 Section summary

The key points of the above studies are summarized in the following:

1. The accurate and correct output of a TC with a separate measuring junction is assumed only when the isothermal conditions are guaranteed for both the reference and the measuring junctions in the TC thermometry.
2. During the air-cooling, the attachment of TC wires on the surface has negligible influence on the surface temperature distribution. The isothermal condition at the measuring junction with a separation installation is approximately assured, and the top surface temperature measurement may be assumed free of installation error.
3. In the case of water impingement cooling of hot steel plates, the conductions of wires lead to two kinds of effects. First, the surface temperature field is disturbed and becomes non-uniform. The average temperature around the measuring junction would be about 45 °C less than the true temperature. Second, the measuring junction with a separation installation is no longer an isothermal junction. A temperature difference of about 30 °C between the two wire roots may occur as the water impingement starts. This difference will be held constant thereafter. The plate metal works as the third wire. This may cause an additional difference of about 10–15 °C lower than the average temperature around the measuring junction. The combination of these two effects leads to a measurement error of about 60 °C lower than the true value. The attachment of TC on the surface has little effect on the internal temperature 1 mm below.
4. The disturbance of the temperature field due to the hole for the installation of internal TC is not significant during the air-cooling. However, a hole with a depth of 6 mm deforms both the internal and surface temperature fields in the case of water-cooling. The effect would be to lower the temperatures at the top surface and at 6 mm height. Without considering the wire conduction effect, the differences of temperatures at the top surface and at 6 mm height are 25 °C and 40 °C after 2 seconds of water impingement, respectively.
5. The deformation of the temperature field is worse when the TC is attached on the top surface just 1 mm above the bottom surface of the hole.

6. The 4 mm hole will slightly affect the internal temperature field only. The hole depth should be reduced as much as possible in experimental tests.
7. The contacting due to water may contribute to the errors in the surface temperature measurement during the water-cooling. Some measures such as insulation to these wires should be taken to eliminate or decrease such an influence.

### **5.3 Moving Case [61]**

This section addresses the effects of the progressing speed of black zone front, heat flux profile and magnitude, hole depth, and specific heat on the accuracy of temperature measurements. Most of these analyses are performed using our own FE code, while a small portion is carried out using the commercial FE package ANSYS [59]. The plate material is DQSK and the temperature dependence of thermal conductivity is considered.

#### **5.3.1 Motivation of study**

To obtain an overall view of heat transfer characteristics on the top surface, several TCs should be installed at suitable locations to measure the temperatures. In our tests [27] of water jet cooling of stationary plates, 8 intrinsic TCs, numbered TC1 to TC8, with a fixed radial distance of 15.9 mm, are used; and the two TC wires are separated approximately 1–1.2 mm. Roughly, the TC1 and TC2 are inside the impingement zone, while the others are outside of it, as shown in Figure 5.13. In such cases, the cooling water would reach the individual TC wire at a slightly different time instant when the connection line (see Figure 5.13) between the two wires is inclined or parallel to the water moving direction. Even if the connection line between the two wires is perpendicular to the water moving direction, there may still be a very small time difference in reaching the wires because the water movement can not be perfectly radial. Therefore, the situation in which the individual TC wire is cooled at a slightly different time instant always exists.

#### **5.3.2 FE Model**

##### **1. Geometry**

One of the critical issues in the FE modeling of this problem is to set up a typical and representative geometry of the plate. In our tests the nominal thickness of plates is 7 mm,

and the diameter and depth of hole drilling from the bottom are about 1.6 mm and 6 mm, respectively. These parameters are used in our FE model.

The existence of a hole will generally deform the temperature field. When considering the effect of water movement, the cooling behaviour is three-dimensional. The initial studies above show that the effect of a hole may be confined within a region 5 times the diameter of the hole. Therefore, a block of 20 mm × 20mm × 7 mm with a centred hole of 1.6 mm in diameter and 6 mm in depth is used in the 3D model.

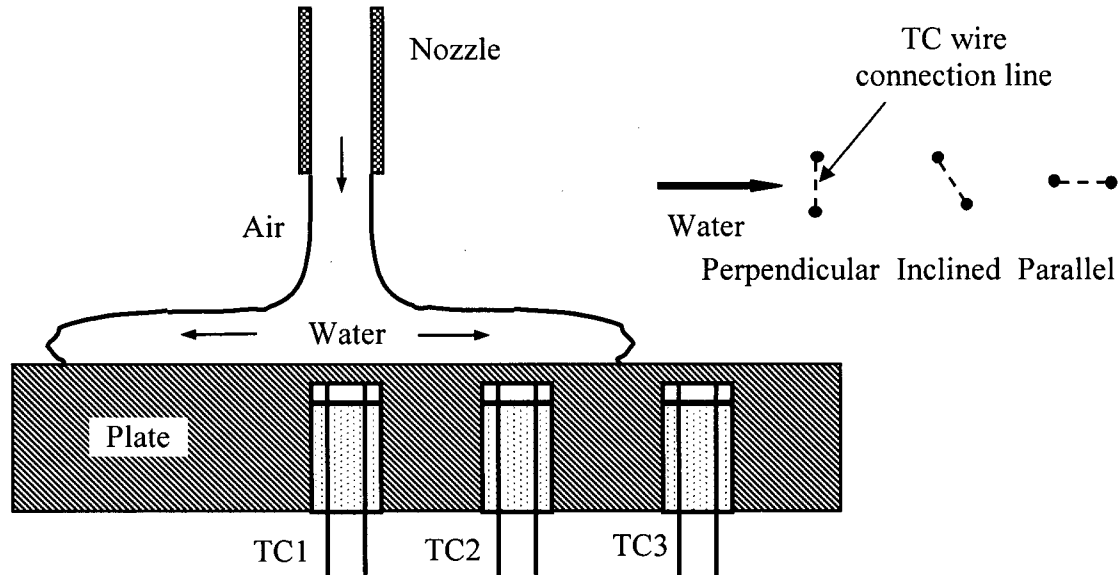


Figure 5.13 Cooling water and TCs

In the current work, a variety of 2D models are used to save the calculation costs and time. In these models, the thickness of the plate is fixed at 7 mm, the width of a two-dimensional groove is 1.6 mm, and the depth is taken as 6 mm, 5mm and 4 mm, respectively. These models will facilitate the study of the effect of hole depth.

The elements in 2D models are uniform at the plate's top surface to ensure an unbiased simulation of the progression of water cooling zones, while they are variable in the thickness direction, and a relatively denser mesh is adopted around the hole. A typical 2D mesh is shown in Figure 5.14.

## 2. Specification of boundary conditions

The main objective of the current work is to investigate the effect of the progression of water cooling zones on the accuracy of temperature measurement using a TC with a separation measuring junction. Therefore, it may be assumed that all sides, except the top surface, are thermally insulated. This may not be practically true, but it should not significantly influence the results obtained around the TC junction area.

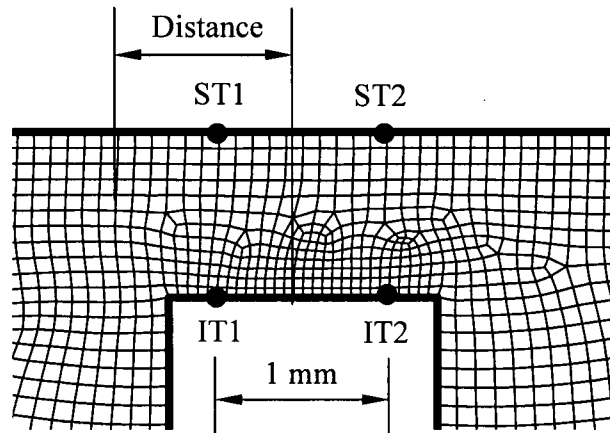


Figure 5.14 Typical mesh and sampling points

For the 2D model, the heat flux boundary conditions are calculated from a space-time marching approach, and then applied on the nodes on the plate's top surface. This space-time marching approach has already been explained in Section 4.4.3. The method to apply the boundary condition to the top surface in 3D model will be discussed in Section 5.3.3.

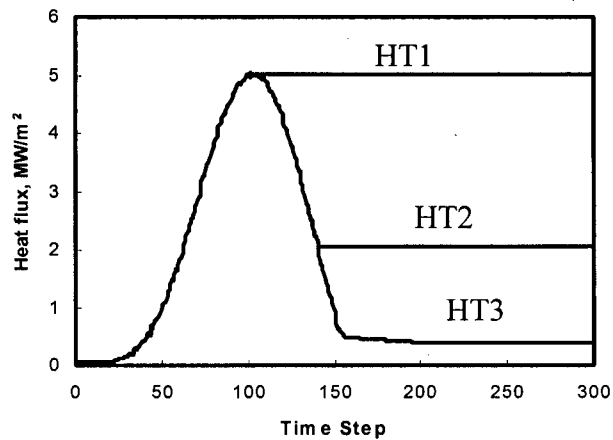


Figure 5.15 Types of heat flux profiles

### 3. Heat flux profiles

As discussed above, a formula is used for calculating the new heat flux. Three types of heat flux profiles, named HT1, HT2 and HT3, are setup to investigate the effect of possible heat flux changing modes in practice on the magnitude of the temperature difference, as shown in Figure 5.15.

All three types of heat flux can be used to present the cooling process on a stationary plate. It may be assumed that the heat flux at any location increases before the black zone front reaches this point, and that the heat flux reaches its maximum value as the point turns black. Afterwards, the heat flux of type HT1 is kept at the maximum value while it decreases for types HT2 and HT3. After reaching the maximum, the heat flux of type HT3 decreases continuously with a similar rate as that of the increasing one until it reaches a very small value that is again assumed to be equivalent to the air-cooling with some residual water-cooling. Type HT3 may also be looked at as the case with a moving plate.

For each type of heat flux profile, three peak values are used, as shown in Table 5.2. The notation is used in the following sections.

Table 5.2 Heat flux type notation

Notation	Type	Peak Value (MW/m <sup>2</sup> )
HT1-Q2	HT1	2.5
HT1-Q5		5
HT1-Q10		10
HT2-Q2	HT2	2.5
HT2-Q5		5
HT3-Q10		10
HT3-Q2	HT3	2.5
HT3-Q5		5
HT3-Q10		10

At any time instant, there is a space distribution of heat fluxes. The space distribution changes step by step, and one example is shown in Figure 5.16. In this example, the water cooling stage starts at step 50, and 40% of the top surface is already cooled by water at step 75. At step 120, all areas of the top surface enter the water cooling stage, and the peak of the heat flux locates at element 20. With the passing of time, the temperatures at the back part decreases, the heat transfer capacity decreases, and then the peak of heat

flux moves forward. At step 175 the heat flux peak moves to element 70. At step 250 the plate is cooled down for stationary cases, or the water cooling zones move away from this part of the material for moving cases, and finally all the heat fluxes are at low values.

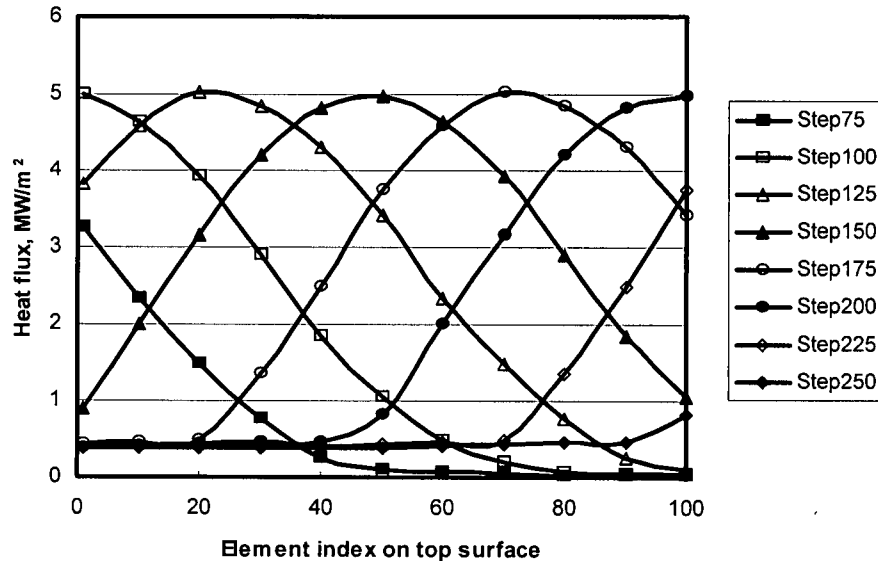


Figure 5.16 Space distribution of heat flux

### 5.3.3 Results and discussion

In this study, four sampling points are considered, as shown in Figure 5.14. Two points are on the hole's bottom surface, which is used for installing the TCs. The two points correspond to the two roots of the separately soldered TC wires.

Correspondingly, there are two points on the plate's top surface or the cooling surface. The two surface points may be looked at as the two roots of the separately soldered TC wires if surface TCs are used.

The paired two points are 1 mm apart from each other. The connection line between the two points is parallel to the water moving direction.

The temperatures at those four points are defined as IT1 and IT2 for the inner points, and ST1 and ST2 for the surface points. The temperature difference between IT1 and IT2 is defined as IDT, and that between ST1 and ST2 is defined as SDT. Since IDT and SDT may change with time, they are mostly regarded as the maximum values of these temperature differences during the cooling process in the following analyses.

Initial simulations have been performed. In those cases, finer TC wires are included in the mesh model. The results show that the attachment of wires has little impact on the temperature differences at the un-simultaneous cooling conditions, and that the above trends hold irrespective of the material properties of the TC wires. Therefore, the TC wires are not included in the subsequent models.

### 1. Appropriateness of 2D model as a replacement of 3D model

In this section, both 2D and 3D simulations are performed using the commercial FE package ANSYS [59]. There are two 3D models used in the analysis: one with a hole of 1.6 mm in diameter, the other with a width-through groove of 1.6 mm in width. The 3D model with a hole contains 56,140 nodes and 38,029 brick elements, whereas that with a groove contains 8,389 nodes and 19,065 brick elements. The 2D model has a width of 20 mm and contains only 314 nodes and 520 triangle elements.

A region-jumping approach is used to apply the heat flux boundary condition because the method described in Section 5.3.2 for 2D models can not be used in 3D models. Here, the top surface is divided into four regions. At the initial cooling steps, all regions are air-cooled (the heat flux is  $30,000 \text{ W/m}^2$ ), and then each region is water-cooled ( $10 \text{ MW/m}^2$ ) sequentially. The two regions covering the two nominal roots of the TC wires are water-cooled consequently with a time shift of 0.1 second. The equivalent progressing speed of the water cooling zones is 10 mm/s.

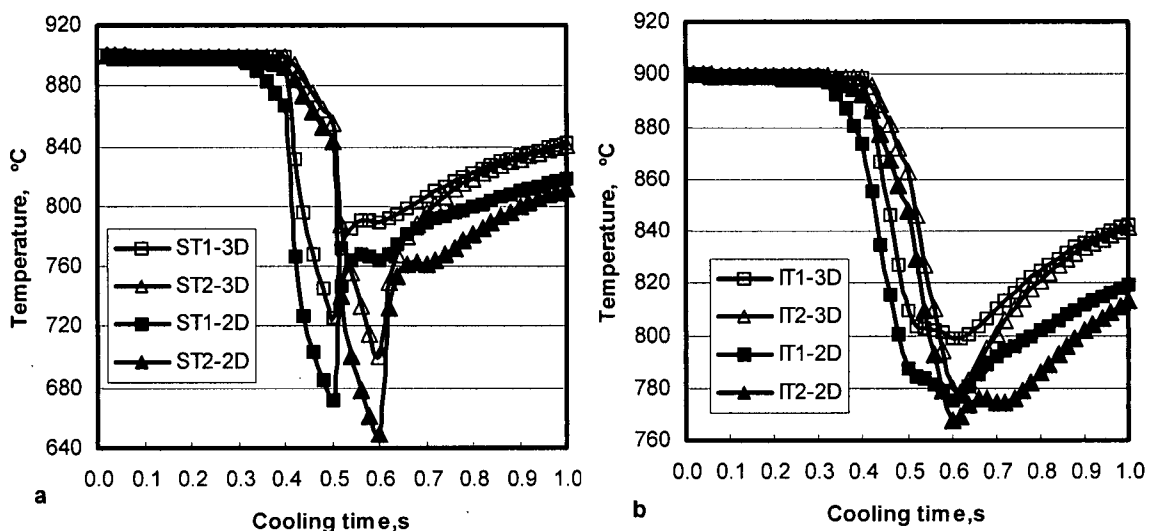


Figure 5.17 Temperature profile results of 3D and 2D analyses

The data show that there is little discrepancy in results from the grove-3D model and 2D model. So the results from the grove-3D are neglected and not discussed. The comparisons between the 2D and 3D results are shown in Figure 5.17 and Figure 5.18.

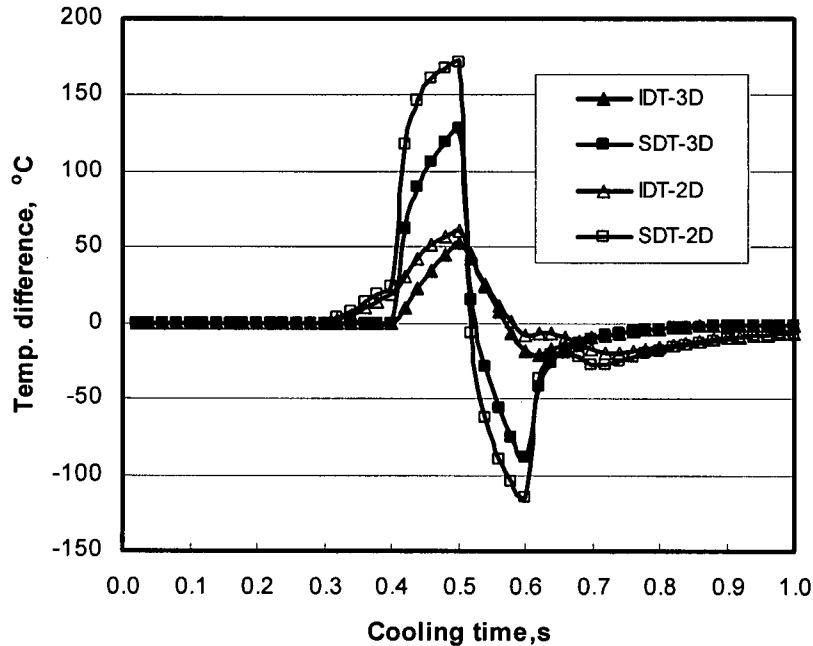


Figure 5.18 Comparison of temperature difference in 2D and 3D  
Constant heat flux=  $10\text{MW/m}^2$ ;  $V=10\text{ mm/s}$

Figure 5.17 compares the temperature profile results of 3D and 2D analyses. It is apparent that the temperatures at the two roots are not the same for all conditions. The temperature difference is shown in Figure 5.18. It is obvious that the temperature difference is quite small during air cooling and becomes significant after water cooling. The temperature difference obtained from the 3D model is, generally, less than that obtained from the 2D model. However, the discrepancy in temperature difference for the interior TC is not significant, and the maximum temperature difference is approximately identical. It is worth noting that the above results are obtained for an input heat flux of  $10\text{MW/m}^2$ .

From the above discoveries and discussions, 2D models are used in all analyses in the following sections.

## 2. Effect of progressing speed of water cooling zones and depth of hole

The progressing speed of water cooling zones is a critical factor that influences the temperature difference between the two wire roots. The faster the speed, the shorter the time difference that the water takes to reach the nominal points of the two wires.

It is, however, not a simple task to obtain this progressing speed. The cooling water is heated when it spreads outwards, and some of it becomes vapour. The ratio of water to vapour is difficult to quantify in time and space, and it affects the progressing speed. In addition, water pressure and plate surface roughness will also affect this speed.

An alternative way to approximately quantify the progressing speed of water cooling zones is to rely on the experimental data. As mentioned in Section 4.1.3, the water movement is not uniform and the average speed changes from 1 mm/s to 6 mm/s. Taking other factors and test conditions into account, it is assumed that the progressing speeds are 5 mm/s to 40 mm/s. At those speeds, the root of one wire is cooled 0.2 second to 0.025 second later than the other root.

The effect of the progressing speed is shown in Figure 5.19. In these cases, the heat flux type is HT3, and the input peak value of  $5 \text{ MW/m}^2$  is used.

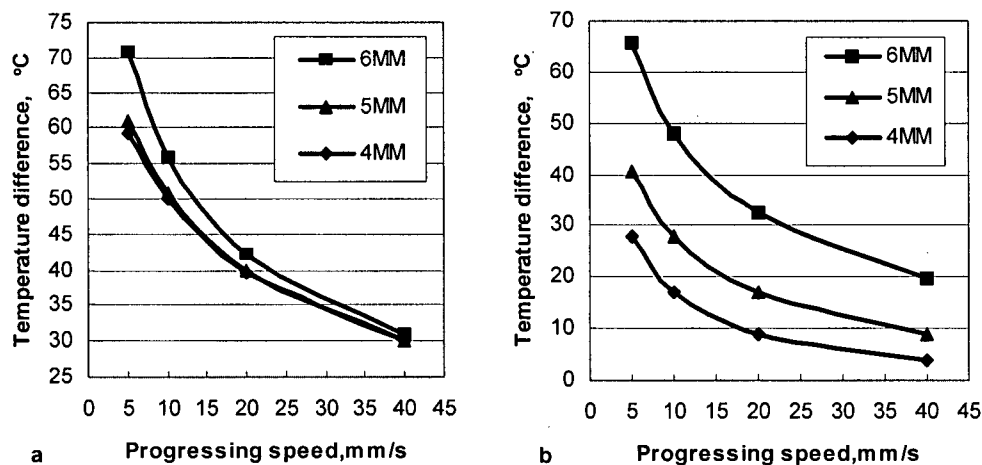


Figure 5.19 Effect of the progressing speed of water cooling zones  
Flux: HT3-Q5  
a: Surface; b: Interior

It is clear that the temperature difference between the wire roots both on the surface (Figure 5.19 a) and inside (Figure 5.19.b) decreases with the increase in the progressing

speed for all models with the different hole depths. Such a trend is more evident when the speed increases from 20 to 40 mm/s. For the surface TCs in the 6 mm-hole model, the temperature difference is as high as about 71 °C when the speed is only 5 mm/s, and is still about 31 °C when the speed increases to 40 mm/s.

The error in the internal TC measurements is much less than that in the surface ones; for example, with a 5 mm-hole model the interior temperature difference is 40 °C while the surface temperature difference is 61 °C.

When the hole depth decreases from 6 mm to 5 mm the surface temperature difference decreases. However, the situation for the 4 mm-hole model is nearly identical to that for the 5 mm-hole model, which means that decreasing the depth to less than 4 mm will not affect the temperature difference between the surface wire roots. This is consistent with conclusion 6 in Section 5.2.5.

It may be concluded that the depth of the hole has a significant effect on the error; and that decreasing the depth of the hole will decrease the temperature difference at a relatively fast rate.

If the water is moving faster enough to cover the two TC wires roughly simultaneously, there should be no error from the water movement. Based on the above results and discussion, the following simple correlation is proposed:

$$\Delta T = \frac{C_1}{V^{C_2}} \quad (5.5)$$

where  $\Delta T$  is the temperature difference, °C,  $V$  is the progressing speed, mm/s, and  $C_1$  and  $C_2$  are constants that may be a function of the hole depth, flux magnitude and other factors.

For the 6 mm-hole model with HT3-Q5, the equation is  $\Delta T = 100/V^{0.6}$ . Based on this formula, the temperature difference is 6.4 °C yet as the moving speed is as fast as 100 mm/s, while the temperature difference is as high as 100°C as the moving speed is only 1 mm/s.

A special situation is considered where the water does not move and the front of the cooling zone is distant from the middle point of two TC wires, say 15, 20, 25 mm, as shown in Figure 5.14. For these study cases, the sampling time is fixed at 1.5 seconds

because the temperature difference steadily increases with time in this condition, and the heat flux for the cooling zone is kept at  $5 \text{ MW/m}^2$ .

Figure 5.20 shows the effect of stopping distance. It is interesting to point out that the temperature difference for the interior TC is always larger than that for the surface one during the cooling time for this case. And it is clear that the closer the front of water cooling zones is to the first wire root, the larger the temperature difference will be, and that the relationship between them is almost linear.

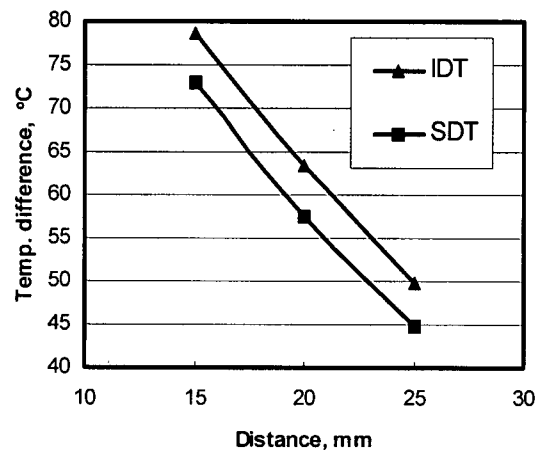


Figure 5.20 Effect of stopping distance  
6 mm hole-model

### 3. Effect of heat flux magnitude

Figure 5.21 and Figure 5.22 show the effect of heat flux magnitude on the temperature difference in the interior (IDT) for a 6 mm-hole model with the flux type HT3. The figures indicate that when the progressing speed is fixed at  $20 \text{ mm/s}$ , the temperature difference can be neglected during air-cooling. As the cooling water gets closer to the first wire, the temperature difference starts to show up. The maximum temperature differences are about  $17 \text{ }^\circ\text{C}$ ,  $32 \text{ }^\circ\text{C}$  and  $59 \text{ }^\circ\text{C}$  with respect to different heat flux peak values. It is quite possible in industry that the peak value of heat flux could be as high as  $10 \text{ MW/m}^2$  or more. At such a condition the temperature difference is as high as  $59 \text{ }^\circ\text{C}$  even if the two points are only  $1 \text{ mm}$  apart. This is a huge difference.

Another important point to note is that the maximum temperature difference appears earlier as the heat flux magnitude increases. For the lower heat flux case, the maximum

temperature difference appears at about 0.86 second, which is later than the time instant when the water reaches the first wire (0.23 second), and is also later than that when the heat flux reaches its peak at the first wire location (0.73 second). For the medium and high flux cases, the maximum temperature difference occurs at about 0.72 second, earlier than the time instant when the heat flux reaches its peak at the first wire location (0.73 second).

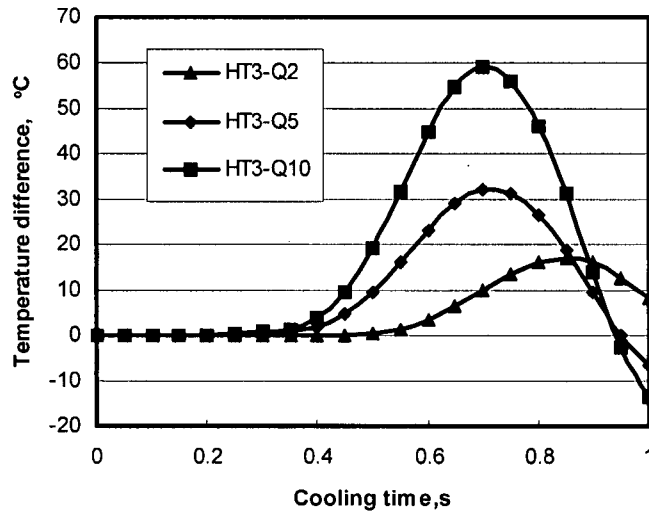


Figure 5.21 Effect of heat flux magnitude  
 $V=20$  mm/s; 6 mm-hole model

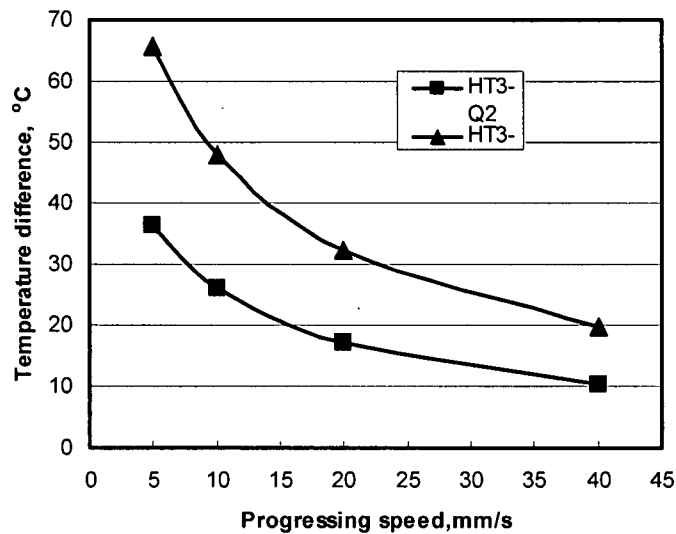


Figure 5.22 Effect of heat flux magnitude  
 and progressing speed  
 6 mm-hole model

It is clear that the temperature difference between wire roots decreases with the increase of the progressing speed of water cooling zones when the heat flux type is fixed. For a peak value of  $2.5 \text{ MW/m}^2$ , the difference is about  $36 \text{ }^\circ\text{C}$  with a speed of only  $5 \text{ mm/s}$ , and is about  $26^\circ\text{C}$  ( $10 \text{ }^\circ\text{C}$  less) when the speed is doubled to  $10 \text{ mm/s}$ . As the speed increases to  $20 \text{ mm/s}$ , the difference becomes about  $17 \text{ }^\circ\text{C}$ . When the peak value is doubled to  $5 \text{ MW/m}^2$ , all the values of the temperature differences are also approximately doubled (the corresponding values are  $66, 48$  and  $32 \text{ }^\circ\text{C}$ ). There would be a linear correlation between the peak value of the heat flux and the maximum temperature difference.

#### 4. Effect of the heat flux type and the depth of hole

The effects of the heat flux type and the hole depth on the temperature difference are shown in Figure 5.23. In these cases, the peak value of heat flux is  $5 \text{ MW/m}^2$ , and the progressing speed of black one front is  $20 \text{ mm/s}$ .

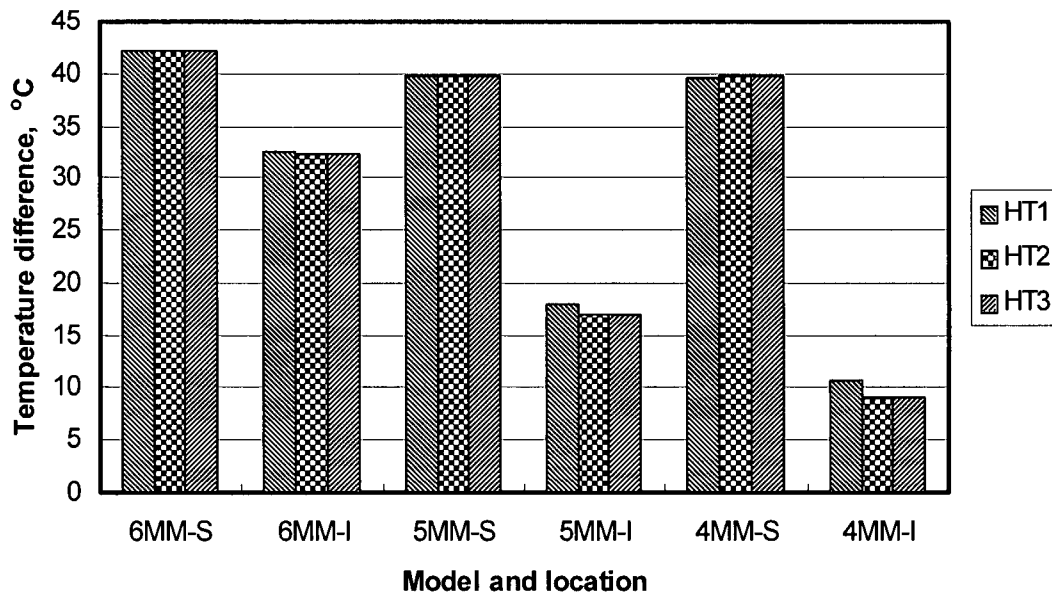


Figure 5.23 Effect of the depth of hole and heat flux type  
 $q_p=5 \text{ MW/m}^2$ ;  $V=20 \text{ mm/s}$

It is apparent in Figure 5.23 that there is no significant variation in temperature differences due to the different patterns of the heat flux for both the top surface and interior points. This implies that the maximum temperature difference depends mostly on

the peak value of the heat flux, which is the same as the conclusion in the previous section.

It can also be seen that the temperature difference decreases as the hole depth decreases (since it takes less time for the cooling water to reach the wire). Take the interior points for example; the maximum temperature difference is about 32 °C for a 6 mm hole. The corresponding value decreases to 17 °C and 10 °C when the hole depth decreases to 5 mm and 4 mm, respectively. It may be inferred that the decreasing rate of maximum temperature difference becomes small when the depth of hole decreases.

In contrast to the situations at the interior points, the maximum temperature difference between the top surface points slightly decreases from about 42 °C for a 6 mm hole to about 40 °C for a 5 mm or a 4 mm hole. This means that the surface temperature difference is hardly affected by the hole depth, which is again consistent with the findings in Section 5.1.

Similar trends hold for the time instant when the maximum temperature difference takes place. It can be easy to find from Figure 24 that the time instants are almost at the same value for the surface TCs in all cases, and that they steadily decrease with the deepening of the hole.

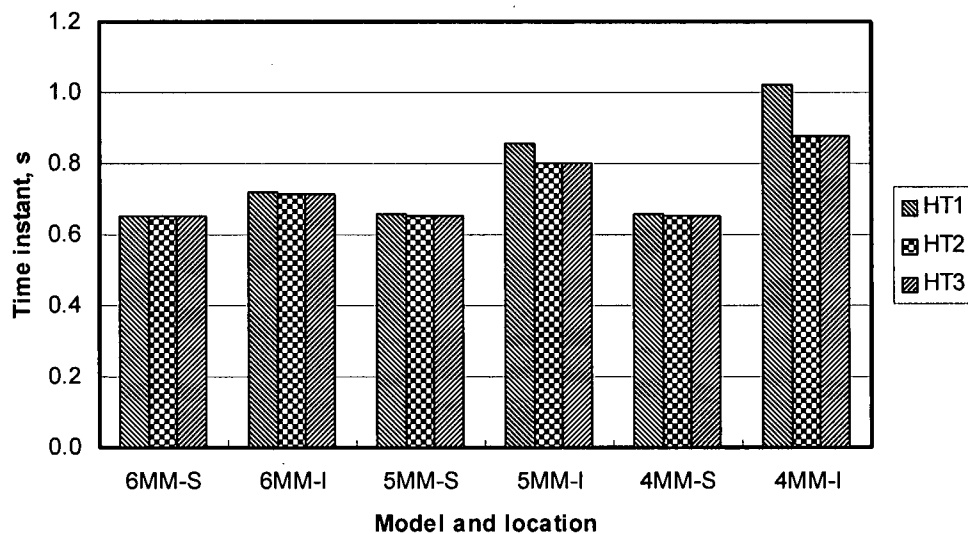


Figure 5.24 Time instant vs. the hole depth and heat flux type  
 $q_p=5 \text{ MW/m}^2$ ;  $V=20 \text{ mm/s}$

## 5. Effect of the initial temperature and the specific heat

The plate initial temperatures in our current stationary tests have been mostly set to around 800–900 °C. For a moving plate, the plate passes the water jet several times; the initial temperature at each pass varies and may be as low as 500 °C. It is, therefore, important to study the effect of the different initial plate temperatures. In the following cases, the heat flux type is HT3-Q5, and the progressing speed of water cooling zones is assumed to be 10 mm/s.

The numerical cases studied indicate that the initial temperature has little impact for both the surface and interior temperature measurements, as shown in Figure 5.25. The maximum temperature difference between the surface TC wire roots only decreases from around 42 °C to 38 °C as the initial temperature decreases from 890 °C to 610 °C. For the same drop of initial temperature the maximum temperature difference between the interior TC wire roots differs only by about 2 °C.

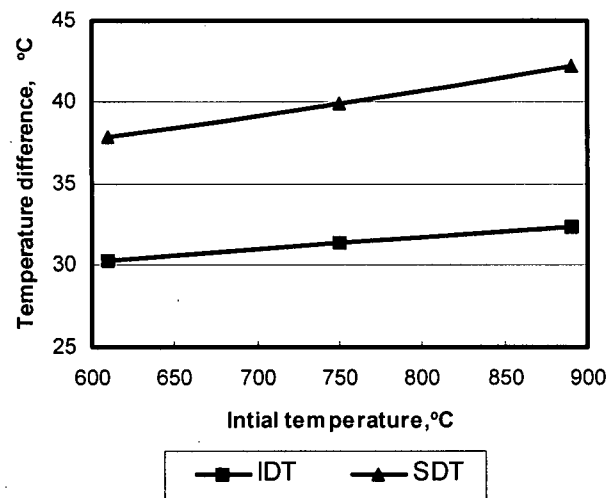


Figure 5.25 Effect of initial temperature  
Flux: HT3-Q5; V=10 mm/s

It is generally known that the temperature field does not change with the initial temperature, and depends mainly on the boundary conditions and time if the properties of material are constant. Accordingly, it may be concluded that the above small change of maximum temperature difference may be attributed to the change of material conductivity. A linear formula is used to calculate the conductivity, and the value

increases with the lowering of temperature. That is, the average conductivity for a lower initial temperature case is higher than that for a higher initial temperature case. A higher conductivity will decrease the temperature gradient, which reflects a small temperature difference.

The effect of the specific heat on the maximum temperature difference between the TC wire roots is depicted in Figure 5.26. In these cases, the heat flux type is also HT3-Q5, and the progressing speed of water cooling zones is assumed to be 10 mm/s. It can be seen that the temperature difference for both the surface and interior measurements decreases approximately linearly with the increase of the specific heat. Such a trend is in agreement with the understanding that the higher the specific heat, the larger the heat capacity and the less the temperature drops.

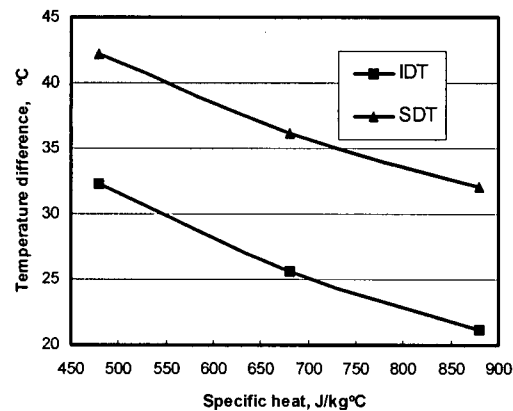


Figure 5.26 Effect of specific heat  
Flux: HT3-Q5; V=10 mm/s

### 5.3.4 Section summary

It can be concluded that the isothermal condition for the TC measurement does not exist for the separate roots of the TC wires, especially when the connection line of the two roots is parallel to the water moving direction. The maximum temperature difference between the TC wire roots will be affected strongly by the progressing speed of the water cooling zones and the heat flux magnitude, and mildly or slightly by the heat flux profile, the hole depth, and the specific heat value.

The temperature difference between the two roots may reach a significant level for both the surface and interior TCs, especially for the situations in which a deeper hole (closer to

the cooling surface) is used to install TCs, and the water moves slowly with a higher cooling capacity. Therefore, it may be concluded that TCs with a separation measuring junction should be, generally, avoided in the temperature measurement of water-cooling in the moving cases, i.e., when the water moves or the plate moves or both.

#### **5.4 Appropriate TC Position**

The appropriate distance  $l$  and depth  $h$ , as shown in Figure 5.27, are investigated using direct FE analysis in this section. The cooling conditions are designed for the impingement cooling using one circular water jet. The “null-calorimeter” technique is examined, and an effective depth concept is suggested through intensive numerical simulations. Correlations for the minimum TC depth and equivalent depth are provided. Note that the TC is of the bead type.

##### **5.4.1 General modelling aspects**

Axisymmetric conditions are assumed in this study, although this assumption is not necessary and does not affect the validness of results. Two kinds of FE models are used, one being the hole model as shown in Figure 5.7, the other being a solid model. As an example, the solid model is a cylinder of 7 mm in height and 8mm in radius and is used as reference in most cases for comparisons.

For both models, only the top surface is specified with heat flux as the boundary condition; and the thermal insulation condition is used on all other surfaces. In the direct calculations, the applied heat flux may be different constant values during the entire cooling process; it may be of the heat flux profile shown in Figure 5.27, which is a simplified version of Figure 4.7 and called a practical input in the following sections.

A transient cooling process is assumed for all cases and the time span is 2 seconds. The rationale for the span of 2 s is that in all experimental tests the material points are already cooled down significantly within 2 s after the cooling water hits the top cooling surface.

If not specifically mentioned, the material of plate is the carbon steel DQSK, and the temperature dependence of conductivity is considered.

It would be too much work to compare all the temperature values during the cooling process from the two models, and may not be practical and necessary. In this study the

temperatures at the cooling end, i.e., at time 2 s, are compared for all direction calculations. Some point-to-point comparisons show that the above approach can be used, and no significant difference exists for the entire cooling process.

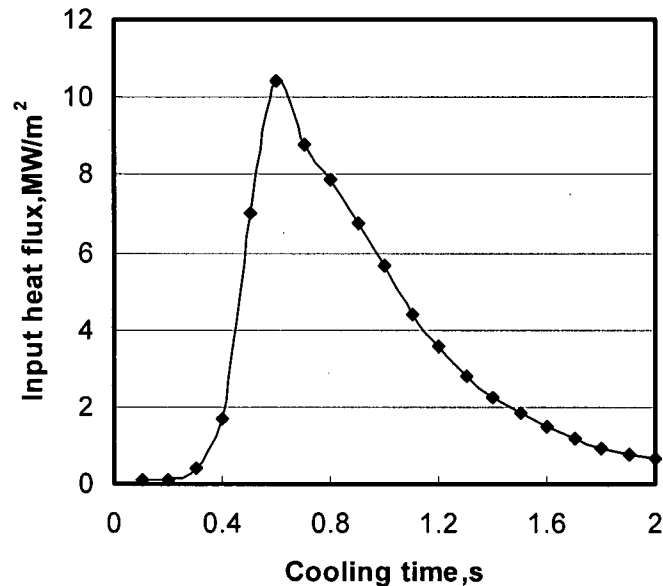


Figure 5.27 Input of practical heat flux

#### 5.4.2 Appropriate horizontal distance

In this subsection, the top surface is equally divided into two subregions; and one sampling point is located in the middle of each subregion and 1.0 mm beneath the top surface. A constant heat flux of 2 MW/m<sup>2</sup> is applied only to the left subregion (relating to TC1) and thermal insulation is specified on the right subregion (relating to TC2). The initial temperature is 900 °C and a constant conductivity of 30 W/m·°C is used. Note that the width of the surface with the assigned heat flux increases with the increase of TC distance. Eventually this width is equal to the TC distance.

The calculation results are shown in Figure 5.28. As can be seen, the temperature TC1 for the sampling point directly under the specified heat flux decreases dramatically when the TC distance increases from 1 mm to 10 mm. This is because more material at the two sides of the sampling point is involved in the cooling process. As the TC distance increases from 10 mm to 16 mm, the temperature TC1 shows little change, which means

that the cooling process at the points 5 mm or more away from the sampling point has little influence on the temperature profile at the sampling point.

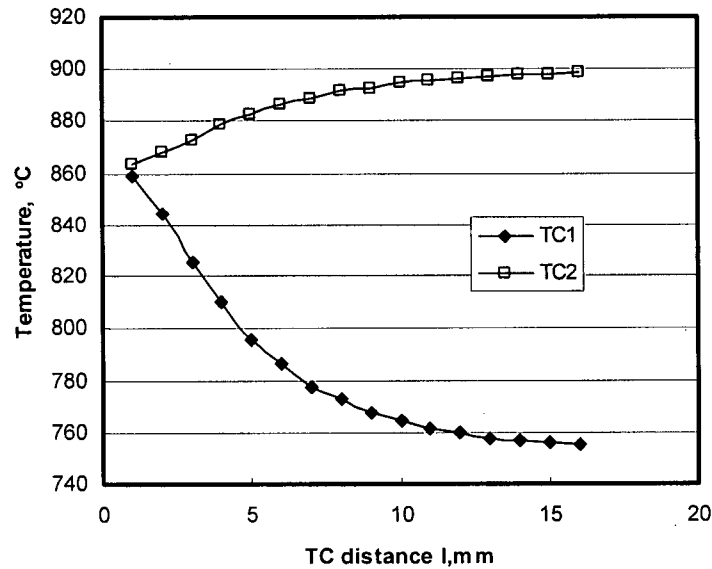


Figure 5.28 Temperature vs. TC distance

The temperature TC2 at the second sampling point more clearly illustrates the distance effect. When the cooling source is close to the sampling point, the temperature may decrease slightly. As the TC distance increases to 10 mm and more there is nearly no drop in temperature at that sampling point.

This calculation uncovers the following important inferences. As the sampling points are 10 mm or more apart and the top surface is accordingly divided into subregions in inverse calculation using the FZM, the heat fluxes may not be interactive; in other words, the other temperature profiles may not stabilize the inverse calculation. Thus, the 2D problem in reality may be incorrectly handled by the FZM as several individual 1D problems if the distance between two TCs is larger than 10 mm. In other words, the distance between two TCs should be less than 10 mm if a 2D problem should be fairly correctly reflected by the FZM.

From these results and those in Section 4.2, it may be concluded that the horizontal distance of TC should be less than 10 mm to attain a real 2D inverse simulation. That is the basis for the model geometry setup in Section 3.3.1.

#### 5.4.3 Appropriate vertical depth

As mentioned in Section 2.5, it is preferred that a TC be implanted at a depth at which the surface temperature is nearly unaffected and at the same time the detection of a higher frequency of boundary condition can be realized.

Figure 5.29 shows the minimum depth of TC if the surface temperature is not to be influenced. In these cases, different levels of constant heat fluxes are applied on the top surface. It is clear that for a fixed hole radius the minimum depth increases with the increase of heat flux, and that the relationship is linear. This is reasonable because the higher flux represents a stronger cooling capacity, and the more the plate portion is cooled down the less heat will be transferred to the TC location and to the surface.

As can be seen, the minimum depth increases as the hole radius increases; and the curves for different hole radii are nearly parallel, which indicates that the correlation between the minimum depth and the radius is also linear. The following equation presents the bilinear correlations:

$$h = 0.081 + 1.642 \times R + 0.245 \times q + 0.087 \times R \times q \quad (5.6)$$

where  $h$  is the minimum depth in mm,  $R$  is the hole radius in mm and  $q$  is the applied heat flux in  $\text{MW/m}^2$ . This correlation may be used for the cooling process in which the heat flux does change with time or does not rely on the interaction between the coolant and the cooled surface.

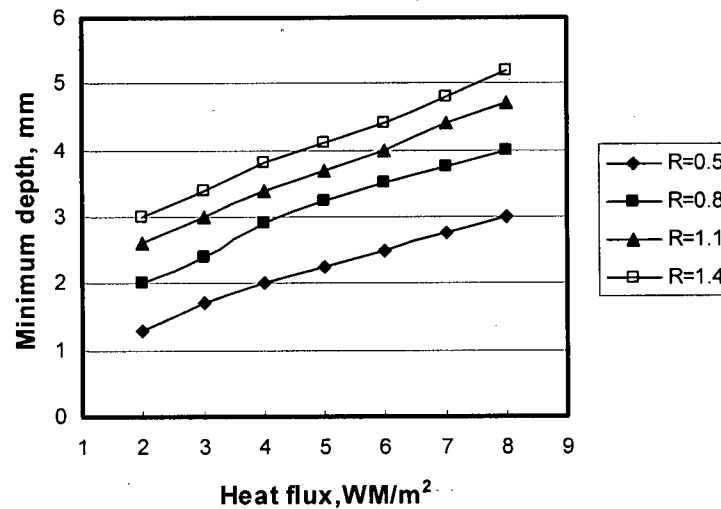


Figure 5.29 Minimum depth of TC for ideal cooling

The heat flux changes with the locations and times for the practical water cooling process. The minimum depth is rechecked with the heat flux input shown in Figure 5.27, and the resulting data is presented in Table 5.3 and Figure 5.30. It is clear that the minimum depth greatly depends on the allowable deviation of the disturbed temperature from the undisturbed one.

Table 5.3 Minimum depth for practical water cooling

	R=0.5	R=0.8	R=1.1	R=1.4
0.92%	1.02	2.68	3.69	4.31
0.73%	1.35	3.04	4.02	4.65
0.55%	1.93	3.52	4.35	5.04
0.37%	2.60	4.12	4.95	5.53
0.19%	3.55	5.12	5.83	6.44

If a surface temperature of 1% lower than the undisturbed one is acceptable, the minimum depth is already up to 2.68 mm for a hole of 0.8 mm in radius. For this depth the detection sensitivity is around 1.3% for a fluctuation of 10 Hz. From the view point of the suppression effect, any value of depth greater than 2 mm is not acceptable. For a hole of 0.5 mm in radius the corresponding values are 1.02 mm of minimum depth of TC and 19% of detection sensitivity for a fluctuation of 10 Hz or 5% of detection sensitivity for a fluctuation of 34 Hz.

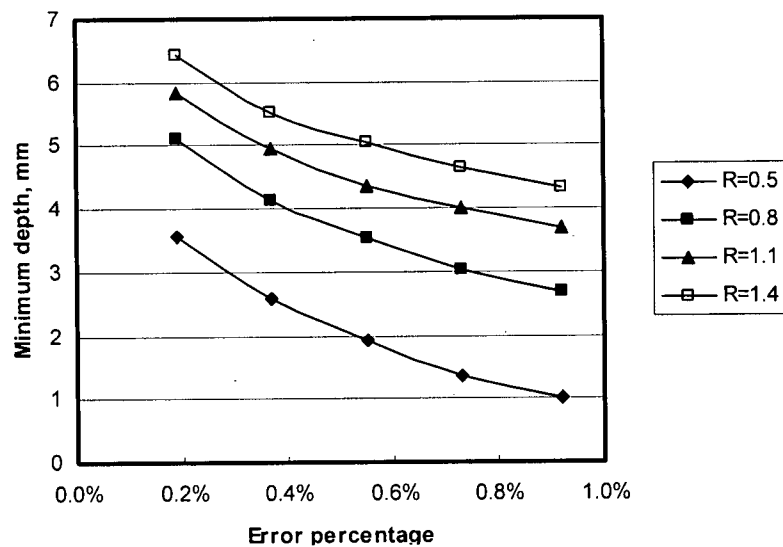


Figure 5.30 Minimum depth of TC for practical water cooling

It can be concluded from the above discussion that one blind hole of 1 mm in diameter ( $R=0.5$  mm) and 1 mm distance from the cooled surface is the best choice. However, there may be some difficulty in the machining operation for the hole and the installation manipulation of TC in this hole.

#### 5.4.4 Effective TC depth

The “null-calorimeter” technique is examined through extensive simulations and comparisons, and the results are shown in Figure 5.31 for the ideal cooling conditions. The curves reveal that the “null-calorimeter” does exist for the carbon steel; i.e. the disturbed internal temperature at the TC tip will be very close to the undisturbed surface temperature if the ratio of the hole radius to the TC depth is properly determined.

The important discrepancy from the conclusions for light metals in the reference [54], though, is that the ratio is not a constant, and depends on both the TC depth and the applied heat flux. This ratio increases with the TC depth for any constant applied heat flux. This means that a relatively thinner remaining disk (referring to the material above TC) is needed for a higher TC depth. By contrast, the ratio decreases with the applied heat flux for any fixed TC depth, which implies that a relative thicker remaining disk makes the null-calorimeter for a stronger cooling capacity. These tendencies are fairly reasonable from the view point of thermodynamics.

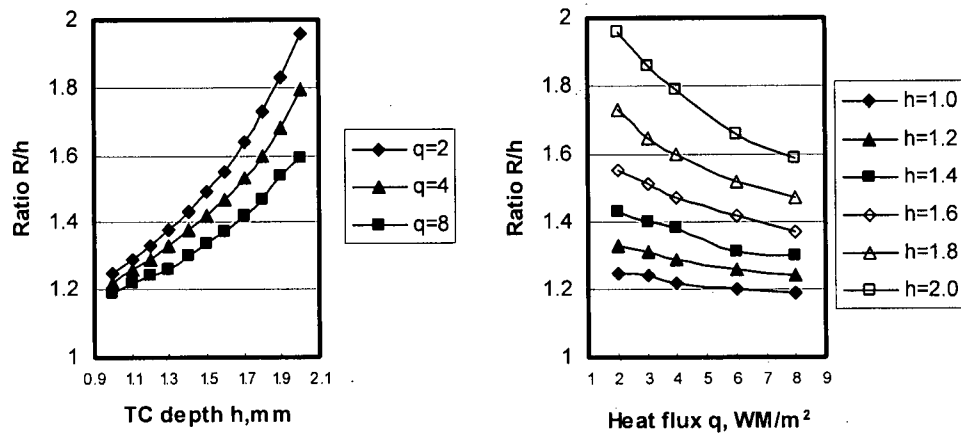


Figure 5.31 Null-calorimeter techniques for carbon steel

Another important difference may be found in the ratio values. For the cases studied, the ratio  $R/h$  is greater than 1.2, and not fixed at 1.1 as for the light metals reported. The

rationale behind this phenomenon may lie in the fact that the conductivity and the specific heat of light metals are much higher than those of carbon steel, although there may be a variety of reasons for it.

It may be inferred from these results that the “null-calorimeter” technique is fairly difficult to apply to the carbon steel, even in the case of the ideal water cooling conditions. Also, studies using practical cooling conditions are skipped.

It is desired that the hole effect can be considered to attain a higher accurate solution in inverse analysis. The direct choice is to include the hole in the calculation model. However, this approach will generally make the analysis being a three-dimensional one. Here, the “null-calorimeter” idea is extended to define an “effective depth”. The undisturbed temperature at this depth is equal to or closely follows the temperature measured at the TC tip. It is obvious that the effective depth should be less than the actual TC depth.

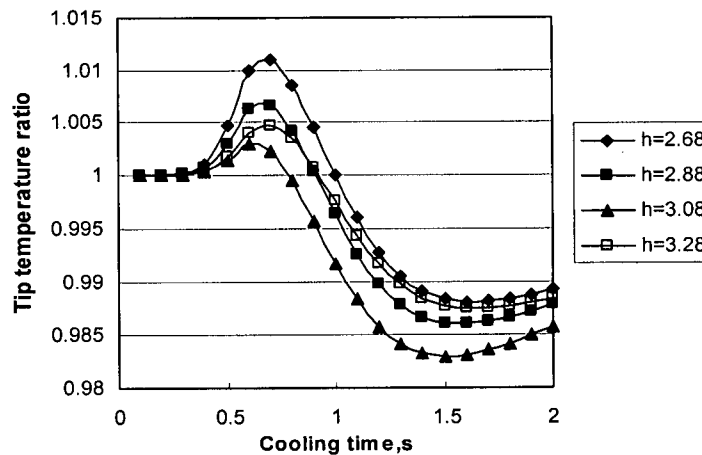


Figure 5.32 Coincidence of temperature for practical cooling

The studies in this part focus on one case in which the hole is 0.8 mm in radius and the actual TC depth is larger than the minimum depth, and the practical heat flux is applied. The results are shown in Figure 5.32. Figure 5.32 shows the ratio of the undisturbed temperature at a few depths to the measured one at the TC tip for four different actual depths for the practical cooling condition. It is readily concluded that the temperature histories coincide very well in all cases, and that the difference tends to be smaller when the depth increases. It seems likely that such an effective depth does exist for each case,

and the two temperatures can be identical at the engineering level for the whole cooling period.

The relationship between the actual depth  $h_{act}$  and effective depth  $h_{eff}$  is shown in Figure 5.33. The data signify that a linear correlation may probably exist and can be expressed with a correlation coefficient of 0.994 in

$$h_{eff} = 1.08h_{act} - 0.752 \quad (5.7)$$

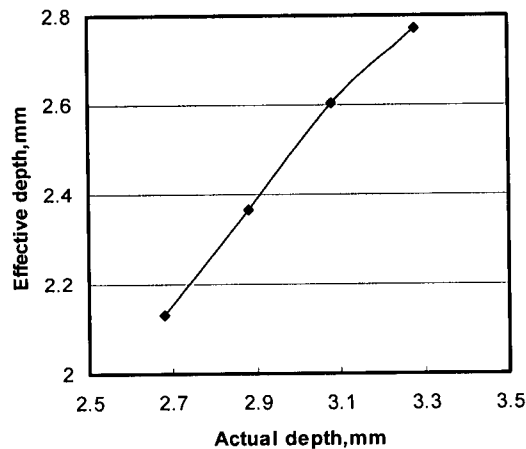


Figure 5.33 Effective and actual depth of TC

#### 5.4.5 Section summary

The appropriate distance  $l$  between TCs and the TC depth  $h$  are first investigated using direct FE analysis. It is concluded that the distance  $l$  should be less than 8–10 mm to attain a real 2D inverse calculation and to improve the stability of inverse calculation, and that the ratio of TC depth to the hole radius should be larger than a minimum value to attain a nearly undisturbed surface temperature.

The “null-calorimeter” technique is then examined. It is found that this technique is fairly difficult to use for the carbon steel, even in the case of the ideal water cooling conditions. The effective depth concept is suggested through intensive numerical simulations, and a linear correlation is found between the actual TC depth and the effective TC depth. Correlations for the minimum TC depth and the effective depth are provided.

## 5.5 Conclusions

The reliability of TCs with a separation measuring junction in the temperature measurement of water jet cooling has been extensively investigated using FE analyses. Two kinds of situations have been considered: one for a simultaneous cooling of two wires of TCs in the impingement zone; the other for a sequential cooling of two wires of TCs in the parallel zone. It is found that the conduction of surface TC wires in a water jet cooling process has a significant effect on the measured temperature, and that the un-simultaneous cooling of the two wires of the internal TCs produces pronounced effects.

The disturbance of the temperature field due to the introduction of a small hole for the installation of an internal TC has also been studied, which shows similar but less pronounced effects on the surface measurement. An increased distortion of the temperature field is evident when TC is attached on the top surface directly above the bottom surface of the hole. It is concluded that TCs should not, generally, be installed on the surface and TCs with a separation measuring junction should not be used in the temperature measurement of water-cooling in moving cases, i.e., when the water moves or the plate is not stationary or both.

When the measured internal temperatures are used for inverse calculations by the FZM, the horizontal distance of TCs should be less than 10 mm for a real 2D problem. Also, there is a minimum depth for an embedded TC at which the surface temperature may not be disturbed by the inclusion of a hole for the embedded TC, and thus the cooling behaviour may not be affected. The proposed "effective depth approach" may be a possible method to include the hole effect in the inverse calculations of heat flux without the hole in the model.

## Chapter 6

### HEAT TRANSFER BEHAVIOR UNDER A CIRCULAR WATER JET

In this chapter, the flux zoning method (FZM), the flux marching method (FMM) as well as the effective depth approach (EDA) are used to determine the heat fluxes and surface temperatures of stationary and moving plates cooled by a circular water jet in an industry scale test facility. A detailed analysis of the results reveals the complex nature of the cooling process and provides appropriate procedure and certain numerical bases for the simulation of the problem [62].

#### 6.1 Experimental Tests

The heat transfer in water jet impingement is a complex phenomenon that depends on many factors, such as water temperature, plate surface temperature, jet velocity, as well as the physical properties of both the water and the plate. It is generally believed that on the top surface, various cooling modes, such as film boiling, transition boiling, nucleate boiling and single convective heat transfer, may occur simultaneously.

In our experimental tests, the effects of steel grade, water temperature, water flow rate, and moving speed on the heat transfer modes have been investigated using the facility described in Section 2.1.3. In all tests carried out, only one nozzle is used.

##### 6.1.1 Tests using stationary plates

For the tests using stationary plates, the test plates are heated in the furnace to the predetermined temperatures, discharged from the heating furnace, and transferred to the test position. The nozzle is closed before the test plates are positioned at the predetermined location where the water hits the centre of the test plates.

The cooling water is then turned on and impinged onto the plate's surface. The cooling times to room temperature varies greatly for different water temperatures. During the whole cooling process, the water flow rate and water temperature are maintained constant.

The configuration of TCs shown in Figure 2.6 is used. The plate's temperatures at all measurement points are recorded with a rate of 100 Hz during the whole cooling period. Note that the initial plate temperatures are the ones measured at the very instant when the plates are pulled out from the heating furnace. The time for translating and setting up the plate from the heating furnace to the predetermined position is normally not constant, so the plate's starting cooling temperature may be slightly different even if the initial temperature is the same.

Twenty-seven tests are selected from the more than thirty tests conducted using stationary plates. They are numbered and listed with their corresponding parameters in Table 6.1. The hydrodynamic parameters at the stagnation point, such as the jet velocity and the water saturation temperature for these tests, are listed in Table 6.2. They are calculated with the equations presented in Section 2.1.1.

Table 6.1 Experimental tests using stationary plates

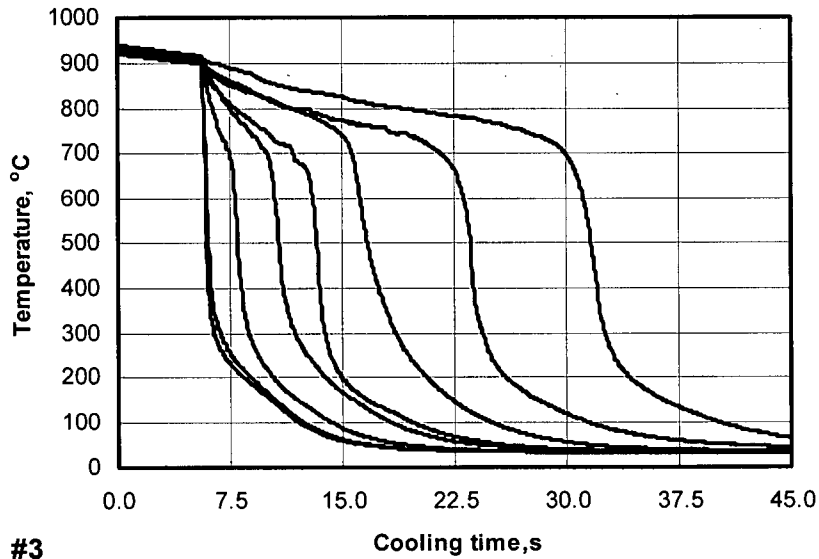
Steel	Water temperature, $T_w, ^\circ\text{C}$	Water flow rate, $Q_w, \text{l/min}$		
		15	30	45
DQSK	30	#1	#2, #3	#4
	40	#5	#6	#7
	50	#8	#9	#10
	60	#11	#12	
	70	#13, #14	#15	#16
	80	#17	#18	#19
SS316	30	#20, #21	#22, #23	#24
	50	#25	#26	#27

Table 6.2 Hydrodynamic parameters at the stagnation point

No.	$Q_w, \text{l/min}$	$D_n, \text{mm}$	$V_n, \text{m/s}$	$D_j, \text{mm}$	$V_j, \text{m/s}$	$P_s, \text{Pa}$	$T_{\text{sat}}, ^\circ\text{C}$
1	15	19	0.88	7.6	5.49	116,389	103.6
2	30	19	1.76	10.6	5.70	117,556	103.9
3	45	19	2.64	12.6	6.03	119,502	104.4

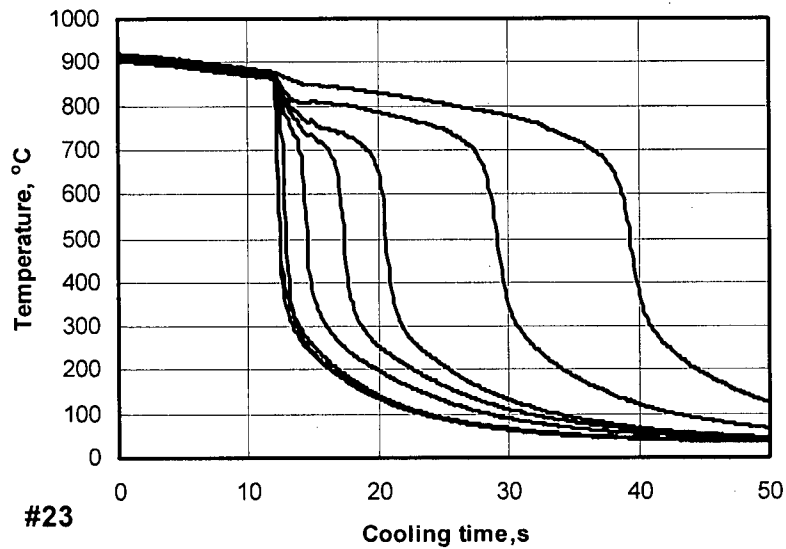
In addition to Figure 4.2, Figure 6.1 and Figure 6.2 show another two examples of typical measured internal temperature profiles using stationary plates (the measured temperatures

refer only to the internal ones in the following sections). The cooling conditions for these two tests are almost identical, but the steel grade is different.



#3

Figure 6.1 Example A of measured temperatures  
 From left to right:  $T_1$  to  $T_8$   
 DQSK;  $Q_w = 30$  l/min;  $T_w = 30$  °C;  $D_n = 19$  mm



#23

Figure 6.2 Example B of measured temperatures  
 From left to right:  $T_1$  to  $T_8$  ( $T_1$  and  $T_2$  are overlapped)  
 SS316;  $Q_w = 30$  l/min;  $T_w = 30$  °C;  $D_n = 19$  mm

Note that the curves from left to right present the temperatures at locations TC1 to TC8. Also, the data shown in the figures and used in the inverse calculations is smoothed and filtered by using the running filtration approach stated in Section 5.1. Careful checks and comparisons show that all the features of the actual cooling curves are retained in the smoothed profiles and that the peak temperature gradients are not affected. This smoothing technique is also used to filter out the noises in the measured temperatures using moving plates.

It is proven that the random errors in the internal temperatures are reduced to  $\pm 1$  °C after the filtration operations. That implies that the inversely calculated heat fluxes and surface temperatures have an accuracy of 90% according to the numerical test results presented in Chapter 3.

It is clear that the cooling curves of the temperatures at locations TC1 and TC2 are almost identical for the whole cooling time for all tests using stationary plates. From a thermodynamical viewpoint, these two locations fall within the boundaries of the impingement zone.

It is apparent from the two figures that, at the air-cooling stage, the plate temperature is fairly uniform, and it decreases gradually and almost linearly due to radiation and air convection heat transfer. As soon as the water impinges onto the plate, the temperatures at locations TC1 and TC2 have an immediate and remarkable drop, and then the gradient decreases from a temperature of around 300–400 °C. With the spreading of cooling water on the plate surface, the temperatures at locations TC3–TC8 begin to decrease. Although the starting temperatures of the quick drop at those locations outside of the impingement zone becomes smaller with the increased distance from the stagnation point, the temperature curves at those locations also change their slopes to much smaller values when the temperature reaches about 300–400°C.

### **6.1.2 Tests using moving plates**

The tests using stationary plates are supplemented with initial tests using moving plates. After the plate is heated to the desired initial temperature, it is discharged from the furnace and accelerated to the nominal test speed at which the plate passes through the cooling section. A specially designed mechanism realizes the plate's movement.

A single-pass test is a more conservative test in which the plate is simply brought to a stop after leaving the cooling section. However, a multiple-pass test has been proven possible for moderate speeds, and permits a significant improvement of test efficiency. In the multiple-pass case, the plate is quickly decelerated after leaving the cooling section, and then quickly accelerated in the reverse direction to the nominal test speed. The plate enters the cooling section again with a lower initial temperature. This procedure can be repeated until the plate is cooled to the water temperature. Note that the nozzle is always open when the plate passes the cooling section.

The combined deceleration and acceleration period outside the water-cooling section can be designed such that a sufficiently homogeneous temperature distribution throughout the plate can be re-established; i.e., the surface chilling is eliminated by the heat conduction from the plate's hot center. The plate's moving speed is around 0.3 m/s and 1.0 m/s in these initial moving plate tests.

The test plates are also instrumented with up to 16 internal intrinsic TCs, which are positioned about 1 mm below the plate surface at different locations across the plate. An example of an employed configuration with 8 TCs is shown in Figure 6.3.

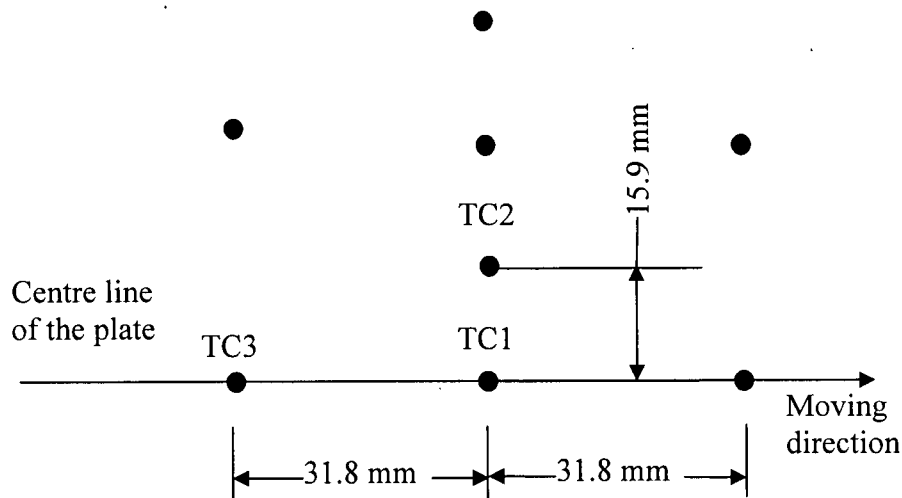


Figure 6.3 Example of TC arrangements for moving plates

Figure 6.4 shows an example of temperature profiles measured at the central location TC1 in the moving plate tests. Figure 6.5 is an enlarged portion showing the temperature recovery. It is clear that the initial temperature (cooling start temperature) at the current

cooling pass is equal to or slightly higher than the recovered temperature at the prior pass, and that the temperature between two passes is fairly constant for the period, showing a full recovery to uniform temperature distribution through thickness.

Note that the temperatures at locations TC2–TC4 are almost identical, which is important for the modelling to estimate the heat flux and surface temperature.

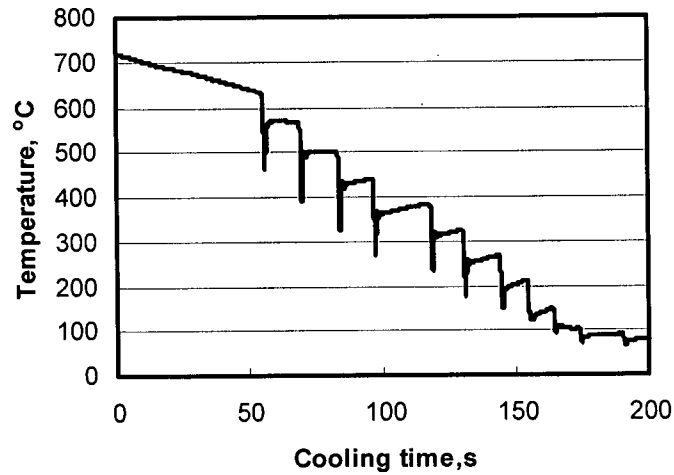


Figure 6.4 Example of measured temperatures in moving plate tests  
DQSK;  $Q_w = 30$  l/min;  $T_w = 30$  °C;  $D_n = 19$  mm;  $V_p = 0.3$  m/s

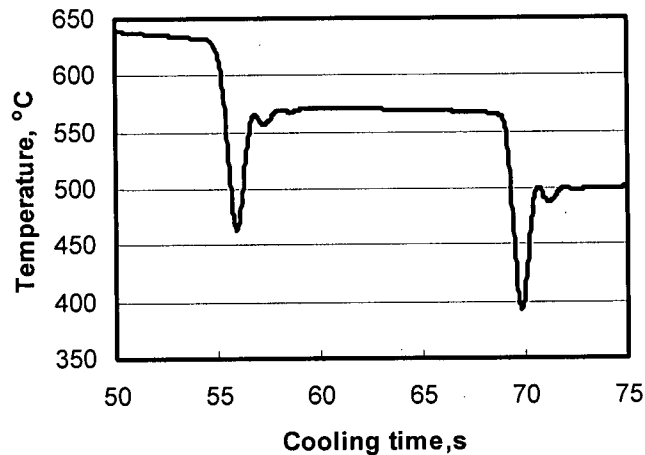


Figure 6.5 An enlarged portion of Figure 6.4

## 6.2 Validation and Application of the EDA

In this section, the EDA is checked for its suitability with 18 tests. The analyses are confined to the stagnation point. In the calculations, sincere efforts have been made to match the maximum heat fluxes using the 1D model with the EDA with those using the 2D model (Section 6.3), by adjusting the effective depth.

The results are shown in Table 6.3 and Figures 6.6, 6.7 and 6.8. In Table 6.3, the heat flux is the maximum heat flux for the entire cooling period, and the temperature is the one corresponding to the maximum heat flux. In addition, the notations “1DwEDA” and “1DwtEDA” mean the results from the models with the EDA and without the EDA, respectively. These two notations are also used in the relevant figures. It may be seen that it is possible to find an effective depth at which the maximum heat fluxes as well as the temperatures are very close to each other. It is also clear that the maximum heat flux and the temperature from the 1D model, without considering the hole effect, will be different from those from 2D: higher maximum heat fluxes and lower temperatures.

Table 6.3 Comparison of results using different approaches

Test	2D		1DwEDA		1DwtEDA	
	Flux, MW/m <sup>2</sup>	Temp, °C	Flux, MW/m <sup>2</sup>	Temp, °C	Flux, MW/m <sup>2</sup>	Temp, °C
#1	17.0	170.50	17.6	168.51	23.4	-4.98
#2	20.1	-58.21	20.3	-60.63	27.3	-245.53
#3	20.0	170.99	20.6	175.42	28.3	-41.67
#4	14.2	280.19	14.4	308.51	19.5	126.61
#5	11.9	351.16	12.1	385.85	16.9	225.08
#6	10.0	412.34	10.1	436.00	13.6	297.11
#7	11.5	267.93	12.0	286.16	16.0	280.14
#8	13.4	256.87	13.8	304.57	19.6	201.13
#9	10.4	403.89	10.7	429.79	14.5	286.00
#10	12.8	177.45	12.5	214.75	16.6	66.11
#20	12.0	346.79	12.2	428.11	18.6	229.62
#21	14.4	365.43	14.0	371.43	23.1	110.39
#22	13.0	361.72	13.4	424.46	19.9	230.86
#23	11.3	252.86	13.4	403.99	22.4	152.66
#24	11.4	450.13	11.5	441.04	22.3	127.91
#25	9.7	455.91	10.0	364.58	15.7	347.55
#26	12.6	399.06	12.4	400.42	20.1	162.60
#27	13.1	350.40	13.4	350.77	19.8	223.77

Figures 6.6 and 6.7 show the examples in which the boiling curves from 2D and 1D models with the EDA are nearly identical during the entire cooling period. It can be suggested from this result that the EDA is an appropriate option for considering the hole effect without including the hole in the model.

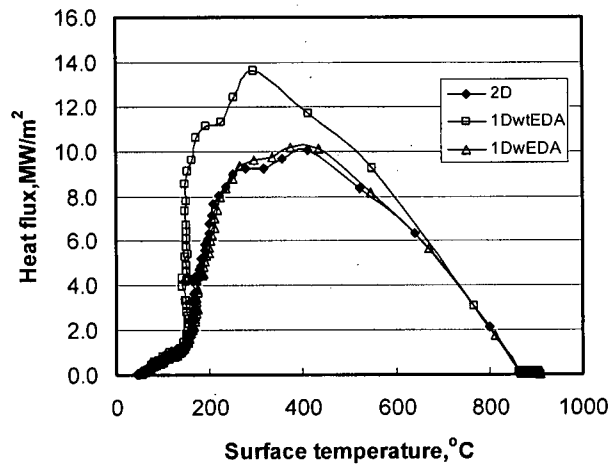


Figure 6.6 Boiling curves using different modellings for test #6

The two figures also show that the boiling curves from 1D without the EDA are above those from 2D modelling, indicating that the heat fluxes from 1D without the EDA are generally larger than those from 2D. However, the boiling curves from 1D without the EDA still reflect all the features of heat transfer modes like those from 2D modelling, and do not produce erroneous heat transfer phenomena. The latter is informative.

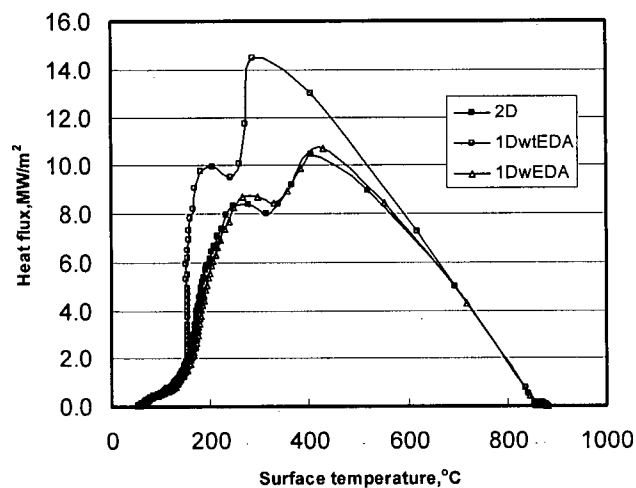


Figure 6.7 Boiling curves using different modellings for test #9

These two examples suggest that the EDA may be considered as another option to account for the hole effect. However, several difficulties arise when applying the EDA in the extensive investigations of the experimental tests. First, it is in some cases difficult to find an effective depth, and the inverse calculation results are very sensitive to the value of the effective depth. Figure 6.8 shows one example for this situation. For this test, the boiling curve from 1D analysis without the EDA is still above that from 2D modelling, and the peak value of the heat flux from 1D without the EDA nearly doubles that from 2D modelling. This result is consistent with the above two cases. However, whatever the effective depth value, the boiling curves from 1D with the EDA are not close to that from 2D modelling. Note that the difference between two adjacent values is only 0.07 mm for the four trial effective depths. With this small variation in the depth value, the difference in the maximum heat flux is about 7–10%, showing the high sensitivity of the calculated heat flux to the effective depth. This unsuitability and sensitivity of the EDA occurs for both the carbon steel and the stainless steel.

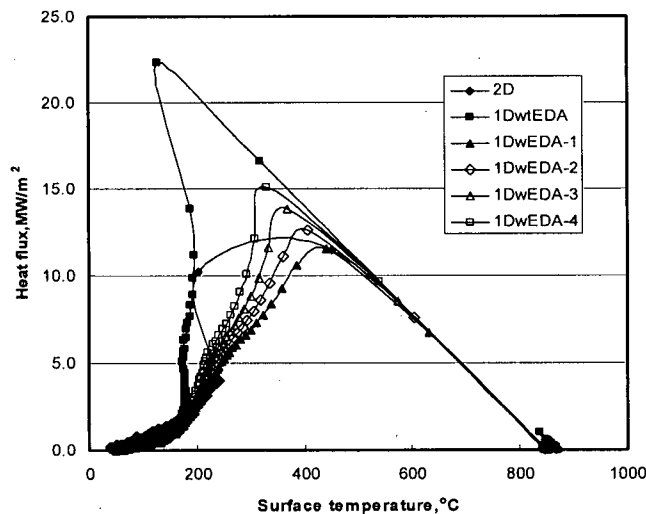


Figure 6.8 Sensitivity of results to the effective depth, #24

The second difficulty is that the correlation shown in equation (5.7) is not valid for all real cooling tests; i.e., there is no general valid correlation between the actual depth and the effective depth at which the maximum heat flux is close to that from 2D, irrespective of the difference in the boiling curve shape. Figure 6.9 shows that the effective depth hardly relates to the actual depth with a fixed relationship. However, it is apparent that the effective depth is on average about 40% less than the actual depth.

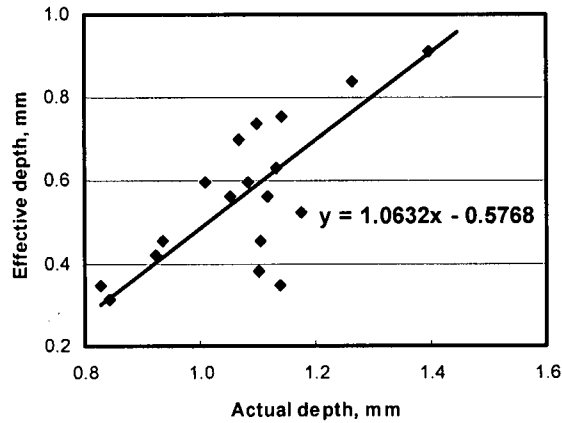


Figure 6.9 Relationship between the actual depth and effective depth

Even for the stagnation point, to finding an appropriate effective depth takes much effort and time because the value changes from case to case. It is possible that the effective depth depends on both the actual depth and the cooling parameters. It may be impractical to find such a correlation.

The last difficulty is a conflicting one. The intention of developing the EDA is to take the hole effect into account without including the hole in the model, especially for the holes outside the impingement zone. In this regard, the calculation conditions should be close to those outside the impingement zone. However, it is not possible to realize such calculations from the numerical simulation side. In fact, the actual cooling conditions outside the impingement zone are unknown and are to be determined. Therefore, no appropriate boundary conditions can be used in the direct simulations. Second, the correlation between the actual depth and the effective depth obtained from the simulations at the stagnation point, if the correlation could be obtained, may not be suitable to the points in the parallel zone.

From the above discussion, it may be concluded that the proposed EDA in Section 5.4.4 may not be an effective and general approach used in the water jet cooling process. However, an alternative approach can be obtained from the above studies on the EDA. In this alternative approach, the used depth for the TC location is 30% less than the actual depth in the inverse calculations. The value of 30% is conservative and is based on the data in Figure 2.9. Although this reduction of the TC depth may not have a strong basis

and may not create an accurate account of the hole effect, it will definitely reduce the deviation of the calculated boiling curves from the true one.

This approach is nevertheless still called an effective depth approach (EDA).

The application of the modified EDA is illustrated by the following example. In this example, the results from the FZM with and without the EDA are compared. An overall view of the heat fluxes on the top surface of a stationary stainless steel plate is obtained first using the FZM without the EDA, as shown in Figure 6.10. In this calculation, a full 2D axisymmetrical FE model has been used. The model has 115 mm radius and 7 mm thickness. The model has 2430 quadratic elements. The elements are uniform in the radial direction and vary from fine on the top surface to coarse on the bottom surface in the thickness direction. In the calculation, the right hand surface, i.e., the outside of the cylindrical disc, is assumed thermally insulated, and a constant heat flux equivalent to air cooling is applied to the bottom surface. A constant average conductivity value of 20 W/m·°C is used, and phase transformation heat is not considered.

The FZM is used in which the top surface is divided into eight sub-regions; each sub-region is symmetric with respect to the location of the corresponding TC. The heat fluxes for all nodes in each individual sub-region are assumed to have the same value; i.e., there are only eight heat fluxes corresponding to the eight measurement locations. The actual values of heat fluxes at the eight points corresponding to measurements of temperatures are determined using inverse analysis. Only the data at the current time step is used, the regularization parameter is fixed at 1e-10, and only several iterations are required to get convergent results for each time step.

The results in Figure 6.10 reveal all the features of its corresponding temperature curves. Note that the heat fluxes at all locations have relatively close values of about 14 KW/m<sup>2</sup> for the air cooling stage, which is typical due to the combination of radiation and air convection cooling.

As the water hits the plate, the heat fluxes at locations 1 and 2 instantaneously jump to very high values. The flux profiles at these two locations are almost identical in shape with a slight difference in the peak values for all performed tests and times; the peak value of the heat flux at the second location is generally higher than that at the stagnation point. This is a point to be further studied. The difference in peak heat fluxes may come

from the slight difference in the measured temperatures, which ascertains the sensitivity of the inverse problem. It is also noted that the peak value of the heat flux is generally 50% higher for the stainless steel than that for the carbon steel.

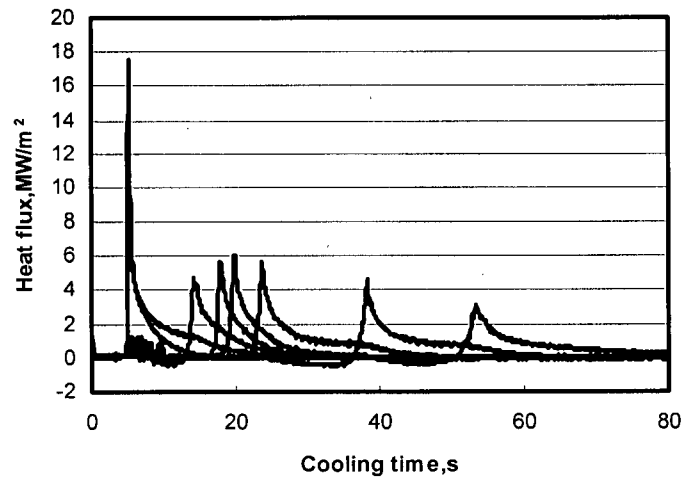


Figure 6.10 Overall view of heat flux on the top surface, Test #25

The heat fluxes at locations 3–8 jump at different time instants proportional to the distance from the stagnation point. The shapes of heat flux profiles are, again, almost identical. The magnitudes of the peak heat fluxes at these locations are much lower than those at locations 1 and 2; the former are 3 times less than the latter.

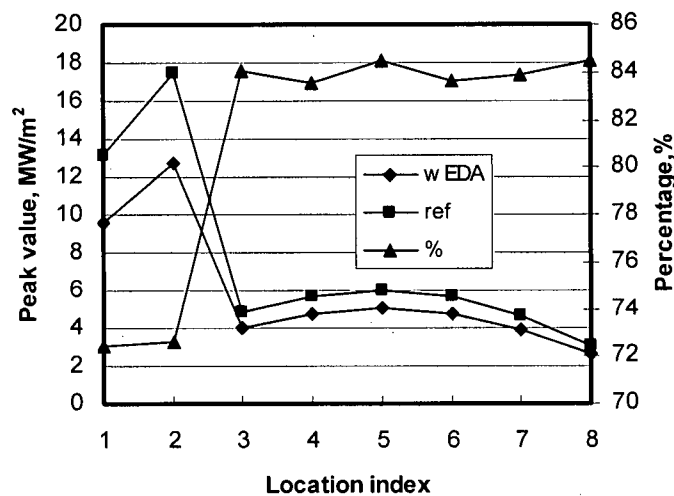


Figure 6.11 Comparison of results with and without EDA, Test #25

The modified EDA is also applied to this test whereas the TC depths in the calculation are 30% less than the actual ones. The results are shown in Figure 6.11. In this figure, the peak values of the heat flux at 8 locations are compared. It is clear that the values with the EDA are lower than those without the EDA. It is interesting to note that the percentages at the first two locations in the impingement zone are around 72% while those in the parallel zone are nearly fixed around 84% irrespective of the individual locations. This discovery may be very informative and may provide means to simplifying the calculations.

For the stagnation point (location 1), the peak value from the modified EDA is  $9.6 \text{ MW/m}^2$  and is very close to those from the 2D hole-model and the actual EDA (Table 6.3). This point shows that the modified EDA may compensate for the hole effect. At the same time, the peak value from the full model is  $13.2 \text{ MW/m}^2$  and is close to those from the 1D model without the EDA. This discovery again reveals that the FZM may not correctly reflect the real heat transfer in the water jet cooling.

### **6.3 Heat Transfer in the Impingement Zone of Stationary Plates [62]**

In this section, the discussion is confined to the heat transfer behaviour in the impingement zone or at the stagnation point because the internal temperature at the stagnation is the most reliable one and is not affected by the water movement. Under this condition, the FZM can be easily applied.

#### **6.3.1 Initial investigations**

Initial investigations are conducted on Test #15. As discussed above, the temperature at locations TC1 and TC2 are nearly identical during the entire cooling period for all tests. So, it can be assumed that both of them are inside the impingement zone. And it is further assumed that the impingement zone extends to the centre between TC2 and TC3; i.e., the radius of the impingement zone is 24 mm. Thus, the ratio of the diameter of the impingement zone to the nozzle diameter is about 2.53.

Two-dimensional axisymmetrical conditions are assumed in the inverse calculations, and the holes are not included in the mesh. The measured temperatures at locations TC1 and TC2 are used. The right-hand surface, i.e., the outside of the cylindrical part, is assumed

to be thermally insulated, and a constant heat flux equivalent to air cooling is applied to the bottom surface. A constant weighted averaged conductivity value of  $35 \text{ W/m}\cdot\text{°C}$  (considering that the critical heat transfer occurs above  $400 \text{ °C}$ ) is used for the whole time span, and phase transformation heat is not considered.

Two cases are studied. In the first case, the top surface is divided into two subregions corresponding to the two measured temperature histories, and two different heat flux components are specified on the subregions. In the second case, the top surface is only one subregion and only one heat flux component is prescribed on the plate's top surface. The second situation means that the unknowns are less than the temperature measurements, and so an overdetermined inverse problem exists, which would be, generally, more stable. In these two cases, different numbers of future time steps are adopted to investigate the effect on stability. The results obtained from this model are shown in Figure 6.12 and 6.13. In the two figures 0F and 3F indicate the heat flux with 0 and 3 future steps.

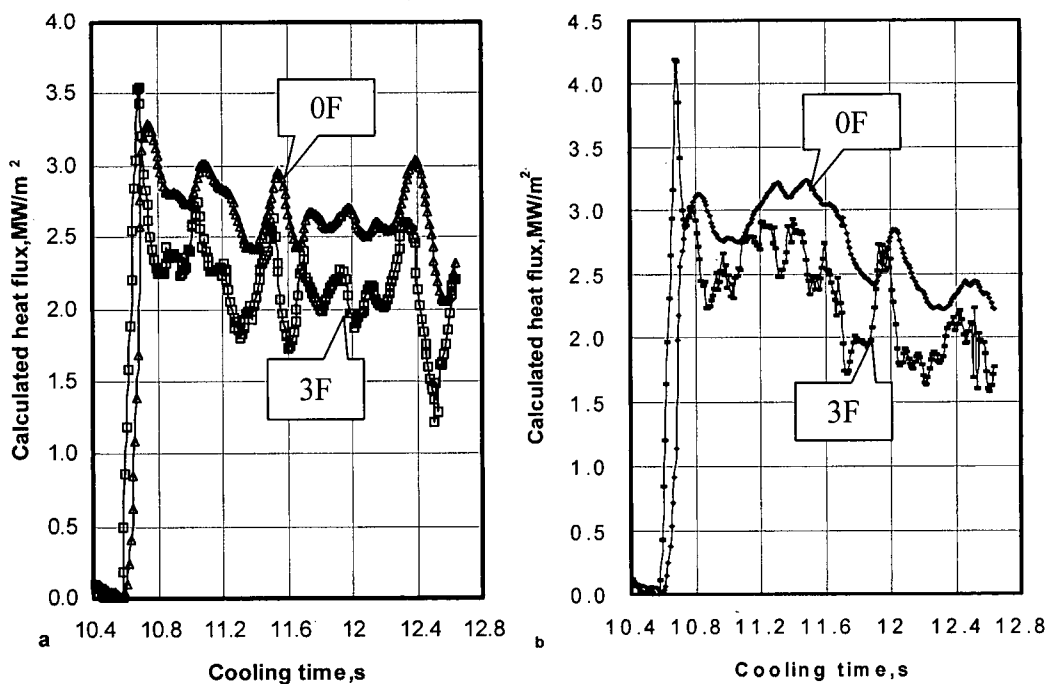


Figure 6.12 Heat flux in the impingement zone  
Two components of heat flux assumed  
a: Component 1; b: Component 2

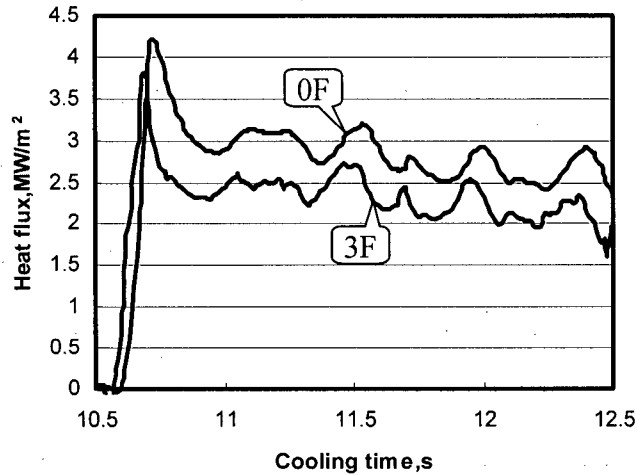


Figure 6.13 Heat flux in the impingement zone  
One heat flux assumed

Figure 6.12 is for the first case and shows the effects of the number of future steps on the inversely calculated heat fluxes in the impingement zone for the instant of impingement and shortly thereafter. There is a sharp jump in the heat flux values at the instant of impingement, followed by a much smaller but sharp decrease to a value that steadily decreases at a slow rate. This indicates that similar cooling conditions exist for a smaller area in the centre of the jet that may be considered as a single cooling zone, the impingement zone. This conclusion may be confirmed by the results shown in Figure 6.13 for the second case.

Analyses also show that there is no considerable difference between the heat fluxes using various numbers of future steps, especially when the number is larger than 3. The insensitivity of these results to the number of future steps may indicate that the random errors in the internal temperatures are filtered out due to the average smoothing technique discussed above.

It can be concluded that the simplified model may be efficiently used to study the heat transfer behaviour in the impingement zone.

### 6.3.2 Heat transfer behaviour

According to the initial investigations, the hole-model shown in Figure 5.7a has been used in this analysis. The radius of the small geometric portion of the plate is fixed at 8 mm, and its height and the hole dimensions correspond to the values at each test. The

temperature dependence of the plate's conductivity is considered. In all calculations, only the data at the current time step is used. The values of the regularization parameters are 10% of the diagonal values of the sensitivity matrices, and the convergence criteria are fixed at 5% and  $\pm 1$  °C.

### 1. Effect of water temperature

Figure 6.14 depicts the calculated surface temperature profiles at different water temperatures at a water flow rate of 15 l/min for the carbon steel. It should be noted that the starting time has been adjusted by shifting to allow the curves to be clearly separated for better comparisons, and that the time interval for two adjacent points on the curves is the same, that is, 0.1 s. It is clear that the surface temperature drops sharply in several time steps to around 300–200 °C as the cooling water of 40 °C or 50 °C impinges onto the plate surface, and that the cooling rate is as high as 2000–2400 °C /s. After this fast dropping stage the cooling process starts to level off. For a water temperature of 60 °C, much more time is needed to cool the surface from around 880 °C to 200 °C, which can be verified by the point density at the higher temperature part of the curves.

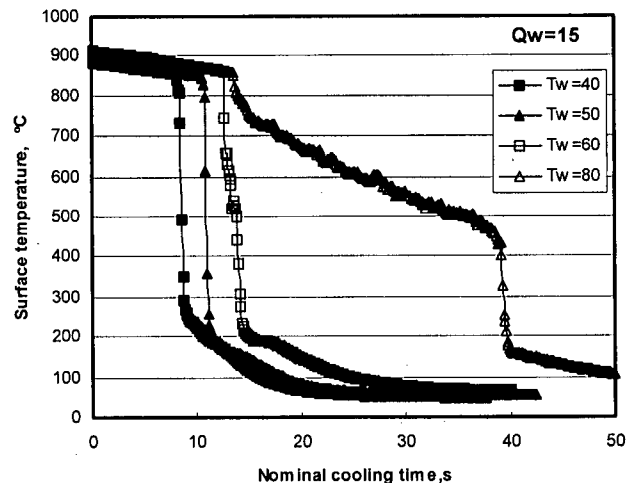


Figure 6.14 Water temperature vs. surface temperature at  $Q_w = 15$  l/min

The cooling curve at a water temperature of 80 °C is quite different from the first two. When the cooling water hits the plate surface there is a fairly long and gentle cooling process, which implies that the cooling capacity is low. As the surface temperature

reaches around 450 °C a faster cooling stage appears, and the surface temperature drops to around 200 °C in several time steps.

The cooling curves at different water levels at a water flow rate of 30 l/min reveals a similar trend, as shown in Figure 6.15.

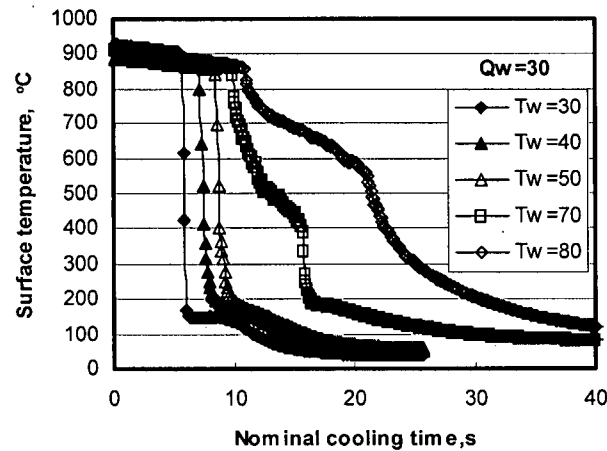


Figure 6.15 Water temperature vs. surface temperature at  $Q_w = 30$  l/min

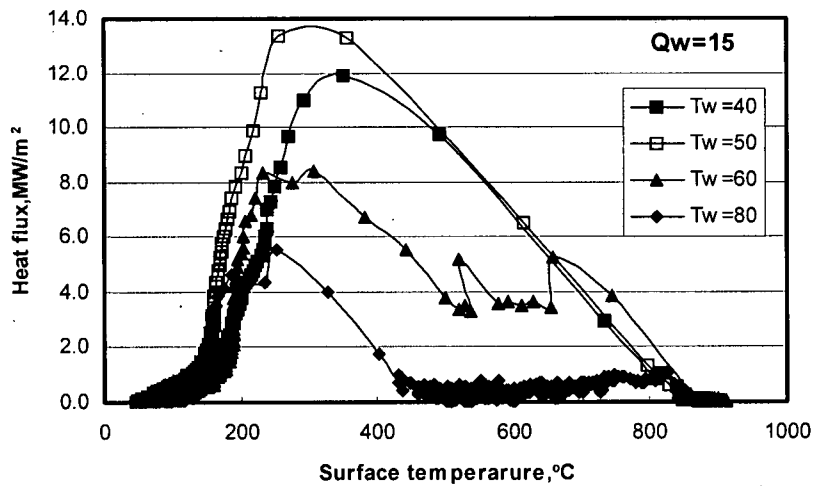


Figure 6.16 Effect of water temperature at  $Q_w = 15$  l/min

Figure 6.16 shows the effect of water temperature on the cooling behaviour at a water flow rate of 15 l/min for the carbon steel. Generally, the heat flux increases by decreasing the water temperature. The highest value is around 14 MW/m<sup>2</sup> for a water temperature of

40 °C and 6 MW/m<sup>2</sup> for a water temperature of 80 °C. It may be concluded that increasing the water temperature significantly reduces the heat extraction from the plate. Water temperature also affects the cooling pattern or thermodynamics. At a lower water temperature (<50°C), the heat flux monotonically increases with the decrease of surface temperature until a value of about 300 °C and then again monotonically decreases with the decrease of surface temperature. This may indicate that there is no film boiling regime at the beginning, and that the heat transfer is due to transition boiling and then it shifts to nucleate boiling. The reason for this phenomenon is the sharp drop of the surface temperature at the beginning and the incapacity to heat the water to the vaporization temperature. It may be concluded that the surface around the stagnation point is immediately wetted by water at lower water temperatures.

In contrast to the situation at lower water temperatures, there is a film boiling regime when the water temperature is higher than 60 °C. When the cooling water of higher temperatures impinges onto the surface, it is easily heated to its boiling temperature and the heat flux is kept at a lower value. The duration of film boiling depends mainly on the water temperatures in the test conditions. From a comparison of the boiling curve for 60 °C water temperature with that for 80 °C, it is clear that the higher the water temperature, the longer the film boiling period and the lower the heat flux for this period.

From the above discussion it may be postulated that the maximum water temperature for immediate wetting is around 60 °C, which is in good agreement with that in reference [16] where such a temperature is 68 °C.

It is worthwhile to point out the difference of the film boiling mode shown in Figure 6.16 from that corresponding to the water pool cooling. For the film boiling in water pool cooling, the heat flux decreases with the decrease of the surface temperature to a minimum heat flux value. This feature was also reported in reference [15] for water jet cooling. In the case shown in Figure 6.16, the heat flux during the film boiling period does not change much, and is kept at nearly a constant value. This trend is more obvious when the water temperature is 80 °C, i.e., the subcooling is around 20 °C.

The temperature at which the heat flux reaches its minimum value and the heat transfer shifts from film boiling to transition one is commonly referred to as the Leidenfrost point.

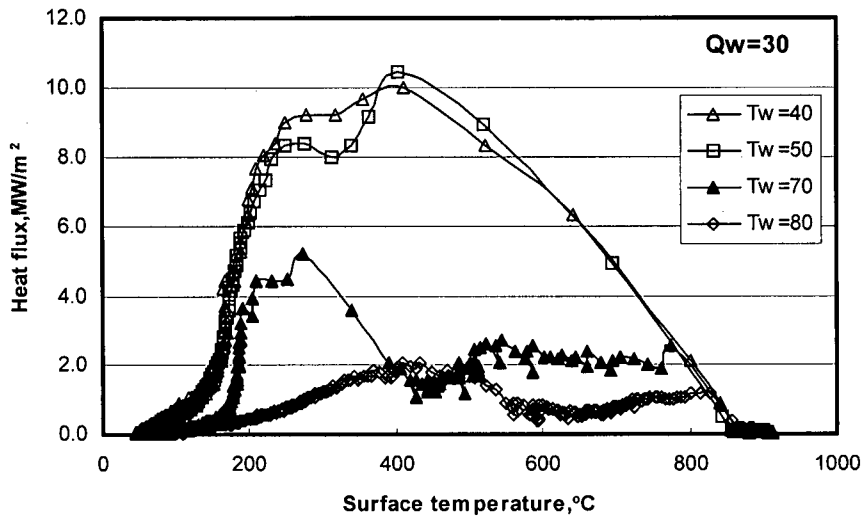


Figure 6.17 Effect of water temperature at  $Q_w = 30$  l/min

According to Figure 6.16, the Leidenfrost point is around 510 °C and 430°C for a water temperature of 60 °C and 80 °C, respectively. Also, the figure indicates that there is a single forced convection regime when the surface temperature is lower than about 150 °C where the slope of the boiling curve changes from a mild one to a sharp one.

Experiments with different flow rates of 30 l/min and 45 l/min have been conducted and the results are shown in Figures 6.17 and 6.18. These figures show trends similar to those discussed above.

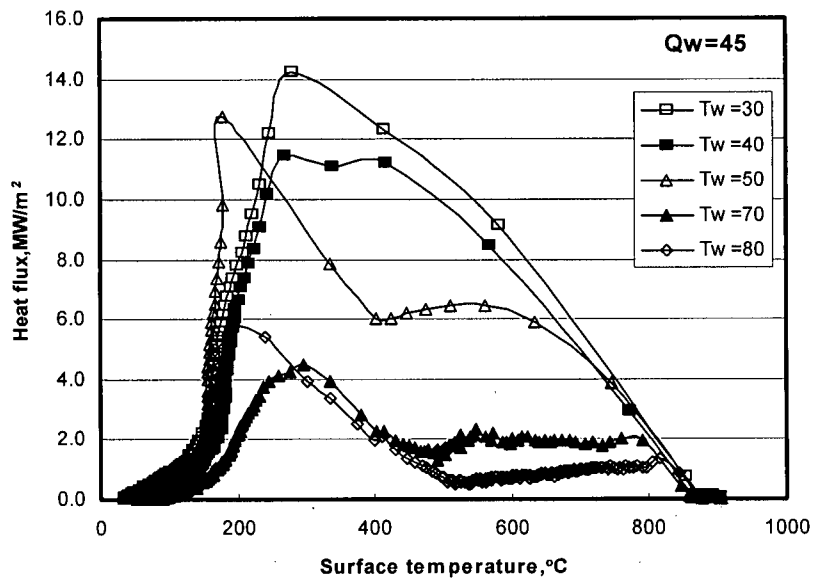


Figure 6.18 Effect of water temperature at  $Q_w = 45$  l/min

## 2. Effect of water flow rate

The impingement velocity is proportional to the water flow rate when the distance of the nozzle exit to the plate and the nozzle diameter are fixed, as in the conditions in this study. Thus, the effect of the impingement velocity can be represented by the effect of the water flow rate, as shown in Figure 6.19 to Figure 6.23.

The figures indicate a somewhat ambiguous phenomenon. The water flow rate has little effect on the heat transfer for all cases in which the water temperatures are 30 °C, 40 °C, 70 °C and 80 °C (Figure 6.19 through Figure 6.22); but it has a noticeable effect when the water temperature is 50 °C (Figure 6.23). This is a characteristic to be carefully checked.

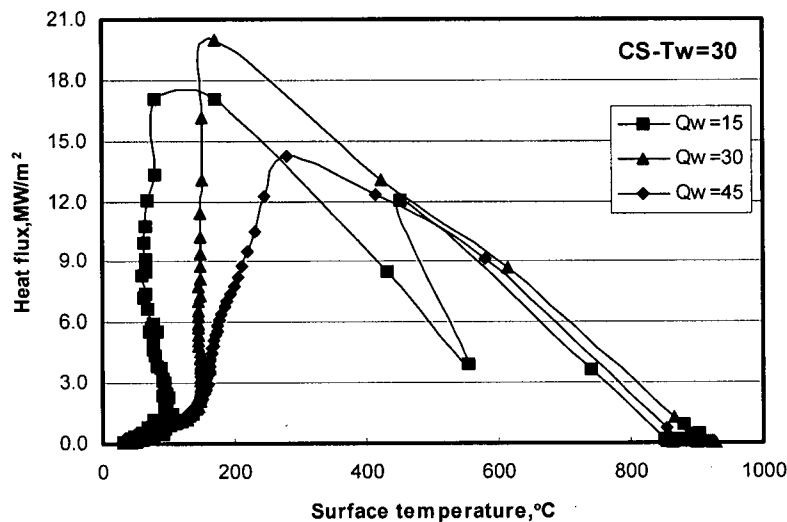


Figure 6.19 Effect of water flow rate at  $T_w = 30$  °C

It may be seen from Figure 6.19 and Figure 6.20 that the heat transfer regimes are, sequentially, transition boiling, nucleate boiling and convective boiling when the surface temperature decreases from 880 °C to the room temperature. There are some differences among the maximum heat flux values and the temperatures at which the maximum heat flux occurs when the water temperature is 30 °C. This difference does not appear when the water temperature is 40 °C.

It may be generally stated that the heat flux should increase with the increase in the jet velocity because a higher velocity increases the pressure as well as the saturation temperature of water at the stagnation point and, therefore, the subcooling increases. In the test conditions presented, when the water flow rate varies from 15 to 45 l/min, i.e., an

increase of 3 folds, the jet velocity increases only from 5.49 to 6.03 m/s, and both pressure and saturation temperature show modest changes. Such small changes should not cause significant changes in the heat flux.

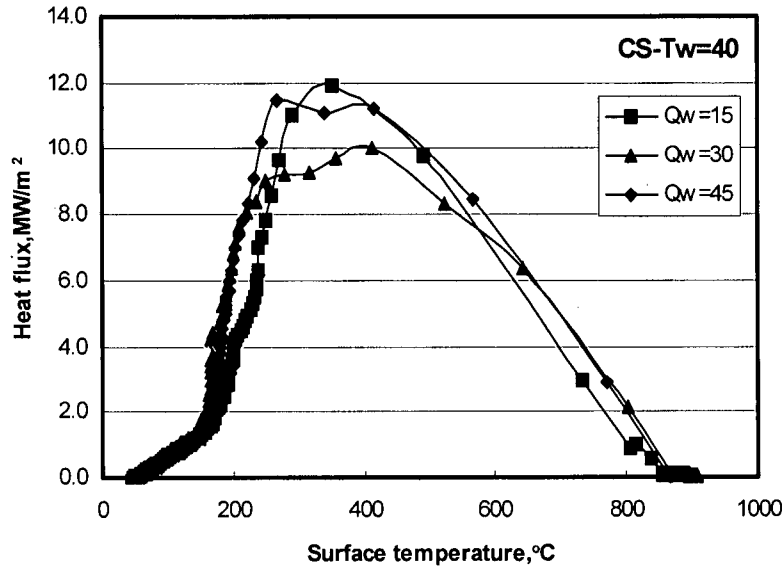


Figure 6.20 Effect of water flow rate at  $T_w = 40\text{ }^\circ\text{C}$

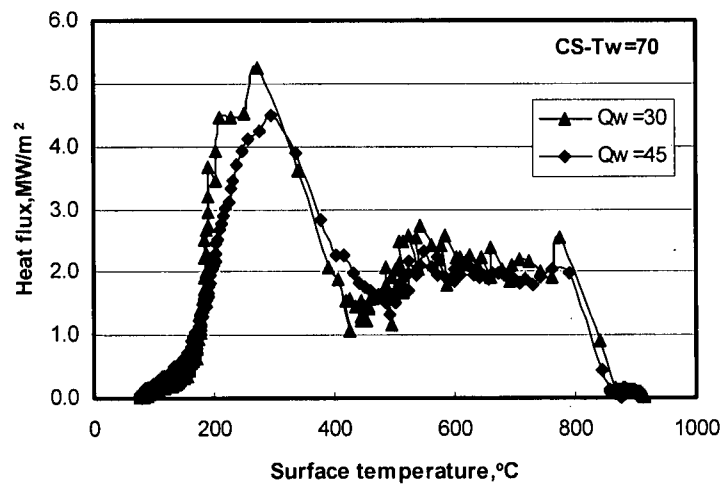


Figure 6.21 Effect of water flow rate at  $T_w = 70\text{ }^\circ\text{C}$

The above discussion may also be applied to the heat flux values at higher water temperatures, as shown in Figure 6.21 and Figure 6.22. The difference among the boiling curves at lower and higher water temperatures lies in the existence of film boiling

regimes. For the film boiling regime, the heat flux decreases slightly with the decline in surface temperature. There is no clear and defined relationship between the Leidenfrost point and the water flow rate at different water temperature levels.

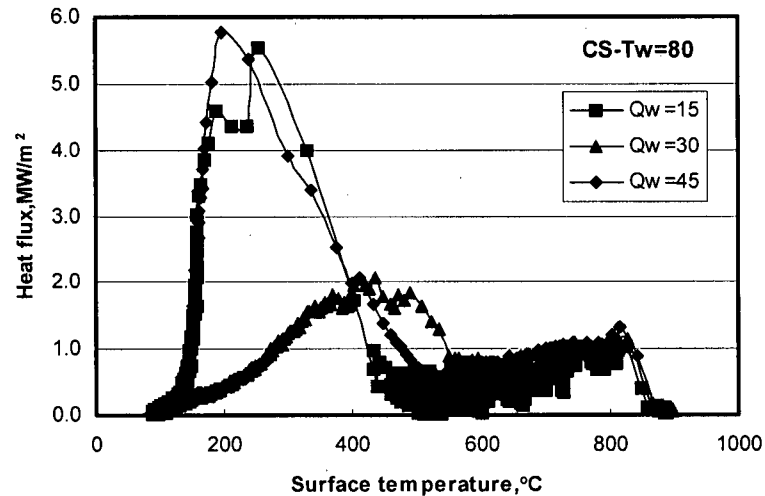


Figure 6.22 Effect of water flow rate at  $T_w = 80\text{ }^\circ\text{C}$

Although the boiling curve for the water flow rate of 30 l/min shows the same combination of the heat transfer modes as those for the water flow rate of 15 l/min or 45 l/min, its magnitude is much less than the values at the corresponding points. Whether this may be attributed to measurement errors or to a complex relationship at the higher temperature is an issue to be explored in future work.

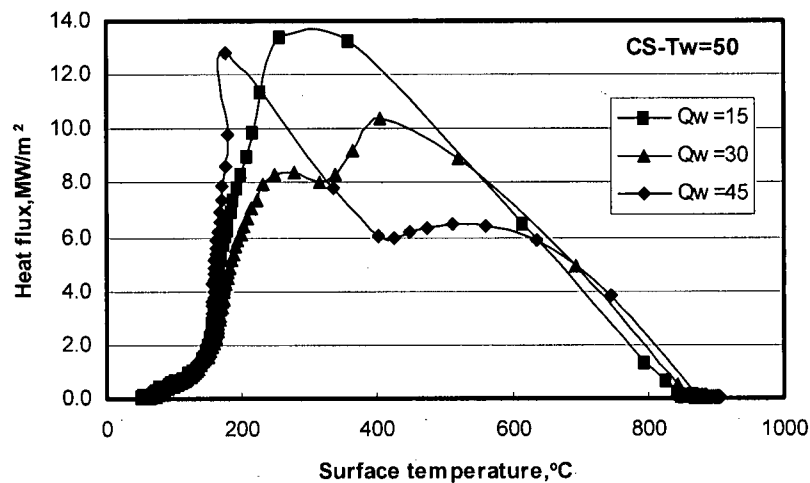


Figure 6.23 Effect of water flow rate at  $T_w = 50\text{ }^\circ\text{C}$

Figure 6.23 shows the boiling curves at the stagnation point for the water temperature of 50 °C at different flow rates for the carbon steel. It is clear that there is no film boiling regime, and that little effect of the water flow rate can be observed at the beginning of the transition boiling region and the later period of the nucleate boiling. The higher effect of the water flow rate occurs when the surface temperature varies from 600 to 200 °C. It is to be noted that this kind of effect is, generally, against the commonly accepted trend; i.e., the increase of the water flow rate does not increase the heat transfer capacity. This is quite abnormal, and further investigation would be needed to verify the phenomenon.

Figure 6.24 clarifies the effect of the water flow rate on the heat transfer behaviour at the water temperature of 50°C for the case of stainless steel SS316. It is clear that the maximum heat flux at the water flow rate of 30 l/min or 45 l/min is higher than that at 15 l/min and that little effect can be seen for the overall cooling process for both flow rates of 30 l/min and 45 l/min.

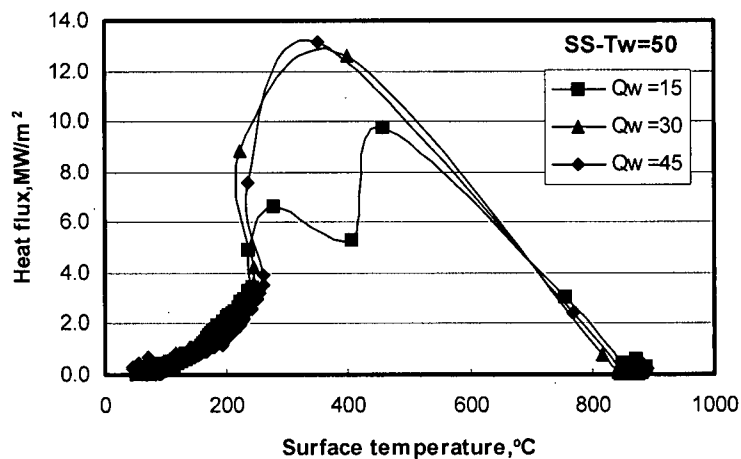


Figure 6.24 Effect of water flow rate at  $T_w = 50$  °C for SS316

From the above discussions it may be concluded that the water flow rate generally has little effect on heat flux magnitude at all water temperature levels or subcooling levels. This may be attributed to the consideration that the large variation of water flow rate has a slight effect on the jet impinging velocity as well as the pressure and the saturation temperature. Also, it should be reported that some discrepancies are evident, and further investigation is needed.

### 3. Effect of steel grade

The effect of steel grade on the heat transfer behaviour is considered by the change in material properties, especially the heat conductivity in this study. Figure 6.25 shows this kind of effect at the water temperature of 30 °C. It can be seen that for two levels of water flow rates, the heat fluxes with SS316 are always smaller than those with the carbon steel DQSK. The DQSK has generally higher conductivity than SS316, and the difference in conductivities increases with the decline in temperature, as shown in Figure 6.26 (refer to equations (2.8) and (2.9)). When the temperature is around 500 °C, the conductivity of DQSK is nearly twice that of SS316. It incites the cooling effect of water on the plate surface and instigates a faster decrease of the temperature at the target location. On the other hand, the heat from the bottom part is also easily transferred to the target location, and this tends to increase the target temperature. To reduce the temperature at the target location to the same value, a higher heat flux may be needed for cooling the material with higher conductivity. This may be the reason why the heat fluxes for the SS316 are always smaller than those for the carbon steel DQSK for the water temperature of 30 °C.

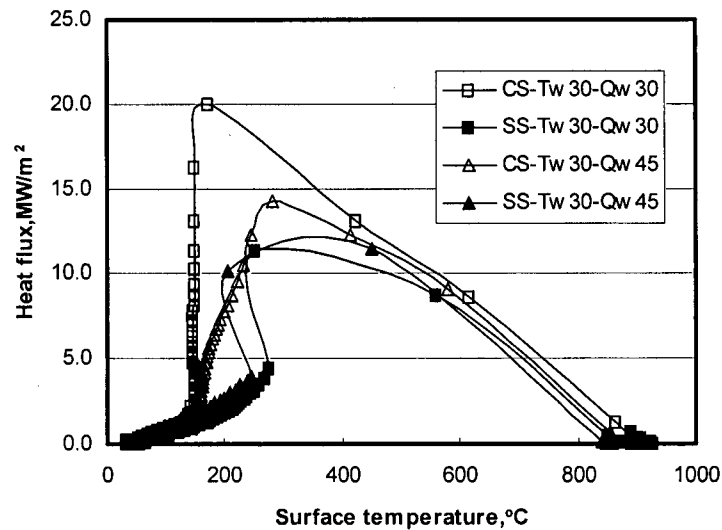


Figure 6.25 Effect of steel grade at  $T_w = 30$  °C

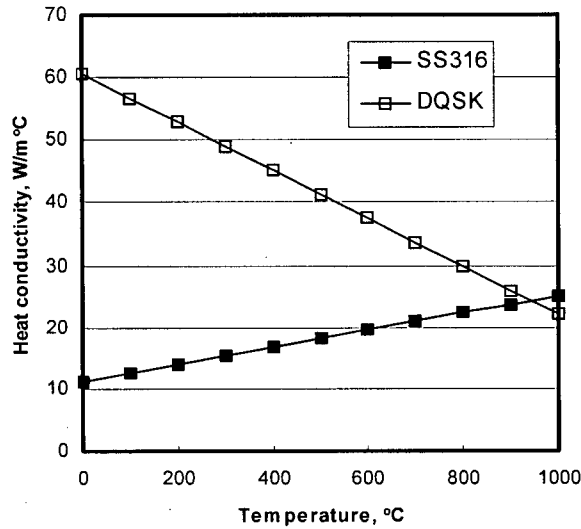


Figure 6.26 Temperature-dependent conductivity

The effect of steel grade on the heat flux at the water temperature of 50 °C is shown in Figure 6.27. In contrast to the correlation at 30 °C, for the same levels of water flow rates as those in Figure 6.23, the heat fluxes for the SS316 are mostly higher than those for the carbon steel DQSK. As discussed above, the cooling capacity depends mainly on the water temperature and not the water flow rates. With the increase of the water temperature, the cooling efficiency decreases. This means that the interior temperature decreases at a much lower rate with higher water temperatures than with lower water temperatures, which can be verified by the point densities at the starting stages of cooling in Figure 6.23 and Figure 6.25. Also, this indicates that the cooling is more confined at the top surface, and it is easier to cool down the surface with a higher conductivity than with a lower conductivity; i.e., less heat flux is needed to reduce the surface temperature to a given value for the material with higher conductivity than for that with lower conductivity.

### 6.3.3 Section summary

The heat fluxes and surface temperature at the stagnation points or in the impingement zone of stationary plates in the circular water jet cooling is successfully determined by using the FZM and a small model. An analysis of the data shows that the heat transfer

behaviour at the stagnation point is mainly and greatly affected by the water temperature, slightly affected by the steel grade and hardly affected by the water flow rate. When the water temperature is lower than 60 °C the cooling process is governed by the transition boiling and nucleate boiling. When the water temperature is higher than 60 °C, there is evidence of the existence of a film boiling regime. The features of boiling curves and the typical values obtained are in close agreement with other resources.

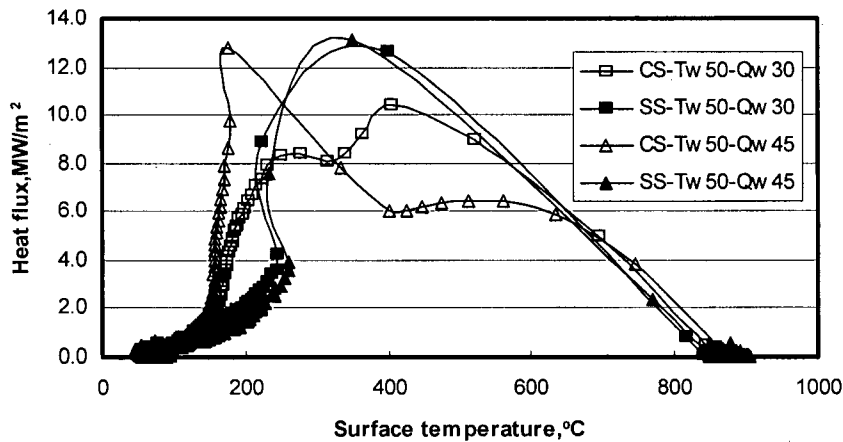


Figure 6.27 Effect of steel grade at  $T_w = 50\text{ }^\circ\text{C}$

#### 6.4 Heat Transfer in the Parallel Zone of Stationary Plates

Generally, the heat transfer in the parallel zone is different from that in the impingement zone. The results shown in Figure 6.10, which are obtained using the FZM without the EDA, show that the maximum heat fluxes at different locations in the parallel zone are fairly close to each other and are all much smaller than those in the impingement zone.

In this section, the focus is on the heat transfer at location TC3 for stationary plates. The FMM is used together with the EDA. The two reasons why only the heat transfer at location TC3 is studied are that the heat flux profiles at different locations in the parallel zone are nearly identical, and that a great effort is needed to apply the FMM.

For all calculations in this section, a 2D axisymmetrical condition is adopted and a single mesh model is used, whereas 896 quadratic elements are used to discretize a geometry of 64 (radius)  $\times$  7 (thickness) mm. The data at the first four locations are used in the inverse calculations. There are uniformly 64 elements in the radius direction. For the carbon

steel, the temperature dependence of conductivity is considered, and an average value of  $20 \text{ W/m}\cdot\text{°C}$  is used for the conductivity of the SS316.

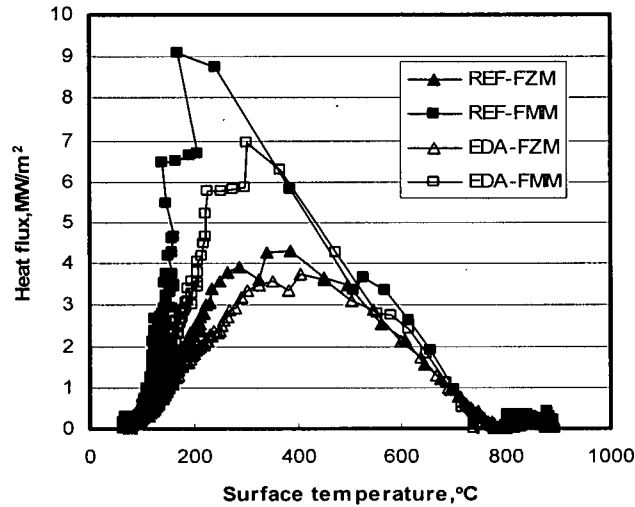


Figure 6.28 Comparison of cooling curves at TC3 using different approaches, #25

#### 6.4.1 Case study

Test #25 is studied in detail. The results are shown in Figures 6.28, 6.29 and 6.30.

Figure 6.28 compares the cooling curves from different approaches. As expected, the cooling curves with using the EDA are always below the corresponding ones without the EDA for both methods of specifying heat flux. With the FZM, the peak value of heat flux with the EDA is 20% lower than that without the EDA, while the former is around 30% lower than the latter with the FMM. This illustrates that the EDA has more influence with the FMM than with the FZM. This is reasonable because the FMM is point-oriented while the FZM has an averaging feature.

The cooling curves either from the FZM or the FMM show similar heat transfer modes. That means that the results without the EDA can be used to obtain a qualitative correlation, which may turn to a quantitative one with an appropriate coefficient.

However, the cooling curves from the FMM present a heat transfer mode slightly different from the FZM cooling curves. These curves show that the heat flux increases from the start of cooling to a temperature, and then decreases. This temperature is about

400 °C for the FZM and 200–300 °C for the FZM. This point should be carefully checked with the other test results.

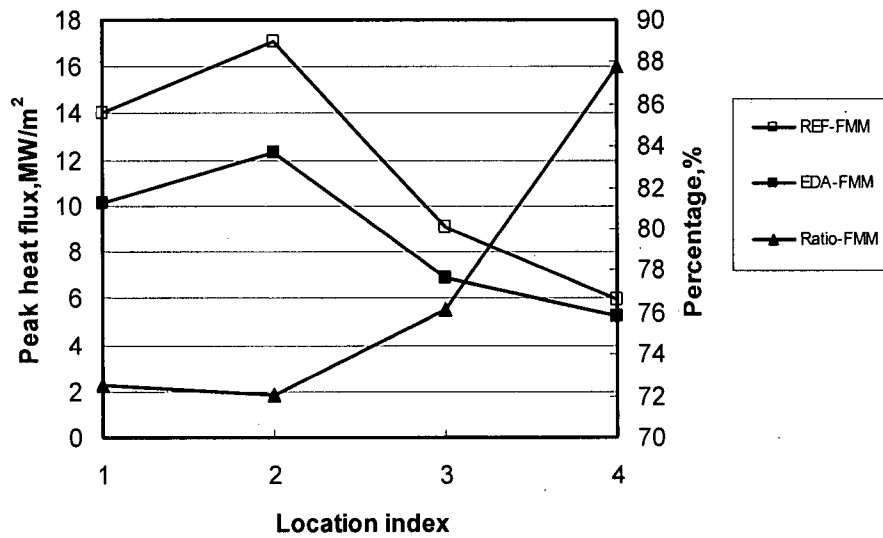


Figure 6.29 Comparison of peak heat fluxes at the first four locations, #25

The comparison of peak heat fluxes at the four locations from the FMM is presented in Figure 6.29. Similar to those shown in Figure 6.20, the percentages at the two points in the impingement zone are nearly the same and lower than those at the other points in the parallel zone. In fact, FMM results are similar to FZM ones for the impingement zone.

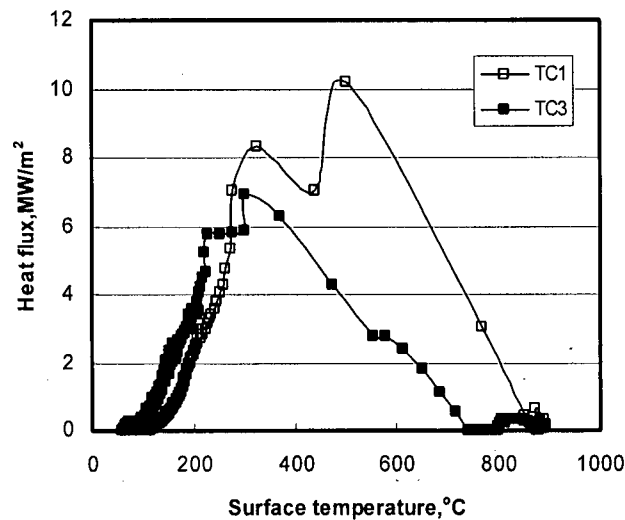


Figure 6.30 Comparison of cooling curves by FMM and EDA, #25

Figure 6.30 illustrates the difference in the heat transfer modes at the locations TC1 and TC3. The first conclusion is that the difference in heat flux magnitudes at the two locations is not remarkable as shown by the FZM, in Figure 6.10, as well as in the reference.

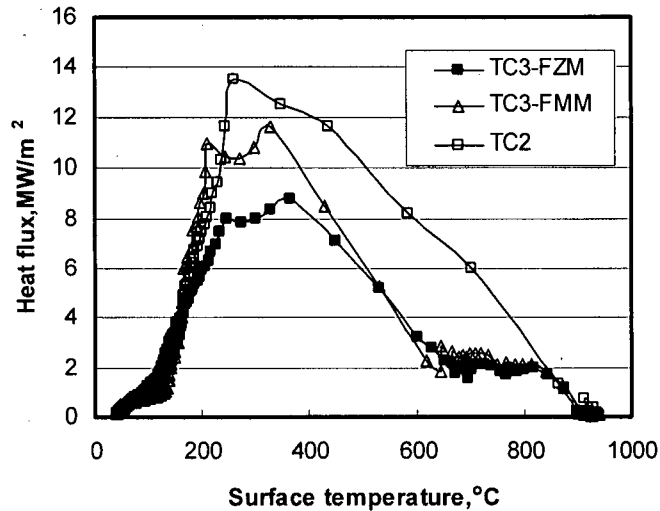


Figure 6.31 Comparison of cooling curves, #3

The second point is that the difference may be due to the difference in surface. It can be seen that the surface temperature at TC1 at the very beginning of water cooling is around 900 °C while this temperature is around 720 °C at TC3. For this test, the surface temperature at TC3 decreases due to a combination of effects: a longer air cooling period, the transversal temperature gradient before the water reaches this location, and the film boiling cooling before the location is rewetted. For some tests, the surface temperature at TC3 decreases to a lower value mainly due to the film boiling cooling process before this location is rewetted, as shown in Figure 6.31.

#### 6.4.2 Parameter effects

In this section, the effects of the cooling parameters on the cooling behaviour at TC3 are briefly discussed using a limited number of examples with typical experiment conditions: the flow rate is fixed at 30 l/min and/or the water temperature is fixed at 30 °C. Therefore, the conclusions may be confined to the tests discussed and are not general.

## 1. Effect of water temperature

The effect of water temperature on the heat transfer at TC3 with a water flow rate of 45 l/min is shown in Figure 6.32. It may be seen that the water temperature has little influence on both the mode and the magnitude of heat transfer behaviour, an observation which is totally different from that at the stagnation, whereas the heat transfer is affected greatly by the water temperature.

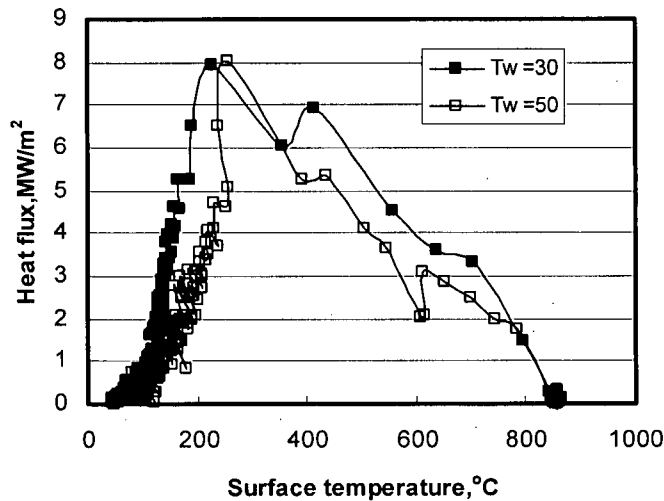


Figure 6.32 Boiling curves at TC3 by FMM for #24 ( $T_w = 30^\circ\text{C}$ ) and #27 ( $T_w = 50^\circ\text{C}$ )

The rationale behind this phenomenon at TC3 may lie in the local water temperature. When water impinges onto the hot surface and spreads streamwise, it is heated to a higher temperature. It can be inferred that the water temperature at TC3 and afterwards have similar values irrespective of the initial one, and that the water temperature difference at TC3 will decrease. For the two tests, the initial water temperature difference is only  $20^\circ\text{C}$ ; thus, the local water temperature difference at TC3 will be definitely less than  $20^\circ\text{C}$  and may not cause a big discrepancy in heat transfer at this location.

## 2. Effect of water flow rate

Figure 6.33 shows the effect of flow rate on the heat transfer at TC3 for SS316 at a water temperature of  $30^\circ\text{C}$ .

In contrast to the conclusion discussed in Section 6.2, in which the water flow rate has little effect on the heat transfer at the stagnation point, the water flow rate affects both the

mode and the magnitude of heat transfer in the parallel zone. There is a cooling stage of film boiling for the flow rate 30 l/min, while the film boiling seems not to exist for the flow rate 45 l/min. The increase in the water flow rate means that more fresh water floods location TC3, and this process also progresses faster. Therefore, location TC3 may be rewetted much faster with a higher water flow rate than with a lower water flow rate. Correspondingly, the heat flux with a flow rate of 45 l/min is generally higher than that with a flow rate of 30 l/min. These two trends are consistent and compatible.

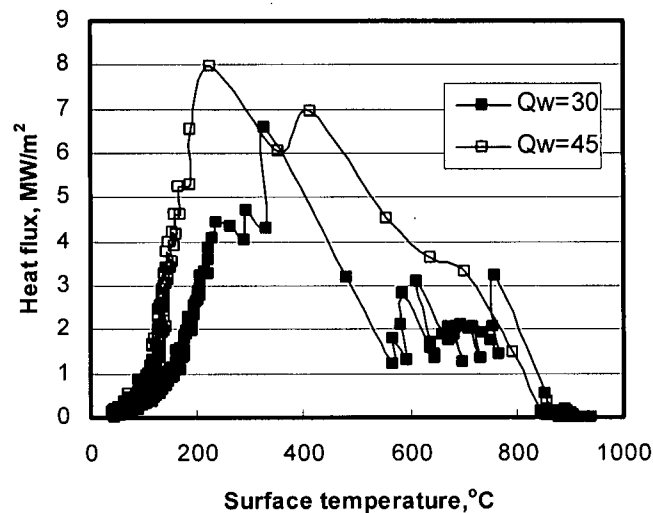


Figure 6.33 Boiling curves at TC3 by FMM for #22 ( $Q_w = 30$ ) and #24 ( $Q_w = 45$ )

### 3. Effect of steel grade (Conductivity)

The effect of steel grade on the heat transfer at TC3 is illustrated in Figure 6.34. For these two tests, the flow rate is fixed at 30 l/min and the water temperature is fixed at 30 °C. The two cooling curves show the same cooling behaviour, and the cooling modes are as complete and typical as those shown in Figure 2.1. This means that the steel grade has no or little effect on the cooling modes.

However, the Leidenfrost point is somewhat lower for the SS316 than for the DQSK; and the maximum heat flux for the DQSK is about 2 times that for the SS316. This is because the conductivity of the DQSK is higher than that of the SS316. Higher conductivity will greatly increase the heat transfer from the bottom hotter part to the top lower part, which increases the heat flux.

These trends at TC3 are similar to that at the stagnation point for the same cooling conditions.

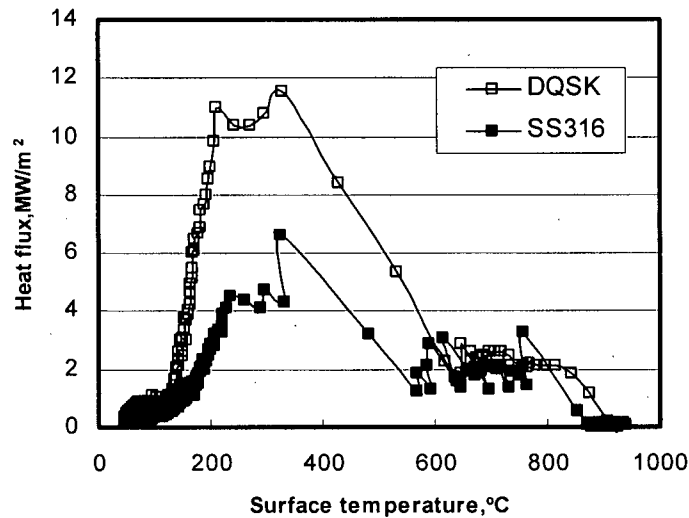


Figure 6.34 Boiling curves at TC3 by FMM for #3 (DQSK) and #22 (SS316)

It can be concluded that the water flow rate is the key factor in the parallel zone and it affects both the mode and the magnitude of heat transfer, and that the conductivity mainly influence the heat flux values.

### 6.5 Heat Transfer for the Moving Plates

First, the modelling for moving plates should be discussed. As discussed above, the impingement zone is about 2.5 times the nozzle diameter for the stationary plates. Although the cooling zone changes to a pearl-shape for the moving plates, the transverse dimension of the cooling zone is not significantly affected. Locations TC1 and TC2 in Figure 6.3 are still in the instant impingement zone; and there is no transverse heat flow around TC1. Moreover, as analyzed in Section 4.2, the material points are nearly cooled by a moving pattern for the moving plates; and the speed of the moving pattern can be assumed to be the plate's moving speed. As the plate's moving speed is greater than 0.3 m/s, two points that are 16 mm apart in the longitudinal direction are cooled down with a time difference of 0.053 s or less. This means that the cooling conditions for the two points are nearly identical, and there are no evident of longitudinal temperature gradients.

The temperature profiles at location TC1, TC2 and TC3 verify this analysis. Therefore, it would be appropriate to simplify the heat transfer at TC1 as 2D (thickness and longitudinal direction) or 1D (thickness direction). In the following example, 2D modelling is used.

Figure 6.35 gives an example of the heat fluxes obtained from moving plate experiments, which provide new insight into heat transfer on ROT and constitute a crucial advancement for developing more realistic heat transfer correlations for industrial ROT cooling. In this example, the water temperature is 30 °C and the water flow rate is 30 l/min, which are all typical values for the cooling on ROT.

It is clear that increasing the plate speed leads to a decrease in heat fluxes for a given water temperature and water flow rate. For example, as the initial temperature is around 260 °C, the peak heat flux is 1.85 MW/m<sup>2</sup> for the plate's moving speed of 0.3 m/s while it decreases to 1.2 MW/m<sup>2</sup> for the plate's moving speed of 1.0 m/s.

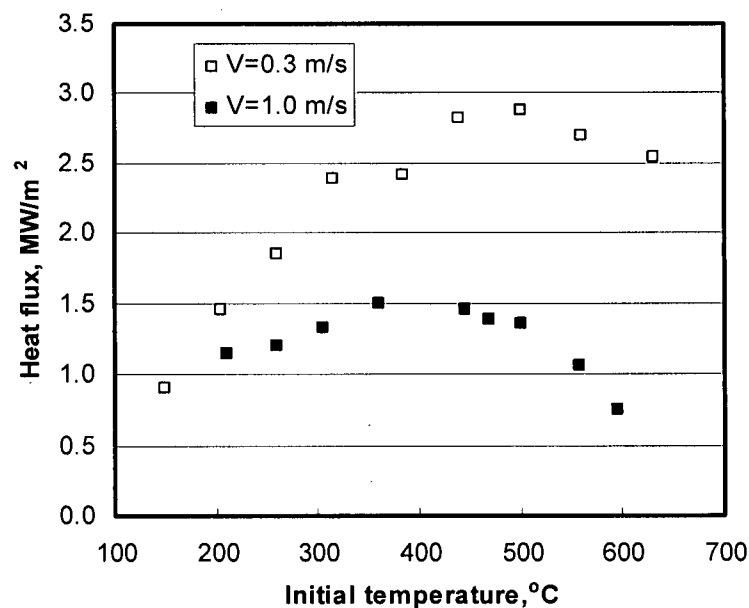


Figure 6.35 Effects of the plate's speed and initial temperature on the peak heat flux  
 $Q_w = 30 \text{ l/min}$ ,  $T_w = 30 \text{ °C}$ , DQSK

The effect of the plate's initial temperature on the peak heat flux is not monotonic. As the initial temperature is lower, the peak heat flux increases with the increase of the initial temperature and reaches a maximum. Afterwards, the peak heat flux decreases with the

increase of the initial temperature. This trend is retained for the two levels of the moving speed. However, the critical temperature at which the peak heat flux reaches its maximum seems at a lower value for a higher speed. The critical temperature is around 400 °C for the speed of 1.0 m/s while it is about 500 °C for the speed of 0.3 m/s.

With an extrapolation, the peak heat flux may be only 2.0 MW/m<sup>2</sup> for the speed of 0.3 m/s as the initial temperature is 850 °C. Recall that the peak heat flux is around 20.6 MW/m<sup>2</sup> for the stationary plate with an initial temperature 850 °C at the same cooling conditions ( $Q_w=30$  l/min and  $T_w=30$  °C). It may be concluded from the two values that the motion of the plate has a great influence on the heat transfer.

The above trends are verified by other tests.

## 6.6 Summary

Experimental test data are successfully analyzed by the developed approaches. The FZM is used for the investigation of the heat transfer behaviour at the stagnation point of stationary plates while the FMM and EDA are used for the parallel zone. The FZM and EDA are used for the moving plate tests.

Results show that the heat transfer behaviour at the stagnation point is mainly and greatly affected by the water temperature, slightly affected by the steel grade and hardly affected by the water flow rate. When the water temperature is lower than 60 °C the cooling process is governed by the transition boiling, nucleate boiling and convective boiling. When the water temperature is higher than 60 °C, there is evidence of the existence of a film boiling regime.

It is apparent that the water flow rate is the key factor in the parallel zone and it affects both the mode and the magnitude of heat transfer, and that the conductivity mainly influence the heat flux values. However, the initial water temperature has little effect on the heat transfer in the parallel zone, which suggests that local water temperatures may be required.

It is found by analyzing the moving plate tests that increasing the plate speed leads to a decrease in heat fluxes for a given water temperature and water flow rate.

## Chapter 7

### SIMULATION OF RUN-OUT TABLE COOLING PROCESS

The cooling process of steel strips on an industrial ROT is simulated using 1D model. The accuracy of the 1D model simulations is discussed with a comparison to the field measurements [64]. Transverse 2D modelling is used to investigate the effect of non-uniform heat flux in the width direction on the final coiling temperature. The necessity of longitudinal 2D modelling is also investigated.

#### 7.1 Simplification of Governing Equation

The general governing equation for conduction heat transfer problems of a moving volume in Lagrangian reference may be written in the form [57]:

$$\nabla(k\nabla T) + q^b = c_p \rho \frac{DT}{Dt} \quad (7.1)$$

where  $k$  is the conductivity,  $T$  is the temperature,  $q^b$  is the heat generation per unit volume,  $\rho$  is the density,  $c_p$  is the specific heat, and  $t$  is the time. It should be noted that the material properties  $k$ ,  $c_p$ , and  $\rho$ , are usually temperature dependent.

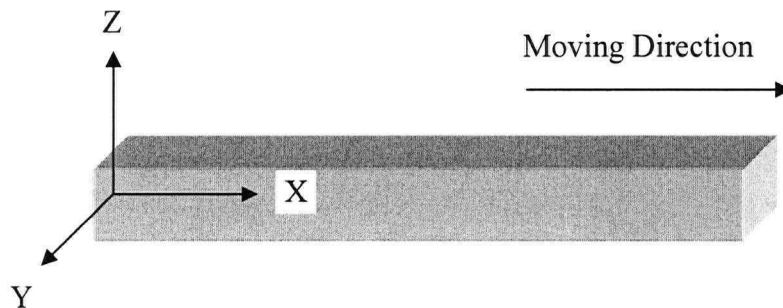


Figure 7.1 Coordinate system used for modelling

The differential operators for a Cartesian coordinate system (Figure 7.1) are defined as:

$$\nabla = \vec{i} \frac{\partial}{\partial x} + \vec{j} \frac{\partial}{\partial y} + \vec{k} \frac{\partial}{\partial z} \quad (7.2)$$

$$\frac{D}{Dt} = \frac{\partial}{\partial t} + u_x \frac{\partial}{\partial x} + u_y \frac{\partial}{\partial y} + u_z \frac{\partial}{\partial z} \quad (7.3)$$

where  $\vec{i}, \vec{j}$  and  $\vec{k}$  are the unit direction vectors along the  $x, y$  and  $z$  direction,  $(x, y, z)$  is the space point position with respect to the Lagrangian coordinate reference, and  $(u_x, u_y, u_z)$  are the components of velocity vector  $\mathbf{u}$  at the point  $(x, y, z)$ .

For the controlled cooling process of the hot strip on ROT, the ranges of coordinate geometry can be assumed as the following:

$$\begin{aligned} 0 &\leq x \leq L \\ -b/2 &\leq y \leq b/2 \\ -h/2 &\leq z \leq h/2 \end{aligned} \quad (7.4)$$

where  $L$  is the total length of the cooling zone from the last finishing stand to the downcoiler, and  $b$  and  $h$  are the width and thickness of the strip, respectively.

To apply the governing equation to the controlled cooling process of the hot strip, a number of assumptions and measures should be made [65–77].

1. It is assumed that the strip does not move vertically up and down and laterally (in practice, such movements eventually exist and may have effects on the cooling results), that is:

$$u_y = u_z = 0 \quad (7.5)$$

2. It is assumed that the strip is continuous, and that no distinction is made between the leading end, trailing end or central portion of the strip, or that the strip is infinitely long; and that the initial temperatures as the strip enters the cooling zone are the same; and that the process operates at a steady state.

From the above assumption, the temperature profile at any fixed location (temperature gradient at a fixed spatial position along the ROT) on ROT does not change with time,

$$\frac{\partial T}{\partial t} = 0 \quad (7.6)$$

The above two assumptions were adopted in all published literature and are used in this study. Under these assumptions, the differential equation for the ROT cooling process becomes:

$$\frac{\partial}{\partial x} \left( k \frac{\partial T}{\partial x} \right) + \frac{\partial}{\partial y} \left( k \frac{\partial T}{\partial y} \right) + \frac{\partial}{\partial z} \left( k \frac{\partial T}{\partial z} \right) + Q = c_p \rho u_x \frac{\partial T}{\partial x} \quad (7.7)$$

Equation (7.7) presents a three-dimensional steady state heat transfer problem, and theoretically there would be no problem to getting the numerical solution. Some researchers [78] did simulations based on those simplifications. The results showed that this kind of 3D simulation has modest effect on the accuracy of the coiling temperature prediction. However, the solution procedure is very time-consuming and not economical because there would be more than 100 thousand elements in the length direction, even with large ratio of element dimensions in the length direction to those in the width and thickness. Therefore, more simplifications are required to render a more economical simulation without sacrificing too much accuracy.

3. Most researchers introduced another assumption that the heat transfer or flux in the strip width direction is neglected:

$$\frac{\partial}{\partial y} \left( k \frac{\partial T}{\partial y} \right) = 0 \quad (7.8)$$

This assumption is only valid for the uniform boundary condition and temperature along the strip width. Because the water on the top surface will flow out transversely for both laminar and curtain cooling, the heat flux or heat transfer coefficient along the strip width may change.

On the other hand, the flow rate along the strip width may be intentionally designed to be non-uniform, slightly higher in the middle, decreasing with the distance from the centre line of the strip, in order to get a final uniform coiling temperature.

These effects are, however, ignored, and by adopting this assumption there is:

$$\frac{\partial}{\partial x} \left( k \frac{\partial T}{\partial x} \right) + \frac{\partial}{\partial z} \left( k \frac{\partial T}{\partial z} \right) + Q = c_p \rho u_x \frac{\partial T}{\partial x} \quad (7.9)$$

4. It can be easily proved that the heat transfer due to the bulk motion in the moving direction ( $x$ -direction) is much larger than the heat conduction in the same direction. A comparison is carried out using Peclet number,  $Pe$ :

$$Pe = \frac{\text{convection}}{\text{diffusion}} = \frac{u_x}{\alpha/l_c} \quad (7.10)$$

where  $\alpha$  is the diffusion coefficient, and  $l_c$  is the typical strip length in the cooling zone under one jet.

The Peclet number is greater than 20,000, i.e. much greater than unity, for typical hot strip mill conditions; therefore, the heat conduction in the moving direction may be neglected,

$$\frac{\partial}{\partial x} \left( k \frac{\partial T}{\partial x} \right) = 0 \quad (7.11)$$

The above assumption renders equation (7.9) to take the simple form of:

$$\frac{\partial}{\partial z} \left( k \frac{\partial T}{\partial z} \right) + Q = c_p \rho u_x \frac{\partial T}{\partial x} \quad (7.12)$$

Equation (7.9) or (7.12) still describes a 2D heat transfer problem in the length and thickness directions. A novel approach is developed in this work to study the intensity of longitudinal heat transfer [66] and will be discussed in Section 7.3.

5. A commonly used approach to further simplify the calculation is the parameter replacement under the assumption that the strip velocity is constant. This approach is in essence a coordinate transformation In the form:

$$x = u_x t \quad (7.13)$$

It is noteworthy that the time is estimated from the beginning of the cooling process, and that the coordinate system becomes a moving one, i.e., the Euler coordinate. The temperature is material-point oriented.

Substitution of equation (7.13) into equation (7.12) or (7.9) leads to:

$$\frac{\partial}{\partial z} \left( k \frac{\partial T}{\partial z} \right) + Q = c_p \rho \frac{\partial T}{\partial t} \quad (7.14)$$

$$\frac{\partial}{\partial y} \left( k \frac{\partial T}{\partial y} \right) + \frac{\partial}{\partial z} \left( k \frac{\partial T}{\partial z} \right) + Q = c_p \rho \frac{\partial T}{\partial t} \quad (7.15)$$

Combining the above assumptions, the heat transfer problem becomes a transient 1D (equation (7.14)) or 2D (equation (7.15)) with changing boundary conditions. Note that  $\frac{\partial T}{\partial t}$  in equations (7.14) and (7.15) is the material derivative of temperature with respect to time.

Thus, while the temperature distribution through the thickness (1D) or on the transverse cross section (2D) at each time instant must be solved simultaneously, the solution in the moving direction can be solved sequentially, which greatly simplifies the calculation and reduces the CPU time.

## 7.2 Modelling and Implementation

There are several issues to be resolved to achieve an appropriate and accurate simulation of the cooling process of steel strip on ROT. In the following, the handling of the main ones is addressed.

### 7.2.1 Numerical method

Both the finite difference and the finite element methods were used to numerically solve equation (7.14) or (7.15) to simulate the temperature field and to predict the coiling temperature in literature [70–75].

In this work, FEM is used. For 1D model, a uniform mesh is used, and the discretization in the thickness direction can be automatically realized with the input of the strip thickness and the number of elements (nodes) required [65]. For the transverse 2D modelling, it is assumed that the cooling conditions are of the same profiles for the top and bottom surfaces and are symmetric to the width centreline. Thus, only part of the cross section is discretized.

### 7.2.2 Initial condition

A literature survey reveals that a uniform initial temperature assumption is most widely adopted; that is, there is no temperature difference through the thickness (1D) or through the thickness and width (2D).

$$\begin{aligned}
 T = T_c \quad t = 0, \quad & -h/2 \leq z \leq h/2 \\
 \text{or} \quad & -h/2 \leq z \leq h/2, -b/2 \leq y \leq b/2
 \end{aligned} \tag{7.16}$$

If the boundary conditions on the top elements and the bottom ones are the same, this assumption will again reduce the element numbers required for discretization.

Although it is very practical, this assumption neglects the fact that the initial temperature is far from uniform, due to the different cooling conditions on the top surface and the bottom surface during the rolling process prior to the cooling process.

For our 1D model, the initial temperatures through the thickness may be different. When implementing this issue, two temperatures are always required, one for the top element, one for the bottom element. Linear interpolation is used to assign the initial temperatures for all other elements (nodes).

### **7.2.3 Boundary condition**

#### **1. Literature review**

The reliability of the simulation to ROT cooling will depend, to a great extent, on the rigor and the accuracy of the mathematical descriptions of the boundary conditions. On the other hand, it is a difficult issue to accurately determine the boundary conditions. Many approaches have been explored and results have been published. In general, they may be classified into three methods.

Some researchers used a very simple approach in which a variety of constant HTC values was assumed from the start to the end of the cooling process. In this approach, the target is normally the coiling temperature and, not the time history profile of temperature [67–71]. Various values of HTC were assumed by different researchers; e.g., 464–1394  $\text{W/m}^2\cdot^\circ\text{C}$  (1670 to 5020  $\text{kJ/m}^2\cdot\text{h}\cdot^\circ\text{C}$ ) in references [67–68] and 2500–4500  $\text{W/m}^2\cdot^\circ\text{C}$  in [69–71]. The HTC value for the best prediction of the coiling temperature was assumed the one for the processing condition and used for later analysis, e.g., the simulation of microstructure evolutions. Although they are very practical, these approaches may underestimate the actual cooling rates and their effects on the microstructure evolution and finally on the properties.

For the second method, different HTC values were adopted for the cooling zones directly around the cooling headers and the cooling zones between cooling headers [72–75]. For example in reference [72], the HTCs were 5500  $\text{W/m}^2\cdot^\circ\text{C}$  and 100  $\text{W/m}^2\cdot^\circ\text{C}$  for the impingement zone and the parallel zone, respectively. Therefore, it is necessary to determine the boundaries between the different zones and the HTC values or their distributions for these zones.

The last approach is to use HTC correlations based on thermodynamic principles that consider the interaction between water and hot surfaces [77–78], or based on empirical equations [79–84]. In these equations, the local water temperature, strip surface temperature, impingement angle and moving speed of the strip may be required to compute the local HTC values. For example, Guo et al. [79–81] used the following equation to determine the absolute maximum HTC of each pair of headers:

$$h_w = K \left( \frac{V_p}{V_{p0}} \right)^{c_1} \left( \frac{t}{t_0} \right)^{c_2} \left( \frac{T_s}{T_{s0}} \right)^{c_3} \left( \frac{Q_w}{Q_{w0}} \right)^{c_4} \quad (7.17)$$

where  $V_p$ ,  $t$ ,  $T_s$  is the speed, thickness, surface temperature of the strip, respectively,  $Q_w$  is the header flow rate; the corresponding values with the subscript “0” are the reference ones.  $K$  and  $c_1$  to  $c_4$  are curve-fitting constants determined by the operation data and experimental ones. Obviously, the reliability and precision of this approach depend greatly on those of the correlations for HTC.

## 2. Division of the cooling surface

A hybrid approach is conducted in this study. First, the cooling surface is divided into a few subregions. Second, different correlations are used for each subregion.

As shown in Figure 7.2, the cooling surface for an active or working jetline (jetline is on and water impinges onto the strip) is divided into a maximum of 5 cooling zones: air cooling zone-B, parallel water cooling zone-B, impingement water cooling zone, parallel water cooling zone-F and air cooling zone-F. However, there is only an air cooling zone for a dead jetline (jetline is off and no water flows out).

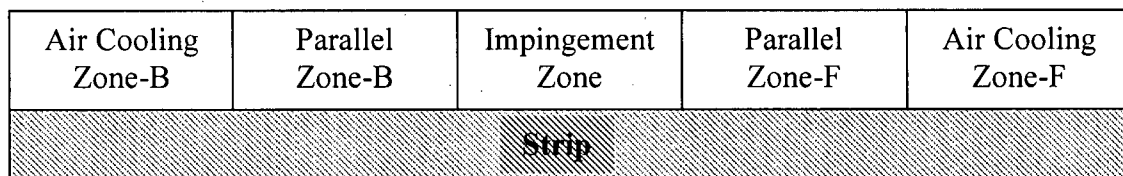


Figure 7.2 Cooling zones under one active jetline

The actual divisions of the cooling zones and their corresponding lengths depend on the on-off status of two adjacent jetlines.

The critical issue is to determine the length of the impingement zone. Two assumptions are made for the sake of calculation simplicity in this study. The first one is that for any active jetline, the impingement zone is symmetrical to the jetline and its total length is proportional to the nozzle diameter. The ratio of the impingement zone length to the nozzle diameter is defined as the width coefficient in this study.

The second assumption is that there is no air cooling zone for a working jetline. Thus, the parallel zone extends to the middle of two adjacent jetlines, and the length of one parallel zone is equal to half of the distance between two adjacent jetlines minus the impingement zone width. Because the jetline distances may be different, the lengths of the parallel zone-B and zone-F may not be equal even if the impingement width is the same.

This setup is schematically shown in Figure 7.3. If the jetline  $i$  is active, the characteristic length  $L_{chai}$  is divided into three subregions: the parallel zone-B:  $0.5(L_i - L_{impi})$ , the impingement zone  $L_{imgi}$  and the parallel zone-F:  $0.5(L_{i+1} - L_{imgi})$ .

If the jetline  $i$  is not active, all  $L_{chai}$  belongs to the air cooling zone.

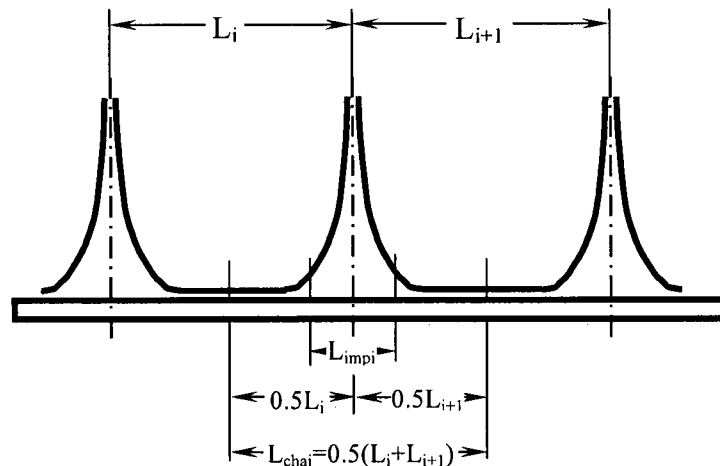


Figure 7.3 Design of the cooling zone lengths

### 3. Correlations used in this study

#### i) Air cooling zone

While the strip surface is exposed to the air, the heat loss is due to forced convection and radiation. The heat transfer may depend on the moving speed and the surface temperature. A correlation is set up and used based on the equation in the reference [79]

for the HTC of forced air convection with various strip speeds and the equation in the reference [80] for the HTC of radiation:

$$h_{air} = 4.5 \cdot V_p^{0.926} + [-3038 + 0.954T_s + 2.14 \times 10^{-8}(T_s + 273)^4]/(T_s - 20) \quad (7.18)$$

where  $h_{air}$  is the HTC in  $W/m^2 \cdot ^\circ C$ ,  $V_p$  is the strip speed in m/s, and  $T_s$  is the surface temperature in  $^\circ C$ .

The relationship of HTC to the surface temperature at two levels of the plate's speed is shown in Figure 7.4. It is evident that the HTC is mainly determined by the surface temperature while the plate moving speed has only a slight effect on the HTC.

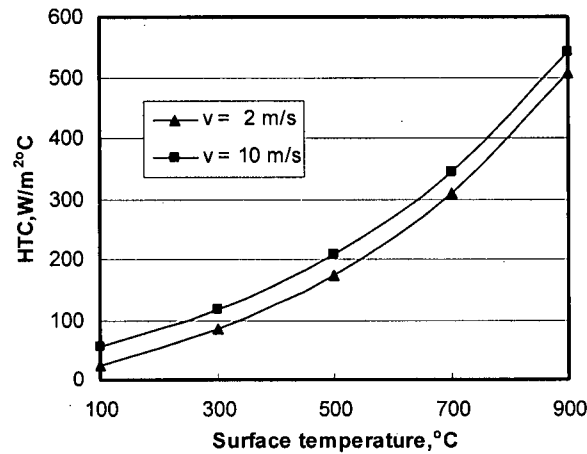


Figure 7.4 HTC in air cooling zone

## ii) Impingement zone and parallel zone

The empirical model for HTC in the reference [83] is used to calculate the HTC in the impingement zone. The formula is:

$$\begin{aligned} h_{imp} &= 2186.7 \cdot (T_s/1000)^{2.5} \cdot (V_p/20)^{-0.4} \\ &= 2.292 \times 10^{-4} \cdot T_s^{2.5} \cdot V_p^{-0.4} \end{aligned} \quad (7.19)$$

where  $h_{imp}$  is the HTC in the impingement zone in  $W/m^2 \cdot ^\circ C$ ,  $T_s$  is the surface temperature of the strip in  $^\circ C$ , and the  $V_p$  is the strip speed in m/s.

Figure 7.5 illustrates the HTC profiles. It can be seen that the surface temperature is the critical factor affecting the HTC, and that the strip speed has a larger effect when the surface temperature is at a higher level.

For the common operation conditions on ROT, i.e., when the strip speed is 6–10 m/s and the surface temperature is 500–900 °C, the HTC varies from 500–2700 W/m<sup>2</sup>·°C. This range seems fairly reasonable in a comparison with the data in the literature.

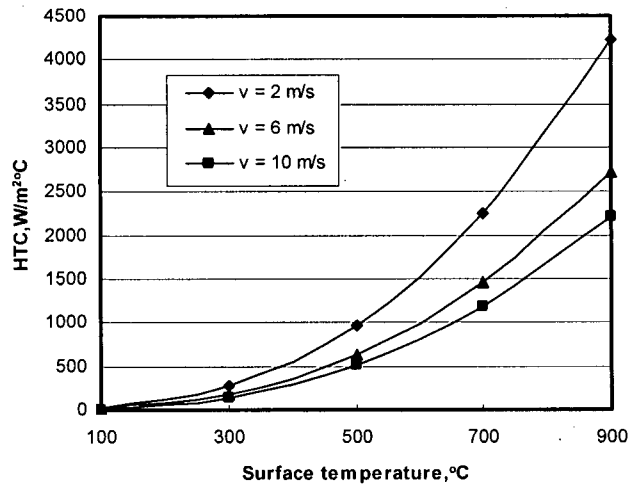


Figure 7.5 HTC in impingement cooling zone

It is found that equation (7.19) with a modification to the coefficient is also the best choice of the HTC correlation for the parallel zone in this study. The coefficients are presented in Section 7.4.1.

When the whole thickness is modelled, both the top and bottom surfaces should have the appropriate boundary conditions; when half the thickness is modeled, the centre is assumed thermally insulated and appropriate boundary condition are applied on the top surface. In this study, the second option is used because there are no appropriate correlations for the bottom impingement cooling zone.

#### 7.2.4 Temperature dependences of thermophysical properties

The thermophysical properties of material may change with temperature. In general, the specific heat decreases with the decrease of temperature while the conductivity decreases before phase transformation and increases again thereafter.

There are two approaches to deal with this kind of dependence. In most cases, the changes were neglected, and average values were used. Another approach is to use correlations of properties as function of the temperature. In such cases, the simulation will be nonlinear and iterative solutions are required [70–71, 74–75].

In our implementation, the thermal conductivity and specific heat are considered as temperature dependent are considered and specific available data may be used to find the best fit for the properties.

### **7.2.5 Latent heat**

During the cooling process on ROT, the deformed austenite will change to other phases at some temperatures. The latent heat is released due to this phase transformation and may affect the coiling temperature and finally the properties of the strip.

Some researchers have neglected or ignored the effect of the latent heat [85] whereas others have included the effect. In a more appropriate simulation, the transformation of austenite to ferrite and pearlite is usually taken account into, and the effect of the corresponding latent heat on the cooling temperature profile is analyzed [70–71].

In our implementation there is an option to consider latent heat in the analysis. In this case, the heat generation per volume is calculated by:

$$Q = H \cdot \dot{F} \quad (7.20)$$

where  $H$  is the mole of the material considered, W/kg;  $\dot{F}$  is the transformation rate of austenite to ferrite and pearlite per volume and will be calculated in the module for microstructural evolution.

### **7.2.6 Microstructure evolution and property prediction**

It is becoming customary to integrate models for microstructural evolution and property prediction in heat transfer analyses [83–88]. Most of these models have paid attention to the transformation of austenite to ferrite and pearlite, and to the grain sizes and proportion of ferrite and pearlite or bainite. Properties such as yield strength and toughness may be calculated from the compositions of phases. Some models [86] utilized more complicated equations to take account of the dislocation change and its effect. Few reports investigated the distributions of microstructures and properties along the strip width and/or length [83].

The model developed in this study is intended to predict the composition of transformation products and the mean ferrite grain size as well as the mechanical properties of the steel considered. Equations describing the transformation of austenite to ferrite, pearlite, and bainite would be implemented and applied under the cooling conditions of strip on ROT. The correlations for calculating the product properties will also be included in the final full version of this program. These correlations are not presented here because they are lengthy, and this study focuses on the prediction of the coiling temperature.

### **7.2.7 Program structure**

All of the above issues have been implemented in an FEM code to simulate the cooling process on ROT. This code for 1D modelling is called **RealROT**. The **RealROT** is written as modular interactive program. The code is composed of a read-in module, a ROT data module, an initial condition module, a material module, a HTC correlation module, a microstructure module and an FEM module.

#### **1. Read-in module**

This module is designed to be interactive and user friendly. Main parameter inputs to the program include: the material type identification number, the strip thickness, the top and bottom surface temperatures, the element (node) number (even number) required to discretize the strip, and whether the heat generation should be considered or not. In addition, the user is required to specify the heat flux or the HTC condition as the boundary condition. The residual strain is also input here, if applicable.

#### **2. Initialization module**

This module performs meshing, specification of initial temperature and time stepping. The half strip thickness will automatically be discretized into elements (nodes) that are of same size. It was proven that 40 elements are enough to get reasonably accurate result. The module also calculates the initial temperatures of the strip after the strip is meshed. The calculation is based on the two input temperatures and the linear interpolation. In addition, the residual strain is assigned to each node.

The common method for time stepping is first to determine the total number of time steps or the analysis duration and then to calculate the time step size. Existing approaches generally use equal time steps sizes. This has the deficiency of need to track the location of the target material slice and to determine in which zone the target slice exists. In addition, the time step size should be small enough to avoid jumping over the water cooling zones, especially the impingement ones. Normally on such cases, the total number of time step is huge and the calculation time is then considerable.

A novel approach is used here for time stepping. First, five time step numbers for different cooling zones are defined as follows:

NFAIR: number of time steps for the entry air-cooling zone

NLAIR: number of time steps for the exit air-cooling zone

NBAIR: number of time steps for the air-cooling zone if a jetline is not active

NPARA: number of time steps for the parallel cooling zone if a jetline is active

NIMPG: number of time steps for the impingement cooling zone if a jetline is active

Thus, the total number of time steps depends greatly on the number of active jetlines and on the time steps for the parallel and impingement water cooling zone. In addition, each time step is identified with a flag to indicate its belonging to the different zones. With this approach, tracking is not needed and no water cooling zone will be surpassed.

Second, each number of time steps can be determined according to the accuracy requirement and the strip speed. In fact, the number of steps for the air cooling zones can be a small value, which greatly reduces the total number of time steps. Therefore, for this approach, the time step size is not constant.

### **3. ROT data module**

This module deals with the ROT setup, including the ROT length, the jetline number, the jetline on-off status, the jetline distance, the nozzle number and diameter for each jetline, and the water flow rate for each jetline.

The common approach is first to set up the water banks, including the number and distance, and then to set up the jetlines under each water bank, including the number and distance of the jetlines. In this program, instead, the water bank information is not handled; i.e., ROT directly consists of the jetlines. Numerically, this approach saves one tag to identify the belongings of the jetlines. Practically, this creates an advantage to

study the spacing of jetlines on the cooling effect independently and provide more information for the design of new ROT.

In this program, the jetline distance means the spacing between the current jetline and the previous one. The jetline distance for the first jetline is the distance between the first jetline and the finishing mill stand.

There is a special arrangement for the length of the cooling zone for the first and the last jetline if they are active. For the first jetline, the Parallel-Zone-B is equal to the Parallel-Zone-F, which is calculated, while the Parallel-Zone-F is set up to the Parallel-Zone-B, which is also calculated.

#### **4. Material module**

This module calculates the thermodynamic properties of the materials, including heat conductivity, heat capacity and density. The constant values or correlations for the material properties are implemented in this module. All the correlations are assumed being linear. This module is called each time step when the temperature dependences of the properties are considered.

#### **5. HTC correlation module**

In this module, HTC is performed and used as boundary condition to avoid strip temperature lower than the ambient (water) temperature.

#### **6. Microstructure module**

The models for the microstructure evolution and final mechanical properties are input in this module. The composition of the final microstructure, i.e. the percentages of ferrite, pearlite and bainite, is estimated. This module is not discussed in this chapter.

#### **7. FEM module**

This module assembles all the necessary data, converts them to FEM format, solves the FEM equation, and outputs the required data.

### 7.3 Studies on ROT Cooling

The developed program is used to study the industrial ROT cooling process and some typical results are presented in the following section.

#### 7.3.1 Case study

In this section, simulations are performed using the **RealROT** to the practical cooling processes on a full-scale ROT. The predicted coiling temperatures are compared with the measured ones.

##### 1. ROT setup

Figure 7.6 schematically shows a typical industrial ROT. This ROT consists of five top banks and five bottom banks. Each bank has six jetlines. In the following, only the data about the top banks are presented.

The entry length ( $L1$ ) and the exit one ( $L3$ ) are 8.46 m and 70.6 m, respectively. The distance between two adjacent banks ( $L2$ ) is 2.74 m; and the distance between jetlines within one bank ( $b1$ ) is 1.37 m. The strip speed is up to 16 m/s.

For each top jetline, there are fifty-one circular nozzles of 30 mm in diameter. All of the nozzles impinge the cooling water vertically onto the strip surface. The spike (distance) of the top nozzle exit to the strip surface is 1.79 m. The cooling water has a temperature of 20–40 °C and a flow rate of 39.2 l/s per jetline.

The starting and ending temperatures of the cooling process are measured by pyrometers at the exit of the finishing mill (FM) and at the entry of the down coiler (DC). The ending temperature of the cooling process is usually called the coiling temperature.

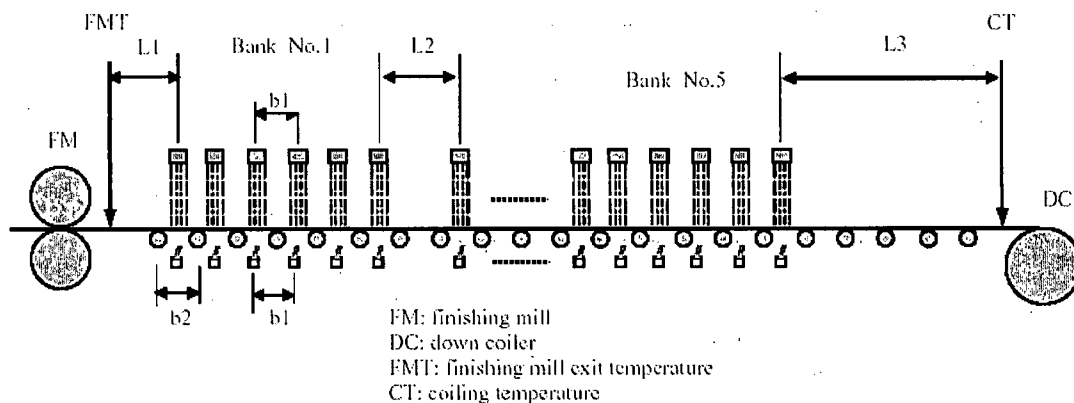


Figure 7.6 Schematic illustration of a typical ROT

For the products with the same thickness, the cooling temperature profile along ROT and the coiling temperature can be changed and controlled by adjusting the strip speed and the on-off status of the jetlines (banks) for the different temperatures at the exit of the finishing mill stand. Generally, the bank state is coded to present the combinations of the on/off of jetlines. The code used in the particular case examined is shown in Table 7.1.

Table 7.1 Bank state code

Code number	2	6	12	14	22	28	30	54	60	62	118	124	126	Down stream	
Jet Line	1										On	On	On	↓	
	2							On	On	On	On	On	On		
	3					On	On	On	On	On	On	On	On		
	4			On	On		On	On		On	On		On		On
	5		On	On	On		On								
	6	On	On		On	On		On	On		On	On			On

Examples of the strip production data are shown in Table 7.2. Selected from 1160 production cases, these examples show the diversity of production parameters. For these 1160 examples, the starting cooling temperature varies from 861 °C to 938 °C, and the strip thickness varies from 2.03 mm to 7.61 mm. The strip speed changes from 3.52 m/s to 10.45 m/s. The strip material is DQSK.

Table 7.2 Examples of cooling parameters

No.	Finish Temp. °C	Water Temp. °C	Water Flow Rate	Strip Speed m/min	Thickness mm	Bank State Code									
						BK1		BK2		BK3		BK4		BK5	
						T	B	T	B	T	B	T	B	T	B
2	884.61	25.78	F	627.1	2.03	124	124	62	62	0	0	0	0	30	30
5	879.12	24.34	F	619.0	2.03	124	124	126	126	2	2	0	0	14	14
17	893.77	26.37	F	625.7	2.03	124	124	126	126	14	14	0	0	14	14
34	881.26	28.29	F	592.5	2.17	124	124	126	126	6	6	0	0	14	14
40	873.63	25.78	F	467.1	2.29	124	124	2	2	0	0	0	0	14	14
55	893.95	28.77	F	598.4	2.29	124	124	126	126	30	30	0	0	30	30
68	877.42	26.10	F	557.4	2.42	124	124	126	126	126	126	14	14	14	0
79	876.86	26.31	H	506.3	2.54	124	124	30	30	0	0	0	0	14	0
86	895.96	25.19	H	585.8	2.79	124	124	126	126	62	62	0	0	14	0
99	890.02	23.16	H	451.5	2.92	124	124	62	62	0	0	0	0	6	0
130	907.12	24.18	H	516.9	3.26	124	124	126	126	126	126	6	6	14	0
149	901.75	25.89	H	467.5	3.56	124	124	126	126	62	62	0	0	14	0
155	891.03	22.41	H	424.8	3.68	124	124	126	126	6	6	0	0	14	0
160	901.46	29.25	H	393.3	4.19	124	124	126	126	2	2	0	0	126	126
165	891.14	21.13	H	303.9	5.08	124	124	126	126	14	14	0	0	6	6
178	904.03	24.71	H	343.5	5.46	124	124	126	126	126	126	62	62	14	0
192	902.04	26.15	H	225.6	7.61	124	124	126	126	126	126	0	0	14	14

BK: Bank; T: Top jets; B: Bottom jets; F: Normal flow rate; H: High flow rate

## 2. Results and discussion

All 1160 cooling processes are simulated by the developed program. In the simulations, half of the thickness is discretized with 40 elements. For reducing the calculation time, only 2 time steps and 4 time steps are assigned for each impingement zone and for each parallel zone, respectively. Also, the number of time steps is 2 for the air cooling zone between jetlines, and it is 10 for both of the entry and exit air cooling zones. The number of the total time steps is only 178 to 280 depending on the on-off status, as shown in Table 7.3. The smallest value of time step is 0.0022 s. Numerical experiments showed that using more time steps has little or no effect on the predicted coiling temperatures (Table 7.4).

The width coefficient of the impingement cooling zone to the nozzle diameter is fixed at 1.5. Moreover, the HTC factor for the parallel cooling zone is found to be 0.15 and 0.25 for the lower and higher flow rate, respectively. The temperature dependence of conductivity is considered while the latent heat is not considered.

Table 7.3 Examples of calculation results

Strip No.	Strip Thickness mm	Time Step No.	Measured Coiling Temp, $T_m$ , °C	Calculated Coiling Temp, $T_c$ , °C	$T_m/T_c$
2	2.03	192	664.31	651.0133	1.02042
5	2.03	200	639.21	640.6026	0.99783
17	2.03	216	641.96	641.9504	1.00002
34	2.17	208	642.76	643.0853	0.99949
40	2.29	152	639.95	646.4410	0.98996
55	2.29	232	651.39	649.4726	1.00295
68	2.42	264	649.56	627.0100	1.03596
79	2.54	176	638.64	630.2401	1.01333
86	2.79	232	644.25	639.1925	1.00791
99	2.92	176	638.88	640.4161	0.99760
130	3.26	256	640.20	632.1535	1.01273
149	3.56	232	637.65	643.3785	0.99110
155	3.68	208	641.49	642.5314	0.99838
160	4.19	224	642.91	642.7898	1.00019
165	5.08	208	640.36	637.2108	1.00494
178	5.46	280	639.65	630.0060	1.01531
192	7.61	240	639.38	629.7765	1.01525

Table 7.3 shows the calculation results of the coiling temperatures for the production examples shown in Table 7.2. It is apparent that the predictions are in good agreement with the measured coiling temperatures.

Figure 7.7 illustrates the ratios of the measured coiling temperatures to the calculated ones for the first 200 production cases among 1160 cases. It is clear that the prediction is within  $\pm 8\%$ , which is a reasonable and acceptable engineering range. Note that the prediction accuracy for all 1160 cases is also within  $\pm 10\%$ .

The general prediction accuracy postulates that the setup of the modelling and the coefficients are practical.

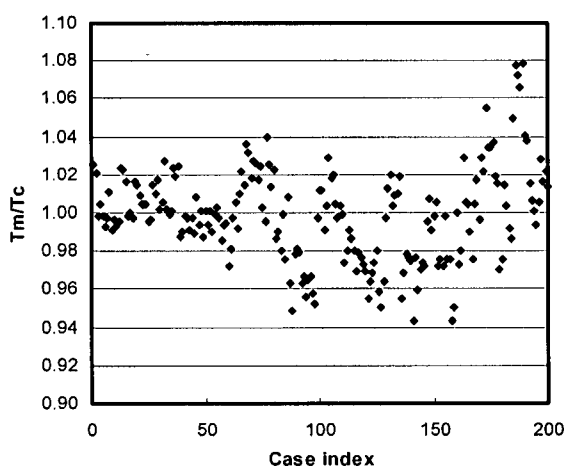


Figure 7.7 Prediction accuracy

Figure 7.8 shows the profiles of the top temperature and centre one along the thickness for Case 192. For this cooling case, four banks are active, which can be easily observed from the cooling curves. It is clear that for each of the water cooling zones (each active bank and jetline) the centre temperature is higher than that at the top surface. It is also evident that the top surface recovers between two banks, and that the recovery is much more obvious after the first bank and the third one. The fourth bank is not working and the strip experiences air cooling; therefore, the top surface quickly recovers to the centre one. The top temperature and centre one are nearly identical after the strip enters the exit air cooling stage.

The predicted coiling temperature is approximately  $629.78\text{ }^{\circ}\text{C}$  and is lower than the measured average one of  $639.38\text{ }^{\circ}\text{C}$ . However, this level of accuracy is acceptable.

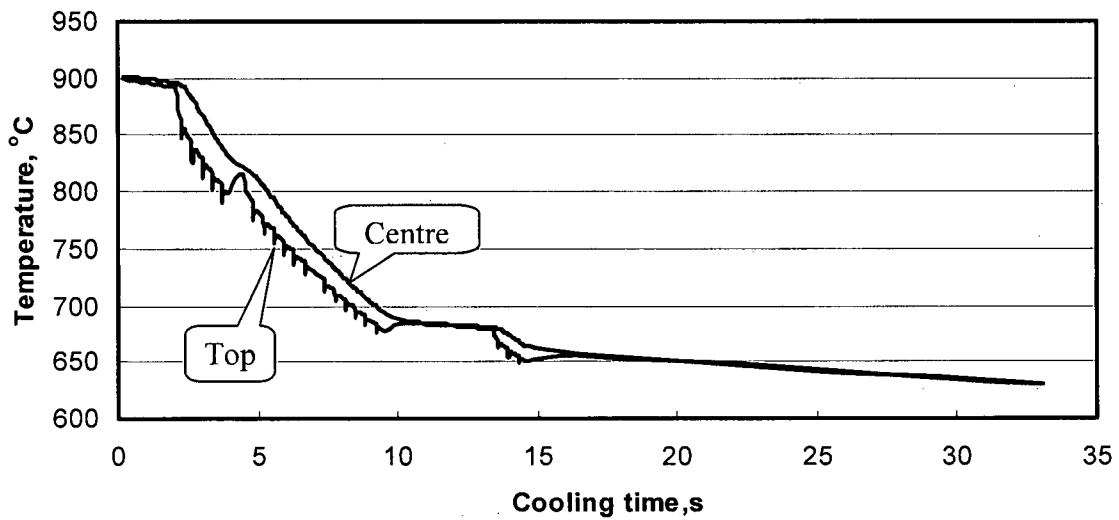


Figure 7.8 Temperature profiles for Case 192

Figures 7.9 and 7.10 illustrate the HTC values and the cooling behaviour around the first active bank (Bank1), respectively. At the air cooling stage, the HTC is small; the temperature difference between the top and the centre is small. When the strip enters the first parallel cooling zone, the HTC increases sharply and thus the surface temperature remarkably decreases accordingly. Note that the centre temperature decreases slightly.

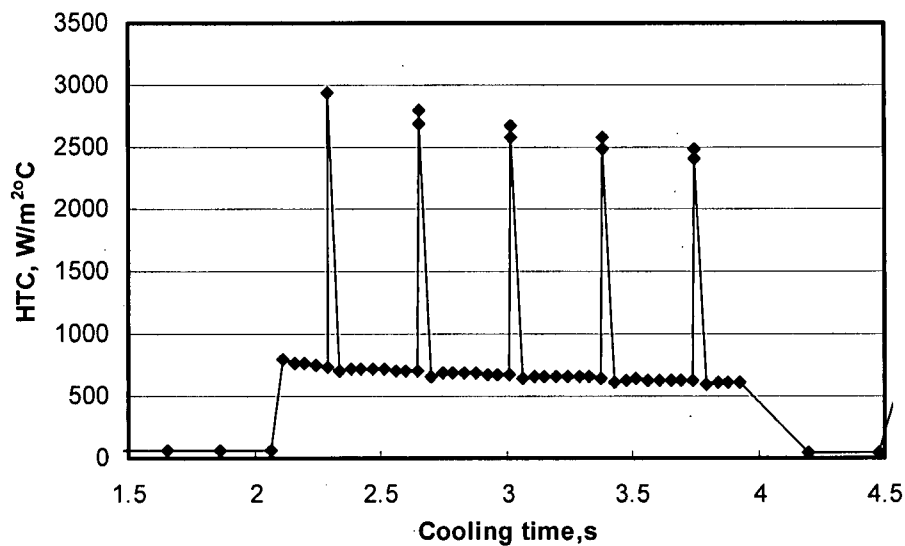


Figure 7.9 HTC profiles around the first bank for Case 192

As expected, the HTC increases to a higher value as the strip enters the first impingement cooling zone, and causes the surface temperature to drop suddenly. Because the impinging cooling time is very short, the cooling effect is confined within a limited depth beneath the surface. The heat transfers from the slightly cooled centre part to the surface, and then the surface temperature recovers. This sharp drop and recovery of the surface temperature repeats for each active jetline.

After the water cooling stage, the strip enters the spacing between two banks where air cooling is dominant. The surface temperature promptly comes back nearly to the centre temperature.

All of the cooling phenomena are reasonable and consistent with those in the literature.

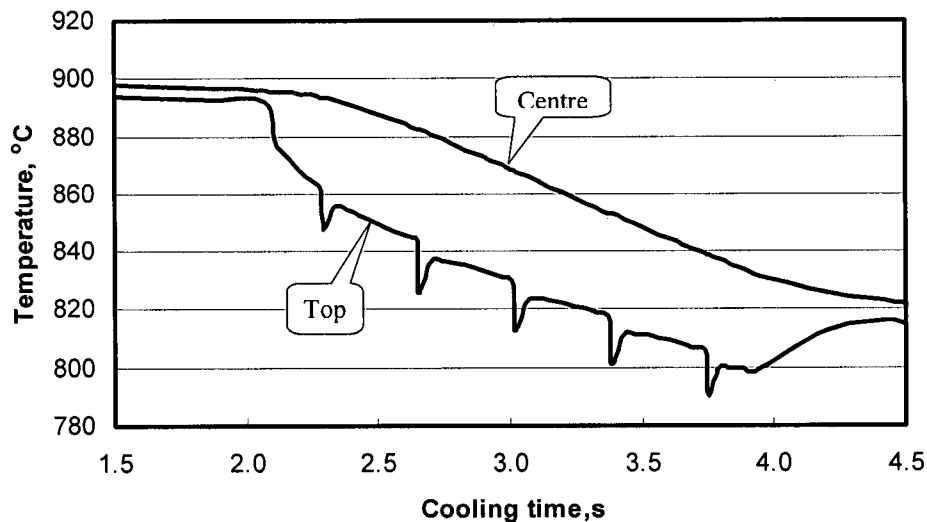


Figure 7.10 Temperature profiles around the first bank for Case 192

### 7.3.2 Parametric study

In this section, Case 192 is chosen to study the effects of various parameters on the coiling temperature, such as time stepping, impingement zone width (nozzle diameter), production parameters, material properties, and ROT configuration.

#### 1. Time step and impingement zone width

It is generally expected that time stepping may affect the simulation results and accuracy. As shown in Table 7.4, the predicted temperatures in this case have only a slight

difference as the total number of time steps increases as much as 8 times. This means that the size of time step (below the ones chosen for the simulation) has little effect on the predicted temperature. Therefore, the results in Section 7.4.1 can be assumed being independent of the time stepping. In addition, Set 1 in Table 7.4 can be used for other parameter studies.

Table 7.4 Effect of time step on the coiling temperature for Case 192

Set	NFAIR	NLAIR	NBAIR	NPARA	NIMPG	TOTAL	T <sub>c</sub> , °C
1	10	10	2	4	2	240	629.78
2	10	10	10	10	10	720	629.90
3	10	10	20	20	20	1420	630.00
4	100	100	20	20	20	1600	629.96
5	250	250	20	20	20	1900	629.96

The impingement zone width has dual-meanings. First, it is a numerically assigned value for a given nozzle and it may be adjusted to better predict the coiling temperature. Second, the impingement zone width may also be linked to the nozzle diameter and it should generally increase with the increase in nozzle diameter.

The effect of the impingement width on the coiling temperature is shown in Figure 7.11. It is obvious that the coiling temperature decreases nearly linearly with the increase of the impingement width. This is reasonable because the HTC in the impingement zone is much higher than that in the parallel zone.

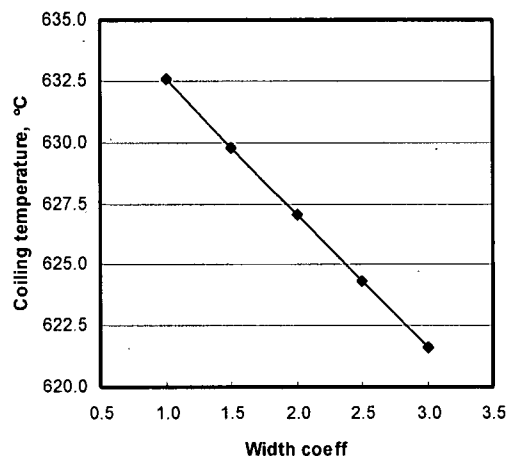


Figure 7.11 Effect of impingement width on the coiling temperature for Case 192

Note that the increase of the impingement zone width implies a decrease of the parallel zone length under the current setup of the cooling zone divisions. This may be the reason why the predicted coiling temperature decreases only 10 °C as the impingement zone width triples.

Based on the above finding and the general ratio of the impingement zone width to the nozzle diameter, the coefficient of 1.5 is reasonable and is used for the other parameter studies.

## 2. Production parameters

The production parameters included here are the starting cooling temperature, strip speed and thickness, and flow rate. The production parameters are artificially changed to investigate their effects on the coiling temperature and to check the reliability of the developed program.

Figure 7.12 illustrates the effect of the starting cooling temperature on the coiling temperature. Simulations show that the coiling temperature decreases from 661 °C to 572 °C with the decrease of the starting temperature from 1000 °C to 750 °C, and that the relationship can be correlated as linear for the common temperature range. Every drop of 50 °C in the starting temperature will lead to a decrease of 18 °C in the coiling temperature. This means that a certain decrease of the coiling temperature cannot be realized by reducing the starting temperature with a same magnitude; i.e., the influence of the decrease in the starting temperature is diminished.

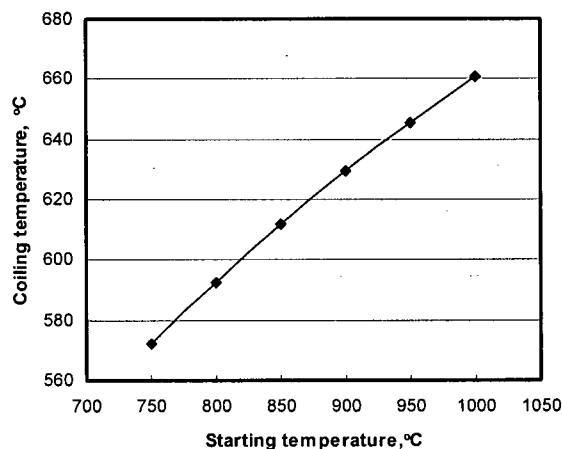


Figure 7.12 Effect of the starting temperature on the coiling temperature for Case 192

The strip speed is a critical parameter in the strip production. In general, the cooling time decreases as the strip moves faster. The effect of the strip speed on the coiling temperature is depicted in Figure 7.13. For the fixed on/off status of the jetlines, the coiling temperature increases significantly from 585 °C to 700 °C as the strip speed changes from 3.0 m/s to 5.5 m/s. It is clear that the strip speed has a significant effect on the strip coiling temperature.

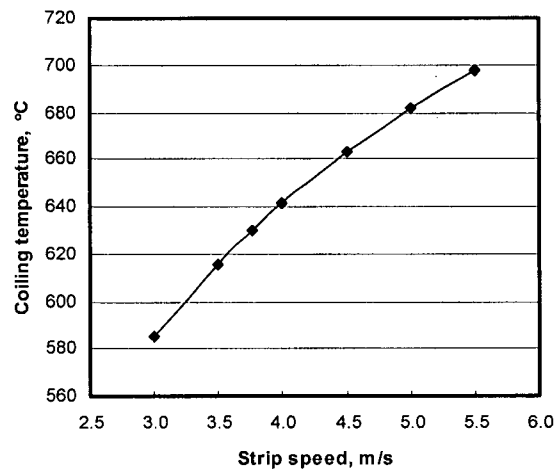


Figure 7.13 Effect of the strip speed on the coiling temperature for Case 192

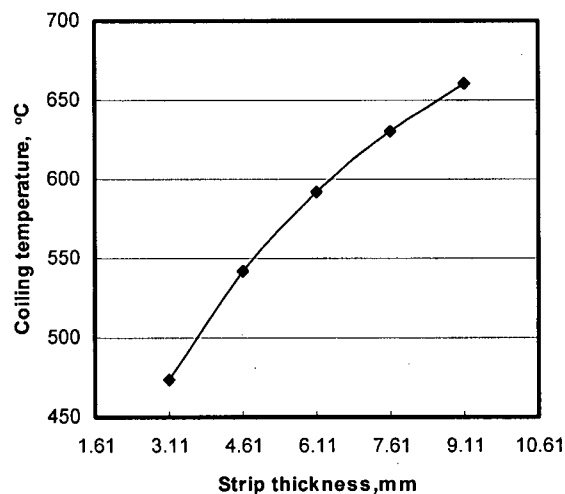


Figure 7.14 Effect of the strip thickness on the coiling temperature for Case 192

Similarly, for the fixed on/off status of the jetlines, the coiling temperature increases considerably from 473 °C to 660 °C as the strip thickness changes from 3.11 mm to 9.11

mm, as shown in Figure 7.14. The total heat amount is proportional to the thickness and is larger for a thicker strip than for a thinner one. As the heat that can be extracted by the cooling apparatus is mainly determined by the on-off status, the coiling temperature is higher for the thicker strip.

The water flow rate can be another important parameter affecting the coiling temperature. In the developed program, this parameter is not explicitly present in any correlation. It is found by the simulations that to obtain consistent and satisfactory predictions a larger coefficient should be used for the HTC correlation for the parallel zone when a higher water flow rate is used. This is consistent with the discovery in Section 6.4. For Case 192, the coiling temperature is 629.78 °C as the water flow rate is of the higher level. If the water flow rate is changed to the lower level, the coiling temperature becomes 677.38 °C with an increase of about 50 °C.

### 3. Material properties

Material properties refer to the strip conductivity and specific heat in this discussion. Their effects on the coiling temperature are shown in Figures 7.15 and 7.16. In these investigations, constant values are input.

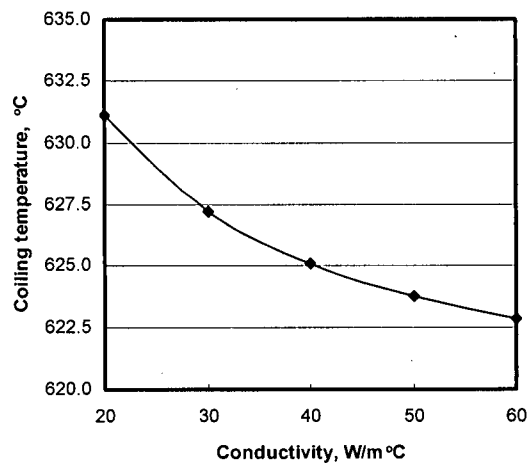


Figure 7.15 Effect of the strip conductivity on the coiling temperature for Case 192

Figure 7.15 shows that the conductivity has a slight effect on the coiling temperature. The coiling temperature decreases only by 10 °C as the conductivity triples. It is interesting to point out that the coiling temperature is 627.17 °C with a constant conductivity of 30

$W/m \cdot ^\circ C$ , which is just the average value for the temperature range of 100–1000  $^\circ C$ . Recall that the coiling temperature is 629.78  $^\circ C$  as the temperature dependence of conductivity is considered. Thus, an average value may be a good option to replace the temperature dependence. This approach may greatly reduce the calculation time, and is used in the 2D modelling.

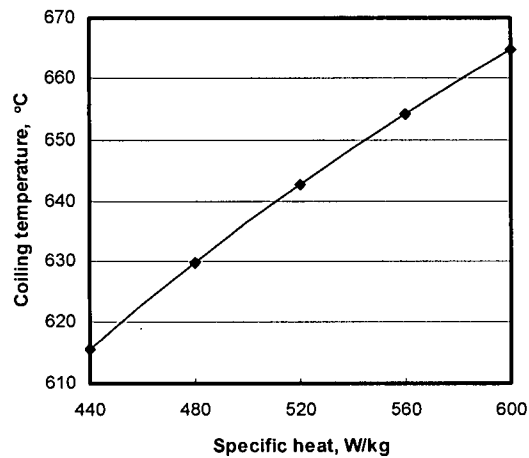


Figure 7.16 Effect of the strip specific heat on the coiling temperature for Case 192

In all calculations except those in Figure 7.16, the specific heat is fixed at 480 W/kg. The specific heat of the DQSK has a weak temperature dependence and does not change much. The values of the specific heat in Figure 7.16 are artificial and may not be practical.

While the increase of the conductivity slightly reduces the coiling temperature, the increase of the specific heat increases to some extent the coiling temperature. This is because a higher specific heat represents a higher heat amount in a unit volume. This result is similar to the case of increasing the strip thickness.

#### 4. ROT configuration

In this section, the jetline distance  $b_1$  and the bank distance  $L_2$  are changed to investigate the effect of ROT configuration on the coiling temperature.

Two situations are designed for changing the jetline distance  $b_1$ . In the first one all jetline distances are changed while in the second one only the jetlines within the first bank is adjusted to new values. The results are shown in Figure 7.17.

It is clear that the coiling temperature decreases when the distances  $b_1$  increase. This is because in this program the increase of jetline distance is equivalent to the increase of the parallel zone lengths. The water cooling time increases as the parallel zone lengths increase. Therefore, the coiling temperature decreases. The nearly linear correlations also reveal that the decrease of the coiling temperature is mainly caused by the increase in the cooling time.

Comparing the two curves leads to another conclusion that the contribution from the first bank to the reduction of the coiling temperature is about 26.9%, only slightly higher than 25%. Recall that four banks are active and 20 jetlines are working for Case 192 (Tables 7.1 and 7.2). Five jetlines in the first bank are active and are exactly one quarter of the total working jetlines. The reason the contribution of the first bank is slightly higher may be because the surface temperature at the first bank is at the highest level for the four banks and the HTC is higher.

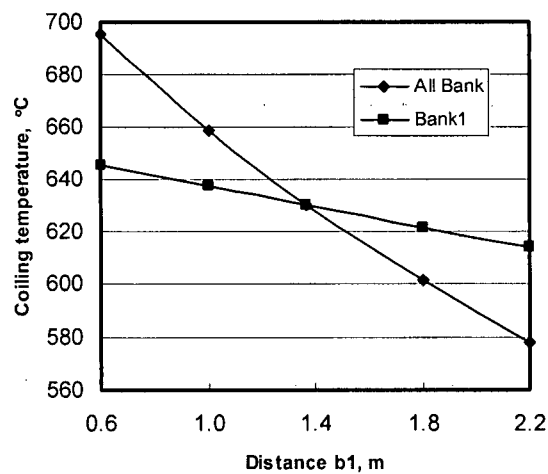


Figure 7.17 Effect of the distance  $b_1$  on the coiling temperature for Case 192

The increase of the bank distance may create two phenomena: first, the air cooling time increases; second, the top surface temperature may recover close to the centre temperature, which increases the cooling efficiency during the subsequent water cooling process. Both of the phenomena result in a decrease in the coiling temperature. The curve shown in Figure 7.18 verifies this analysis. The reason why the change of the coiling temperature is very small is that the increase of the cooling time is only about 1 s.

All of the findings discussed above are consistent and reasonable. This means that the developed program is reliable and can be used to predict the coiling temperature and the profiles of cooling temperature with an acceptable accuracy.

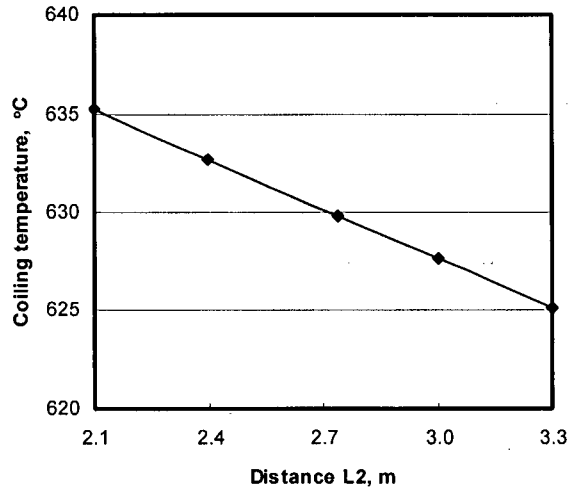


Figure 7.18 Effect of the distance L2 on the coiling temperature for Case 192

#### 7.4 Investigation of Necessity of 2D Simulation of ROT Cooling

It is proposed that the simulation of ROT cooling be performed using 2D or 3D modelling to uncover the effect of heat transfer in the longitudinal (moving) direction or/and in the transverse (width) direction on the temperature profile and to get a more accurate prediction of the coiling temperature. In this section, both 2D transverse and 2D longitudinal modelling are conducted to assess this matter.

##### 7.4.1 2D transverse modelling

###### 1. Modelling aspects

One of the basic requirements for the ROT cooling system is that the cooling must be uniform in every location of the top and bottom surfaces, edge and center, and leading and trailing ends. Setting appropriate transverse gradient for water flow from centre to edge along with edge masking devices may greatly reduce or prevent transverse temperature gradient and buckling leading to edge weaves. However, the cooling along

the width cannot be uniform in practical productions. A difference of 10% between the HTC's at the width centre and at the edge was reported and used in simulations in literature [83].

For the cooling with multiple jets in one jetline, there is an interaction zone between two adjacent jets except for the parallel and impingement zones. The local HTC's are definitely different between two adjacent jets.

Though the width of strips depends on the rolling facilities and the product specifications, it is, generally, in the order of one meter and it is not practical to model the whole width. Note that the distance between two adjacent jets in one jetline is usually 200–400 mm and that the temperature gradient may be changed by artificially adjusting the magnitude of the HTC difference. Therefore, a width of 150 mm is assumed in the modelling by assuming that the average jet distance is 300 mm and the cooling is symmetrical to the middle of the two jets.

Case 192 is simulated with 2D modelling. Thus, a cross-section of 150×3.805 mm is discretized with 150 uniform elements in the width direction and 10 fine-to-coarse elements in the thickness direction.

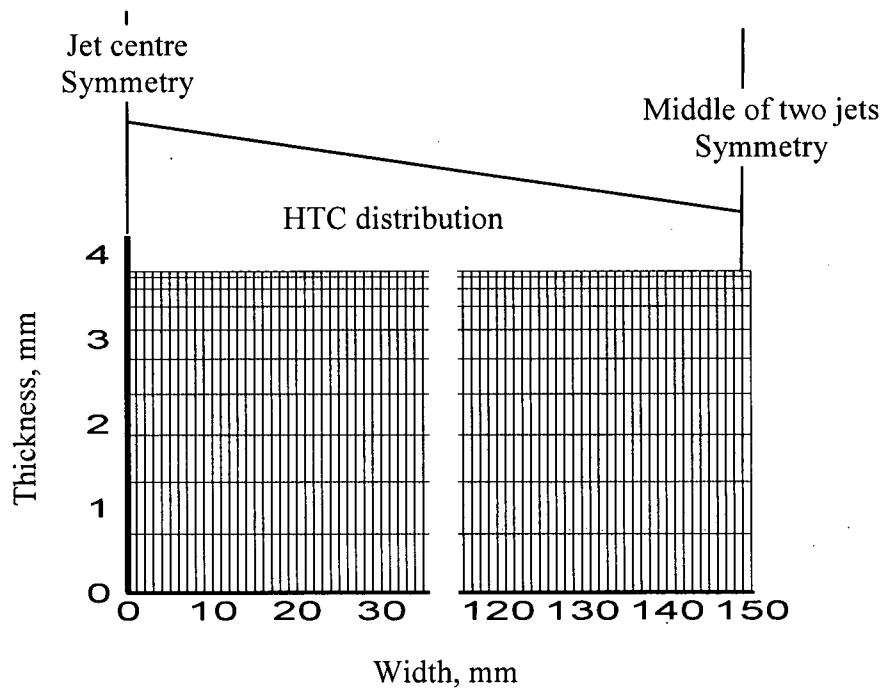


Figure 7.19 2D transverse modelling

The HTC on the top surface is still calculated based on equation (7.18) with a linear correlation in the function of the width. The nominal HTC difference is assumed being 2.5% to 15% across the 150 mm. The other three sides are assumed thermally insulated because all of them are have symmetrical conditions. The above arrangements are schematically shown in Figure 7.19. Note that the dimension sizes are not to scale.

The reason why the difference in HTC is nominal is that the actual HTC also depends on the surface temperature. The surface temperature is higher at a point with a smaller HTC coefficient than at a point with a larger HTC coefficient. Therefore, the actual HTC difference is slightly less than the nominal one. The time stepping scheme is chosen to Set 1 in Table 7.4.

## 2. Results and discussion

The simulation results are shown in Figure 7.20. In this graph, there are two curves for the coiling temperatures, one with higher HTCs (H-HTC) and the other with lower HTCs (L-HTC).

It should first be mentioned that the coiling temperatures at the two corner points are 629.64 °C if the HTC is uniform. Recall that the coiling temperature is 629.78 °C by 1D model with 100 elements in the thickness direction. These two temperatures are very close, which implies that the number of elements (higher than 40) has little effect on the predicted coiling temperature, and that 40 elements are enough to get an accurate result with respect to the discretization.

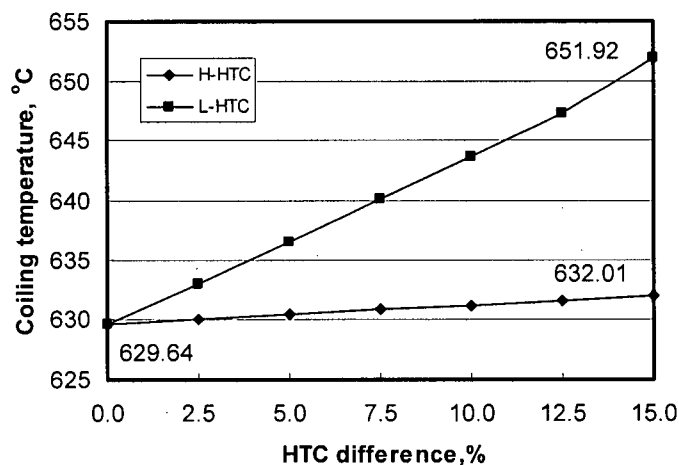


Figure 7.20 Effect of transverse HTC difference on the coiling temperature for Case 192

As expected, the coiling temperatures at the top corner point with higher HTC's are always lower than those at the top corner point with lower HTC's. This is reasonable because more heat is extracted away when HTC is higher. It is clear that as the HTC difference increases from zero to 15%, the coiling temperatures at the top corner point with higher HTC's do not evidently change while the coiling temperatures at the top corner point with lower HTC's increases from 629.64 °C to 651.92 °C. It may be inferred that the transverse heat transfer is not active.

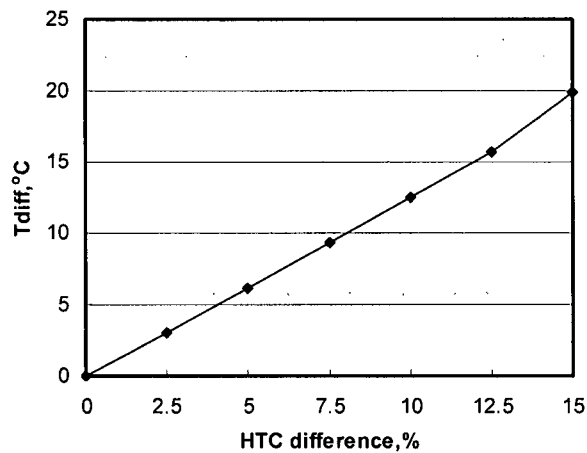


Figure 7.21 Effect of transverse HTC difference on the coiling temperature for Case 192

The difference between the two coiling temperatures is shown in Figure 7.21. The coiling temperature difference is about 20 °C when the HTC difference is 15%. These two values uncover very important messages.

First, it is possible that there is a 15% difference in the HTC's between the jet centre and the middle of two jets. In this case, the local coiling temperature difference reaches 20 °C. The importance lies in that the overall coiling temperature difference across the width is also around 20 °C because the HTC difference changes periodically for every two adjacent jets.

Second, it is assumed that in practice the 15% difference in the HTC's is for a half width of the strip of 1.0 m. In this case, the overall coiling temperature difference across the width may be less than, or at maximum equal to, 20 °C.

A temperature difference of 20 °C is acceptable for a 15% HTC difference. In steel strip production a variety of measures is adopted to keep the cooling temperature across the width as uniform as possible. The HTC difference would be less than 15% and cause less change in the coiling temperature across the width. Therefore, it can be concluded that the 2D transverse simulations has little impact on the final coiling temperature.

Figure 7.22 shows the temperature distributions on the cross-section at the time step 100 and 240 for a 15% HTC difference. It clearly shows that the temperature becomes more and more uniform over time.

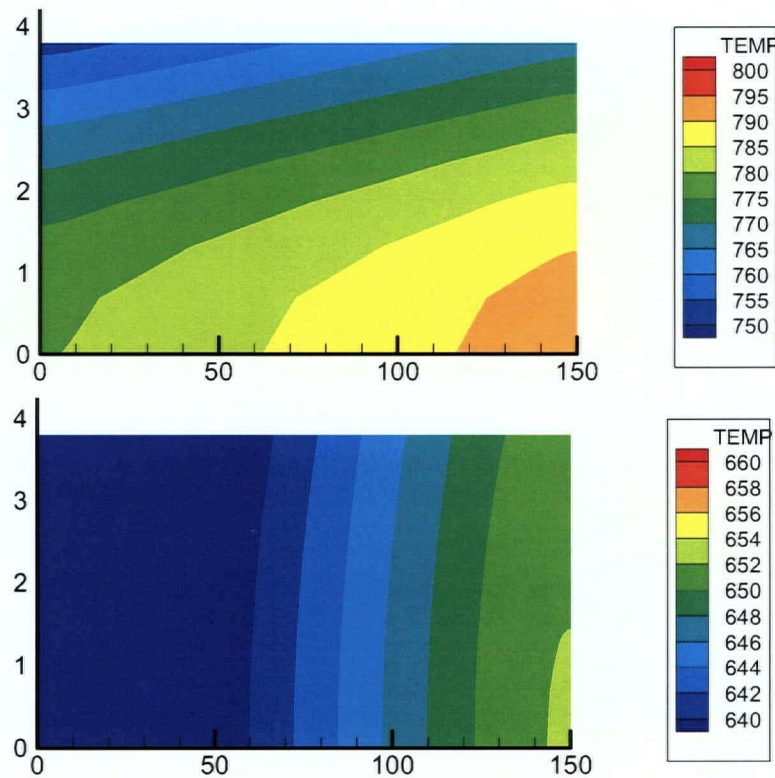


Figure 7.22 Temperature distributions on cross-section  
Upper: time step 100; bottom: time step 240

## 7.5.2 2D longitudinal modelling

### 1. Modelling

The geometry and mesh stated in Section 7.5.1 are also used here with the difference that the length direction of the model is along the longitudinal direction. The choice of the

length of 150 mm is because the impingement zone is 45 mm in length in the above reference 1D calculations.

Four cases are studied, as shown in Table 7.5. For all one and two jetline cases, the entire model is in the parallel cooling zone-B and its right side is 250 mm apart from the jetline centre for the first time step. Then it moves through the impingement zone. It stops as its right side passes the jetline centre with a distance of 250 mm. The movement of the model is illustrated in Figure 7.23. . There is no heat transfer assumed due to bulk motion.

Table 7.5 Longitudinal modelling parameters and results

Case		752-1	752-2	752-3	752-4
Initial Temp, °C		902	902	902	650
Moving speed, m/s		1.0	10.0	1.0	1.0
Moving distance, m		0.5	0.5	1.0	1.0
Time step		500	500	1000	1000
Jetlines passed		1	1	2	2
1 <sup>st</sup> jetline	-ve T <sub>diff</sub> , °C*	-2.6249	-0.5998	-2.6249	-1.6663
	+ve T <sub>diff</sub> , °C*	2.2107	0.5084	2.2107	1.4276
2 <sup>nd</sup> jetline	-ve T <sub>diff</sub> , °C*	-	-	-2.4808	-1.5900
	+ve T <sub>diff</sub> , °C*	-	-	2.1031	1.3667
Final T <sub>diff</sub> , °C*		0.0172	0.0063	0.0000	0.0108

\* More significant digits are intentionally kept for comparison

The bottom of the model is assumed to be thermally insulated. The critical issue is how to assign the boundary conditions on the left side and right side. Thermal insulations were assumed for both sides in reference [83]. Our numerical studies also showed that the influences of the boundary conditions on these two sides are extremely localized and will not affect the temperature at the middle of the piece. Even though this approach may not reflect the reality on ROT it is still used in this study.

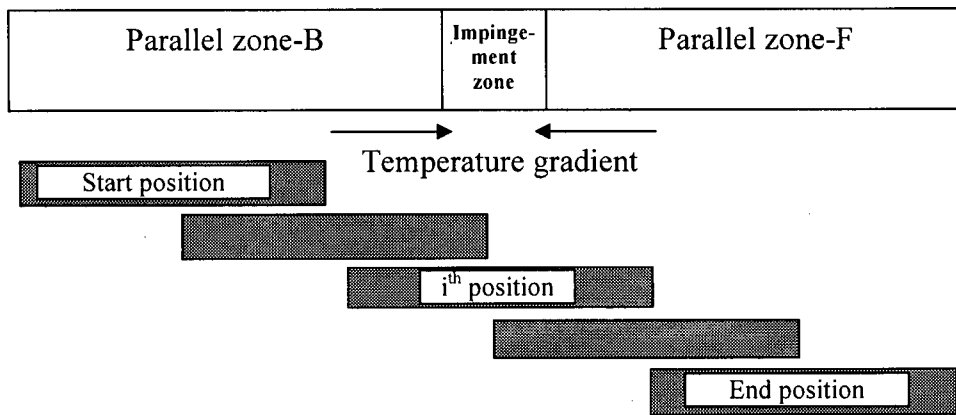


Figure 7.23 Movement of model piece

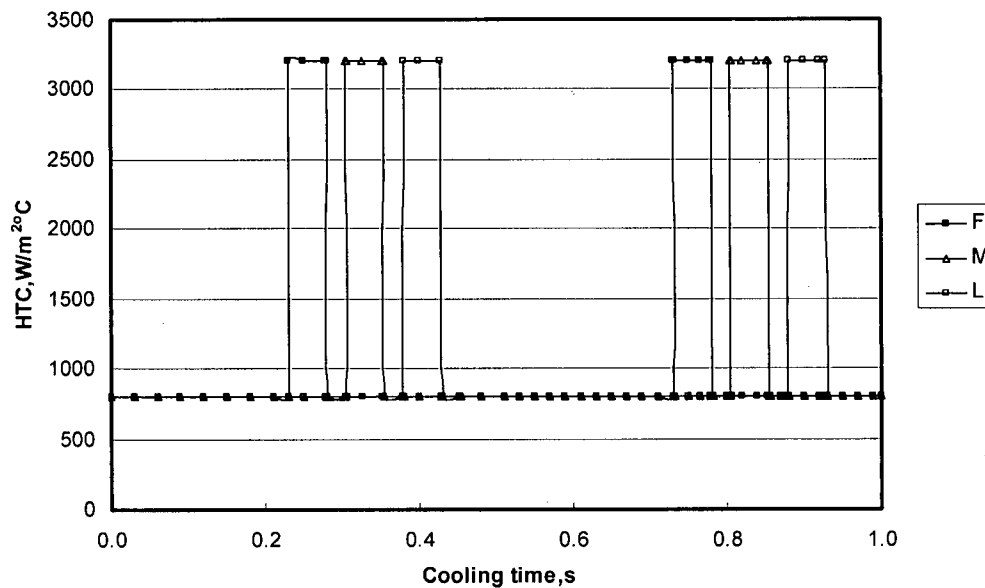


Figure 7.24 HTC values for the two-jetlines cases

The HTC condition is applied to the top surface. The time-space shift scheme discussed in Section 4.4.3 is adopted and is not repeated here. Based on the HTC shown in Figure 7.9, two constant values of  $800 W/m^2 \cdot ^\circ C$  and  $3200 W/m^2 \cdot ^\circ C$  are assumed here for the parallel and impingement zone, respectively. Figure 7.24 shows the HTCs on the first, middle and last nodes (F, M, and L in the figure) for the two-jetlines cases.

Note that the temperatures at the middle node on the top surface in the 2D models are compared with those from the 1D model with the same HTC profiles. This is more

reasonable because the effect of the alternative change of heat flux in the longitudinal direction can be included in the temperature profile at the middle node, and because the influence of the boundary conditions at the left and right sides is diminished.

## 2. Results and discussion

The surface temperature differences from 1D and 2D modelling are also shown in Table 7.5. It is apparent that there is very little discrepancy between 2D predictions and 1D ones. Some detailed discussion follows.

Figure 7.25 shows the 2D-temperature and 1D-2D-temperature difference for Case 752-1. Note that all the simulations have shown that the 1D temperature and 2D temperature are nearly identical for the middle nodes for the entire cooling time.

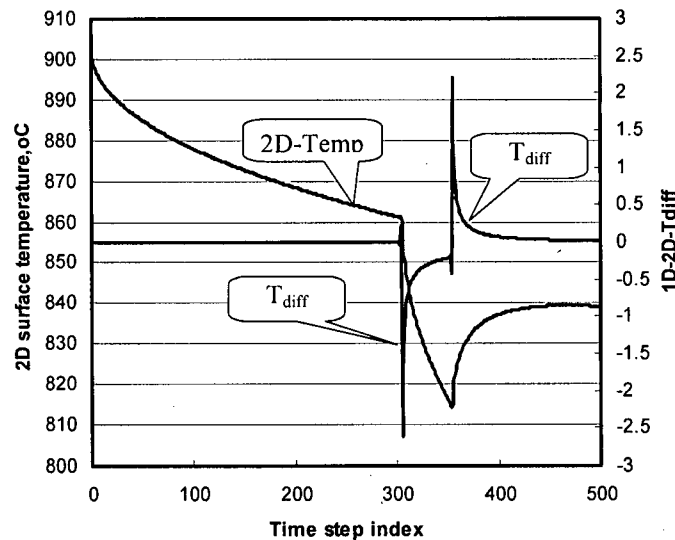


Figure 7.25 2D-temperature and 1D-2D-temperature difference for Case 752-1

For all cases, the middle point enters and leaves the first impingement zone at time step 305 and at time step 355, respectively. It is clear that the temperature decreases smoothly before the material enters the impingement zone, and there is no difference between the temperatures from 1D and 2D predictions.

The temperature drops sharply as the material enters the impingement zone. Correspondingly, the temperature difference  $T_{2D}-T_{1D}$  suddenly increases from zero to a negative value of 2.63 °C, which is the maximum temperature difference. This can be explained as follows. For the 2D model, the left side of the middle point is still in the

parallel zone as the middle point enters the impingement zone; and a temperature gradient appears and longitudinal heat transfer occurs from left to right (Figure 7.23), which leads to a 2D temperature lower than the 1D one. As more material points enter the impingement zone, the temperature gradient around the middle point promptly decreases and then the temperature difference decreases.

In contrast, the temperature starts to recover as the middle point leaves the impingement zone and enters the parallel zone-F. At this time instant, more heat is transferred from the right side of the materials, which have already recovered, and makes the 2D temperature at the middle point recover faster. Thus, the 2D temperature is higher than the 1D one and the temperature difference  $T_{2D}-T_{1D}$  is positive. Note that the positive temperature difference is 2.21 °C. Because the temperature in the parallel zone-F is lower than that in the parallel zone-B, the value of the temperature gradient at the left side is higher than that at the right side. Therefore, the positive temperature differences are always less than the negative ones. This feature is verified by all cases.

Again, as more and more points enter the parallel zone-F, the temperature gradient decreases and the difference between 2D and 1D diminish. By the end of the simulation, the temperature difference  $T_{2D}-T_{1D}$  is only 0.0172 °C, which has no effect on the prediction of the coiling temperature.

Simulations show that the maximum temperature difference  $T_{2D}-T_{1D}$  decreases with the increase of the strip speed. The reason is that the alternative change of temperature gradient changes in a shorter time and the longitudinal heat transfer has modest influence when the strip speed increases.

Similarly, the maximum temperature difference  $T_{2D}-T_{1D}$  decreases with the decrease of the initial temperature. That is because the temperature gradients are smaller when the temperature is lower.

It is worth examining the two-jetlines cooling process. There are two reasons for setting up the jetline distance at 500 mm. First, it can reduce the calculation time in 2D modelling. In fact, a longer parallel zone contributes little to the temperature difference  $T_{2D}-T_{1D}$ . Second, it is based on industry ROT parameters. For some ROTs, there are two jetlines in a header. The distance for these two jetlines is around 500 mm.

It can be inferred from the data in Table 7.5 that a continuous two-jetlines cooling will not enhance the longitudinal heat transfer.

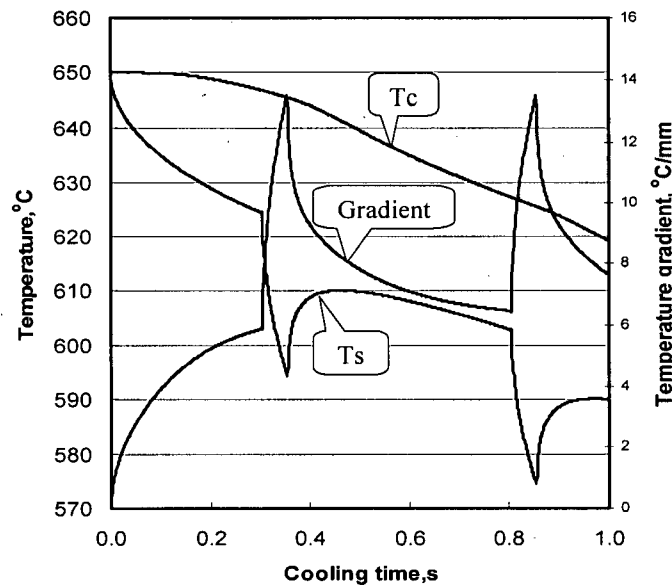


Figure 7.26 2D-temperatures and gradient for Case 752-4

The 2D two-jetlines cooling simulations have an implicit importance. For the one-jetline cooling, the initial temperatures are uniform across the section. However, as shown in Figure 7.26, after the strip is cooled by the first jet during the two-jetline cooling process, the temperatures at the top surface and at the centre are not the same, and there is a larger temperature gradient along the thickness direction. This means that the initial temperature condition for the second jetline cooling is not uniform. This non-uniformity does not affect the temperature difference  $T_{2D}-T_{1D}$ .

The data of Case 752-4 suggest important information for the ROT cooling. The final cooling stage on ROT takes place around 650 °C, and is a fine-tuning for the right coiling temperature. Usually, one or two jetlines are active. Before this final cooling stage, the strips experience a longer air cooling period; their temperatures are generally uniform through the thickness. The results show that there is no difference between 1D and 2D modellings.

## 7.5 Summary

A special FE program is developed for the simulation of the ROT cooling process. 1160 cooling processes of steel strips on an industrial ROT conditions are successfully simulated using 1D modelling. The predictions of the 1D model simulations are of an accuracy of  $\pm 10\%$  with a comparison to the field measurements. All of the findings in the parametric studies are consistent and reasonable. It is concluded that the developed program is reliable and can be used to predict the coiling temperature and the profiles of the cooling temperature with an acceptable accuracy.

The effect of non-uniform heat flux in the width direction on the coiling temperature is investigated using transverse 2D modelling. The coiling temperature difference may be up to 20 °C when there is a 15% HTC difference across the width. In steel strip production a variety of measures is adopted to keep the cooling across the width as uniform as possible. The HTC difference would be less than 15% and cause less change in the coiling temperature across the width. Therefore, it can be concluded that the 2D transverse simulations may not be necessary.

It is found by the longitudinal modellings that the longitudinal heat transfer is fairly localized and concentrated around the entrance and exit of the impingement zones. It is also found that the temperature differences between 1D and 2D modellings are less than 3 °C and tend to be zero. All of these suggest that the longitudinal 2D modelling is not necessary for simulating the ROT cooling process.

## Chapter 8

### CONCLUSIONS AND FUTURE WORK

#### 8.1 Conclusions

The controlled cooling process of steel strips on ROT is the critical stage for obtaining a desired combination of mechanical properties. Although it has been used in the steel industry for decades, this cooling process is mainly still a trial-and-error procedure as new products are to be developed, because the thermal events during the cooling process are very complex and a fundamental understanding of this process is not yet complete.

A group of researchers at UBC has been performing both experimental investigations using a test facility of industrial scale and numerical simulations on this cooling process in order to develop novel properties of steel strips.

This study engages in acquiring reliable heat transfer data and developing an effective and robust FE simulation of the cooling processes on ROT. Several aspects of this work have been finished to realize the objective. These are summarized in the following points.

##### 1. 2D FE program for direct heat transfer analysis

A general 2D FE heat transfer analysis program has been developed. The 2D FE program is able to analyze both state steady and transient heat conduction problems. Various boundary conditions such as specified surface temperature, surface and nodal flux, convection and radiation as well as heat generation can be considered, all of which can be functions of location and time. In this program, the temperature dependence of thermal properties can be taken into account.

In addition, a choice of implicit and explicit solution algorithm, consistent and lumped capacitance matrix is available. Frontal solver is adopted for the non-symmetric stiffness matrix. Besides, the program is capable of using a mixture of element types. Test cases showed that the developed FE program has compatible accuracy with the commercial program ANSYS [58].

## **2. 2D FE program for inverse heat conduction analysis**

An algorithm for inverse heat conduction analysis is developed and implemented into the above 2D FE program. In this method, the least-squares technique, future time step technique, zeroth order regularization and sequential function specification as well as iterative technique are used. The sensitivity matrix is only calculated once at the beginning of the iterative procedure and used for all steps. The iterative technique can compensate for the use of the regularization parameter and the simplification in sensitivity matrix calculation to reduce the CPU time while maintaining accuracy. Both absolute and relative norms are used to obtain a reasonable convergent solution.

## **3. Characterization of impingement cooling**

The division and progression of water cooling zones on the top surface of hot plate during water jet cooling is analyzed in detail. The cooled surface under one free water jet can be generally divided into the impingement zone and the parallel zone. The cooling zones are symmetrical about the stagnation point for a stationary single circular jet. Only the material points in the impingement zone are simultaneously cooled; any material point outside of the impingement zone is sequentially cooled. The further the point from the stagnation point, the later it is cooled. The progressing speed of the water cooling zones is much lower than the jet velocity and is of  $\sim 10$  mm/s for the tests described in this study. For the moving plate case, the cooling zones are only symmetric about the plate moving direction and become a pearl shape or a comet shape whose long axis follows the moving direction. The velocity of water can be neglected, and the plate is cooled by a moving pattern of cooling water. The moving speed of the cooling pattern is fairly close to the plate's moving speed.

## **4. Flux Zoning Method (FZM)**

The commonly used Flux Zoning Method (FZM) is clarified and first used to specify the heat fluxes on the cooled surface. The approach is to divide the target surface into several subregions and each subregion corresponds to one temperature measurement and one heat flux value that is calculated using the proposed inverse algorithm.

Parametric study results of the inverse calculations using the FZM approach indicate that the fluctuation of inversely calculated heat flux due to random error in the measurement

data may be damped by increasing the number of future steps and regularization parameter. It is shown that the presented algorithm and procedures are very simple, and effective in recovering the heat flux history around the impingement zone. It has been found that the FZM may not be an appropriate method for the cooled surface outside of the impingement zone because it does not consider the water movement.

### **5. Time-space shift scheme**

A time-space shift scheme has been designed to assign the heat flux boundary condition for the moving water situations. The heat flux history on the precedent nodes is shifted to the subsequent nodes according to the assigned speed and element length. This scheme means a space-time-marching approach and implies that the cooling condition for all points in the parallel zone is almost identical except for a time shift and small temperature drop due to the longer air cooling period.

### **6. Flux Marching Method (FMM)**

A new approach named Flux Marching Method (FMM) is developed for considering the water movement. A main feature of the FMM is the essence of wave propagation. In this method, the cooling surface is still divided into several subregions and each subregion corresponds to one temperature measurement. The heat flux at the first node for each subregion is inversely calculated from the internal measured temperature, and functions as the impetus of the wave and the flood of the heat flux would sweep the points in each individual subregion. Numerical tests show that the FMM provides a more accurate recognition of input heat flux for the parallel zone in the inverse calculations if the flux marching speed matches correctly with the progressing speed of water cooling zones.

### **7. Investigations of temperature measurement errors**

Two kinds of situations have been considered for the assessments of measurement errors associated with both surface and imbedded TCs with separation measuring junction: one for the simultaneous cooling of the two wires of TCs referring to those in the impingement zone, and the other for the sequential cooling of the two wires of TCs in the parallel zone. In these numerical tests, the input heat flux is of the order of practical cooling. For the sequential cooling simulation, the space-time shift scheme is used.

It has been found that the conduction of surface TC wires in a water jet cooling process leads to two kinds of effects on the measured temperature in the case of water impingement cooling. First, the surface temperature field is disturbed and becomes non-uniform and the average temperature around the measuring junction would be lower than the true temperature. Second, the measuring junction with a separation installation is no longer an isothermal junction. The plate metal works as the third wire and may cause an additional deviation in measurements. The combination of these two effects leads to a measurement error of about 60 °C lower than the true value. It has also been found that the attachment of TC on the surface has little effect on the internal temperature 1 mm below, and that the attachment of TC in the hole has little effect on the surface temperature.

The disturbance of the temperature field due to the introduction of a small hole for the installation of interior TC is similar but has less pronounced effects on the surface measurement. An increased distortion of the temperature field is evident when TC is attached to the top surface directly above the bottom surface of the hole.

Numerical tests show that the non-simultaneous cooling of the two wires of internal TCs has pronounced effects. It has been found that the isothermal condition does not exist for the separate roots of TC wires, as the connection line of the two roots is parallel to the water moving direction. The maximum temperature difference between the TC wire roots will be affected strongly by the progressing speeds of water cooling zones and heat flux magnitudes, and mildly or slightly by heat flux profiles and the depths of the hole and specific heat values. The temperature difference between the two roots may reach a significant level for both surface and interior TCs, especially for the situations in which a deeper hole (close to cooling surface) is used to install TCs and the water moves slowly with a higher cooling capacity.

It may be concluded that TC with separate measuring junction should be, generally, avoided in temperature measurements of water cooling in moving cases; i.e., when the water moves or the plate is not stationery or both.

## **8. Investigation of appropriate locations of TCs**

Appropriate distance  $l$  between TCs and TC depth  $h$  are investigated using direct FE analysis in this study. It has been found that the distance  $l$  should be less than 8–10 mm to attain a real 2D inverse calculation and to improve the stability of inverse calculation when the measured temperatures are used for inverse calculations by the FZM. It is also postulated that there is a minimum depth for the embedded TC, at which the surface temperature may not be disturbed by the inclusion of the hole for the embedded TC and the cooling behaviour may not be affected.

## **9. Effective depth approach**

An effective depth approach (EDA) is suggested through intensive numerical simulations. A linear correlation is found between the actual TC depth and the effective TC depth for the actual depth of 1 mm to 3 mm. This approach is a possible method for including the hole effect in the inverse calculations of heat flux, without including the hole itself.

## **10. Investigation of heat transfer behaviour in the impingement zone**

The developed inverse analysis program and techniques are used to determine the surface heat flux and heat transfer behaviour during the water jet cooling process using both stationary and moving plates. The FZM and FMM for specifying the heat flux distribution on the cooling surfaces as well as the EDA are used in those analyses.

The heat transfer at the stagnation point or in the impingement zone of stationary plates cooled by an industry scale circular water jet cooling is successfully determined using 2D models with the FZM. Analysis results show that the heat transfer behaviour at the stagnation is mainly and greatly affected by water temperature, slightly affected by the steel grade and hardly affected by water flow rate. When the water temperature is lower than 60 °C the cooling process is governed by transition boiling, nucleate boiling. When the water temperature is higher than 60 °C, there is evidence of a film boiling regime. The features of boiling curves and the typical values obtained are in good agreement with other resources.

### **11. Investigation of heat transfer behaviour in the parallel zone**

The FMM and EDA are used for the parallel zone. It has been found that the water flow rate is the key factor in the parallel zone, that it affects both the mode and the magnitude of heat transfer, and that the conductivity mainly influences the heat flux values. However, the initial water temperature has little effect on the heat transfer in the parallel zone.

### **12. Investigation of plate motion effect**

The FZM and EDA are used for the moving plate tests. It has been found that increasing the plate speed leads to a decrease in heat fluxes for a given water temperature and water flow rate.

### **13. 1D simulation of ROT cooling process**

Special FE programs are developed to simulate the ROT cooling process. The 1D FE modular program is an interactive one and can be referred to special designs of ROT by the input files. It is user friendly and convenient to implement microstructure evolution equations for different steel grades, formula or empirical models for heat transfer, and correlations between cooling parameters, microstructure and mechanical properties.

1160 cooling processes of steel strips on an industry ROT are successfully simulated using the 1D modelling. The predictions of 1D model simulations are of an accuracy of  $\pm 10\%$  when compared to field measurements. The developed program is reliable and can be used to predict the coiling temperature and the profiles of cooling temperature with an acceptable accuracy.

### **14. Investigation of necessity 2D simulation of ROT cooling process**

The effect of non-uniform heat flux in the width direction on the coiling temperature is investigated using a transverse 2D modelling. The coiling temperature difference may be up to 20 °C when there is a 15% HTC difference across the width. It has been found that the heat transfer in the longitudinal direction is fairly localized and concentrated around the entrance and exit of the impingement zones, and that it has little effect on the prediction accuracy. These observations suggest that both 2D transverse and 2D

longitudinal modellings would have slight but not significant effect on the ROT cooling process.

## **8.2 Suggestions and Future Work**

### **1. TC installation**

To realize more reliable temperature measurement in experimental tests and then to obtain more accurate inverse calculation results in the future, several modifications to TC installations should be conducted.

First, surface TCs should not be used on the cooled surface since it may cause significant measurement error and disturbs the heat transfer behaviour. This modification has been performed in the moving plate tests.

Second, TCs with separation measuring junction should be avoided in water jet cooling even if it is installed inside of the plate and opposite to the cooled surface. It is not guaranteed that the connection line of the two wires is perpendicular to the water moving direction. TCs should be, generally, of the bead type.

Third, the imbedded bead-type TCs should be installed in a carefully designed hole. The hole diameter should be as small as possible, and its distance to the cooled surface should have a minimum value to avoid disturbing the surface temperature profile and the heat transfer behaviour.

Finally, the distance between two TCs should be less than 10 mm for stationary plates if the FZM will be used for inverse calculations. The results from the FZM may be a good approximation to real ones with a smaller distance. By contrast, the distance between two TCs in the moving direction for the moving plate may be larger than 10 mm even if the FZM is used.

### **2. Single nozzle tests using stationary plates**

Further tests using a single nozzle should be designed to investigate the thermodynamics in the impingement zone and to determine the impingement zone size and the progressing speeds of water cooling zones because they are of importance to the moving plate cooling and to the application of the FMM in inverse calculations. Thus, more temperature measurements should be conducted in one test. With an increased number of measurements the stagnation point may be also accurately located.

Further experimental studies should extend to heat transfer using lower initial temperature of plates, by changing the nozzle geometry and orientation, jet profile and velocity, different surface roughness and plunging jet.

### 3. Multiple nozzle tests

The cooling condition using one nozzle is mostly for academic interest and is far from the real situation. To make the experimental condition closer to the real ROT conditions, at least three nozzles in one jetline should be used. For stationary plates, TC can be arranged in the scheme shown in Figure 8.1. Besides, extra TCs should be arranged along lines that are perpendicular to the jetline. It is better to install two groups of TCs as shown in Figure 8.1a. This setup can also be used for moving plates. In this case, the plate moving direction is perpendicular to the jetline and TCs should be in the upstream side.

With this setup, the interaction on the cooled surface that does not occur in the case of single jets can be included and investigated. The interaction is mostly associated with adjacent impinging jets and refers to the collision of the surface flow, i.e., the wall jets. This interaction is of increasing importance when the jets are closely spaced, and when the distance from the nozzle exit to the plate is small, and the jet velocity is large.

A better scenario is shown in Figure 8.1b. With such a design the cooling conditions will be close to those on real ROT. And the obtained data may be of great accuracy and useful for the simulation of the ROT cooling process.

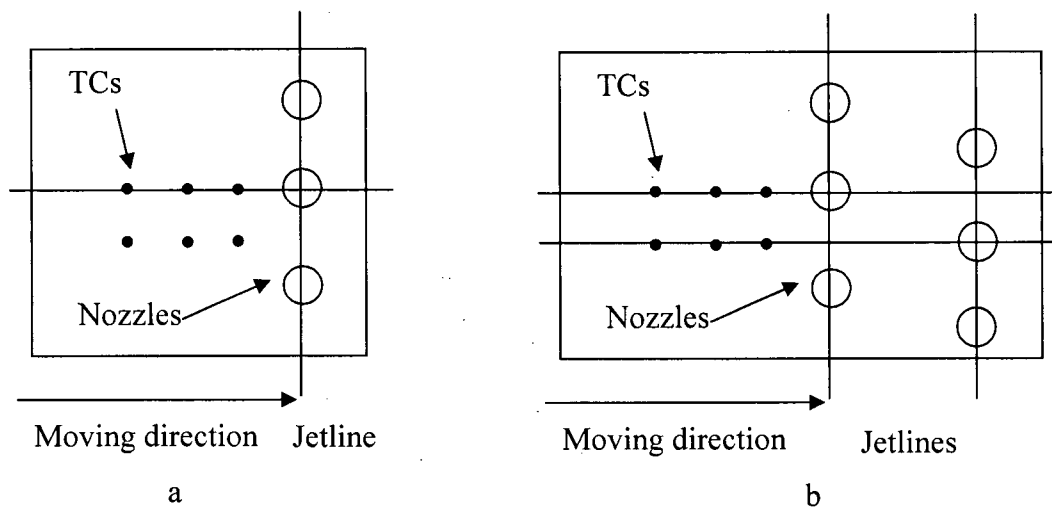


Figure 8.1 Extra TCs and nozzles for future tests

The nozzles should be opened to stabilize the flow rate before the plate arrives underneath the nozzles. The flow rate, water pressure (water height level in the tank) should be kept constant as much as possible during the cooling process. This means that there should be a source of water supply to the tank during the experiment.

#### **4. New IHCP models**

New IHCP models are to be developed to determine the surface heat fluxes and surface temperatures from the internal temperatures measured in tests using higher moving plates and multiple jets.

The existing IHCP model has been tested for the single circular jet with stationary or slow moving plates. It is necessary to extend the model for cases using higher moving plates whose speeds are comparable to those used in industrial ROTs. The possibility of modelling the moving case with one single jet as a quasi-2D problem should be investigated and the effect of moving speed should be studied.

Significantly different heat fluxes may be generated when using multiple jets, and may create large temperature gradients across the jetline between two jets. A new 3D model for multiple jets should be developed, tested and optimized. The model should consider the interaction between two or more jets. Special numerical tests, which are similar or equivalent to the physical tests, should be used to validate 3D FE IHCP modelling.

#### **5. Analyses of thermal stresses on ROT cooling**

Another area for future work is to develop a 2D/3D FE model to investigate the thermal stresses due to the large temperature gradients that occur in the jet impingement cooling process, especially when multiple jets and/or strips/plates of larger thickness are used.

The 2D modelling should be able to predict the thermal stresses under the cooling conditions using one single jet, either stationary or moving plate. The 3D model should be able to predict the thermal stresses under the cooling conditions using multiple water circular jets or one single water curtain jet with non-uniform water capacity setup.

This study will help provide information for balancing water on the top and bottom surfaces at an optimum ratio and for setting the appropriate transverse water amount gradient from centre to edge to prevent operation problems and/ or non-uniform mechanical properties.

## **6. Water jet hydrodynamic simulation**

Appropriate heat transfer modelling requires information about velocities, temperatures and phase changes on the plate surface. The physical experiments entail many problems such as cost, time, efficiency and accuracy. It is not possible to experimentally investigate the vast number of parameters in this complex process. Therefore, an important area of future work in the numerical aspect is to develop FE models for the hydrodynamics of the flow. These models would enable an efficient and inexpensive parametric study on the various parameters affecting the flow and pressure conditions of water jet and then predict the heat transfer modes along the interactive surface under conditions similar to industry practice. This study can significantly improve the understanding of the heat transfer of jet impingement and compliment the experimental data.

## Bibliography

- [1] M. Korchynsky, Development of "controlled cooling" practice, *Accelerated Cooling of Steel*, P. D. Southwick (ed.), 1986, pp. 3–14.
- [2] G. Tacke, H. Litzke and E. Raquet, Investigations into the efficiency of cooling systems for wide-strip hot rolling mills and computer-aided control of strip cooling, *Accelerated Cooling of Steel*, P. D. Southwick (ed.), 1986, pp. 35–54.
- [3] S. J. Chen, A. A. Tseng and F. Han, Spray and jet cooling in steel rolling, *Heat Transfer in Metals and Containerless Processing and Manufacturing American Society of Mechanical Engineers, Heat-Transfer*, Vol. 162, 1991, pp. 1–11, or *International Journal of heat and fluid flow*, Vol. 13 No. 4, 1992, pp. 358–369.
- [4] D. H. Wolf, F. P. Incropera and R. Viskanta, Jet impingement boiling, *Advances in Heat Transfer*, Vol.23, 1992, pp. 5–132.
- [5] D. A. Zumbrennen, F. P. Incropera and R. Viskanta, Method and Apparatus for measuring heat transfer distributions on moving and stationary plates cooled by a planar liquid jet, *Experimental Thermal and Fluid Science*, Vol. 3, 1990, pp. 202–213.
- [6] B. W. Webb and C. F. Ma, Single-phase liquid jet impingement heat transfer, *Advances in Heat Transfer*, Vol.26, 1995, pp. 105–217.
- [7] V. Olden and M. Raudensky, Water spray cooling of stainless and C-Mn steel, *Steel Research*, Vol. 69 No.6, 1998, pp 240–246.
- [8] T. Ochi, S. Nakanishi, M. Kaji and S. Ishigai, Cooling of a hot plate with an impinging circular jet, *Multi-Phase flow and heat transfer III, proceedings of the third multi-phase heat and flow transfer symposium workshop*, Miami Beach, Florida, USA, Apr 18–20,1983, pp. 671–681.
- [9] S. Ishigai, S. Nakanishi and T. Ochi, Boiling heat transfer for plane water jet impinging on a hot surface, *Sixth International Heat Transfer Conference*, Toronto, Ontario, Canada, August 1978.
- [10] D. T. Vader, F. P., Incropera and R. Viskanta, A method for measuring steady local heat transfer to an impinging liquid jet, *Experimental Thermal and Fluid Science*, Vol. 4, 1991, pp. 1–11.

- [11] D. T. Vader, F. P. Incropera and R. Viskanta, Convective nucleate boiling on a heated surface cooled by an impinging, planar jet of water, *Journal of Heat Transfer*, Vol. 114, 1992, pp. 152–160.
- [12] D. H. Wolf, F. P. Incropera, R. Viskanta, Local jet impingement boiling heat transfer, *International Journal of Heat and Mass Transfer*, Vol. 39, 1996, pp. 1395–1406
- [13] S. J. Chen, J. Kothari and A. A. Tseng, Cooling of a moving plate with an impinging circular water jet, *Experimental Thermal and Fluid Science*, Vol. 4, 1991, pp. 343–353.
- [14] F. Han, S. J. Chen and C. C. Chang, Effect of surface motion on liquid jet impingement heat transfer, *Fundamentals of Forced and Mixed Convection and Transport Phenomena*, American Society of Mechanical Engineers, Heat Transfer, Vol. 180, 1991, pp. 73–81.
- [15] S. J. Chen and S. K. Biswas et al, A., Modeling and analysis of controlled cooling for hot moving metal plates, *Monitoring and Control for Manufacturing Processes*, American Society of Mechanical Engineers, Production Engineering Division (Publication) PED, Vol. 44, 1990, pp. 465–474.
- [16] J. Stevens and B. W. Webb, Local heat transfer coefficients under an axisymmetric, single-phase liquid jet, *Journal of Heat Transfer*, Vol. 113, 1991, pp. 71–78.
- [17] D. A. Zumbrunnen, R. Viskanta and F. P. Incropera, The effect of surface motion on forced convection film boiling heat transfer, *Journal of Heat Transfer*, Vol. 111, 1989, pp. 760–766.
- [18] J. Chen, T. Wang, and D. A. Zumbrunnen, Numerical analysis of convective heat transfer from a moving plate cooled by an array of submerged planar jets, *Heat Transfer in Metals and Containerless Processing and Manufacturing American Society of Mechanical Engineers, Heat-Transfer*, Vol. 162, pp. 25–34.
- [19] J. Filipovic, J. Viskanta and F. P. Incropera, Thermal behavior of a moving steel strip cooled by an array of planar water jets, *Steel Research*, Vol. 63 No. 10, 1992, pp. 438–446.
- [20] J. Filipovic, J. Viskanta and F. P. Incropera, Cooling of a moving steel strip by an array of round jets, *Steel Research*, Vol. 65 No. 12, 1994, pp. 541–547.

- [21] N. Hatta and Y. Tanaka, A numerical study on cooling process of hot steel plates by a water curtain, *ISIJ International*, Vol. 29 No. 8, 1989, pp. 673–679.
- [22] N. Hatta and H. Osakabe, Numerical modeling for cooling process of a moving hot plate by a laminar water curtain, *ISIJ International*, Vol. 29 No. 11, 1989, pp. 919–925.
- [23] Z. Liu, Experiments and mathematical modeling of controlled run-out table cooling in a hot rolling mill, *Ph. D. Thesis*, the University of British Columbia, 2001.
- [24] Z. Liu, D. Fraser and I.V. Samarasekera, Experimental study and calculation of boiling heat transfer on steel plates during run-out table operation, *Canadian Metallurgical Quarterly*, Vol.41, 2002, pp. 63–74.
- [25] Z. Liu, D. Fraser, I.V. Samarasekera and G. T. Lockhart, Experimental observation and modeling of thermal history within a steel plate during water jet impingement, *Canadian Metallurgical Quarterly*, Vol.41, 2002, pp. 75–86.
- [26] A. T. Hauksson, Experimental study of boiling heat transfer during water jet impingement on a hot steel plate, *Master Thesis*, the University of British Columbia, 2001.
- [27] Q. Meng, Experimental study of transient cooling of a hot steel plate by an impinging circular jet, *Master Thesis*, the University of British Columbia, 2002.
- [28] L. Michalski, K. Eckersdorf and J. McGhee, *Temperature Measurement*, John Wiley & Sons Ltd., 1991, pp.334–360.
- [29] R. E. Bentley, *Theory and Practice of Thermoelectric Thermometry*, Handbook of Temperature Measurement, Vol. 3, Springer-Verlag, 1998.
- [30] R. J. Moffat, The gradient approach to thermocouple circuitry, *Temperature-Its Measurement and Control in Science and Industry*, Reinhold, New York, 1962, pp. 33-38.
- [31] D. K. Hennecke and E. M. Sparrow, Local heat sink on a convectively cooled surface-Application to temperature measurement error, *International Journal of Heat and Mass Transfer*, Vol. 13, 1970, pp.287–304.
- [32] J. E. Park, K. W. Childs, G. M. Ludtka and W. Chu, Correction of errors in intrinsic thermocouple signals recorded during quenching, *National Heat Treat Conference*, Minneapolis, MN, July 26-31, 1991, pp. 309–318.

- [33] F. White, Accuracy of TCs in radiant-heat testing, *Experimental Mechanics*, Vol.2, 1962, pp.204–210.
- [34] M. H. Attia and L. Kops, Distortion in thermal field around inserted thermocouples in experimental interfacial studies, *Journal of Engineering for Industry*, Vol. 108, 1986, pp. 241–246.
- [35] M. H. Attia and L. Kops, Distortion in thermal field around inserted thermocouples in experimental interfacial studies - Part 2: Effect of the heat flow through the thermocouple, *Journal of Engineering for Industry*, Vol. 110, 1988, pp. 7–14.
- [36] M. H. Attia and L. Kops, Distortion in thermal field around inserted thermocouples in experimental interfacial studies - Part 3: Experimental and numerical verification, *Journal of Engineering for Industry*, Vol. 115, 1993, pp. 444–449.
- [37] M. H. Attia, A. Cameron and L. Kops, Distortion in thermal field around inserted thermocouples in experimental interfacial studies - Part 4: End effect, *Journal of Manufacturing Science and Engineering*, Vol. 124, 2002, pp. 135–145.
- [38] T. C. Tszeng and V. Saraf, A study of fin effects in the measurement of temperature using surface-mounted thermocouples, *Journal of Heat Transfer*, Vol. 125, 2003, pp. 926–935.
- [39] D. Li, Boling water heat transfer during quenching of steel plates and tubes, *Ph.D. thesis*, the University of British Columbia, 2003.
- [40] J. V. Beck, B. Blackwell and C. R. S. Clair Jr., *Inverse Heat Conduction: Ill-posed Problem*, Wiley-Interscience Publication, New York, 1985.
- [41] O. M. Alifanov, *Inverse Heat Transfer Problem*, Springer, Berlin, 1994.
- [42] N. Al-Khalidy, A general space marching algorithm for the solution of two-dimensional boundary inverse heat conduction problems, *Numerical Heat Transfer*, Part B, Vol. 34, 1998, pp.339–360.
- [43] R. A. Khache and Y. Jarny, Determination of heat sources and heat transfer coefficient for two-dimensional heat flow—numerical and experimental study, *International Journal of Heat and Mass Transfer*, Vol. 44, 2001, pp.1309–1322.
- [44] S. K. Kim, W. I. Lee, Solution of inverse heat conduction problems using maximum entropy method, *International Journal of Heat and Mass Transfer*, Vol. 45, 2002, pp. 381–391.

- [45] E. Videcoq, D. Petit, Model reduction for the resolution of multidimensional inverse heat conduction problems, *International Journal of Heat and Mass Transfer*, Vol. 44, 2001, pp. 1899–1911.
- [46] C. F. Weber, Analysis and solution of the ill-posed inverse heat conduction problem, *International Journal of Heat and Mass Transfer*, Vol. 24, 1981, pp. 1783–1792.
- [47] B. R. Bass, Application of the finite element method to the nonlinear inverse heat conduction problem using Beck's second method, *Journal of Engineering and Industry*, Transaction ASME, Vol. 102, 1980, pp. 168–176.
- [48] A.S. Osman, Investigation of transient heat transfer coefficients in quenching experiments, *Journal of Heat Transfer*, Transaction ASME, Vol. 112, 1990, pp. 843–848.
- [49] S. Kumagai, S. Suzuki, Y. R. Sano and M. Kawazoe, Transient cooling of a hot slab by an impinging jet with boiling heat transfer, *ASME/JSME Thermal Engineering Conference*, Vol. 2 ASME 1995, pp. 347–352.
- [50] H. Louahia-Gualous, P. K. Panday and E. A. Artioukhine, Inverse determination of the local heat transfer coefficients for nucleate boiling on a horizontal pipe cylinder, *Journal of Heat Transfer*, Vol. 125, 2003, pp. 1087–1095.
- [51] H. K. Kim, S. I. Oh, Evaluation of heat transfer coefficient during heat treatment by inverse analysis, *Journal of Material Processing Technology*, Vol. 112, 2001, pp. 157–165.
- [52] M. Pietrzyk, J. G. Lenard, A study of heat transfer during flat rolling, *International Journal for Numerical Methods in Engineering*, Vol. 30, 1990, pp. 1459–1469.
- [53] J. V. Beck and H. Hurwicz, Effect of thermocouple cavity on heat sink temperature, *Journal of Heat Transfer*, Vol.2, 1960, pp. 27–36.
- [54] C. T. Kidd, High heat flux measurements and experimental calibrations, *NASA Conf. Publish*, No.31, 1992, pp.31–50.
- [55] F. Xu and M. S. Gadala, A simple FE-inverse heat conduction algorithm and its application to the determination of surface heat flux during water jet cooling, *5<sup>th</sup> International Symposium on Multiphase Flow, Heat Mass Transfer and Energy Conversion*, Xi'an, China, 3–6 July 2005.

- [56] M. S. Gadala and F. Xu, A FE-based sequential algorithm for the determination of heat flux during impingement water cooling, *International Journal of Numerical Methods for Heat & Flow Fluid*, in press.
- [57] K. J. Bathe, *Finite Element Procedures in Engineering Analysis*, Prentice-Hall, 1982.
- [58] R. W. Lewis, *The Finite Element Method in Heat Transfer Analysis*, Wiley-Interscience Publication, New York, 1996.
- [59] ANSYS, *User's Manual*, Swanson Analysis Systems Inc., 2002.
- [60] F. Xu and M. S. Gadala, Investigation of error sources in temperature measurement using thermocouples in water impingement cooling, *Experimental Heat Transfer*, Vol. 18, No.3/July-September, 2005, pp.153–177.
- [61] F. Xu and M.S. Gadala, Study on the application of thermocouple with separate measuring junction in temperature measurement in water-cooling, submitted to *Numerical Heat Transfer-B*.
- [62] F. Xu and M.S. Gadala, Heat transfer behavior in the impingement zone under circular water jet, *International Journal of Heat and Mass Transfer*, accepted in Feb., 2006.
- [63] G. Wei, X. Dong and J. Wang, Study on convective heat transfer coefficient of high temperature plate during water curtain cooling, *Kang-T'ieh-Iron and Steel-(In Chinese)*, Vol. 29, 1994, p 22–26.
- [64] F. Xu and M.S. Gadala, A novel FE approach to simulate the run-out table cooling of steel strips, submitted to *Steel Research*.
- [65] R. Colas, Modelling run out table cooling, *Manufacturing Science and Engineering American Society of Mechanical Engineers*, Production Engineering Division (Publication) PED, Vol. 68-2, 1994, ASME, New York, NY, USA, pp. 611–617.
- [66] H. Dyja and P. Korczak, The thermal-mechanical and microstructural model for the FEM simulation of hot plate rolling, *Journal of Materials Processing Technology*, 92-93 (1999), pp. 463-467.
- [67] M. Suehiro and K. Sato, Mathematical model for predicting microstructural changes and strength of low carbon steels in hot strip rolling, THERMC-88: *International conference on physical metallurgy of thermomechanical processing of steels and*

- other metals*: Proceedings, June 6–10, 1988, Keidanren Kaikan, Tokyo, Japan, pp. 791–798.
- [68] M. Suehiro, T. Senuma and H. Yada et al, Application of mathematical model for predicting microstructural evolution to high carbon steels, *ISIJ International*, Vol. 32 No. 3, 1992, pp. 433–439.
- [69] A. Prasad, S. Jha and N. S. Mishra, Modelling of microstructural evolution during accelerated cooling of hot strip on the run-out table, *Steel Research*, Vol. 66, 1995, pp. 416–423.
- [70] A. Kumar and C. McCulloch, Modelling thermal and microstructural evolution on run-out table of hot strip mill, *Material Science and Technology*, Vol. 7, 1991, pp. 360–368.
- [71] C. A. McCulloch, Characterization of the cooling and transformation of steels on a run-out table of hot-strip mill, *Master Thesis*, the University of British Columbia, 1989.
- [72] M. Packo, H. Kusiak and M. Pietrzyk, Modelling water cooling of steel strip during hot rolling, *Steel Research*, Vol. 64, 1993, pp. 128–131.
- [73] M. Pietrzyk, Finite element based model of structure development in the hot rolling process, *Steel Research*, Vol. 61, 1990, pp. 603–607.
- [74] R. K. Kumar, S. K. Sinha and A. K. Lahiri, Modelling of the cooling process on the run-out table of a hot strip mill - a parallel approach, *Conference Record IAS Annual Meeting (IEEE Industry Applications Society)*, Vol. 4, 1996, pp. 2563–2571.
- [75] R. K. Kumar, S. K. Sinha and A. K. Lahiri, Real time simulator for the run-out table of hot strip mills, *Conference Record IAS Annual Meeting (IEEE Industry Applications Society)*, Vol. 4, 1996, pp. 2547–2554.
- [76] V. H. Hernandez-Avila, Heat transfer model of the hot rolling run-out table cooling and coil cooling of steel, *Master Thesis*, the University of British Columbia, 1994.
- [77] V. H. Hernandez-Avila, Modelling of the thermal evolution of steel strips cooled in the hot rolling run-out table, *PhD Thesis*, the University of British Columbia, 2000.
- [78] J. Filipovic, J. Viskanta and F. P. Incropera, A parameter study of the accelerated cooling of steel strip, *Steel Research*, Vol. 63, 1992, pp. 496–499.

- [79] R. M. Guo, Heat transfer of laminar flow cooling during strip acceleration on hot strip mill run-out tables, *Iron and Steelmaker*, Vol. 20 No. 8, Aug 1993, pp. 49–59.
- [80] R. M. Guo, Modeling and simulation of run-out table cooling control using feedforward-feedback and element tracking system, *IEEE Transactions on Industry Applications*, Vol. 33, 1997, pp. 304–311.
- [81] R. M. Guo and S. T. Hwang, Investigation of strip cooling behavior in the run-out section of hot strip mills, *Journal of Materials Processing and Manufacturing Science*, Vol. 4, Apr 1996, pp. 339–351.
- [82] M. M. Prieto, L. S. Ruiz and J. A. Menendez, Thermal performance of numerical model of hot strip mill run-out table, *Ironmaking and Steelmaking*, Vol. 28, 2001, pp. 474–480.
- [83] C. G. Sun, H. N. Han and J. K. Lee, A finite element model for the prediction of thermal and metallurgical behavior of strip on run-out table in hot rolling, *ISIJ International*, Vol. 42, 2002, pp.392-400.
- [84] C. A. Muojekwu, Modeling of thermomechanical and metallurgical phenomena in steel strip during hot direct rolling and run-out table cooling of thin-cast slabs, *PhD Thesis*, the University of British Columbia, 1998.
- [85] M. Miyake, J. M. Too and I. V. Samarasekera, Mathematical modelling of hot rolling of steel strip with microstructure analysis, *Simulation of Materials Processing: Theory, Methods and Application*, Mori (ed.), 2001 Sweits & Zeitlinger, Lisse, pp. 275–280.
- [86] C. M. Sellars, Modelling microstructural development during hot rolling, *Materials Science and Technology*, Vol. 6, 1990, pp. 1072–1081.
- [87] H. Yada, Prediction of microstructural changes and mechanical properties in hot strip rolling, *Accelerated Cooling of Steel*, P. D. Southwick (ed.), 1986, pp. 105–119.
- [88] G. Uetz, G. Woelk and T. Bishops, Influencing the formation of the steel structure by suitable temperature control in the run-out sections of hot-strip mills, *Steel Research*, Vol. 62, 1991, pp.216–232.

## Appendix A

### Finite Element Matrix Equations for Conduction Heat Transfer

The governing equation for conduction heat transfer in three dimensional solid is given by:

$$\rho c \frac{\partial T}{\partial t} = \left[ \frac{\partial}{\partial x} \left( k_x \frac{\partial T}{\partial x} \right) + \frac{\partial}{\partial y} \left( k_y \frac{\partial T}{\partial y} \right) + \frac{\partial}{\partial z} \left( k_z \frac{\partial T}{\partial z} \right) \right] + q^b \quad (\text{A.1})$$

where  $k_x, k_y, k_z$  are the thermal conductivities in  $x, y$  and  $z$  directions, respectively,  $T$  is the temperature,  $q^b$  is the internal rate of heat generated per unit volume,  $t$  is time,  $\rho$  is the density and  $c$  is the specific heat.

The above equation may be subject to the general form of the boundary conditions of:

$$-k_n \frac{\partial T}{\partial n} = q^s + h(T_f - T_s) + \varepsilon \sigma (T_{sr}^4 - T_r^4) \quad (\text{A.2})$$

where  $n$  is the normal to the boundary.

The input heat flux is considered only on pertinent surfaces, i.e., surfaces that have specified boundary conditions and are given by:

Concentrated or distributed flux ( $q^s$ );

Convection BC:  $h(T_f - T_s)$ ,  $h$  is the convection HTC,  $T_f$  is the fluid temperature and  $T_s$  is the surface temperature;

Radiation BC:  $\varepsilon \sigma (T_r^4 - T_{sr}^4)$ ,  $\varepsilon$  is the emissivity of the surface,  $\sigma$  is the Stefan-Boltzmann constant,  $T_{sr}$  is the absolute temperature of surface and  $T_r$  is the known temperature of the external radiative source.

The sources of nonlinearity in equation (A.1) may be due to temperature dependent material properties or dependency of the boundary conditions on temperature.

Now, we assume an approximation function for the temperature given by:

$$T(\mathbf{x}) = N_i(\mathbf{x})T_i \quad (\text{A.3})$$

where  $N_i(\mathbf{x})$  is the approximation function with  $i$  varying from one to the number of nodes per element, the vector  $\mathbf{x}$  has the components  $x$ ,  $y$  and  $z$ , and  $T_i$  are the nodal temperature. Note that we consider only a typical element and assume that the normal finite element assembly procedures apply.

Applying Galerkin approach and utilizing Gauss theorem, the equivalent finite element equations representing equations (A.1) and (A.2) may be written in the following final form:

$$[C] \cdot \{T^e\} + [[K_c] + [K_h] + [K_r]] \cdot \{T^e\} = \{Q\}^b + \{Q\}^s + \{Q\}^h + \{Q\}^r \quad (\text{A.4})$$

where the definitions of terms in equation (A.4) are summarized in Table A.1.

Considering the general nonlinear and transient case of equation (A.4), the solution may be realized by re-writing the equation at time  $(t+\Delta t)$  and iteration  $(i)$  in the following form:

$${}^{t+\Delta t} \mathbf{C}^{(i)} \cdot {}^{t+\Delta t} \mathbf{T}^{(i)} + {}^{t+\Delta t} (\mathbf{K}^c + \mathbf{K}^h + \mathbf{K}^r) \cdot {}^{t+\Delta t} \mathbf{T}^{(i)} = ({}^{t+\Delta t} \mathbf{Q}^b + {}^{t+\Delta t} \mathbf{Q}^s + {}^{t+\Delta t} \mathbf{Q}^h + {}^{t+\Delta t} \mathbf{Q}^r)^{(i)} \quad (\text{A.5})$$

It may be shown that using Newton-Raphson approximation and the  $\alpha$ -method, the solution to the above equation yields:

$${}^{t+\alpha\Delta t} \left[ (\mathbf{K}^c + \mathbf{K}^h + \mathbf{K}^r) + \left( \frac{1}{\alpha\Delta t} \right) \cdot \mathbf{C} \right] \cdot \Delta \mathbf{T}^{(i)} = {}^{t+\alpha\Delta t} (\mathbf{Q}^b + \mathbf{Q}^s) + {}^{t+\alpha\Delta t} (\hat{\mathbf{Q}}^h + \hat{\mathbf{Q}}^r)^{(i-1)} - {}^{t+\alpha\Delta t} (\hat{\mathbf{Q}}^c + \hat{\mathbf{q}}^c)^{(i-1)} \quad (\text{A.6})$$

where the definition of the new terms introduced here are given in Table A.2.

Table A.1 Definition of the terms in the general FE heat conduction equation

Term	Definition
$[C] = \int \rho c [N]^T [N] dV$	Thermal capacity matrix
$[K_c] = \int [B]^T [K] [B] dV$	Thermal conductivity matrix
$[K_h] = \int h [N^s]^T [N^s] dS$	Thermal conductivity matrix due to convection BC
$[K_r] = \int \kappa [N^s]^T [N^s] dS$	Thermal conductivity matrix due to radiation BC
$\{Q\}^b = \int q^b [N]^T dV$	Heat flux vector due to internal heat generation
$\{Q\}^s = \int q^s [N^s]^T dS$	Heat flux vector due to input surface flux
$\{Q\}^h = \int h T_f [N^s]^T dS$	Heat flux vector due to convection BC
$\{Q\}^r = \int \kappa T_r [N^s]^T dS$	Heat flux vector due to radiation BC
$\{T\}, \{\bar{T}\}$	Vector of global nodal temperatures and temperature gradients, respectively
$\kappa = \epsilon \sigma (T_r^2 + T_{sr}^2)(T_r + T_{sr})$	Equivalent heat transfer coefficient due to radiation
$\left\{ \frac{\partial T}{\partial \mathbf{x}} \right\} = \frac{\partial}{\partial \mathbf{x}} (N_i \bar{T}_i) = [B] \{\bar{T}\}^e$	Partial derivative of temperature
$[K] = \begin{bmatrix} k_x & 0 & 0 \\ & k_y & 0 \\ sym & & k_z \end{bmatrix}$	Element conductivity matrix
$[N] = [N_1 \quad N_2 \quad \dots \quad N_n]$	Approximation or shape function, $n$ is the number of nodes per element

Table A.2 Definition of the terms in heat transfer equation

Term	Meaning	Expression
${}^{t+\Delta t} \hat{\mathbf{Q}}_h^{(i-1)}$	Nodal heat flux contribution due to convection BC, nonlinear and transient effects	${}^{t+\Delta t} \hat{\mathbf{Q}}_h^{(i-1)} = \int_{S_h} {}^{t+\Delta t} h^{(i-1)} \mathbf{N}^{S^T} \mathbf{N}^S ({}^{t+\Delta t} \mathbf{T}_f - {}^{t+\Delta t} \mathbf{T}^{(i-1)}) \cdot dS$ <p>Note: <math>\int_{S_h} {}^{t+\Delta t} h^{(i-1)} \mathbf{N}^{S^T} \mathbf{N}^S \cdot dS = {}^{t+\Delta t} \mathbf{K}^h^{(i-1)}</math></p>
${}^{t+\Delta t} \hat{\mathbf{Q}}_r^{(i-1)}$	Nodal heat flux contribution due to radiation B.C., nonlinear and transient effects	${}^{t+\Delta t} \hat{\mathbf{Q}}_r^{(i-1)} = \int_{S_h} {}^{t+\Delta t} \kappa^{(i-1)} \mathbf{N}^{S^T} \mathbf{N}^S ({}^{t+\Delta t} \mathbf{T}_r - {}^{t+\Delta t} \mathbf{T}^{(i-1)}) \cdot dS$ <p>Note: <math>\int_{S_h} {}^{t+\Delta t} \kappa^{(i-1)} \mathbf{N}^{S^T} \mathbf{N}^S \cdot dS = {}^{t+\Delta t} \mathbf{K}^r^{(i-1)}</math></p>
${}^{t+\Delta t} \hat{\mathbf{Q}}_c^{(i-1)}$	Nodal heat flux contribution due to conductivity, nonlinear and transient effects	${}^{t+\Delta t} \hat{\mathbf{Q}}_c^{(i-1)} = \int \mathbf{B}^T {}^{t+\Delta t} \mathbf{K}^{(i-1)} \mathbf{B} {}^{t+\Delta t} \mathbf{T}^{(i-1)} \cdot dV$ <p>Note: <math>\int \mathbf{B}^T {}^{t+\Delta t} \mathbf{K}^{(i-1)} \mathbf{B} dV = {}^{t+\Delta t} \mathbf{K}^C^{(i-1)}</math></p>
${}^{t+\Delta t} \hat{\mathbf{q}}^{(i-1)}$	Nodal heat flux contribution due to thermal capacity, nonlinear and transient effects	${}^{t+\Delta t} \hat{\mathbf{q}}^{(i-1)} = \int {}^{t+\Delta t} (\rho c)^{(i-1)} \mathbf{N}^T \mathbf{N} \cdot [({}^{t+\Delta t} \mathbf{T}^{(i-1)} - {}^t \mathbf{T}) / \Delta t] \cdot dV$ $\equiv {}^{t+\Delta t} \mathbf{C}^{(i-1)} [{}^{t+\Delta t} \mathbf{T}^{(i-1)} - {}^t \mathbf{T}] / \Delta t$